UNIVERSITY OF CALIFORNIA, SAN DIEGO

Biological and Synthetic Locomotion in Newtonian and Complex Fluids at Low Reynolds Number

A dissertation submitted in partial satisfaction of the
requirements for the degree
Doctor of Philosophy

in

Engineering Sciences (Mechanical Engineering)

by

On Shun Pak

Committee in charge:

Professor Eric Lauga, Chair
Professor Juan Carlos del Alamo
Professor Marcos Intaglietta
Professor Daniel Tartakovsky
Professor Qiang Zhu

2013

The dissertation of On Shun Pak is approved, and it is acceptable in quality and form for publication on microfilm and electronically:

_____

_____

_____

_____

_____

Chair

University of California, San Diego

2013

DEDICATION

To my brother.

EPIGRAPH

No pressure, but you have to be awesome.
—Eric Lauga

TABLE OF CONTENTS

LIST OF FIGURES

LIST OF TABLES

ACKNOWLEDGEMENTS

First of all, I would like to thank my thesis advisor, Eric Lauga, for being an awesome advisor. Eric has been a source of inspiration, encouragement, joy and fun throughout the journey of bringing me up as a scientist and a better person. Eric will remain my personal hero for the rest of my life. My favorite quotes of him are "No pressure, but you have to be awesome!" "You should be happy!" and "May the Force be with you."

I want to thank my thesis committee members Juan Carlos del Alamo, Marcos Intaglietta, Daniel Tartakovsky, and Qiang Zhu for guiding me through the journey. Juan Carlos also taught one of the classes I learned the most at UCSD. A special thanks goes to Daniel for his valuable advice on my personal and academic growth, which I can only pay back through my valuable advice on Dim Sum.

I have been very fortunate to be surrounded by wonderful colleagues, who formed a bath of awesomeness for me to improve by diffusion. Foremost is my very good friend Gwynn Elfring, with whom I grew up academically and shared all the joys and heart attacks. Gwynn is my great companion in the pursuit of science and happiness in life. I am also extremely grateful to have found a dear friend and mentor, Saverio Spagnolie, from whom I learned a lot about science and myself. Art Evans is always the funny and knowledgeable physicist I look up to. I also thank the younger members, Greg Wagner and Yi Man, for asking questions that I don't know the answers to. I enjoyed very much the days when I shared an office with Mario Espinoza and Rodrigo Velez from Mexico, and Diego Lopez and Francois Nadal from France.

I also thank my collaborators Joseph Wang and his student Wei Gao at UCSD, and Luca Brandt and his student Lailai Zhu from KTH (Sweden), for their important contributions to different aspects of this thesis. I especially thank Joseph Wang for his guidance and help on my career development.

Besides research, I have really enjoyed my teaching experiences at UCSD, thanks to all the professors (David Miller, Hidenori Murakami, Eric Lauga, and Daniel Tartakovsky) I worked with as a TA. My teaching experiences with students at UCSD contain some of the most encouraging and touching moments in my PhD studies. I owe my students a big thanks.

I wish to thank Bill Kuo, Kit Lee, Gary Ng, Jian Wang, Kang Wang, Peng Wang, Weiguang Yang, Gardon Yang, and Kevin Zhao for being them. I am blessed to find these sincere friends in San Diego. I also appreciate the prayers and support from my church.

I want to thank my parents for their unconditional love and support, my sister for taking care of things in Hong Kong, and my brother for being the reason I study biological fluid mechanics. I thank Jing for loving and supporting me through the ups and downs in this journey, and the coming ones.

Finally, I would like to express my heartfelt gratitude to the funding I received from the Croucher Foundation (through a Croucher Foundation Scholarship), the Siebel Foundation, the Kaplan Dissertation Year Fellowship and the Cal-RA Fellowship from UCSD, NSF(CTS-0624830) and NSF(CBET-0746285).

Chapter 1, in small part, is a reprint of the material as it appears in Journal of The Royal Society Interface 2012. Pak, On Shun; Spagnolie, Saverio E.; Lauga, Eric, the Royal Society, 2012. The dissertation author was the primary investigator and author of this paper.

Chapter 2, in full, is a reprint of the material as it appears in Proceedings of the Royal Society A 2009. Pak, On Shun; Lauga, Eric, the Royal Society, 2009. The dissertation author was the primary investigator and author of this paper.

Chapter 3, in full, is a reprint of the material as it appears in Journal of The Royal Society Interface 2012. Pak, On Shun; Spagnolie, Saverio E.; Lauga, Eric, the Royal Society, 2012. The dissertation author was the primary investigator and author of this paper. Useful conversations with Dr. Michael Werner and Dr. Anne Swan are gratefully acknowledged.

Chapter 4, in full, is a reprint of the material as it appears in Soft Matter 2011. Pak, On Shun; Gao, Wei; Wang, Joseph; Lauga, Eric, the Royal Society of Chemistry, 2011. The dissertation author was the primary investigator and author of this paper. The dissertation author thanks Professor Eric Fullerton, Erik Shipton, and Daniel Kagan for their help on the magnetic setup, and Allen Pei, Adam Ponedal for assisting in the nanowire preparation. Useful discussions with Saverio Spagnolie are acknowledged.

Chapter 5, in full, is a reprint of the material as it appears in Physics of Fluids 2011. Pak, On Shun; Lauga, Eric, the American Institute of Physics, 2011.

The dissertation author was the primary investigator and author of this paper. The dissertation author thanks Saverio Spagnolie and Gwynn Elfring for useful discussions.

Chapter 6, in full, is a reprint of the material as it appears in Physical Review E 2010. Pak, On Shun; Normand, Thibaud; Lauga, Eric, the American Physical Society, 2010. The dissertation author was the primary investigator and author of this paper.

Chapter 7, in full, is a reprint of the material as it appears in Physics of Fluids 2012. Pak, On Shun; Zhu, Lailai; Brandt, Luca; Lauga, Eric, the American Institute of Physics, 2012. The dissertation author was the primary investigator and author of this paper.

Also as part of the author's PhD experience, the author co-authored two other papers not appearing in this dissertation. They are the article published in Journal of Fluid Mechanics 2010 entitled "Two-dimensional flagellar synchronization in viscoelastic fluids" by Elfring, Gwynn; Pak, On Shun; Lauga, Eric, and the article published in Small 2012 entitled "Cargo-towing fuel-free magnetic nanoswimmers for targeted drug delivery" by Gao, Wei; Kagan, Dnaiel; Pak, On Shun; Clawon, Corbin; Campuzano, Susana; Chuluun-Erdene, Erdembileg; Shipton, Erik; Fullerton, Eric; Zhang, Liangfang; Lauga, Eric; Wang, Joseph.

VITA

2008	B. Eng. in Mechanical Engineering (*First Class Honours*), University of Hong Kong
2010	M. S. in Engineering Sciences (Mechanical Engineering), University of California, San Diego
2013	Ph. D. in Engineering Sciences (Mechanical Engineering), University of California, San Diego

PUBLICATIONS

O. S. Pak, L. Zhu, L. Brandt, E. Lauga, "Micro-propulsion and micro-rheology in complex fluids via symmetry breaking", *Physics of Fluids*, **24** (2012), 103102.

O. S. Pak, S. E. Spagnolie, E. Lauga, "Hydrodynamics of the double-wave structure of insect spermatozoa flagella", *Journal of the Royal Society Interface*, **9** (2012), 1908-1924.

W. Gao, D. Kagan, O. S. Pak, C. Clawon, S. Campuzano, E. Chuluun-Erdene, E. Shipton, E. Fullerton, L. Zhang, E. Lauga, J. Wang, "Cargo-towing fuel-free magnetic nanoswimmers for targeted drug delivery", *Small*, **8** (2012), 460-467. (Highlighted in "Chemistry Views").

O. S. Pak, E. Lauga, "Extensibility enables locomotion under isotropic drag", *Physics of Fluids*, **23** (2011), 081702. (Also selected to appear in the Virtual Journal of Biological Physics Research, September 1 2011).

O. S. Pak, W. Gao, J. Wang, E. Lauga, "High-speed propulsion of flexible nanowire motors: theory and experiments", *Soft Matter*, **7** (2011), 8169-8181. (Highlighted in "Chemistry World").

O. S. Pak, T. Normand, E. Lauga, "Pumping by flapping in a viscoelastic fluid", *Physical Review E*, **81** (2010), 036312.

G. J. Elfring, O. S. Pak, E. Lauga, "Two-dimensional flagellar synchronization in viscoelastic fluids", *Journal of Fluid Mechanics*, **646** (2010), 505-515.

O. S. Pak, E. Lauga, "The transient swimming of a waving sheet", *Proceedings of the Royal Society London A*, **466** (2009), 107-126.

O. S. Pak, C. K. Lam, K. Nakkeeran, B. A. Malomed, K. W. Chow, K. Senthilnathan, "Dissipative Solitons in coupled complex Ginzburg-Landau equations", *Journal of the Physical Society of Japan*, **78** (2009), 084001.

O. S. Pak, K. W. Chow, "Free surface waves on shear currents with non-uniform vorticity: third order solutions", *Fluid Dynamics Research*, **41** (2009),035511.

ABSTRACT OF THE DISSERTATION

Biological and Synthetic Locomotion in Newtonian and Complex Fluids at Low Reynolds Number

by

On Shun Pak

Doctor of Philosophy in Engineering Sciences (Mechanical Engineering)

University of California, San Diego, 2013

Professor Eric Lauga, Chair

Life under the microscope is significantly different from our experiences in the macroscopic world. Inertial effects, which govern motion at the macroscopic world, become subdominant to viscous forces at small length scales. The Reynolds number (Re) quantifies the relative importance of inertial to viscous forces. Microorganisms, such as bacteria and spermatozoa, inhabit environments with typical Re between 10^{-5} and 10^{-2}. The absence of inertia imposes stringent constraints on the types of effective locomotion strategies. This also poses a fundamental challenge in designing synthetic swimmers and fluid transport systems at microscopic scales. Interestingly, microorganisms have evolved diverse strategies to achieve locomotion. This thesis is devoted to studying the fluid mechanics of biological

and synthetic locomotion at low Reynolds number under three themes: swimming microorganisms, synthetic locomotion, and locomotion in complex fluids. The first theme focuses on using different idealized hydrodynamic models to study the swimming of microorganisms. Under this theme, we extend the classical Taylor's swimming sheet model to analyze the unsteady inertial effects in flagellar swimming. We also present a hydrodynamic investigation of an interesting double-wave structure observed in insect sperm flagella. We turn our attention to synthetic locomotion in the second theme. Different physical mechanisms are explored to design synthetic micro-swimmers, which have many potential biomedical applications, such as microsurgery and targeted drug delivery systems. Specifically, we exploit elasticity and extensibility of a body to design locomotion strategies. Finally, the third theme concerns locomotion in complex fluids. Most biological fluids are indeed polymeric and hence display non-Newtonian rheological properties. We investigate the idea of taking advantage of the nonlinear rheological properties of a complex fluid to enable locomotion otherwise impossible in a Newtonian fluid. Simple mechanisms are designed to exploit the non-Newtonian stresses for micropropulsion and micropumping. The results are also applied to developing a microrheological technique based on information from locomotion.

Chapter 1

Introduction

Locomotion in fluids is ubiquitous in nature, with examples spanning a wide range in size from bacterial motility to the swimming of whales. It plays fundamental roles throughout the lives of animals in such endeavors as predation and finding a mate for reproduction [14]. Lying along the interface between biology and fluid dynamics, biological locomotion at small scales has received substantial attention from biologists and engineers in recent years [15, 16].

The physics governing locomotion in fluids is very different for microscopic organisms (e.g. bacteria, spermatozoa) and macroscopic organisms (e.g. fish, humans). The dramatic difference is due to the competition between inertial and viscous effects in the fluid medium. The Reynolds number, $Re = \rho U\, L/\mu$, (with U and L characteristic velocity and length scales, and ρ and μ are the density and dynamic shear viscosity of the fluid) is a dimensionless parameter which measures the relative importance of the inertial forces to viscous forces in a fluid. Locomotion of larger animals in fluids takes place at moderate to large Reynolds numbers, where inertial forces dominate. At this scale, swimming and flying are generally accomplished by imparting momentum into the fluid opposite the direction of locomotion. Microorganisms meanwhile inhabit in a world of low Reynolds numbers, where inertia plays a negligible role and viscous damping is paramount. The Reynolds number ranges from 10^{-5} for bacteria to 10^{-2} for spermatozoa [17]. The absence of inertia imposes stringent constraints on a microorganism's locomotive capabilities.

In general, the locomotion in this regime is governed by the Stokes equation

$$\nabla p = \mu \nabla^2 \mathbf{u}, \tag{1.1}$$

$$\nabla \cdot \mathbf{u} = 0, \tag{1.2}$$

for a Newtonian and incompressible flow, where p and $\mathbf{u}$ are the pressure and velocity fields of the fluid. Notice that time does not appear explicitly in the Stokes equation, but only as a parameter through the boundary conditions. The absence of inertia, mathematically manifested by the linearity and time independence of the Stokes equations, leads to an important property associated with motion at zero Reynolds number – kinematic reversibility [16]. The effects of kinematic reversibility on locomotion without inertia are summarized by an interesting theorem called Purcell's scallop theorem [18], which says that any periodically deforming swimmers with the sequence of shapes identical under a time-reversal transformation (reciprocal motion) cannot swim at zero Reynolds number. This theorem does not concern the rates at which the forward or backward sequence is performed but only the sequence itself. While a macroscopic scallop can swim by closing its rigid shell fast and opening the shell slowly (a reciprocal motion), a microscopic scallop using the same strategy goes nowhere on average. Flapping motion of a rigid flapper is another example of reciprocal motion. Such flapping motion is a common propulsion mechanism in the inertial regime, but is rendered ineffective without inertia. In short, locomotion at low Reynolds number encounters stringent physicial constraints.

1.1 Swimming microorganisms

Natural microorganisms have to escape from the constraints of the scallop theorem to swim and transport fluids. They evolved a variety of propulsion strategies. Many of them use one or more appendages, called flagella, for propulsion. For some eukaryotic spermatozoa (such as sea-urchin spermatozoa), they swim by propagating a planar traveling wave along the flagellum (Fig. 1.1a). Such a bending flagellar wave is caused by the sliding of microtubules due to the action of molecular motors distributed along the flagellum. For bacteria *Escherichia coli*, the flagellum is a relatively rigid helix and is rotated by a motor embedded in the

cell wall, propagating a helical traveling wave (Fig. 1.1b). Some microorganisms such as ciliates (*Opalina* and *Paramecium*) and colonies of flagellates (*Volvox*) swim by beating arrays of cilia (short flagella) covering their surfaces (Fig. 1.1c). The cilia can beat in a coordinated manner to produce a wave-like squirming of the envelope covering the cilia tips. Despite the diversity of propulsion mechanisms and flagellar waveform among different cells, a common feature is the presence of a wave propagation, which breaks the time-reversal symmetry: the direction of wave propagation (sequence of shapes) is reversed under a time-reversal transformation, rendering flagellar wave propagation a non-reciprocal deformation. In this thesis, we apply tools from fluid mechanics to take a closer look at different locomotion strategies observed in nature.

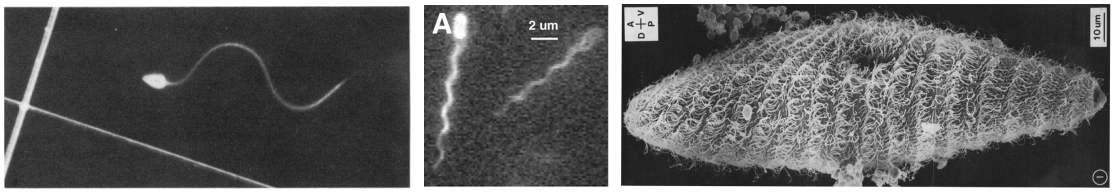

(**a**) (**b**) (**c**)

Figure 1.1: (a) A sea-urchin spermatozoon displaying a planar flagellar wave [1]. (b) Bacteria *Escherichia coli* swimming by rotating their helical flagella, propagating a helical flagellar wave [2]. (c) Ciliary motion in *Paramecium* [3]. All images reproduced with permission; (a) from R. Rikmenspoel and C. A. Isles, Biophys. J., 47, 395-410, 1985, copyright 1985 Elsevier; (b) from L. Turner, W. S. Ryu, and H. C. Berg, J. Bacteriol., 182, 2793-2801, 2000, copyright 2000 American Society for Microbiology; (c) from S. L. Tamm, J. Cell Biol., 55, 250-255, 1972, copyright 1972 The Rockefeller University Press.

1.2 Synthetic microswimmers

Advances in micro-/nano-manufacturing technology have allowed scientists and engineers to take inspiration from locomotion strategies found in nature and design artificial swimmers and fluid transport systems at small scales. Micro-/nano-sized machines have vast potential in future biomedical applications [19], such as targeted drug delivery and microsurgery. For instance, targeted drug delivery enhances the efficacy of the drug and reduces side effects of conventional

chemo-/radio-therapies by targeting the drug only to specific locations – the cancer cells. This new approach could revolutionize medical treatments of many diseases, but there are still fundamental questions and technological challenges to overcome. One major fundamental question for this technology is: how should these micro-robots move? Because of their small sizes, synthetic micro-swimmers are subject to same stringent constrains faced by swimming microorganisms [20]. This poses fundamental challenges to designing these small-scale systems. Interdisciplinary efforts have recently resulted in major advances in the design and fabrication of artificial micro/nano-scale locomotive systems [21–24]. We investigate new strategies to produce synthetic locomotion at small-scales in this thesis.

1.3 Locomotion in complex fluids

Most biological fluids are indeed polymeric and hence display non-Newtonian rheological properties. Examples include respiratory and cervical mucus, and bacterial suspensions. However, most studies in biological locomotion in the past have been limited to Newtonian fluids for the relatively simple constitutive relation. Experiments show that complexity of the fluid medium can play important roles in cell motility [15, 25–31]. Physically, properties such as time-reversibility and linearity in Stokes flows no longer exist in non-Newtonian flows even in the absence of inertia; instead, we have new properties such as fluid memory or relaxation coming into play. Small-scale Newtonian fluid physics no longer applies, and a list of fundamental questions of locomotion in complex fluids remains unanswered. In particular, we are interested in a fundamental question: can we exploit the fluid medium – the nonlinear rheological properties – to produce novel locomotion that is not possible in Newtonian fluids? We provide insights on this question by considering specific mechanisms and their potential applications in micropumping, micropropulsion, and microrheology.

1.4 Thesis outline

This thesis is devoted to investigating ways to live with the scallop theorem. The chapters are grouped under three themes: swimming microorganisms

(Chapters 2 & 3), synthetic micro-swimmers (Chapters 4 & 5), and locomotion in complex fluids (Chapters 6 & 7).

The first theme focuses on the hydrodynamics of swimming microorganisms. We consider different idealized models for flagellar swimming to investigate how microorganisms escape from the constraints of the scallop theorem for locomotion:

- Chapter 2 revisits arguably the first model in flagellar hydrodynamics – a two-dimensional waving sheet. We extend this classical model to study the unsteady inertial effects and reveal the transient dynamics of a waving sheet in an unsteady Stokes flow.

- Chapter 3 presents a hydrodynamic investigation of an interesting double-wave structure observed in insect sperm flagella. We explore the dependence of motility on geometric and kinematic parameters and provide hydrodynamic explanations to biologically relevant questions.

In the second theme, we explore different mechanisms offered by physics to achieve synthetic locomotion at small scales. Specifically, we exploit elasticity and extensibility of a body to design locomotion strategies:

- Chapter 4 presents a theoretical modeling of the propulsion of a flexible nanowire motor and the comparison with experiments, showing how elasticity of a body enables locomotion in the absence of inertia. These nanowire motors may be useful for future biomedical applications, such as targeted drug delivery systems.

- Chapter 5 demonstrates that extensibility provides a new degree of freedom making inertialess locomotion possible even without drag anisotropy, which is usually believed to be a critical requirement for low Reynolds number locomotion of slender bodies (such as flagella and cilia).

Finally, the third theme concerns locomotion in complex fluids. We investigate the effects of non-Newtonian stresses on locomotion in the context of micropumping, micropropulsion and microrheology. While we discuss in the second theme how elasticity in the body makes micropropulsion possible, we demonstrate here how fluid elasticity can also enable micropropulsion:

- Chapter 6 considers the fluid transport of a polymeric fluid by a reciprocal flapping motion. We evaluate the extent to which the nonlinear rheological behavior of viscoelastic fluids can be exploited to break the constraints of the scallop theorem.

- Chapter 7 investigates how fluid elasticity can enable micropropulsion, and symmetrically, how locomotion can be used to infer the non-Newtonian rheological properties of the fluid as an application in microrheology. We propose a simple dual-purpose mechanism that can function either as a non-Newtonian micro-propeller or as a micro-rheometer.

Chapter 1, in small part, is a reprint of the material as it appears in Journal of The Royal Society Interface 2012. Pak, On Shun; Spagnolie, Saverio E.; Lauga, Eric, the Royal Society, 2012. The dissertation author was the primary investigator and author of this paper.

Chapter 2

The transient swimming of a waving sheet

Small-scale locomotion plays an important role in biology. Different modeling approaches have been proposed in the past. The simplest model is an infinite inextensible two-dimensional waving sheet, originally introduced by Taylor, which serves as an idealized geometrical model for both spermatozoa locomotion and ciliary transport in Stokes flow. Here we complement classic steady-state calculations by deriving the transient low-Reynolds number swimming speed of such a waving sheet when starting from rest (small-amplitude initial-value problem). We also determine the transient fluid flow in the 'pumping' setup where the sheet is not free to move but instead generates a net fluid flow around it. The time scales for these two problems, which in general govern transient effects in transport and locomotion at low Reynolds numbers, are also derived using physical arguments.

2.1 Introduction

The locomotion of microorganisms plays a vital role in biology. Examples include the locomotion of mammalian spermatozoa during reproduction, or the swimming of bacteria and algae to locate better nutrient sources [32, 33]. Many of such small organisms propel themselves by propagating progressive waves along their flagella. The geometrical characteristics of these microorganisms and the waves they propagate have been reviewed by Brennen & Winet [17]. For example,

for animal spermatozoa, typical wavelengths range from 11 to 65μm and wave amplitudes range from 4 to 15 μm, while the ratio between their swimming speeds and the wave speeds range from 0.07 to 0.3. Taylor [34] initiated the studies on hydrodynamics of microorganisms by modeling flagella swimming. After his pioneering work, much progress has been made towards addressing the basic mechanisms of propulsion for swimming microorganisms, and we refer to Brennen & Winet [17] and Childress [32] for detailed reviews. In this chapter, we focus on unsteady effects in low-Reynolds number locomotion. We start below with a brief overview of relevant works before summarizing the approach and outline of our chapter.

In 1951, Taylor first showed that self-propulsion of a waving sheet is possible in a viscous fluid in the absence of inertia [34]. The sheet moves in a direction opposite to that of the wave propagation, and the steady state swimming speed was computed explicitly to be $a^2k^2c/2$ at leading order in the wave amplitude, where a, k and c are the wave amplitude, wave number and wave propagation speed respectively. Drummond [35] extended Taylor's results to larger amplitudes of motion. Reynolds [36] and Tuck [37] included inertial effects in the analysis and found that the swimming speed decreases with Reynolds number. In the inertial realm, Wu [38,39] also considered the problem of a waving sheet, but with finite chord and in the inviscid limit, as a model for fish propulsion. Recently, Childress [40] discussed the nature of the high Reynolds number limit of Taylor's swimming problem and applied the results to the idea of recoil swimming, where propulsion is achieved by movements of the center of mass and center of volume of the body.

Despite its simplicity, the waving sheet serves as an idealized geometrical model for both spermatozoa locomotion and ciliary transport. Cilia are short flagella beating collaboratively to produce fluid motion. They are important in many biological transport processes, for example, the transport of mucus in the respiratory tract of humans. Blake [41] represented the envelope formed by the cilia tips as an infinite impenetrable oscillating surface, assuming that the cilia are sufficiently closely packed together. The use of an infinite sheet to model finite length organisms is particularly well justified for elongated and flat organisms such as *Paramecium* or *Opalina* [41]. If the waving sheet is not allowed to move, there will be a net flow of the fluid in one direction. In this case, the sheet acts as a

pump for transporting the fluid. We shall refer this as the 'pumping problem' in this chapter. In addition, when a second waving sheet is present above the original waving surface, one recovers the problem of peristaltic pumping, a useful fluid-transport mechanism in physiology and many industrial processes. Readers are referred to reviews on this subject [15, 42].

Another scenario of interest is the propulsion of microorganisms near solid boundaries. Natural microorganisms often swim in narrow passages such as the swimming of spermatozoa in the cervix [43]. In addition, during most laboratory examinations, the presence of coverslips imposes solid boundaries near the microorganisms. Reynolds [36] adopted Taylor's swimming sheet model to study swimming near solid walls for small-amplitude waving motion; another approximation, the long wavelength limit, was considered by Shack & Lardner [44] and Katz [45]. The oscillating wall models by Smelser *et al.* [46] and Shukla *et al.* [47] and the layered fluid medium model by Shukla *et al.* [25] were also proposed to study the interaction between the cervical wall and the cell.

The fact that many biological fluids are non-Newtonian has also received considerable attention. Chaudhury [48] first extended Taylor's swimming problem to viscoelastic fluids. The same problem was then considered by Sturges [49] using a more rigorous integral constitutive equation. Fulford *et al.* [50] modified the resistive force theory to model the swimming of a spermatozoon in a general linear viscoelastic fluid. Recently, Lauga [51] revisited Taylor's original calculation using more realistic, nonlinear non-Newtonian fluid models.

This brief literature review shows that most studies in small-scale biological locomotion focus on solving for the swimming speed of a model organism. Since previous work derived solutions for steady-state swimming only, we propose in this chapter to go beyond the steady limit and study a prototypical time-varying situation, namely the initial-value problem of a model microorganism (Taylor's waving sheet) starting from rest. Physically, such a process is governed by the small time scale necessary for vorticity created at the swimmer surface to propagate diffusively into the fluid, and belongs to the general class of unsteady Stokes problems.

As expected, this transient swimming process is also dependent upon the development of the propagating wave from rest; we present here a general analytical treatment for a waving sheet which develops its frequency (or phase speed) from

rest to the steady state in an arbitrary manner. An analytical formula describing the general transient propulsion speed of the sheet is then derived, complementing Taylor's well-known steady state solution. We also solve the transient pumping problem, where the sheet is not free to move, but instead entrains the surrounding fluid in an unsteady manner. Unlike their steady counterparts, these two problems are not equivalent in the unsteady case because of time-dependent inertial forces.

The chapter is structured as follows. In Sec. 2.2, the swimming sheet problem is mathematically formulated with the appropriate non-dimensionalization, governing equations, and boundary conditions. In Sec. 2.3, the calculations at first and second order are presented. The results of Sec. 2.3 are then applied to study the transient pumping problem (Sec. 2.4) and the swimming problem (Sec. 2.5). Finally, a physical discussion of our results and a derivation of the time scales involved in transient low-Reynolds number swimming are offered in Sec. 2.6.

2.2 Formulation

We consider here an infinite sheet swimming in an incompressible fluid, similar to the model proposed by Taylor [34]. We also allow the wave of displacement along the sheet to include not only normal but also tangential motion [32,41]. Here, the waving motion is observed in the frame moving at the unknown swimming speed. As the swimming speed is time-dependent during the transient motion, the reference frame is non-inertial and hence a fictitious (inertial) force has to be introduced (see below). In the moving frame, the position of material points, (x_m, y_m), on the waving sheet is written as

$$\begin{aligned} x_m(x,t) &= x + a\hat{A}\cos(kx - \omega(t)t - \phi), \\ y_m(x,t) &= b\hat{A}\sin(kx - \omega(t)t), \end{aligned} \tag{2.1}$$

where a and b are dimensionless, $\hat{A}$ is a typical wave amplitude and ϕ is the phase difference between the longitudinal and transverse motion. The angular frequency $\omega(t)$ is an arbitrary function of time which initially starts from zero and eventually reaches a steady state value of ω_∞. The functions describe a traveling wave with tangential motion of wavelength $\lambda = 2\pi/k$ moving in the positive x direction at a time-varying speed $c = \omega(t)/k$. We keep $\omega(t)$ arbitrary in the analysis below to

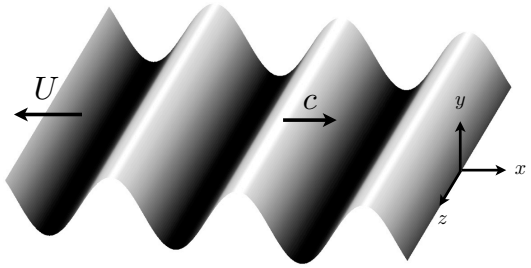

Figure 2.1: Geometrical setup of a two-dimensional swimming sheet. The sheet propagates a wave in the positive x direction at a speed c, and the unknown swimming velocity U is assumed to occur in the direction opposite to that of the wave propagation.

derive general formulas describing the transient net flow and transient swimming velocity. Specific examples for $\omega(t)$ will then be considered for illustration. The transverse traveling wave considered by Taylor [34] is obtained when $a = 0$, and the $b = 0$ case represents a longitudinal traveling wave. The unknown swimming speed of the sheet is denoted by $U(t)$ and is assumed to occur in the direction opposite to that of the wave propagation (see Fig. 2.1 for notation).

2.2.1 Non-dimensionalization

We non-dimensionalize lengths by $1/k$ and velocities by the wave speed c. The time scale in this problem shall characterize changes in velocity in the fluid during the transient motion. The appropriate, physically-motivated time scale, is that required for the vorticity created by the start-up of the sheet to propagate diffusively into the fluid over the characteristic length scale, and therefore time is non-dimensionalized by $1/k^2\nu$, where ν is the kinematic viscosity of the fluid. For a wavelength on the order of 10 μm, and in water, the time scale considered is on the order of milliseconds. The angular frequency, $\omega(t)$, is non-dimensionalized by its steady state value, ω_∞. The dimensionless quantities (starred) are summarized as follows, with ρ being the density of the fluid:

$$\mathbf{x}^* = \frac{\mathbf{x}}{1/k}, \quad t^* = \frac{t}{1/(k^2\nu)}, \quad \mathbf{u}^* = \frac{\mathbf{u}}{c}, \quad p^* = \frac{p}{\rho\nu ck}, \quad \omega^* = \frac{\omega}{\omega_\infty}, \tag{2.2}$$

and the Reynolds number is given by $\mathrm{Re} = c/\nu k = \omega_\infty/\nu k^2$. The dimensionless position of material points on the sheet is written as

$$\begin{aligned} {x_m}^*(x^*, t^*) &= x^* + \epsilon a \cos(x^* - \mathrm{Re}\ \omega^*(t^*)t^* - \phi), \\ {y_m}^*(x^*, t^*) &= \epsilon b \sin(x^* - \mathrm{Re}\ \omega^*(t^*)t^*), \end{aligned} \tag{2.3}$$

where $\epsilon = \hat{A}k$. We assume that the wave amplitude is much smaller than the wavelength, and derive the results in the limit where $\epsilon \ll 1$.

2.2.2 Governing equation

We consider an incompressible Newtonian fluid surrounding the sheet. Since we have a two-dimensional setup, the continuity equation, $\nabla \cdot \mathbf{u} = 0$, is satisfied by introducing the stream function $\psi(x, y, t)$ such that $u = \partial\psi/\partial y$ and $v = -\partial\psi/\partial x$, where $\mathbf{u} = u\mathbf{e}_x + v\mathbf{e}_y$. In the laboratory frame, the governing equation is the Navier-Stokes equation

$$\rho \frac{\partial \mathbf{u}}{\partial t} + \rho\left(\mathbf{u} \cdot \nabla\right)\mathbf{u} = -\nabla p + \mu \nabla^2 \mathbf{u}, \tag{2.4}$$

where p is the pressure and μ the dynamic viscosity of the fluid. In the non-inertial frame considered in this chapter, as we accelerate with the swimming sheet, a time dependent uniform fictitious force $\mathbf{F}(t) = (F_x(t), 0, 0)$ has to be introduced into the equation as

$$\rho \frac{\partial \mathbf{u}}{\partial t} + \rho\left(\mathbf{u} \cdot \nabla\right)\mathbf{u} = -\nabla p + \mu \nabla^2 \mathbf{u} + \mathbf{F}. \tag{2.5}$$

Since the swimming sheet accelerates uniformly in the x-direction, the non-zero component of the fictitious force, F_x, is uniform (independent of space) and is a function of time only. The non-dimensionalized form of the equation (with non-dimensionalization described above) is given by

$$\frac{\partial \mathbf{u}^*}{\partial t^*} + \mathrm{Re}\left(\mathbf{u}^* \cdot \nabla^*\right)\mathbf{u}^* = -\nabla^* p^* + {\nabla^*}^2 \mathbf{u}^* + \mathbf{F}^*. \tag{2.6}$$

For small-scale biological locomotion, we consider the low Reynolds number limit $\mathrm{Re} \to 0$, where the convective term vanishes, resulting in the unsteady Stokes' equation

$$\frac{\partial \mathbf{u}^*}{\partial t^*} = -\nabla^* p^* + {\nabla^*}^2 \mathbf{u}^* + \mathbf{F}^*. \tag{2.7}$$

Upon taking the curl of the equation, both the pressure gradient and the fictitious force terms vanish, resulting in an equation for the z-component of the vorticity, ω^*. With the relation $\omega^* = -\nabla^{*2}\psi^*$, the equation for the stream function is given by

$$\left(\frac{\partial}{\partial t^*} - \nabla^{*2}\right)\nabla^{*2}\psi^* = 0. \tag{2.8}$$

Hereafter, we shall mostly deal with the dimensionless quantities, and therefore the stars will be omitted for simplicity.

2.2.3 Boundary conditions

The unknown swimming velocity of the sheet is denoted by $-U(t)\mathbf{e_x}$. In the frame moving with the swimming sheet, the velocity of the fluid in the far field ($y = \infty$) is therefore given by $U(t)\mathbf{e_x}$. Hence, the far-field boundary conditions are

$$\nabla\psi\mid_{(x_m,\infty)} = U(t)\mathbf{e_y}. \tag{2.9}$$

On the swimming sheet, the boundary conditions are given by the velocity components of a particle of the sheet

$$\nabla\psi\mid_{(x_m,y_m)} = \epsilon f(t)\left[b\cos\left(x - \mathrm{Re}\cdot\omega(t)t\right)\mathbf{e_x} + a\sin\left(x - \mathrm{Re}\cdot\omega(t)t - \phi\right)\mathbf{e_y}\right], \tag{2.10}$$

where $f(t)$ is a function of time, defined by $f(t) = d\left(\omega(t)t\right)/dt$. The conditions simplify to

$$\nabla\psi\mid_{(x_m,y_m)} = \epsilon f(t)\left[b\cos\left(x\right)\mathbf{e_x} + a\sin\left(x - \phi\right)\mathbf{e_y}\right], \tag{2.11}$$

in the low Reynolds number limit ($\mathrm{Re} \to 0$). Note that $\mathrm{Re} = \omega_\infty/\nu k^2$ can be re-written as $\mathrm{Re} = [1/\nu k^2]/[1/\omega_\infty]$, and can therefore be interpreted as the ratio between the relevant time scale for viscous diffusion into the fluid and the typical time scale of the wave (its period). The $\mathrm{Re} \to 0$ limit physically means that the diffusion of vorticity occurs much faster than the propagation of the wave, and therefore the wave appears to be stationary on the time scale where viscous diffusion is taking place.

2.3 Analysis

In this section, we seek regular perturbation expansions for the stream function, swimming speed and the pressure in powers of ϵ in the form

$$\{\psi, U, p\} = \epsilon\{\psi_1, U_1, p_1\} + \epsilon^2\{\psi_2, U_2, p_2\} + \dots . \tag{2.12}$$

The order ϵ and order ϵ^2 solutions are presented in the following subsections.

2.3.1 First-order solution

At order ϵ, the governing equation is given by

$$\left(\frac{\partial}{\partial t} - \nabla^2\right)\nabla^2\psi_1 = 0. \tag{2.13}$$

Expanding the boundary conditions on the sheet using Taylor expansion, they become at order ϵ

$$\psi_{1,y}\mid_{(x,0)} = af(t)\sin(x-\phi), \tag{2.14}$$

$$\psi_{1,x}\mid_{(x,0)} = bf(t)\cos x, \tag{2.15}$$

$$\psi_{1,y}\mid_{(x,\infty)} = U_1(t), \tag{2.16}$$

$$\psi_{1,x}\mid_{(x,\infty)} = 0. \tag{2.17}$$

The initial condition is that the vorticity in the fluid ($\omega = -\nabla^2\psi$) is initially zero, *i.e.* $\omega_1\mid_{t=0} = (-\nabla^2\psi_1)\mid_{t=0} = 0$.

To allow an easy implementation of the initial condition, we solve the problem using the Laplace transform method. A similar technique has been applied to study the transient solution of Stokes' second problem [52]. The Laplace transform of the stream function ψ_1 is defined by the relation

$$\tilde{\psi_1}(x, y, s) = \int_0^\infty \psi_1(x, y, t)\mathrm{e}^{-st}dt, \tag{2.18}$$

where s is the Laplace variable and tilde variables represent transformed quantities. Taking the Laplace transform of the governing equation at this order, Eq. (2.13) becomes

$$\left(s - \nabla^2\right)\nabla^2\tilde{\psi_1} = 0. \tag{2.19}$$

The boundary conditions in Laplace domain are given by

$$\tilde{\psi}_{1,y}\mid_{(x,0)} = a\tilde{f}(s)\sin(x-\phi), \tag{2.20}$$

$$\tilde{\psi}_{1,x}\mid_{(x,0)} = b\tilde{f}(s)\cos x, \tag{2.21}$$

$$\tilde{\psi}_{1,y}\mid_{(x,\infty)} = \tilde{U}_1(s), \tag{2.22}$$

$$\tilde{\psi}_{1,x}\mid_{(x,\infty)} = 0. \tag{2.23}$$

The solution satisfying all the boundary condition is found to be

$$\tilde{\psi}_1 = \tilde{U}_1\left(y+\frac{\mathrm{e}^{-\sqrt{s}y}}{\sqrt{s}}\right)+\frac{\tilde{f}(s)}{\sqrt{s+1}-1}a\sin\phi(\mathrm{e}^{-\sqrt{s+1}y}-\mathrm{e}^{-y})\cos x$$
$$+\frac{\tilde{f}(s)}{\sqrt{s+1}-1}\left[(b\sqrt{s+1}+a\cos\phi)\mathrm{e}^{-y}-(b+a\cos\phi)\mathrm{e}^{-\sqrt{s+1}y}\right]\sin x. \tag{2.24}$$

2.3.2 Second-order solution

We proceed to the analysis at order ϵ^2 using a similar procedure. The governing equation at this order is

$$\left(\frac{\partial}{\partial t}-\nabla^2\right)\nabla^2\psi_2 = 0, \tag{2.25}$$

with boundary conditions

$$\psi_{2,y}\mid_{(x,0)} = -a\cos(x-\phi)\frac{\partial^2\psi_1}{\partial x\partial y}\mid_{y=0} -b\sin x\frac{\partial^2\psi_1}{\partial y^2}\mid_{y=0}, \tag{2.26}$$

$$\psi_{2,x}\mid_{(x,0)} = -a\cos(x-\phi)\frac{\partial^2\psi_1}{\partial x^2}\mid_{y=0} -b\sin x\frac{\partial^2\psi_1}{\partial x\partial y}\mid_{y=0}, \tag{2.27}$$

$$\psi_{2,y}\mid_{(x,\infty)} = U_2(t), \tag{2.28}$$

$$\psi_{2,x}\mid_{(x,\infty)} = 0, \tag{2.29}$$

where we have used Taylor expansion to obtain the boundary conditions on the moving sheet surface. Using Laplace transform, the governing equation for the stream function becomes

$$\left(s-\nabla^2\right)\nabla^2\tilde{\psi}_2 = 0. \tag{2.30}$$

The boundary conditions are now

$$\tilde{\psi}_{2,y}\,|_{(x,0)} = \tilde{f}(s)\left[b^2\sqrt{s+1}\sin^2 x + ab\frac{s\sin x\sin(x-\phi)}{\sqrt{s+1}-1} - a^2\cos^2(x-\phi)\right], \tag{2.31}$$

$$\tilde{\psi}_{2,x}\,|_{(x,0)} = 0, \tag{2.32}$$

$$\tilde{\psi}_{2,y}\,|_{(x,\infty)} = \tilde{U}_2(s), \tag{2.33}$$

$$\tilde{\psi}_{2,x}\,|_{(x,\infty)} = 0. \tag{2.34}$$

The solution satisfying all the boundary conditions at this order is obtained to be

$$\begin{aligned}\tilde{\psi}_2 = \tilde{U}_2\left(y+\frac{\mathrm{e}^{-\sqrt{s}y}}{\sqrt{s}}\right) - \frac{\tilde{f}(s)}{2\sqrt{s}}\left(b^2\sqrt{s+1}-a^2+ab\frac{s}{\sqrt{s+1}-1}\cos\phi\right)\mathrm{e}^{-\sqrt{s}y} \\ + \frac{\tilde{f}(s)}{2(\sqrt{s+4}-2)}\Bigg[\left(a^2\sin 2\phi + ab\frac{s}{\sqrt{s+1}-1}\sin\phi\right)(\mathrm{e}^{-\sqrt{s+4}y}-\mathrm{e}^{-2y})\sin 2x \\ + \left(a^2\cos 2\phi + b^2\sqrt{s+1} + ab\frac{s}{\sqrt{s+1}-1}\right)(\mathrm{e}^{-\sqrt{s+4}y}-\mathrm{e}^{-2y})\cos 2x\Bigg].\end{aligned} \tag{2.35}$$

2.4 Pumping problem

The analysis of Sec. 2.3 can first be applied to the pumping problem, where the sheet is not allowed to move and its oscillatory motion entrains a net fluid flow along the x-direction. Since the sheet does not move, we are in the laboratory frame of reference and the introduction of the fictitious force is unnecessary in this case. The velocity in the far field is zero for any finite time, which is analogous to that in Stokes' problems; therefore, $U_1 = U_2 = 0$, and we then take the x-average of the horizontal velocity (denoted by $\langle ... \rangle$), leading to

$$\langle\tilde{u}_1\rangle(y,s) = \frac{\partial\langle\tilde{\psi}_1\rangle}{\partial y} = 0, \tag{2.36}$$

$$\langle\tilde{u}_2\rangle(y,s) = \frac{\partial\langle\tilde{\psi}_2\rangle}{\partial y} = \frac{\tilde{f}(s)}{2}\left(b^2\sqrt{s+1}-a^2+ab\frac{s}{\sqrt{s+1}-1}\cos\phi\right)\mathrm{e}^{-\sqrt{s}y}. \tag{2.37}$$

As expected from the $\epsilon \to -\epsilon$ symmetry, no net flow occurs at order ϵ. At order ϵ^2, there is a net fluid flow and the result of Eq. (2.37) describes the (dimensionless) transient velocity of the driven flow in the Laplace domain. For any finite

distance y, as time goes to infinity, the average horizontal velocity, by the final value theorem, asymptotes to

$$\langle \tilde{u}_2 \rangle (y, t \to \infty) = \frac{1}{2}(b^2 + 2ab\cos\phi - a^2), \tag{2.38}$$

which is the appropriate steady-state value [32, 41] The direction of the net fluid flow is governed by the oscillation mode of the swimming sheet. For a transverse wave ($a = 0$), there is a net fluid flow in the positive x direction, which is the direction of the wave propagation. For a longitudinal wave ($b = 0$), the fluid flows in a direction opposite to the wave propagation. If there is a combination between transverse and longitudinal motion ($a \neq 0, b \neq 0$), the direction of fluid flow is governed by the competition between the amplitudes of the transverse and longitudinal motion and their phase difference, as described by Eq. (2.38). Notably, there are values of a, b and ϕ that will yield a zero net fluid flow, where the propulsion caused by the longitudinal motion exactly balances that produced by the transverse motion.

The detail evolution of the transient flow depends on the development of the propagating wave, described by the function $\omega(t)$ (or $f(t) = d\left(\omega(t)t\right)/dt$). Examples will now be given to illustrate the use of Eq. (2.37) to determine the transient velocity of particular driven flows in the time domain.

2.4.1 Example 1: $\omega(t) = 2\arctan\left(t/T\right)/\pi$

Here, we consider the angular frequency of the wave which develops according to the function $\omega(t) = 2\arctan(t/T)/\pi$, where T characterizes the time taken for the angular frequency to reach its steady state value, non-dimensionalized by the viscous diffusion time scale. When T is equal to zero, it represents the case where the wave starts impulsively. Computing the function $f(t) = d(\omega(t)t)/dt$ and its Laplace transform $\tilde{f}(s)$, the transient velocity of the driven flow in Laplace domain follows from Eq. (2.37) as

$$\langle \tilde{u}_2 \rangle (y, s) = \frac{2\mathrm{Ci}(sT)\left[\sin(sT) - sT\cos(sT)\right] + \left[\cos(sT) + sT\sin(sT)\right]\left[\pi - 2\mathrm{Si}(sT)\right]}{2\pi s} \times \left(b^2\sqrt{s+1} - a^2 + ab\frac{s}{\sqrt{s+1}-1}\cos\phi\right)\mathrm{e}^{-\sqrt{s}y}, \tag{2.39}$$

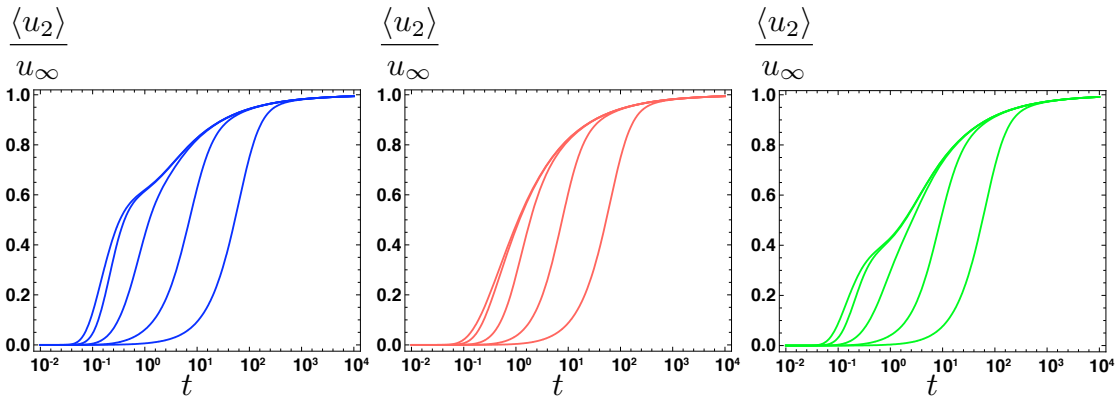

(a) Transverse wave (b) Longitudinal wave (c) Combined wave

Figure 2.2: Average dimensionless horizontal velocity in the fluid for the pumping problem, $\langle u_2 \rangle / u_\infty$, at the non-dimensional position $y = 1$, as a function of the dimensionless time, where the wave frequency increases according to $\omega(t) = 2 \arctan(t/T)/\pi$. (Semi-log plot) (a): transverse wave ($a = 0$); (b): longitudinal wave ($b = 0$); (c): combined transverse and longitudinal wave ($a = b$ and $\phi = \pi/4$). In each graph, from left to right: $T = 0.01, 0.1, 1, 10, 100$.

where Ci and Si are the cosine and sine integrals, defined respectively by

$$\mathrm{Ci}(x) = -\int_x^\infty \frac{\cos t}{t} dt, \quad \mathrm{Si}(x) = \int_0^x \frac{\sin(t)}{t} dt. \tag{2.40}$$

The Laplace transform inversion can be easily implemented numerically [53]. The evolution of the transient swimming speed in the time domain is computed at the non-dimensional position $y = 1$ and shown in Fig. 2.2 for different cases: transverse wave (Fig. 2.2a), longitudinal wave (Fig. 2.2b), and the combined wave where $a = b$ and $\phi = \pi/4$ (Fig. 2.2c). The parameter T is varied from 0.01 to 100 in each case, and as expected an increase in T leads to an increase in the time necessary for the flow speed to reach its steady state value.

2.4.2 Example 2: Impulsive motion

We consider now the extreme case where the angular frequency of the propagating wave attains its steady state value instantaneously, *i.e.* if T is the dimensionless start-up time, we have $T = 0$. The solution to that problem exists as a regular perturbation only in the case where $b = 0$, *i.e.* when the wave has no transverse amplitude. This is due to the fact that in the limit $t \to 0$, and as

in Stokes' first problem for the impulsive motion of a plate in a viscous fluid, an infinite shear is initially created along the surface of the body. Since a Taylor expansion in the wave amplitude is used to obtain the second-order boundary conditions, Eq. (2.26), the presence of an infinite shear leads to an infinite boundary condition unless $b = 0$, in which case the Taylor expansion does no evaluation into the fluid domain (see Sec. 2.6 for further discussion). However, similarly to Stokes' first problem, the solution is well-behaved when $b = 0$, which is the case we now consider. In this case, the function $f(t)$ is a unit step function and its Laplace transform is $\tilde{f}(s) = 1/s$. Again, as expected from the $\epsilon \to -\epsilon$ symmetry, no net fluid flow occurs at order ϵ. Net flow occurs at order ϵ^2. By Eq. (2.37), the x-average horizontal velocity in Laplace domain in this case is given by

$$\langle \tilde{u}_2 \rangle(y, s) = \frac{\partial \langle \tilde{\psi}_2 \rangle}{\partial y} = -\frac{a^2}{2s} \mathrm{e}^{-\sqrt{s}y}, \tag{2.41}$$

which we inverse Laplace transform, yielding

$$\langle u_2 \rangle(y, t) = -\frac{a^2}{2} \mathrm{erfc}\left(\frac{y}{2\sqrt{t}}\right), \tag{2.42}$$

where erfc is the complementary error function.

The fluid flow occurs in the direction opposite to the wave propagation. The result of Eq. (2.42) describes the (dimensionless) transient velocity of the driven flow, and is illustrated in Fig. 2.3. The vorticity perturbation created by the instantaneous motion of the sheet propagates diffusively into the fluid, $y \sim \sqrt{t}$, with a final result very similar to that of Stokes' first problem. For any finite distance y, as time goes to infinity, the average horizontal velocity asymptotes to $-a^2/2$. In other words, the entire fluid will eventually be pumped to move with an average horizontal velocity of $-a^2/2$ for very large times. In dimensional form, the average horizontal velocity is given by

$$\langle u \rangle(y, t) = -\frac{a^2 \hat{A}^2 k^2 c}{2} \mathrm{erfc}\left(\frac{y}{2\sqrt{\nu t}}\right) \tag{2.43}$$

at leading order in sheet amplitude.

2.5 Swimming problem

Next, we consider the swimming problem, where the sheet is free to move. We are now in a frame moving with the sheet, a non-inertial frame of reference

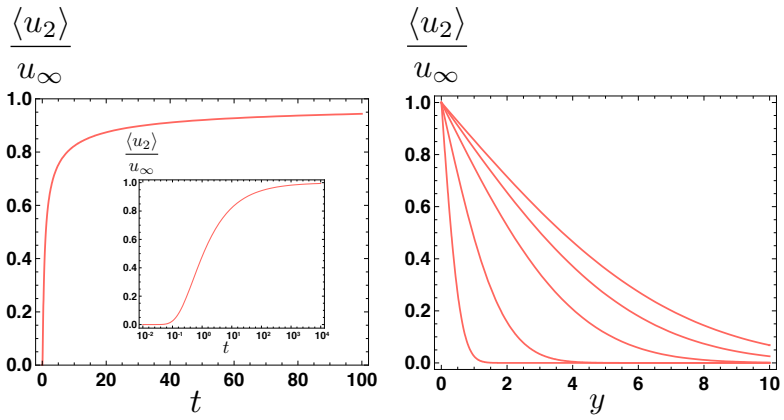

(a) (b)

Figure 2.3: (a): Average dimensionless horizontal velocity in the fluid for the pumping problem, $\langle u_2 \rangle / u_\infty$, at the non-dimensional position $y = 1$, as a function of the dimensionless time for an impulsive longitudinal wave $b = 0$. (Inset: same plot on a semi-log scale); (b): Evolution of the average dimensionless horizontal velocity in the fluid in the y direction at different values of dimensionless time for an impulsive longitudinal wave, from left to right: $t = 0.1, 1, 5, 10, 15$.

(Sec. 2.2.2). In this problem, the swimming speed of the sheet is yet to be determined. An additional condition is required to determine $\tilde{U}_1(s)$ and $\tilde{U}_2(s)$ in Eqs. (2.24) and (2.35) respectively. For this purpose, Newton's second law will be applied on the sheet in the x-direction. By the periodicity of the problem, we consider the forces (per unit width) acting on one wavelength of the sheet. The forces are: (i) the horizontal force per unit width acted on the sheet by the fluid (denoted F_{fluid}), and (ii) the fictitious force per unit width due to the accelerating reference frame (denoted $F_{\text{fictitious}}$). In the frame moving with the sheet, its acceleration is zero, and therefore Newton's second law on the sheet under this non-inertial frame has the form $F_{\text{fluid}} + F_{\text{fictitious}} = 0$. The magnitude of the fictitious force, $F_{\text{fictitious}}$, is given by the mass per unit width of the sheet times the acceleration of the reference frame. The fictitious force is acting in a direction opposite to the acceleration of the moving frame, so that $F_{\text{fictitious}} = (\text{mass of the sheet per unit width}) dU/dt$. Below, we expand both $F_{\text{fictitious}}$ and F_{fluid} in powers of the small parameter ϵ, and enforce Newton's second law at each order.

2.5.1 First-order solution

At order ϵ, and in dimensional variables, F_{fluid} is given by

$$\rho\nu c\int_0^{2\pi}(u_{1y}+v_{1x})\mid_{y=0}dx=\rho\nu c\int_0^{2\pi}\mathcal{L}^{-1}(\tilde{U}_1\sqrt{s})dx=2\pi\rho\nu c\mathcal{L}^{-1}(\tilde{U}_1\sqrt{s}),\quad(2.44)$$

where $\mathcal{L}^{-1}$ is the inverse Laplace transform operator. The fictitious force, $F_{\text{fictitious}}$, at this order reads $(\rho_s h\lambda ck^2\nu)dU_1/dt$, where ρ_s and h are the density and thickness of the swimming sheet respectively. Applying Newton's second law, we have

$$2\pi\rho\nu c\mathcal{L}^{-1}(\tilde{U}_1\sqrt{s})+\rho_s h\lambda ck^2\nu\frac{dU_1}{dt}=0.\quad(2.45)$$

Taking the Laplace transform of the equation yields

$$2\pi\rho\nu c\tilde{U}_1\sqrt{s}+\rho_s h\lambda ck^2\nu s\tilde{U}_1=0.\quad(2.46)$$

Solving for $\tilde{U}_1(s)$, we have $\tilde{U}_1(s)=0$, which implies $U_1(t)=0$. As expected, no self-propulsion occurs at order ϵ. We therefore proceed to the analysis at order ϵ^2.

2.5.2 Second-order solution

A similar analysis is undertaken at this order, with the difference that the order ϵ pressure, p_1, will be required for the calculation of the fluid force, F_{fluid}, at order ϵ^2. The pressure is found by integrating over x the Navier-Stokes equation at order ϵ in the horizontal direction. The forces, $F_{\text{fictitious}}$ and F_{fluid}, are expanded on the sheet using Taylor expansion. At order ϵ^2, F_{fluid} is given by

$$\begin{aligned}&\rho\nu c\int_0^{2\pi}\left[-(2u_{1,x}-p_1)b\cos x+b\sin x(u_{1,y}+v_{1,x})_y+u_{2,y}+v_{2,x}\right]\mid_{y=0}dx\\&=2\pi\rho\nu c\mathcal{L}^{-1}\left[\tilde{U}_2\sqrt{s}-\frac{\tilde{f}(s)}{2}\sqrt{s}\left(b^2\sqrt{s+1}-a^2+ab\cos\phi(\sqrt{s+1}-\sqrt{s}+1)\right)\right].\end{aligned}\quad(2.47)$$

The fictitious force, $F_{\text{fictitious}}$, at this order reads $(\rho_s h\lambda ck^2\nu)dU_2/dt$. Again, applying Newton's second law on the sheet leads to

$$\begin{aligned}&2\pi\rho\nu c\mathcal{L}^{-1}\left[\tilde{U}_2\sqrt{s}-\frac{\tilde{f}(s)}{2}\sqrt{s}\left(b^2\sqrt{s+1}-a^2+ab\cos\phi(\sqrt{s+1}-\sqrt{s}+1)\right)\right]\\&\qquad+\rho_s h\lambda ck^2\nu\frac{dU_2}{dt}=0.\end{aligned}\quad(2.48)$$

Taking the Laplace transform, we have

$$\left[\tilde{U}_2\sqrt{s} - \frac{\tilde{f}(s)}{2}\sqrt{s}\left(b^2\sqrt{s+1} - a^2 + ab\cos\phi(\sqrt{s+1} - \sqrt{s} + 1)\right)\right] + \frac{\rho_s}{\rho}\frac{h}{(1/k)}s\tilde{U}_2 = 0. \tag{2.49}$$

We define the dimensionless parameter $\mathcal{M} = (\rho_s/\rho)(hk)$, which is the product of the density ratio of the sheet to the fluid and the ratio of the thickness of the sheet to the characteristic length scale (wavelength). The swimming velocity at order ϵ^2 is then determined, in the Laplace domain, as

$$\tilde{U}_2(s) = \frac{\tilde{f}(s)}{2(\mathcal{M}\sqrt{s}+1)}\left(b^2\sqrt{s+1} - a^2 + ab\cos\phi(\sqrt{s+1} - \sqrt{s} + 1)\right). \tag{2.50}$$

The steady state swimming velocity, by the final value theorem, is given by

$$U_\infty = \frac{1}{2}\left(b^2 + 2ab\cos\phi - a^2\right), \tag{2.51}$$

which agrees with previous steady-state results [32,41]. When $a = 0$, it corresponds to Taylor's result of a transverse traveling wave. The swimming sheet propels itself in a direction opposite to the wave propagation. The $b = 0$ limit corresponds to the case of a longitudinal traveling wave, and the swimming sheet propels in the direction of wave propagation. If there is a combination of transverse and longitudinal motion, similar to the pumping problem, the swimming direction is governed by the competition of the amplitudes of the transverse and longitudinal motion and their phase difference, as described by Eq. (2.51). Similarly to the pumping problem, there are values of a, b and ϕ that will produce a zero propulsion speed. The transient swimming velocity of the sheet is given by Eq. (2.50) in the Laplace domain for arbitrary function $\tilde{f}(s)$. Here again, we consider different examples of $\tilde{f}(s)$ and compute the transient swimming velocity in the time domain.

2.5.3 Example 1: $\omega(t) = 2\arctan(t/T)/\pi$

Here, we consider the angular frequency of the wave which develops according to the function $\omega(t) = 2\arctan(t/T)/\pi$, the same function as for the pumping problem above. Therefore, the functions $f(t)$ and $\tilde{f}(s)$ are the same as in Sec. 2.4.1.

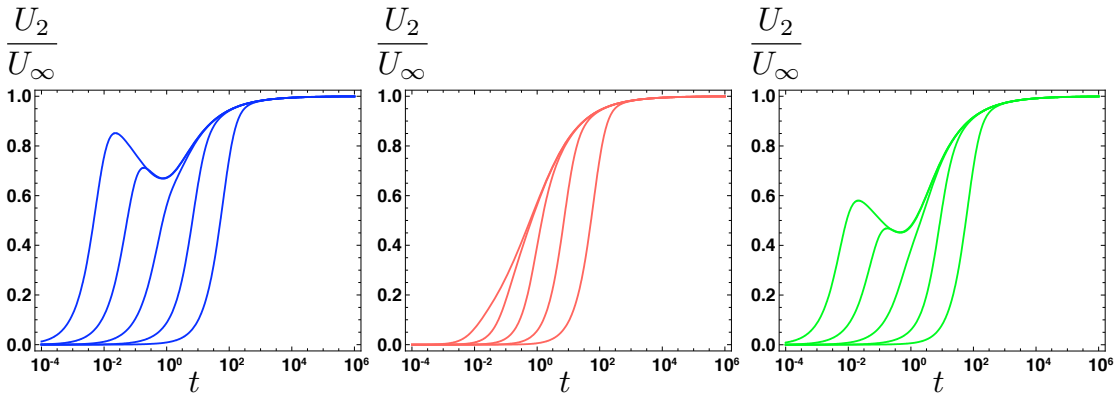

(a) Transverse wave (b) Longitudinal wave (c) Combined wave

Figure 2.4: Dimensionless swimming speed of the sheet, U_2/U_∞, as a function of the dimensionless time, in the case where the dimensionless wave frequency evolves according to $\omega(t) = 2\arctan(t/T)/\pi$, and for $\mathcal{M} = 1$ and different values of the wave start-up time T. (Semi-log plot). (a): transverse wave ($a = 0$); (b): longitudinal wave ($b = 0$); (c): combined transverse and longitudinal wave ($a = b$ and $\phi = \pi/4$). In each graph, from left to right: $T = 0.01, 0.1, 1, 10, 100$.

By Eq. (2.50), hence, the swimming velocity in Laplace domain is given by

$$\tilde{U}_2(s) = \frac{2\mathrm{Ci}(sT)\left[\sin(sT) - sT\cos(sT)\right] + \left[\cos(sT) + sT\sin(sT)\right]\left[\pi - 2\mathrm{Si}(sT)\right]}{2\pi s\left(\mathcal{M}\sqrt{s}+1\right)} \times \left(b^2\sqrt{s+1} - a^2 + ab\cos\phi(\sqrt{s+1} - \sqrt{s} + 1)\right). \tag{2.52}$$

The transient swimming velocity in the time domain is obtained by performing a Laplace transform inversion numerically. The results are displayed in Figs. 2.4 and 2.5 for different modes of oscillation: transverse wave (Figs. 2.4a and 2.5a), longitudinal wave (Figs. 2.4b and 2.5b), and the combined transverse and longitudinal wave where $a = b$ and $\phi = \pi/4$ (Figs. 2.4c and 2.5c). In Fig. 2.4, the mass ratio is fixed to be $\mathcal{M} = 1$ and the wave start-up time T is varied between 0.01 to 100. In Fig. 2.5, we fix $T = 1$, while the parameter $\mathcal{M}$ is varied between 0.01 to 100; the limit where $\mathcal{M} = 0$ is also computed and shown as dashed lines in Fig. 2.5. This limit corresponds to the case where the swimming sheet is mass-less, which is the relevant limit for biological organisms.

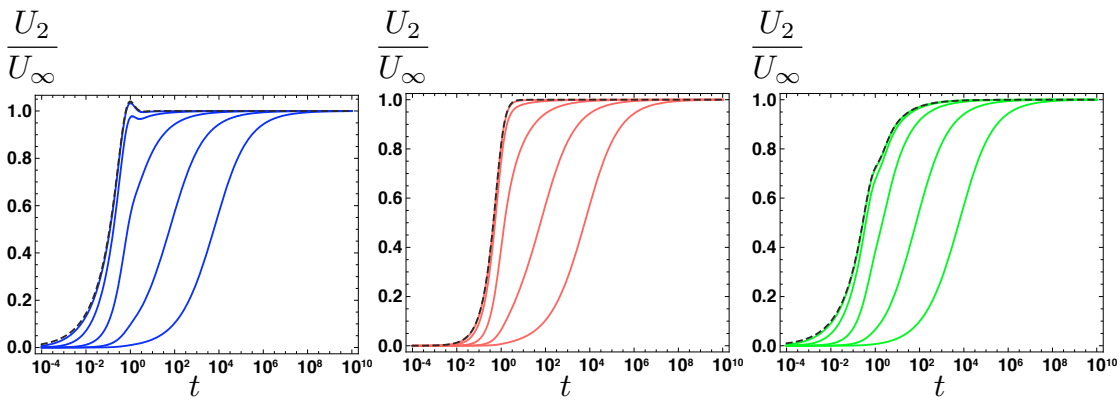

(a) Transverse wave (b) Longitudinal wave (c) Combined wave

Figure 2.5: Dimensionless swimming speed of the sheet, U_2/U_∞, as a function of the dimensionless time, in the case where the dimensionless wave frequency evolves according to $\omega(t) = 2\arctan(t/T)/\pi$, and for $T = 1$ and different values of the mass ratio $\mathcal{M}$. (Semi-log plot). (a): transverse wave ($a = 0$); (b): longitudinal wave ($b = 0$); (c): combined transverse and longitudinal wave ($a = b$ and $\phi = \pi/4$). In each graph, from left to right: $\mathcal{M} = 0.01, 0.1, 1, 10, 100$. The dashed lines (the left-most in each plot) refer to the case of a mass-less sheet *i.e.* $\mathcal{M} = 0$.

2.5.4 Example 2: $\omega(t) = 1 - \exp(-t/T)$

To illustrate the difference between different types of wave start-up, we now consider the case where the angular frequency increases exponentially as: $\omega(t) = 1 - \exp(-t/T)$. Again, computing the corresponding function $f(t)$ and its Laplace transform $\tilde{f}(s)$, the swimming velocity in Laplace domain, by Eq. (2.50), reads

$$\tilde{U}_2(s) = \frac{(1+2sT)}{2s(1+\mathcal{M}\sqrt{s})(1+sT)^2}\left(b^2\sqrt{s+1} - a^2 + ab\cos\phi(\sqrt{s+1} - \sqrt{s} + 1)\right). \tag{2.53}$$

Here again, we invert the Laplace transforms numerically. The influence of the dimensionless parameters T and $\mathcal{M}$ on the transient swimming velocity show trends similar to the first example above. The detailed evolution of the swimming velocity is however, and as expected, quantitatively different due to the different time development of the angular frequency. The two different evolution profiles are illustrated in Fig. 2.6, for the case where $T = 1$ and $\mathcal{M} = 1$, and for the three different waves.

In the limit where the swimmer has no mass, $\mathcal{M} = 0$, the Laplace transform

inversion is simplified and analytical formulas for swimming velocity are obtained for all the three different modes of oscillation. The swimming velocity for a massless sheet, for a transverse wave, reads

$$U_2(t) = b^2 \left[\frac{\mathrm{e}^{-t}\sqrt{t}}{2T\sqrt{\pi}} + \frac{\mathrm{erf}\left(\sqrt{\mathrm{t}}\right)}{2} - \frac{\mathrm{e}^{-\frac{t}{T}}\left(2t - 3T - 2tT + 2T^2\right)\mathrm{erf}\left(\sqrt{\frac{\mathrm{t(T-1)}}{\mathrm{T}}}\right)}{4T^{3/2}\sqrt{T-1}} \right]; \tag{2.54}$$

whereas for a longitudinal wave, it is

$$U_2(t) = -\frac{a^2}{2}\left[1 + \mathrm{e}^{-\frac{t}{T}}\left(\frac{t}{T} - 1\right)\right]; \tag{2.55}$$

for combined motion where, for example, $a = b$ and $\phi = \pi/4$, the formula is

$$\begin{aligned} U_2(t) = {} & \frac{2+\sqrt{2}}{2}a^2 \times \\ & \left[\frac{\mathrm{e}^{-t}\sqrt{t}}{2T\sqrt{\pi}} + \frac{\mathrm{erf}\left(\sqrt{\mathrm{t}}\right)}{2} - \frac{\mathrm{e}^{-\frac{t}{T}}\left(2t - 3T - 2tT + 2T^2\right)\mathrm{erf}\left(\sqrt{\frac{\mathrm{t(T-1)}}{\mathrm{T}}}\right)}{4T^{3/2}\sqrt{T-1}} \right] \\ & - \frac{\sqrt{2}}{4}a^2 \left[\frac{\sqrt{t}}{T\sqrt{\pi}} - \frac{\mathrm{e}^{-\frac{t}{T}}\left(2t^{3/2} - 4T\sqrt{t} + T^{3/2}\sqrt{\frac{t}{T}}\right)\mathrm{erfi}\left(\sqrt{\frac{\mathrm{t}}{\mathrm{T}}}\right)}{2T^{3/2}\sqrt{t}} \right] \\ & + \frac{\sqrt{2}-2}{4}a^2\left[1 + \mathrm{e}^{-\frac{t}{T}}\left(\frac{t}{T} - 1\right)\right], \end{aligned} \tag{2.56}$$

where erf is the error function and erfi is the imaginary error function.

2.5.5 Example 3: Impulsive motion

Similarly to the pumping problem, the case of impulsive motion is singular except in the case where $b = 0$ for which the impulsive swimming speed is well behaved. In this case, and as in the pumping problem, the function $f(t)$ is a unit step function and its Laplace transformation is $\tilde{f}(s) = 1/s$. Hence, the swimming velocity of the sheet, in Laplace domain, is given by

$$\tilde{U}_2(s) = \frac{-a^2}{2s\left(\mathcal{M}\sqrt{s}+1\right)}. \tag{2.57}$$

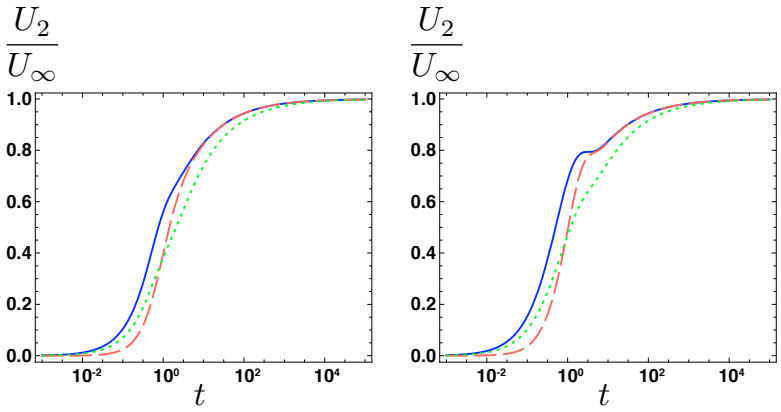

(a) $\omega(t) = 2\arctan(t/T)/\pi$ (b) $\omega(t) = 1 - \mathrm{e}^{-t/T}$

Figure 2.6: Dimensionless swimming speed of the sheet, U_2/U_∞, as a function of the dimensionless time, for $T = 1$, $\mathcal{M} = 1$, and for two different different wave start-up function $\omega(t)$.(Semi-log plot). Blue (solid line): transverse wave ($a = 0$); Red (dashed line): longitudinal wave ($b = 0$); Green (dotted line): combined transverse and longitudinal wave ($a = b$ and $\phi = \pi/4$).

The inverse Laplace transform of Eq. (2.57) yields the leading order swimming velocity in the time domain

$$U_2(t) = -\frac{a^2}{2}\left[1 - \exp\left(\frac{t}{\mathcal{M}^2}\right)\operatorname{erfc}\left(\frac{\sqrt{t}}{\mathcal{M}}\right)\right]. \tag{2.58}$$

As in the corresponding pumping problem, the transient swimming velocity involves the complementary error function, $\operatorname{erfc}(x)$, as illustrated in Fig. 2.7. For large times, the velocity asymptotes to $-a^2/2$. In dimensional form, the swimming velocity of the sheet is given by

$$U(t) = -\frac{a^2}{2}\left[1 - \exp\left(\frac{\nu\rho^2}{h^2\rho_s^2}t\right)\operatorname{erfc}\left(\frac{\sqrt{\nu}\rho}{h\rho_s}\sqrt{t}\right)\right]\hat{A}^2k^2c, \tag{2.59}$$

at the leading order in the wave amplitude.

2.6 Discussion

In this chapter, we have studied two different unsteady Stokes flow problems, and obtained explicit analytical formulas in the Laplace domain for their transient motion. In the pumping problem, the fluid is driven by the waving motion of a fixed sheet, and the Laplace transform of the leading-order dimensionless

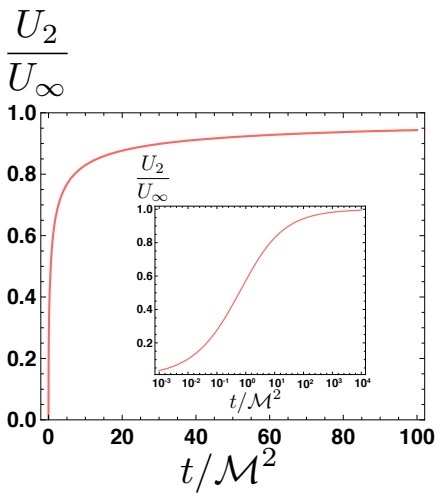

Figure 2.7: Dimensionless swimming speed, U_2/U_∞, for the impulsive longitudinal wave, as a function of the reduced non-dimensionalized time, $t/\mathcal{M}^2$ (Inset: same plot on a semi-log scale).

average horizontal velocity is described by Eq. (2.37). In the swimming problem, where the sheet is free to move, the leading-order swimming velocity of the sheet is given by Eq. (2.50). Higher order terms may be obtained in a similar fashion.

We first note the difference between the form of Eq. (2.37) and Eq. (2.50). In the steady limit, the pumping and swimming problems differ only by a change of reference frame, so the fixed waving sheet pumps a uniform amount of fluid at a velocity equal to minus the steady swimming speed of the free-swimming sheet. In the unsteady case however, the sheet is accelerating, and therefore is subject to additional forces. As a result, the final formula for the swimming speed involves the sheet mass (through the dimensionless parameter $\mathcal{M}$).

To obtain the solution in the time domain, Laplace transform inversion of Eq. (2.37) and Eq. (2.50) is required. Analytical formulas have been obtained for several cases where the Laplace transform inversion is simple. It can be further noted that, if a mass-less waving sheet ($\mathcal{M} = 0$) is considered in the swimming problem, the Laplace transform inversion is particularly straightforward for the case of longitudinal wave ($b = 0$). By Eq. (2.50), we inverse Laplace transform to yield the simple formula $U(t) = -\epsilon^2 a^2 f(t)/2$.

For more complex cases ($\mathcal{M} \neq 0$, $b \neq 0$), the Laplace transform inversion is easily implemented numerically for any admissible $f(t)$ or $\tilde{f}(s)$. Particular exam-

ples have been given for illustration. We have introduced the dimensionless time T characterizing the time scale over which the angular frequency reaches its steady state. As illustrated in Fig. 2.2 for the pumping problem, the development of the flow field can be divided into two stages. In the initial stage, the development of the transient velocity depends on the transient motion of the waving sheet, and the relevant time scale is T: the smaller the values of T, the shorter the time is required to reach a given velocity. For large times, the waving motion of the sheet has effectively reached its steady state, and the subsequent development of the flow field is dominated by the viscous diffusion alone. The values of the parameter T are no longer relevant, and the curves for different values of T collapse onto the same envelop for large times (see Fig. 2.2). In addition, and as could be expected, the detailed evolution of the net velocity depends on the different waving modes of the sheet. Similar trends are observed in the swimming problem, as displayed in Fig. 2.4. In that case, since the sheet is free to move, its mass — characterized by the dimensionless parameter $\mathcal{M}$ — comes into play in its transient swimming velocity, and leads to the presence of a third relevant time scale (see below). As illustrated in Fig. 2.5, the mass of the sheet dictates its acceleration in the initial stage, and the sheet with the smallest mass accelerates the fastest.

The case where $T = 0$, *i.e.* where the wave starts impulsively, has also been discussed. We find that, within the framework of the perturbation expansion proposed in this chapter, this singular start-up behavior for the sheet leads to a singular pumping and swimming solution — except for the case where the wave motion is purely longitudinal, *i.e.* $b = 0$. Physically, as the wave is impulsively starting, it creates an initially infinite shear rate immediately above the sheet. Since the boundary condition for the second order flow is found by the "sampling" of the first order flow by the first-order shape of the sheet (Taylor expansion), any case where the sheet protrudes into the fluid ($b \neq 0$) leads to singular boundary conditions for the second-order flow. This singular behavior could be resolved by incorporating the advective inertial terms in the Navier-Stokes equation. For example, in the case where $\omega(t) = 1 - \exp(-t/T)$, it can be shown that, for a wave with a non-zero transverse amplitude, the convective term scales as $\sim 1/T$ at the sheet position ($y = 0$). Hence, for the convective term to be negligible, it is required that $\mathrm{Re}/T \ll 1$ or $\mathrm{Re} \ll T$, which means that for the results of the

present work to be uniformly valid for all time, a transverse wave needs a finite start-up time. For a longitudinal wave however, the convective term remains order unity for all time, even when the wave is propagated instantaneously, and therefore the impulsive motion problem is well-posed.

A close examination of the results obtained in the impulsive case for the longitudinal wave allows us to understand physically the origin of the time scales involved in the unsteady pumping and swimming processes. In the pumping problem, the net velocity of the fluid averaged over one wavelength occurs in the direction opposite to the wave propagation, with magnitude given by Eq. (2.43). The scaling for the time evolution of the fluid velocity in that case is straightforward and similar to that of Stokes' first problem. It is a diffusive scaling, and the fluid below a diffusive front propagating as $y \sim \sqrt{\nu t}$ into the fluid is pumped roughly at the steady velocity. In the swimming problem, the sheet moves in the same direction as the longitudinal wave with a transient propulsion speed given by Eq. (2.59). In that case, the scaling for the relevant time scale for start-up of the swimmer arises from a consideration of the balance between the inertial force of the sheet and the shear stresses exerted by the fluid. The inertial force is given by the mass per unit width and per unit wavelength of the sheet times its acceleration. Over one wavelength, the small-amplitude swimmer has a mass per unit width equal to $\rho_s h$, and the acceleration scales as U_s/t, where U_s denotes the sheet velocity. On the other hand, the shear stress on the sheet exerted by the fluid is on the order of $\mu U_f/y$, where U_f denotes the fluid velocity and $y \sim \sqrt{\nu t}$ is the typical size in the y direction of velocity gradients in the fluid. Balancing shear stresses in the fluid with inertia in the sheet leads to $\rho_s h U_s/t \sim \mu U_f/\sqrt{\nu t}$. At steady state, we have $U_s \sim U_f$, and the balance suggests a typical time scale, t_M, given by $t_M \sim \rho_s^2 h^2/\rho^2\nu$, which is the time scale involved in Eq. (2.59). Compared to the typical diffusive time scale, $t_D \sim 1/k^2\nu$, we have $t_M/t_D = \mathcal{M}^2$. For typical swimming microorganisms, the ratio of swimmer density to fluid density is about one, and the ratio of thickness h to wavelength $1/k$ is on the order of 0.01 [17, 32], so the steady state swimming problem is reached much earlier than the steady-state pumping problem.

Finally, the results of this chapter can be compared with those given by a quasi-steady approximation, where the steady-state formulas of Taylor are ex-

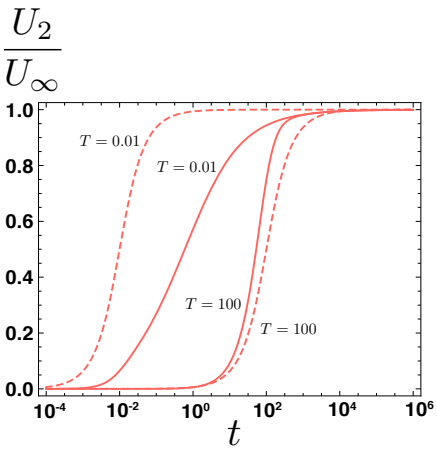

Figure 2.8: Evolution of the dimensionless swimming speed, U_2/U_∞, for the case of longitudinal wave and $\mathcal{M} = 1$, given by the result of this chapter (solid lines) and the quasi-steady approximation (dashed lines) for different values of T.

tended to the unsteady case by replacing the value of the steady-state frequency ω_∞ by the instantaneous value $\omega(t)$. For illustration, we consider the profile $\omega(t) = 2\arctan(t/T)/\pi$ in the case of longitudinal wave, with $\mathcal{M} = 1$. The comparison is displayed in Fig. 2.8; the solid lines show the evolution of the propulsion speed obtained by our analysis while the dashed lines are obtained using the quasi-steady approximation. Two values of T are employed for illustration. For $T = 100$, the development of the wave frequency is slow compared with viscous diffusion, and the quasi-steady approximation leads to a reasonable agreement with our results; the inertial effects are relatively unimportant in this limit. In the other limit for $T = 0.01$, the wave frequency increases quickly compared to the viscous time scale, and the quasi-steady analysis significantly over-estimates the swimming speed; the inclusion of inertial effects as carried out in this chapter is thus critical in this case.

In conclusion, our results complement Taylor's classical swimming sheet calculation by deriving the transient pumping and swimming motion of the sheet. Generally, the two time scales derived above, which control the startup of the flow surrounding the sheet ($t_D \sim 1/k^2\nu$), and the startup of the swimmer ($t_M \sim \mathcal{M}^2/k^2\nu$), are expected to govern transient effects in transport and locomotion at low Reynolds numbers. In addition, our study could be extended to the case of viscoelastic fluids, for which the relaxation time scale of fluid becomes important, and more complex transient processes such as the switching of rotation direction

in bacterial flagella.

Chapter 2, in full, is a reprint of the material as it appears in Proceedings of the Royal Society A 2009. Pak, On Shun; Lauga, Eric, the Royal Society, 2009. The dissertation author was the primary investigator and author of this paper.

Chapter 3

Hydrodynamics of the double-wave structure of insect spermatozoa flagella

In addition to conventional planar and helical flagellar waves, insect sperm flagella have also been observed to display a double-wave structure characterized by the presence of two superimposed helical waves. In this chapter, we present a hydrodynamic investigation of the locomotion of insect spermatozoa exhibiting the double-wave structure, idealized here as superhelical waves. Resolving the hydrodynamic interactions with a non-local slender body theory, we predict the swimming kinematics of these superhelical swimmers based on experimentally collected geometric and kinematic data. Our consideration provides insight into the relative contributions of the major and minor helical waves to swimming; namely, propulsion is due primarily to the minor wave, with negligible contribution from the major wave. We also explore the dependence of the propulsion speed on geometric and kinematic parameters, revealing counter-intuitive results, particularly for the case when the minor and major helical structures are of opposite chirality.

3.1 Introduction

Many microorganisms propel themselves by propagating travelling waves along one or many slender flagella [17]. The motility features of these flagella de-

pend on the cell type, either prokaryotic (cells without a nucleus) or eukaryotic (cells with nuclei). The flagella of prokaryotic bacteria, such as those utilized by *Esherichia coli*, are helical in shape and are passively rotated at their base by a motor embedded in the cell wall. The rotation propagates an apparent helical wave from the sperm head to the distal end of the flagellum, propelling the cell in the opposite direction. Eukaryotic flagella exhibit a different internal structure, called an axoneme, which is composed of microtubules, proteins and protein complexes such as dynein molecular motors. The dynein arms convert chemical energy contained in ATP into mechanical energy, inducing active relative sliding between the microtubules, which in turn leads to bending deformations which propagate along the flagellum. A common structure of the axoneme has a ring of nine microtubule doublets spaced around the circumference and two additional central microtubules (the so-called 9+2 axoneme). Other variations of the axonemal structure have also been observed [12].

Generally, three levels of complexity in undulatory beat patterns are observed in eukaryotic flagella [4, 12], following a hierarchy in the structure of the axoneme: (1) the lowest in the hierarchy is a simple planar beating pattern, as in human and sea-urchin spermatozoa flagella (Fig. 3.1a), with the common 9+2 axoneme structure; (2) a more complicated three-dimensional helical beating pattern is exhibited by some insect spermatozoa with a 9+9+2 axoneme, as in *Gryllotalpa gryllotalpa* (Fig. 3.1b); (3) the highest level of complexity is a double-wave pattern observed in some insect spermatozoa with a 9+9+2 axoneme and accessory bodies endowed with ATPase activity, as in *Haematopinus suis* (Fig. 3.1c). A vast diversity in sperm structure is found in insects [54], and the hierarchy described is also observed even just within the realm of insect spermatozoa flagella [4, 12]. Fig. 3.2 shows a schematic diagram of an pterygote insect flagellosperm and its ultrastructure (reproduced with permission from Ref. [12]). Similar to the 9+2 axoneme observed in cilia and flagella of many plant and animal cells, the central core of the insect sperm axoneme is composed of two central microtubules surrounded by a ring of nine microtubule doublets. However, the ring of nine microtubule doublets is surrounded by another nine accessory tubules, forming the characteristic 9+9+2 arrangement of the insect sperm axoneme. In addition to the more complicated microtubule arrangement, two prominent features of inset spermatozoa flagella are

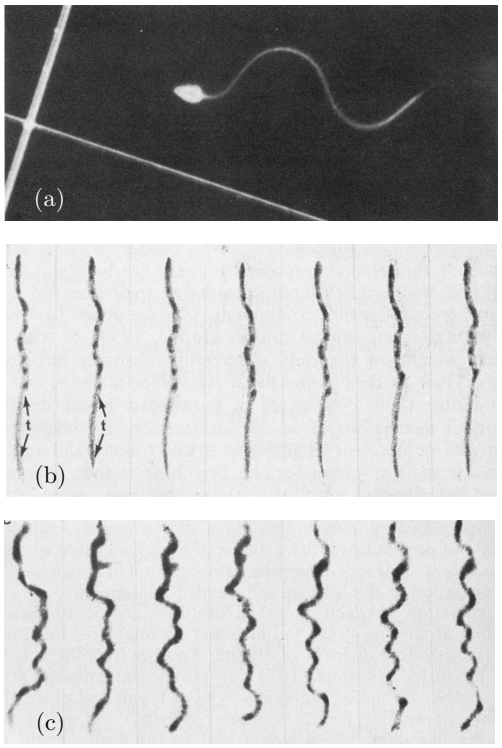

Figure 3.1: A hierarchy of the complexity of flagellar beating pattern observed in eukaryotic cells. (a) Planar-wave pattern in sea-urchin spermatozoa flagella [1]; (b) helical-wave pattern in *Gryllotalpa gryllotalpa* [4]; (c) double-wave pattern in *Haematopinus suis* [4]. All images reproduced with permission; (a) from R. Rikmenspoel and C. A. Isles, *Biophys. J.*, 47, 395–410, 1985, copyright 1985 Elsevier; (b) & (c) from B. Baccetti, *Adv. Insect Physiol.*, 9, 315–397, 1972, copyright 1972 Elsevier.

the mitochondrial derivatives and accessory bodies running along the axoneme (see Ref. [12] for a thorough review of insect sperm structure).

Although the structure of many different spermatozoa has been examined, the rapid and divergent evolution in sperm morphology is not well understood [12, 55]. Hydrodynamic considerations of the relationship between flagellar morphology and functional parameters such as the swimming speed may provide useful information for explaining the evolutionary divergence. Due to its intricate nature, the double-wave structure is less well explored than wave types sitting lower in the hierarchy. Relevant studies on the planar and helical wave structures are abundant and well developed (see the classical and recent reviews [15–17]), but we are not aware of any hydrodynamic studies dedicated to the double-wave structure. Here we present a hydrodynamic study on the motility of insect spermatozoa exhibiting a double-wave beat pattern.

The double-wave pattern is characterized by the simultaneous presence of two kinds of waves, a minor wave with small amplitude and high frequency superimposed on a major helical wave of large amplitude and low frequency. The minor wave has also been observed to be approximately helical [56], and the combined activity of the two is described as a double-helical beating pattern [12]. The double-wave structure was first observed in *Tenebrio molitor* and *Bacillus rossius* by Baccetti *et al.* [7, 11], and was also later found in *Lygaeus* [9], *Culicoides melleus* [6], *Aedes notoscriptus* [10], *Ceratitis capitata* [13], *Drosophila obscura* [8], *Megaselia scalaris* [5], and more recently in *Aleochara curtula* [56] and *Drusilla canaliculata* [57]. Fig. 3.3 compiles a collection of images of spermatozoa exhibiting the double-wave structure. Werner & Simmons [12] have presented a thorough review of this complex structure in insect spermatozoa.

Most studies on insect spermatozoa focus on the sperm ultrastructure, and there are very few studies on insect sperm motility [12]. Many important geometric and kinematic data required for hydrodynamic modeling of the double-wave structure are unavailable. In particular, we are not aware of any information about the chirality of the minor helical structure relative to the major helical structure. The generation and propagation mechanism of the double-wave is also not yet fully understood. Baccetti *et al.* [7, 11] have suggested that the accessory bodies and the axoneme are responsible for the major and minor waves, respectively, whereas

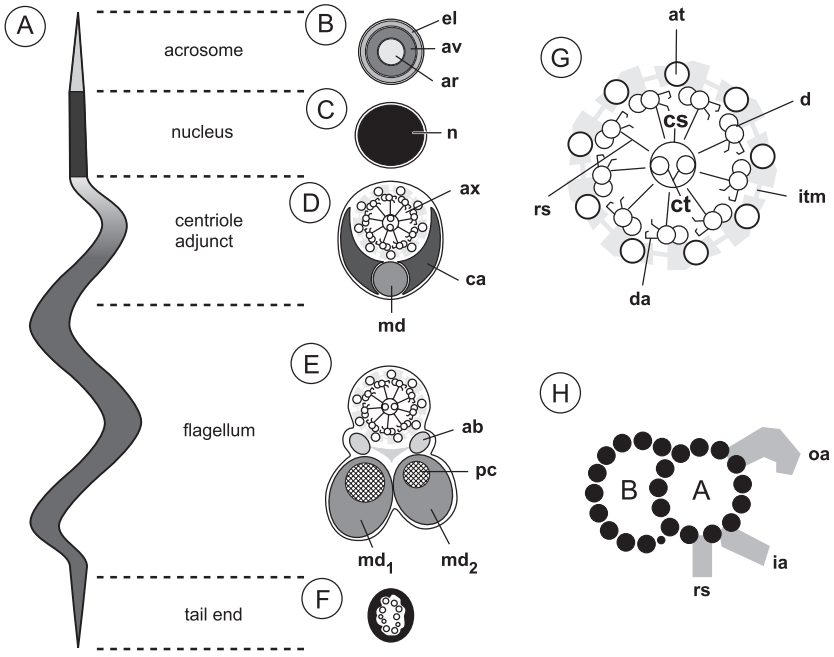

Figure 3.2: Schematic representation of the ground plan of an pterygote insect flagellosperm and its ultrastructure. (A) A typical filiform insect spermatozoon. (B) Cross section of the acrosome. (C) Cross section of the nucleus. (D) Cross section of the posterior centriole adjunct region. (E) Cross section through a representative segment of the flagellum. In addition to the axoneme, two accessory bodies (ab) and the two mitochondrial derivatives of often different size (md1, md2) can be seen. (F) Cross section through the tail end. (G) Cross sectional representation of a typical 9+9+2 insect sperm axoneme. Nine microtubule doublets (d) with associated dynein arms (da) and radial spokes (rs) are connected to two central microtubules (ct) via the central sheath (cs). The doublets are in turn surrounded by nine accessory tubules (at). Accessory tubules and doublets are linked together by intertubular material (itm). (H) Schematic cross sectional drawing of an axonemal doublet showing the protofilament arrangement of the A and B subtubules. The radial spoke (rs), the inner dynein arm (ia) and the outer dynein arm (oa) are attached to the A subtubule. This figure is reproduced with permission from M. Werner and L. W. Simmons, *Biol. Rev.*, 83, 191–208, 2008, copyright 2008 John Wiley and Sons. The caption is adapted and modified from the original article to only keep the portion relevant to this work.

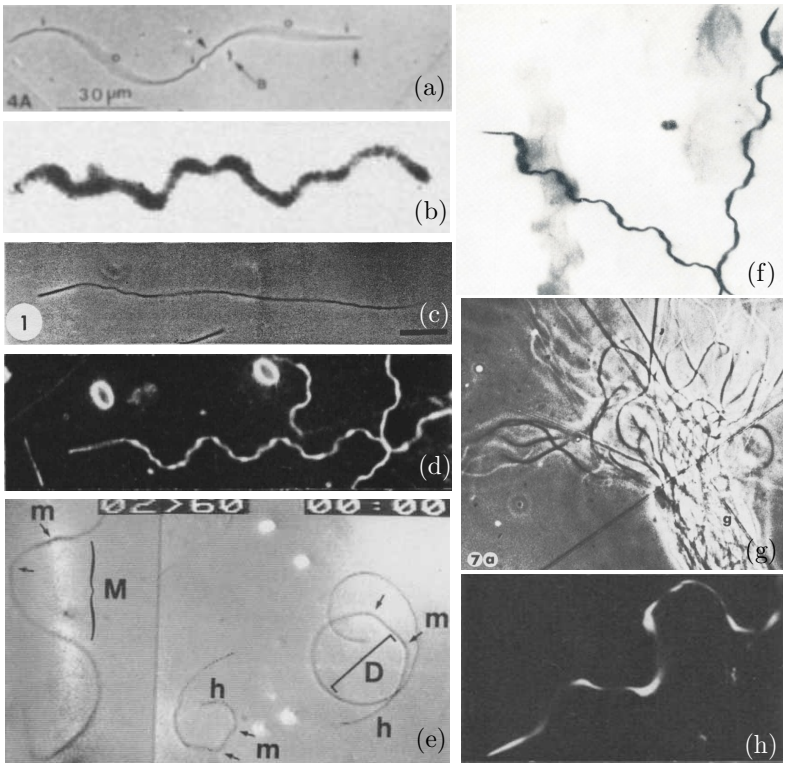

Figure 3.3: The double-wave beating pattern observed in insect spermatozoa flagella of different species: (a) *Megaselia scalaris* [5]; (b) *Haematopinus suis* [4]; (c) *Culicoides melleus* [6]; (d) *Tenebrio molitor* [7]; (e) *Drosophila obscura* [8]; (f) *Tenebrio molitor* [9]; (g) *Aedes notoscriptus* [10]; (h) *Bacillus rossius* [11]. All images reproduced with permission; (a) from S. K. Curtis and D. B. Benner, *J. Morphol.*, 210, 85–99, 1991, copyright 1991 John Wiley and Sons; (b) from B. Baccetti, *Adv. Insect Physiol.*, 9, 315–397, 1972, copyright 1972 Elsevier; (c) from J. R. Linley, *Entomol. Exp. Appl.*, 26, 85–96, 1979, copyright 1979 John Wiley and Sons; (d) from B. Baccetti, A. G. Burrini, R. Dallai, F. Giusti, M. Mazzini, T. Renieri, F. Rosati, and G. Selmi, *J. Mechanochem. Cell Motil.*, 2, 149–161, 1973, copyright 1973 Plenum Publishing Corporation, with kind permission from Springer Science+Business Media B.V; (e) from C. Bressac, D. Joly, J. Devaux, C. Serres, D. Feneus, and D. Lachaise, *Cell Motil. Cytoskel.*, 19, 269–274, 1991, copyright 1991 John Wiley and Sons; (f) from D. M. Philips, in M. A. Sleigh, editor, *Cilia and Flagella*, 379–402, 1974, copyright 1974 John Wiley and Sons; (g) from M. A. Swan, *Gamete Res.*, 4, 241–250, 1981, copyright 1981 John Wiley and Sons; (h) from B. Baccetti, A. G. Burrini, R. Dallai, V. Pallini, P. Periti, F. Piantelli, F. Rosati, and G. Selmi, *J. Ultrastruct. Res.*, 44, 1–73, 1973, copyright 1973 Elsevier.

Swan [10] has stated that the major wave may be due to the sliding of the accessory tubule against the axonemal doublets. More recently, Werner *et al.* [56] have proposed a completely different line of thought, suggesting that the major wave is not in fact a real wave but a static helical structure formed due to the coupling of static forces of the axoneme, mitochondrial derivatives, and plasma membrane. The apparent propagation of the major wave could be due to the passive rolling of the entire cell and might in fact be mistaken for an active, propagating wave under the microscope. It has therefore been suggested that the sperm motility is caused solely by the minor wave. The relative extent of the contribution of the major and minor waves to propulsion is thus still an open question [6]. With the hydrodynamic study presented in this chapter, we hope to provide physical insights on these unresolved problems.

The structure of this chapter is as follows. We idealize the double-wave structure as the propagation of superhelical waves and model the hydrodynamics using non-local slender body theory in Sec. 3.2. In Sec. 3.3, we present the computed hydrodynamic performance of spermatozoa of different species and compare the predictions with available experimental data (Sec. 3.3.1). The features of superhelical swimming are illustrated by a specific model organism, namely the spermatozoa of *Culicoides melleus* (Sec. 3.3.2). We then investigate the effects of kinematic and geometric parameters on the propulsion performance of a superhelical swimmer (Sec. 3.3.3). Finally, the limitations of the present study and directions for future work are discussed in Sec. 3.4.

3.2 Materials and methods

3.2.1 Idealized double-wave structure: superhelical swimmers

The experimentally observed double-wave structure of insect spermatozoa is mathematically idealized in this chapter as a superhelix (a small helix itself coiled into a larger helix); we refer to the helical structure with the larger wavelength as the major helix and the other as the minor helix. To mathematically describe a superhelix, we first construct the position vector of a regular axial

helix (the major helix) to be $\mathbf{H}(s') = [A_M \cos(k_M \alpha s'), A_M \sin(k_M \alpha s'), \alpha s']$, with $\alpha = 1/\sqrt{1 + A_M^2 k_M^2}$. Here k_M is the wave-number, A_M is the amplitude, and $s' \in [0, L']$ and L' are the arc-length parameter and the length of the major helix, respectively. From this basic helix the local unit tangent $\hat{\mathbf{t}}_A$, unit normal $\hat{\mathbf{n}}_A$, and unit binormal $\hat{\mathbf{b}}_A = \hat{\mathbf{t}}_A \times \hat{\mathbf{n}}_A$ vectors are determined, and we take them to define a local coordinate system upon which the minor helix is constructed [58]. The position vector of the combined superhelical shape is then given by

$$\mathbf{X}(s') = [x(s'), y(s'), z(s')] \tag{3.1}$$

$$= \mathbf{H}(s') + A_m \cos(k_m s') \hat{\mathbf{n}}_A(s') \pm A_m \sin(k_m s') \hat{\mathbf{b}}_A(s'), \tag{3.2}$$

where A_m and k_m are the amplitude and wave-number of the minor helix, respectively. Two different configurations will be considered: the '+' sign leads to a superhelical structure where the major and minor helices both have the same chirality, whereas the '$-$' sign represents the case of opposite chirality. Note that s' is no longer the natural arc-length parameter, but merely a regular parameter for describing the swimmer's geometry. The arc-length of the complete superhelix, denoted by s, as a function of the parameter s' is determined by numerical integration, and the total length of the superhelix is denoted by L.

The major and minor helices are free to propagate waves at different wave speeds. Denoting c_M and c_m as the major and minor wave speeds respectively, the position vector at time t, $\mathbf{X}(s', t)$, may be written in component form as

$$\begin{aligned} x(s', t) = {} & A_M \cos[k_M(\alpha s' - c_M t)] - A_m \cos[k_m(s' - c_m t)] \cos[k_M(\alpha s' - c_M t)] \\ & \pm \alpha A_m \sin[k_m(s' - c_m t)] \sin[k_M(\alpha s' - c_M t)], \end{aligned} \tag{3.3}$$

$$\begin{aligned} y(s', t) = {} & A_M \sin[k_M(\alpha s' - c_M t)] - A_m \cos[k_m(s' - c_m t)] \sin[k_M(\alpha s' - c_M t)] \\ & \mp \alpha A_m \sin[k_m(s' - c_m t)] \cos[k_M(\alpha s' - c_M t)], \end{aligned} \tag{3.4}$$

$$z(s', t) = \pm \alpha A_m A_M k_M \sin[k_m(s' - c_m t)] + \alpha s'. \tag{3.5}$$

In addition to the long flagellum, insect spermatozoa have cell bodies which are very slender and short when compared to the flagellum size. We expect that the hydrodynamic influence of the sperm head is negligible and do not include such a body in our consideration. A typical superhelical swimmer is shown in Fig. 3.4, using the dimensionless parameters of *Culicoides melleus* spermatozoa.

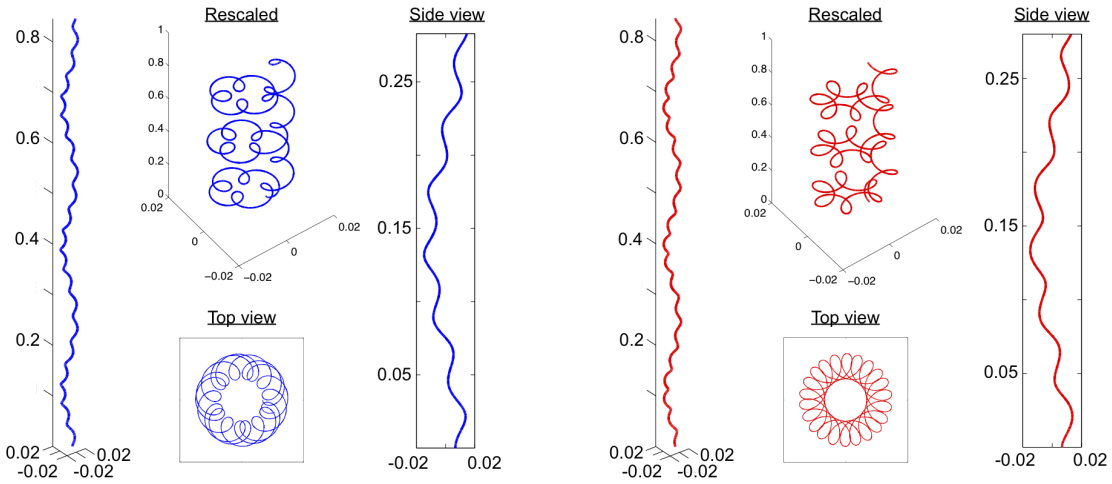

(a) (b)

Figure 3.4: Idealization of the double-wave structure as superhelices for the (a) same-chirality, and (b) opposite-chirality configurations, using the dimensionless parameters of *Culicoides melleus* spermatozoa (Table 3.2).

3.2.2 Hydrodynamic modeling

Flagellar swimming is a result of the interaction between the actuating body and the surrounding fluid. A tractable and accurate approach to studying such hydrodynamic interactions exploits the slenderness of the flagellum, in which the velocity along the flagellar centerline is related to the fluid forces along the same curve. In previous studies, the fluid-body interaction has been modeled using a resistive force theory [59–61], in which local forces acting on the flagellum at any station along the filament are expressed in terms of the local velocity at the same location. Resistive force theory takes only local effects into account and neglects any hydrodynamic interactions between different parts of the deforming body. The local theory works well for simple geometries. However, due to the complexity of the superhelical structure in the problem under consideration here, the local theory is inadequate (see Sec. 3.3.4 for details), and we employ instead the full non-local slender body theory [62] to study the hydrodynamics of the superhelical swimmers. The non-local theory captures the hydrodynamic interactions between distant parts of a curved filament, while still taking advantage of the slenderness of flagellum to simplify the analysis.

The flagellum is modeled as a slender filament of length L and circular cross-section of radius $\epsilon\, L\, r(s)$, where $\epsilon \ll 1$ is the small aspect ratio of the flagellum (the maximum radius along the flagellum a_r divided by its total length L), and $r(s)$ is the dimensionless radius. The non-local slender body theory is algebraically accurate in ratio of the slenderness ϵ; namely, by setting the radius profile to $r(s) = \sqrt{4s(L-s)}/L$, the computed fluid velocity is accurate to $O(\epsilon^2)$ (see [62]).

For a given velocity distribution $\mathbf{v}(s,t)$ along the filament at time t, the corresponding fluid force per unit length $\mathbf{f}(s,t)$ is given implicitly by the non-local relation

$$8\pi\mu\mathbf{v}(s,t) = -\mathbf{\Lambda}[\mathbf{f}(s,t)] - \mathbf{K}[\mathbf{f}(s,t)], \tag{3.6}$$

where

$$\mathbf{\Lambda}[\mathbf{f}](s,t) = \left[c_0(\mathbf{I} + \hat{\mathbf{t}}\hat{\mathbf{t}}) + 2(\mathbf{I} - \hat{\mathbf{t}}\hat{\mathbf{t}})\right]\mathbf{f}(s,t), \tag{3.7}$$

$$\begin{aligned}\mathbf{K}[\mathbf{f}](s,t) = (\mathbf{I} + \hat{\mathbf{t}}\hat{\mathbf{t}})\int_0^L \frac{\mathbf{f}(\tilde{s},t) - \mathbf{f}(s,t)}{|\tilde{s}-s|}\,d\tilde{s} \\ + \int_0^L \left(\frac{\mathbf{I} + \hat{\mathbf{R}}\hat{\mathbf{R}}}{|\mathbf{R}(\tilde{s},s;t)|} - \frac{\mathbf{I} + \hat{\mathbf{t}}\hat{\mathbf{t}}}{|\tilde{s}-s|}\right)\mathbf{f}(\tilde{s},t)\,d\tilde{s},\end{aligned} \tag{3.8}$$

are the local and non-local operators, respectively, μ is the shear viscosity of the fluid, $c_0 = -\ln(\epsilon^2 \mathrm{e}) > 0$, $\mathbf{R}(\tilde{s},s;t) = \mathbf{X}(\tilde{s},t) - \mathbf{X}(s,t)$, $\hat{\mathbf{R}} = \mathbf{R}/|\mathbf{R}|$, and $\hat{\mathbf{t}}$ is the local unit tangent vector at the point s.

The swimmers of interest deform their shapes in a prescribed, time-varying fashion (the superhelical wave pattern, Eqs. 3.3 to 3.5), and the velocity created on its surface by this deformation is given by $\mathbf{v}_{\text{deform}}(s,t) = \partial\mathbf{X}(s,t)/\partial t$. At every time instant t, the swimmer can be seen as a solid body with unknown translational velocity $\mathbf{U}(t)$ and rotation rate $\mathbf{\Omega}(t)$. The velocity created on the swimmer's surface due to swimming is then $\mathbf{v}_{\text{swim}}(s,t) = \mathbf{U} + \mathbf{\Omega} \times [\mathbf{X}(s,t) - \mathbf{X}_0]$, where $\mathbf{X}_0$ is an arbitrary reference point (taken as the origin here for simplicity). Therefore, the local velocity relative to the fluid $\mathbf{v}(s,t)$ is given by the sum of the deformation and swimming velocities: $\mathbf{v}(s,t) = \mathbf{v}_{\text{deform}} + \mathbf{v}_{\text{swim}} = \mathbf{U} + \mathbf{\Omega} \times [\mathbf{X}(s,t) - \mathbf{X}_0] + \partial\mathbf{X}(s,t)/\partial t$. In this work, the wave propagation is towards the positive z direction. Therefore, a negative swimming velocity ($\mathbf{U}$) means the propulsion occurs in a direction opposite to the wave propagation, while a positive swimming velocity means both the propulsion and wave propagation occur in the same direction.

Using a Galerkin method [63], we express the local force $\mathbf{f}(s,t)$ as a finite sum of Legendre polynomials and solve Eq. 3.6 for $\mathbf{f}(s)$ by requiring the equation to hold under inner products against the same basis functions. The first integral in the non-local operator $\mathbf{K}[\mathbf{f}]$ is diagonalized in this space [64, 65]. The system is closed by requiring the entire swimmer to be force free and torque free,

$$\int_0^L \mathbf{f}(s)ds = 0, \tag{3.9}$$

$$\int_0^L [\mathbf{X}(s) - \mathbf{X}_0] \times \mathbf{f}(s)ds = 0, \tag{3.10}$$

providing at each moment in time a system of 6 equations to solve for the 6 unknowns $\mathbf{U}(t)$ and $\mathbf{\Omega}(t)$.

The swimming velocities determined in the manner described above represent velocities in a reference frame fixed on the swimmer. In order to study the full three-dimensional swimming kinematics in the laboratory frame (in which the body moves with velocity $\tilde{\mathbf{U}}(t)$ and rotation rate $\tilde{\mathbf{\Omega}}(t)$), we must include a transformation between the two. We denote the Cartesian coordinate system moving with the swimmer, the body frame, as $[\mathbf{e}_x, \mathbf{e}_y, \mathbf{e}_z]$ and the Cartesian coordinate system in the laboratory frame as $[\mathbf{e}_1, \mathbf{e}_2, \mathbf{e}_3]$. The evolution of the body frame, with respect to the laboratory frame, is then governed by

$$\frac{d\mathbf{E}}{dt} = \mathbf{\Omega}(t) \times \mathbf{E}, \tag{3.11}$$

where $\mathbf{E} = [\mathbf{e}_x, \mathbf{e}_y, \mathbf{e}_z]^T$, along with the initial condition $[\mathbf{e}_x, \mathbf{e}_y, \mathbf{e}_z](t = 0) = [\mathbf{e}_1, \mathbf{e}_2, \mathbf{e}_3]$.

3.2.3 Non-dimensionalization

The process of non-dimensionalization is very useful in science and engineering to identify the relevant dimensionless parameters governing the physics of the problem. In theoretical studies, it always allows a more concise description of the system, while in experimental studies, it reduces the number of independent experiments required to fully explore the problem. The present system is made dimensionless by scaling lengths by $1/k_m$, velocities by c_m, and time by their ratio, $1/c_m k_m$. The dimensionless position vector describing the kinematics of the

superhelix is thus given by

$$x = R\big\{\cos[K(\alpha s' - ct)] - r\cos(s' - t)\cos[K(\alpha s' - ct)] + \alpha r \sin(s' - t)\sin[K(\alpha s' - c\,t)]\big\}, \tag{3.12}$$

$$y = R\big\{\sin[K(\alpha s' - c\,t)] - r\cos(s' - t)\sin[K(\alpha s' - c\,t)] - \alpha r \sin(s' - t)\cos[K(\alpha s' - c\,t)]\big\}, \tag{3.13}$$

$$z = \alpha s' + \alpha r R^2 K \sin(s' - t), \tag{3.14}$$

where all variables are now understood to be dimensionless. Four dimensionless parameters characterizing the kinematics are identified above: the dimensionless amplitude of the major helix, $R = A_M k_m$, the ratio of the wave-numbers characterizing the major and minor helices, $K = k_M/k_m$, the ratio of the minor helix amplitude to the major helix amplitude, $r = A_m/A_M$, and the ratio of the major wave speed to the minor wave speed $c = c_M/c_m$. In the double-wave pattern observed in insect spermatozoa, the major wave amplitude is always larger than the minor wave amplitude ($r < 1$; though this need not be true for a general superhelix). In addition, it is also observed that the minor wave speed is always greater than the major wave speed in the double-wave structure of insect spermatozoa ($c < 1$).

3.2.4 Kinematic and geometric data

From the non-dimensionalization above, we have identified four dimensionless parameters (r, R, K, c) required to fully characterize the centerline motion of a superhelical flagellum. Werner and Simmons [12] have compiled a very useful table containing kinematic and geometric data of the double-wave structure observed in insect spermatozoa in previous studies. The table reveals that experimental measurements of the necessary quantities for hydrodynamic modeling are very limited, due to the difficulties involved in interpreting three-dimensional data from two-dimensional images [6].

Here we follow the table compiled by Werner and Simmons and estimate the missing information based on images of insect spermatozoa reported in the literature. Table 3.1 contains reported and estimated data on the double-wave structure, including the wavelengths, amplitudes, frequencies, major and minor

wave speeds, flagellum thickness, and the swimming speed of different insect spermatozoa. Our estimated quantities are marked with stars to distinguish them from reported quantities by the original chapters. In some studies (e.g. for *Lygaeus* [9]), only relative lengths can be given due to the lack of scale bars in the reported images; these relative quantities are square-bracketed in Tables 3.1 & 3.2. Geometric and kinematic data can display large variations even within a species (*Tenebrio molitor* [7]). When the distribution of the quantities are not given, arithmetic means of the available measurements are used whenever appropriate in the present study.

The measurements are presented in the corresponding dimensionless quantities in Table 3.2, using the scalings defined in Sec. 3.2.3. We have not found in the referenced literature any information about the chirality of the major and minor helical structures. We therefore present results below for both the same-chirality and opposite-chirality configurations. In our measurements (collected in Table 3.1), the wavelength of the minor wave is taken to be the two-dimensional distance between adjacent minor wave peaks. A small correction factor is required to convert these two-dimensional quantities to the appropriate wavelengths in describing the three-dimensional superhelical structure. The correction factor depends on whether the superhelical structure is in the same-chirality $(1/(1-\alpha\lambda_m/\lambda_M))$ or the opposite-chirality $(1/(1+\alpha\lambda_m/\lambda_M))$ configuration.

3.3 Results

In this section, we first use the framework described above to predict the swimming performance of spermatozoa of different species, and compare our hydrodynamic results with available experimental measurements. We then illustrate the basic features of superhelical swimming by focusing on a model organism, namely *Culicoides melleus*, and proceed to perform a parametric study investigating the effects of certain kinematic parameters (minor and major wave speeds) and geometric parameters (minor and major wave amplitudes).

Table 3.1: Kinematic and geometric data of the double-wave structure. We follow the table by Werner and Simmons [12] with our estimations (marked with stars *) of the missing quantities based on the images of the sperm cell reported in the references. a_r refers to the radius of the flagellum.[a]Only forward mode is considered (see [13]).[b]Only male long sperm is considered here (see [8]).[c]Scale bars were not presented with the images in the reference; only relative lengths (square-bracketed) can be estimated.[d]Round brackets denote arithmetic means.

	Major Wave				Minor Wave				$2a_r$	V_{sperm}
Species	$\lambda_M(\mu\text{m})$	$A_M(\mu\text{m})$	f_M(Hz)	c_M (μm/s)	$\lambda_s(\mu\text{m})$	$A_m(\mu\text{m})$	f_m(Hz)	c_m (μm/s)	(μm)	(μm)
Aedes notoscriptus [10]	28*	3.67*	3.4	95.2*	6.8*	1.83*	34	231.2*	0.55*	
Bacillus rossius [11]	40*	12	12	480*	17.9*	1.1	40	716*	0.74*	
Ceratitis capitata [13][a]	30	20	4	120*	7-8	1-2	20	150*	0.68*	16
Culicoides melleus [6]	54.1	2.1			8.7	0.8	8.2	80	0.77*	8.3
Drosophila obscura [8][b]	45*	16			13.3*	0.5*	20.4	271	0.76*	
Lygaeus [9][c]	[1]*	[0.1]*			[0.21]*	[0.014]*	130		[0.024]*	
Megaselia scalaris [5]	68*	9.3*	3.1	210.8*	7*	0.5*			0.78*	12.7
Tenebrio molitor [7][d]	20-30(25)	9-15(12)	0.9-2.8(1.85)	20-90(55)	6-12(9)	3-4(3.5)	7-28(17.5)	40-300(170)	0.79*	16-100(58)

Table 3.2: Dimensionless parameters of superhelical flagella: $K = k_M/k_m$; $R = A_M k_m$; $r = A_m/A_M$; $c = c_M/c_m$; $V = V_{\text{sperm}}/c_m$; $a = a_r k_m$; N refers to number of large wavelengths. $\tilde{U}_+$ and $\tilde{U}_-$ are the predicted average swimming velocities for the same-chirality and opposite-chirality configurations respectively.[e]A value of 4 is adopted in the simulation.[f]Velocity in the z-direction occurs in the same direction as the wave propagation.[g]A value of 1 is adopted in the simulation.[h]Velocity in the z-direction occurs in the same direction as the wave propagation.

Species	K	R	r	c	N	a	V	$\tilde{U}_+$ ($\tilde{U}_-$)	η_+ (η_-)	$\frac{\lvert\tilde{U}_+ - V\rvert}{V}$ $\left(\frac{\lvert\tilde{U}_- - V\rvert}{V}\right)$
Aedes notoscriptus	0.24*	3.4*	0.5*	0.41*	1	0.25*		0.21 (0.16)	1.2%(0.34%)	
Bacillus rossius	0.45*	4.2*	0.092	0.67*	1.5	0.13*		0.031 (0.033)	0.30%(0.14%)	
Ceratitis capitata	0.25	16.8	0.075	0.8*	$4-5^e$	0.28*	0.11*	0.15 (0.039^f)	0.40% (0.021%)	36% (65%)
Culicoides melleus	0.16	1.5	0.38		3	0.28*	0.10	0.051 (0.15)	0.30% (1.5%)	49% (50%)
Drosophila obscura	0.30*	7.6*	0.03*		1	0.18*		0.012 (0.0096)	0.10%(0.036%)	
Lygaeus	0.21*	3*	0.14*		$1-2^g$	0.34*		0.033 (0.081)	0.24%(0.71%)	
Megaselia scalaris	0.10*	8.3*	0.05*		1	0.35*		0.035 (0.065)	0.16%(0.42%)	
Tenebrio molitor	0.36	8.4	0.29	0.32	4	0.28*	0.34	0.40 (0.41^h)	1.2%(0.86%)	18% (21%)

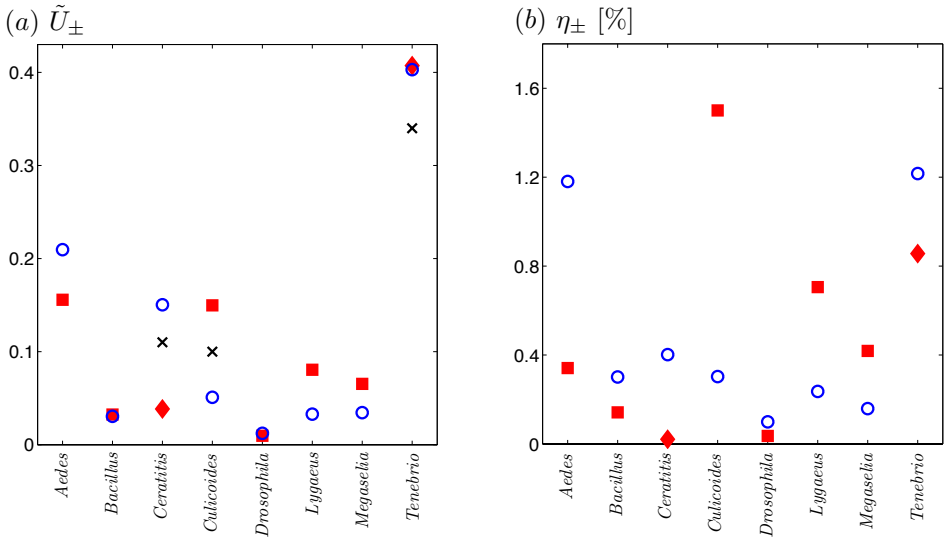

Figure 3.5: Predicted swimming performance: (a) average swimming speed, $\tilde{U}_{\pm}$, of different species; (b) hydrodynamic efficiency, $\eta_{\pm}$, of different species. Open symbols (blue circles) represent the same-chirality configuration (+); filled symbols (red squares and diamonds) represent the opposite-chirality configuration (−); for blue open circles and red squares, swimming occurs in the opposite direction as the wave propagation; on the contrary, red diamonds represent the cases of opposite-chirality configuration where the velocity in the z-direction occurring in the same direction as the wave propagation; black crosses represent experimental measurements of $V = V_{\text{sperm}}/c_m$ (See Tables 3.1 & 3.2).

3.3.1 Hydrodynamic performance

Propulsion speed

The propulsion speed is an important functional parameter characterizing the motility of a sperm cell. There exist only very few measurements of the swimming speed of insect spermatozoa exhibiting the double-wave structure: *Ceratitis capitata* was observed to swim with speed $V_{\text{sperm}} = 16\mu$m/s [13] and the minor wave speed is estimated to be 150μm/s (hence, $V = V_{\text{sperm}}/c_m$=0.11); *Culicoides melleus* [6] was observed to swim with speed 8.3μm/s and minor wave speed 80μm/s ($V = 0.10$). For the case of *Tenebrio molitor*, a wide range of sperm speeds were reported (from 16 to 100μm/s) as well as minor wave speeds (40 to 300μm/s) [7]. The distributions were not reported however, so using the arithmetic means we obtain a swimming speed to minor wave speed ratio of $V = 0.34$.

For a superhelical swimmer in our model, the swimming kinematics are three-dimensional and unsteady in time [1], and the most relevant quantification of the propulsion speed is an average swimming velocity in the laboratory frame, denoted by $\tilde{U}_{\pm}$, where the $+$ and $-$ signs represent the same- and opposite-chirality configurations respectively. The average swimming speed is defined as $\tilde{U}_{\pm} = |[\langle \tilde{U}_x \rangle, \langle \tilde{U}_y \rangle, \langle \tilde{U}_z \rangle]|$, where $|...|$ denotes the magnitude of a vector, and $\langle ... \rangle$ denotes a time average [2]. Since the chirality configuration remains unknown, we present predictions for both cases in Fig. 3.5a. Only the three sets of experimental measurements of the swimming performance ($V = V_{\text{sperm}}/c_m$) mentioned above are available for comparison and are super-imposed on the same figure (see Fig. 3.5 caption). Predictions as ratios of the swimming speed relative to the minor wave speed (dimensionless speed) for species with no measurement of V are also provided in Fig. 3.5a.

In most of the cases considered, the propulsion in the longitudinal direction (z-direction) of these superhelical swimmers is opposite to the direction of wave propagation (the major wave propagates in the positive z-direction, and the minor wave propagates along the curved major helix and distally towards the positive z-direction), regardless of the chirality configuration. This is not unlike the behavior of swimmers propagating a planar sinusoidal or a regular helical wave, for which the swimming direction is also opposite the direction of the wave propagation. In superhelical swimming, however, we also find cases of the opposite-chirality configuration where the body swims in the same direction as the wave propagation. Specifically, we note a qualitative difference between the study of the same-chirality and opposite-chirality configurations for *Ceratitis capitata* and *Tenebrio molitor*. In these simulations, a superhelical wave is set to propagate in the positive z-direction, and both the opposite-chirality configurations of *Ceratitis capitata* and *Tenebrio molitor* generate a positive U_z (swimming is in the same direction as the wave propagation), while their corresponding same-chirality configurations generate a negative U_z (swimming is in the opposite direction as the wave propagation).

[1] The deformations (Eqs. 3.3 to 3.5) are higher frequency oscillations modulated by lower frequency oscillation (a beat). There does not exists a time period T such that the deformation vector repeats itself: $\mathbf{R}(s, t+T) \neq \mathbf{R}(s,t), \forall T$.

[2] The time averaging is defined for a function $f(t)$ as $\int_0^{t_0} f(t)dt/t_0$, where t_0 is a sufficiently large time such that the peak-to-peak fluctuation in time is less than 1% of the final average value

The speed and efficiency of these peculiar swimmers are distinguished from other cases by red diamonds in Fig. 3.5. It remains a question whether this phenomenon may be observed in nature, since the chirality configuration and the swimming direction (relative to the wave propagation) of actual insect spermatozoa displaying the double-wave structure are still unclear. Nevertheless, this phenomenon by itself is intriguing and will be further explored in Sec. 3.3.3.

The swimming speed predictions lie at least within the same order of magnitude of the experimental measurements for both chirality configurations. The same-chiralty results provide slightly better agreement than the opposite-chiralty results (without taking the swimming direction into account). For the same-chirality configuration, the discrepancies, $|\tilde{U}_+ - V|/V$, between the predictions and the experimental measurements read 36% for *Ceratitis capitata*, 49% for *Culicoides melleus*, and 18% for *Tenebrio molitor*. For the opposite-chirality configuration, the discrepancy between our predictions and the experimental measurements, $|\tilde{U}_- - V|/V$, are 65% for *Ceratitis capitata*, 50% for *Culicoides melleus*, and 21% for *Tenebrio molitor*. Given the primitive nature of the data employed (see Sec. 3.2.4), we consider the agreements here to be reasonable. However, we cannot draw definite conclusions on the issue of chirality configuration; further experimental observations are necessary.

It shall be remarked that the present study is largely constrained by the unavailability of experimental measurement data. Critical kinematic information, such as the major and minor wave speeds, are often not reported in the literature and are impossible to estimate from the images available. The speed ratio $c = c_M/c_m$ is not available for simulations for most species. The computations here are still possible because of the independence of the swimming kinematics on the parameter c (verified numerically and will be explained in Sec. 3.3.3). Therefore, the specific value of c is unimportant for all cases considered here; we adopt $c = 0$ in all simulations hereafter unless otherwise stated.

Hydrodynamic efficiency

Another important functional parameter is the hydrodynamic efficiency of the swimmer. In the microscopic world, the hydrodynamic efficiency is typically very low. For a rigid helix, Lighthill [66] calculated theoretically the maximum

efficiency attainable to be about 8.5%, while the typical efficiency of biological cells is around 1-2% [16, 32, 66–69]. For low Reynolds number swimming, a common measure of the hydrodynamic efficiency, η, is the ratio of the rate of work required to drag the straightened flagellum through the fluid to the rate of work done on the fluid by the flagellum during swimming [66],

$$\eta_{\pm} = \frac{\xi_{\parallel} L \tilde{U}_{\pm}^2}{\left\langle \int_0^L \mathbf{v} \cdot \mathbf{f} ds \right\rangle}, \tag{3.15}$$

where $\xi_{\parallel} = 4\pi/c_0$ is the drag coefficient for a straight, slender rod, and the brackets indicate a time average. We calculate the hydrodynamic efficiencies for both the same- and opposite-chirality configurations (see Fig. 3.5b) for spermatozoa of different species. For the same-chirality configuration, the efficiency ranges from 0.16% (*Megaselia scalaris*) to 1.2% (*Aedes notoscriptus* and *Tenebrio molitor*); for the opposite-chirality configuration, the efficiency ranges from 0.036% (*Drosophila obscura*) to 1.5% (*Culicoides melleus*). The efficiencies of these swimmers are comparable with typical biological cells.

3.3.2 Model organism: *Culicoides melleus*

In this section, we illustrate the features of superhelical swimming by singling out a superhelical swimmer defined using the geometric data of the sperm cell of *Culicoides melleus* (Table 3.2). See Fig. 3.4 for the swimmer geometry.

Swimming kinematics

The swimming velocities computed for motion in the body frame $[U_x, U_y, U_z]$ and in the laboratory frame $[\tilde{U}_x, \tilde{U}_y, \tilde{U}_z]$ of the superhelical swimmer with data from the sperm cell of *Culicoides melleus* are plotted in Fig. 3.6 for the same-chirality (Fig. 3.6a) and opposite-chirality (Fig. 3.6b) configurations. We include in these figures the results for ratio of the major and minor wave speeds $c = 0$ (solid lines) and $c = 0.4$ (dotted lines). When $c = 0$, the deformation (Eqs. 3.12 to 3.14) is 2π-periodic, therefore the swimming kinematics in the body frame are also 2π-periodic. However, when observed in the laboratory frame, the coupling between the translational and rotational kinematics renders the swimming velocities no

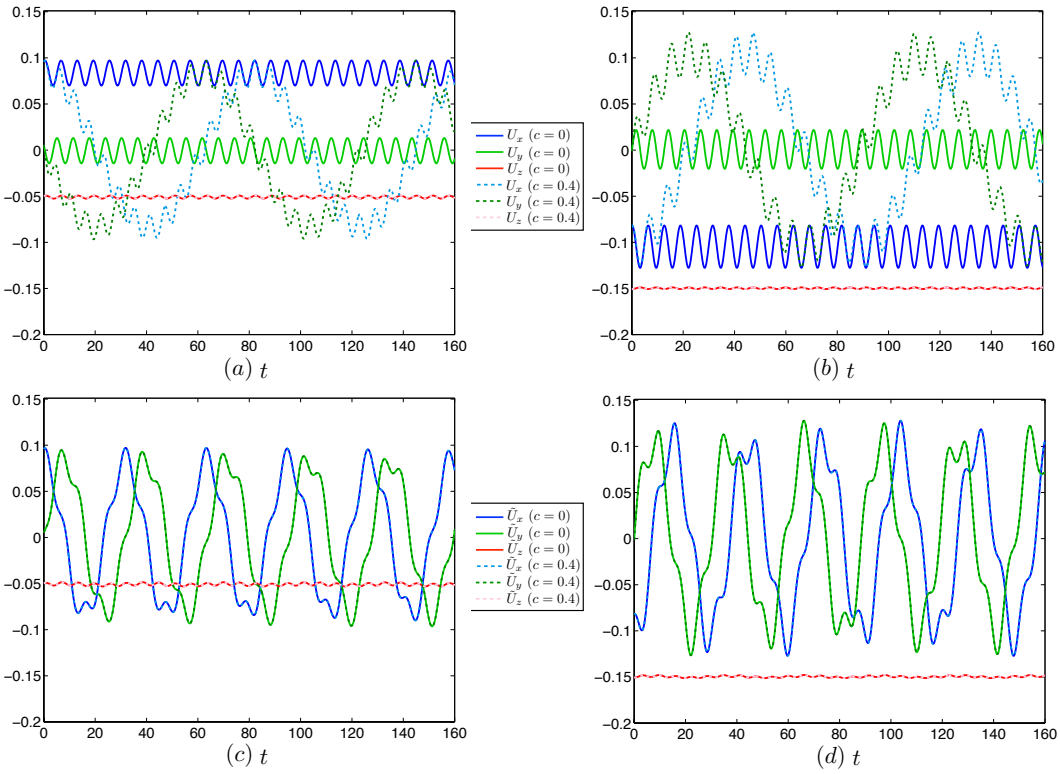

Figure 3.6: Swimming velocities in the body frame $\mathbf{U} = (U_x, U_y, U_z)$ for (a) the same-chirality and (b) the opposite-chirality configurations, and in the laboratory frame $\tilde{\mathbf{U}} = (\tilde{U}_x, \tilde{U}_y, \tilde{U}_z)$ for (c) the same-chirality and (d) the opposite-chirality configurations, for *Culicoides melleus* spermatozoa.

longer 2π-periodic, and the motion is unsteady in time (Fig. 3.6c & d). We observe a pattern consisting of higher frequency oscillations modulated by a lower frequency envelope. For the case of $c = 0.4$, when observed in the body frame, we see modulated waveforms. However, when transformed to the laboratory frame, the cases of $c = 0$ and $c = 0.4$ have identical swimming kinematics (see the overlapped solid and dotted lines in Fig. 3.6c & d), implying that the swimming kinematics in the laboratory frame are independent of the major propagating wave speed. The value of c affects only the kinematics in the body frame; why the relative wavespeed is unimportant is described in greater detail in Sec. 3.3.3.

The three-dimensional swimming velocities give rise to a doubly-helicated trajectory (the presence of a minor structure on top of a major helical structure). However, this could be difficult to observe experimentally, since the major amplitude of the doubly-helicated trajectory is usually much smaller than that of the superhelical swimmer; the swimmer would apparently move with a straight trajectory (with very small oscillations in the transverse direction). Recall that for regular helical swimming ($r = 0$), the trajectory of the helical swimmer reduces to a regular helix.

Head-less swimming

The shape and size of the sperm head vary among spermatozoa of different species: human and bull spermatozoa have relatively large, paddle-shaped heads, whereas insect spermatozoa have elongated heads which are almost indistinguishable from the mid-piece. The additional hydrodynamic resistance from the presence of a head would seemingly degrade the swimming performance of the sperm cell. However, Chwang and Wu [70] showed that a sperm head is actually necessary for helical swimming; without one, the motion is that of a rotating rigid body, which cannot be realized absent an external force or torque [71]. To satisfy the zero net-torque condition, a sperm head is required to balance the reaction torque acting on the flagellum. This constraint does not apply for planar, sinusoidal wave motion, which can swim without an anchor or load.

We pause to point out a subtle but important difference between a rotating prokaryotic helical tail and a eukaryotic tail propagating a bending helical wave. For a eukaryotic tail propagating a bending wave, the fluid forces act to rotate

the flagellum opposite the direction of the apparent helical rotation. The rotation due to the fluid reaction creates torques due to local spinning (rotation of the flagellum about its centerline), which balance the opposing torque generated by the helical wave propagation. Therefore, a eukaryotic cell could theoretically swim without a sperm head, albeit very slowly because the flagellum is very slender and the local torques are correspondingly small. Quantitatively, using a local drag model ([70]) it can be shown that the head-less swimming speed scales as $U/c \sim 2\mu k^2/\xi_{\parallel}(1 + k^2A^2)b^2 + O(b^4)$, where b is the radius of a cross-section of the flagellum, and k and A are the wavenumber and helical radius respectively. Using the geometrical data of flagella of *Euglena viridis* summarized by Brennen and Winet [17], and assuming a flagellar diameter of $2b \approx 0.25\mu$m [72,73], we find $U/c \approx 10^{-3}$. For a prokaryotic tail, however, the helix rotates as a rigid body. In this case, the local spinning torques generated by the active helical rotation and the passive rotation due to the fluid reaction are identical in magnitude but opposite in sign. The torque-free condition therefore requires that the fluid reaction counter-rotates the helix at precisely the rotation rate of the helical wave propagation. Hence there can be no effective helical rotation, and the body cannot swim. Although head-less swimming is theoretically possible for eukaryotic tails, the swimming speed would be exceptionally small as shown by the estimation above. The subtle difference between the two types of helical waves just described is often therefore neglected, and it is generally reasonable to state that head-less swimming is not possible using helical wave propagation.

In superhelical swimming a sperm head is not required for self-propulsion (indeed, all cases reported in this chapter were studied with the absence of a sperm head) since a superhelical wave motion is in general not a rigid body motion. Furthermore, since actual insect spermatozoa heads are very slender and short compared with the entire length of the flagellum, the contribution of its hydrodynamic resistance and the hydrodynamic interactions with the flagellum should be negligible. Therefore, we do not expect the presence of a slender and short sperm head to introduce qualitative differences in the results.

3.3.3 Parametric study

Next, we explore the effects of certain kinematic (wave speeds) and geometric parameters (wave amplitudes) on the swimming velocities of a superhelical swimmer.

The effect of the major/minor wave speed ratio

In this problem, we have scaled the velocities upon the minor wave speed c_m, which implies that the dimensionless swimming velocities scale linearly with the minor wave speed. Here we examine the effect of the major wave speed on the swimming performance of a superhelical swimmer and answer the question: to what relative extent do the two waves contribute to the propulsion of the superhelical swimmer [6]? Specifically, we study the effect of the parameter $c = c_M/c_m$, which is the ratio of the major wave speed to the minor wave speed. For every species shown in Table 3.2, we fix all parameters but vary the value of c from zero to unity ($c < 1$, as $c_M < c_m$). It is found that the swimming velocities in the laboratory frame is independent of the value of c. We have already shown in Fig. 3.6 the results for two values of c for illustration. While the resulting swimming motions in these two cases differ significantly in the body frame, they are identical when observed in a laboratory frame of reference. The numerical results imply that the major wave speed does not contribution to propulsion.

These findings may be understood by noting an ambiguity in definition. First consider a single helical filament (without a sperm head) placed in a fluid. Such a body cannot swim on its own, for there is no load or cell to counter balance the torque it would exert on the surrounding fluid during rotation, so it must be motionless as seen in a fixed, laboratory frame. However, this body may be represented as an active helical body propagating a wave with velocity c plus a rigid body rotation that contributes a wave with speed $-c$. That the body frame may be chosen arbitrarily allows for such an ambiguity in the definition of the swimming speed, but in the laboratory frame this ambiguity disappears.

A similar argument can be used to show that c has no bearing on the swimming speed of a superhelical flagellum in the laboratory frame. For a superhelical flagellum, the propagation of the major wave can be defined as a rigid body rota-

tion of the entire superhelical structure about the longitudinal axis (z-axis) in the body frame. The apparent rotation rate is the sum of the rotation caused by the active propagation of the major wave and the rotation caused by fluid reaction to maintain the force-free and torque-free conditions. For swimming without a head, only the apparent rotation rate is important because the fluid forces and torques are functions of the apparent rotation rate alone (not the absolute value of the rotation rate due to the active major wave propagation). Any alternation of the major wave speed is accompanied by a corresponding change in the rotation rate caused by the fluid reaction, resulting in the same apparent rotation rate and the same force and torque balances. Therefore, the kinematics and dynamics do not depend on the absolute value of the major wave speed c (or c_m). In other words, the major wave speed does not contribute to swimming.

For the case of swimming with a head, the fluid reaction will not only rotate the flagellum but also the sperm head, which creates extra torques and perturbs the original force and torque balances. Altering the absolute value of the major wave speed in this case theoretically will affect the swimming velocities even in the laboratory frame, because it changes the relative portion of the rotation rate caused by the fluid reaction and hence the value of the extra torque from the sperm head. However, since the sperm head is slender and short compared with the overall length of the flagellum of actual insect spermatozoa, the extra resistant forces and torques created should be insignificant. Therefore, we suggest that the propagation of the major wave contributes very little to the propulsion (none in the case of headless swimming), and that it is the minor wavespeed which is primarily responsible for the propulsion. Note also that the hydrodynamic efficiencies in Sec. 3.3.1 are independent of the value of c. Therefore, from a hydrodynamic efficiency point of view, there is no advantage or disadvantage to actively propagate a major wave. However, there are other energy costs not taken into account here (for example, work done to produce the sliding of microtubules within the flagellum) in actively propagating a major wave. Therefore, we speculate that it might be energetically more favorable for a doubly-helicated organism to propagate only a minor wave.

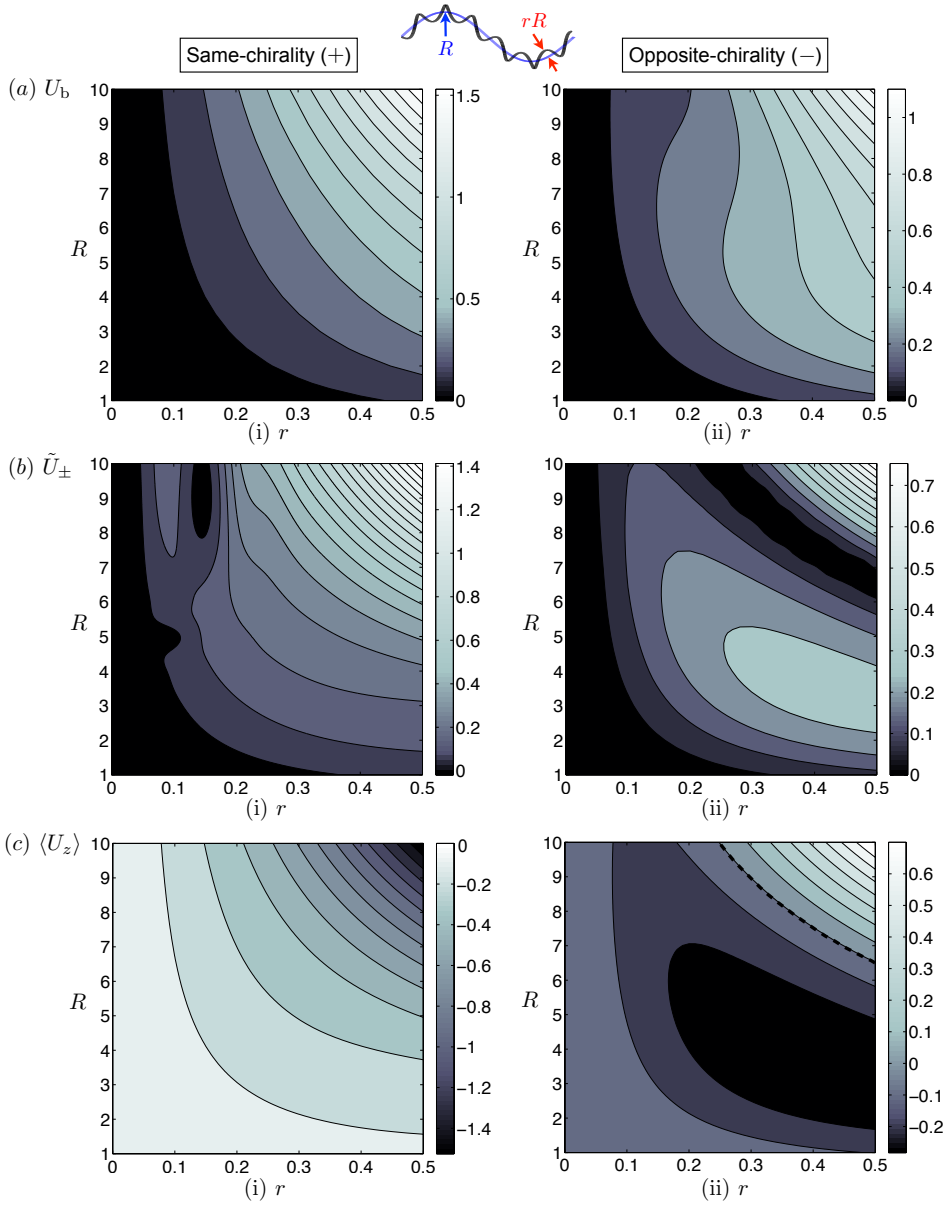

Figure 3.7: Parametric study of the dependence of the average swimming speed in the body fixed frame U_b (a(i)&(ii)) and in the laboratory frame $\tilde{U}_\pm$ (b(i)&(ii)) as a function of the dimensionless parameters R and r (see the schematic for geometrical illustration). Panels c(i) & c(ii) show the average swimming velocity in the z-direction in the body frame, $\langle U_z \rangle$, as a function of R and r. The panels on the left (right) refer to the same- (opposite-) chirality configuration. The dotted line in panel c(ii) represent the contour of $\langle U_z \rangle = 0$. Geometric data of *Culicoides melleus* spermatozoa are used for other fixed parameters.

The effect of the parameters R and r

We now examine the effect of geometrical dimensionless parameters R and r, keeping all other parameters of *Culicoides melleus* spermatozoa fixed. R is the dimensionless major wave amplitude and r is the ratio of minor to major wave amplitude, hence the minor wave amplitude is given by rR (see the schematic in Fig. 3.7). In general, one expects the propulsion speed to increase with the wave amplitude for simple geometries. However, for a superhelical structure, the dependence of the average swimming speed on the minor wave amplitude displays interesting behavior. Physically, both the propulsive force and the bulkiness of the structure are varied upon changing the major or minor wave amplitudes. The competition between these factors and the coupling between kinematics in different directions create interesting geometric dependencies of the average swimming speed. We illustrate this by observing the average swimming speed under different frames of reference.

First, we look at the time-averaged swimming velocity in the body frame $U_{\mathrm{b}} = |[\langle U_x(t)\rangle, \langle U_y(t)\rangle, \langle U_z(t)\rangle]|$. As shown in Fig. 3.7a(i), for the same-chirality configuration the average swimming velocity grows monotonically with R and r. Note that, keeping other parameters fixed, increasing the value of $R = A_M k_m$ for a fixed $r = A_m/A_M$ geometrically means that both the major A_M and minor A_m amplitudes are increased simultaneously by the same proportion. There is a competition between the increase in the overall hydrodynamic resistance due to the increased bulkiness (correlated with increases in A_M and A_m) and an enhanced propulsive force (correlated with an increase in A_m). In the case of the same-chirality configuration, the latter effect dominates. However, for the opposite-chirality configuration, as shown in Fig. 3.7a(ii), non-monotonic variations in the swimming speed with the major amplitude R are observed for certain values of r, the ratio of the minor to major wave amplitudes.

Since the swimming kinematics are three-dimensional, variations of the geometric parameters affect swimming velocities and rotational rates in all directions. In particular, a large propulsion speed in the body frame does not necessarily imply a large net propulsion speed in the laboratory frame. The mean swimming speeds in the laboratory frame for both chirality configurations are shown in Fig. 3.7b(i-ii). The coupling between the swimming kinematics in all directions

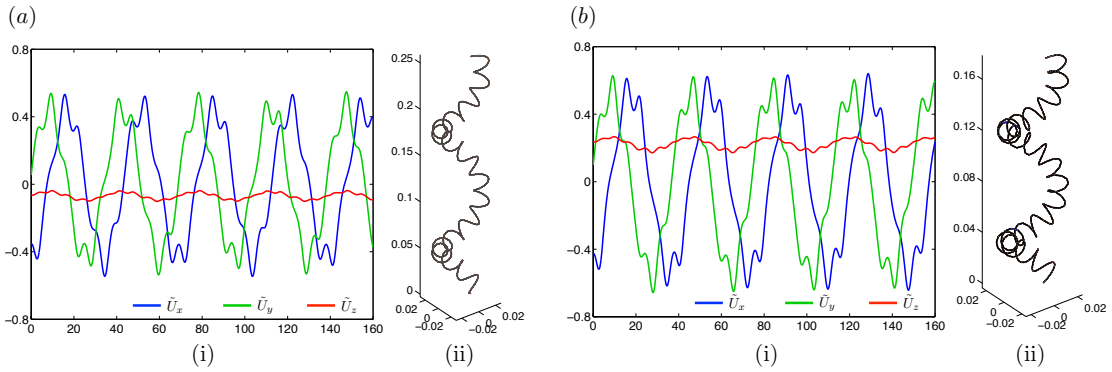

Figure 3.8: Three-dimensional swimming velocities in the laboratory frame ((a)i & (b)i) of two opposite-chirality superhelical swimmers, and their corresponding geometries ((a)ii & (b)ii). (a) $R = 7$, $r = 0.4$, and U_z is negative, while the wave propagation is towards the positive z-direction; (b) $R = 9$, $r = 0.4$, and U_z is positive, while the wave propagation is towards the positive z-direction. Geometric data of *Culicoides melleus* spermatozoa are used for other parameters.

produces more complicated variations in the propulsion speed as a function of R and r. Non-monotonic behaviors are observed in both cases.

We have already noted that some superhelical swimmers propel themselves surprisingly in the same direction as the wave propagation, unlike for planar or single helical wave propulsion. For the range of parameters explored in this chapter, this direction reversal is found to occur only in the opposite-chirality configuration for sufficiently large R and r (Fig. 3.7c(ii)), while the average propagation velocity $\langle U_z \rangle$ is always negative for the same-chirality configuration (i.e. the swimming direction is always opposite to the direction of the propagating wave) (Fig. 3.7c(i)). In Fig. 3.8, we show the detailed swimming velocities of two opposite-chirality superhelical swimmers, where one of them has its longitudinal propulsion in the opposite direction relative to the wave propagation ($R = 7$, $r = 0.4$, Fig. 3.8a), and the other in the same direction as the wave propagation ($R = 9$, $r = 0.4$, Fig. 3.8b). It is intriguing that a small change in the geometry (see the corresponding superhelices in Fig. 3.8a(ii) & b(ii)) can lead to a swimming direction reversal. We argue in the next section (Sec. 3.3.4) that this transition is related to the hydrodynamic interaction between distinct parts of the superhelical flagellum.

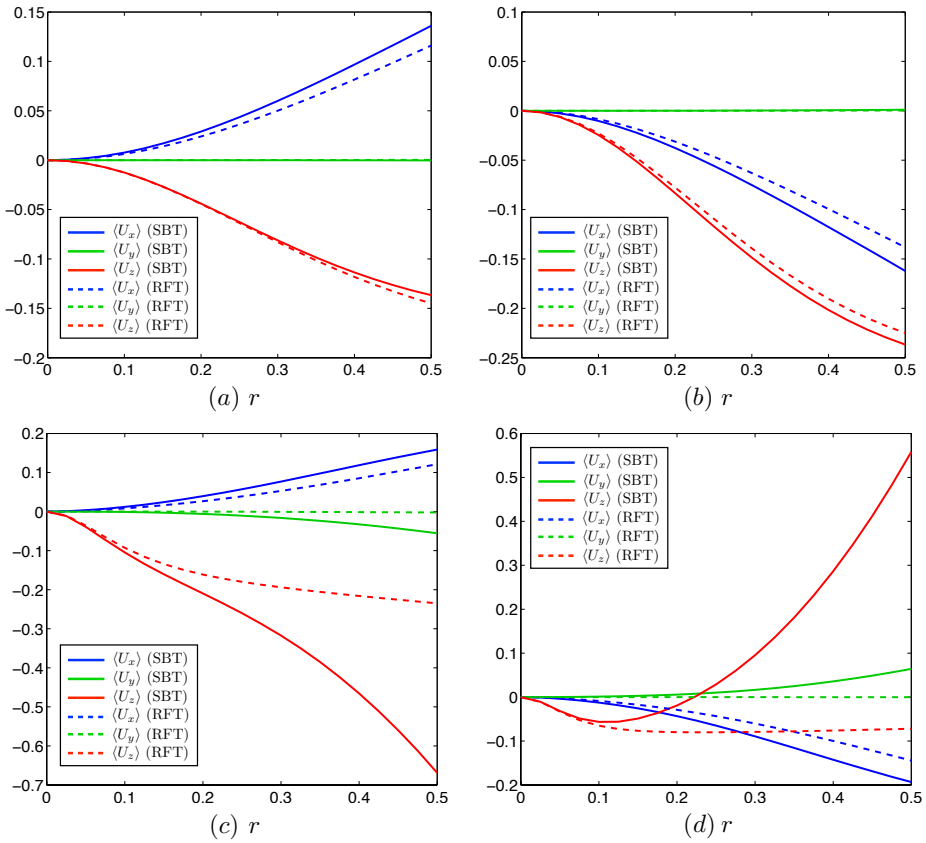

Figure 3.9: Comparison between the resistive force theory (RFT) (dashed lines) and the non-local slender body theory (SBT) (solid lines), using geometric data of *Culicoides melleus* spermatozoa (a) & (b), and *Tenebrio molitor* spermatozoa (c) & (d). The panels on the left (right) refer to the same- (opposite-) chirality configuration.

3.3.4 Comparison between slender body theory and resistive force theory

In order to consider the relative importance of nonlocal hydrodynamic interactions in the swimming of superhelices, we now compare our results to those obtained using the more commonly used local drag model (Eq. (3.6), but neglecting the non-local term **K**). The local drag model (so-called resistive force theory) ignores hydrodynamic interactions between distinct parts of the curved flagellum, and is expected to work well [59–61] for simple geometries where different parts of the body are sufficiently well separated. However, for more complicated geome-

tries, the local drag model may not capture even the correct qualitative features. Recently, Jung *et al.* [58] studied the rotational dynamics of opposite-chirality superhelices and found a qualitative discrepancy (the rotational direction of the superhelix when being towed in a viscous flow) between the experimental results and the predictions from the resistive force theory. Other recent works have also shown the inadequacy of the local drag model [69, 74].

Fig. 3.9 shows the swimming speeds computed with both non-local slender body theory and resistive force theory, using two sets of geometrical data: *Culicoides melleus* (Fig. 3.9a (same-chirality) & b (opposite-chirality)), and *Tenebrio molitor* (Fig. 3.9c (same-chirality) & d (opposite-chirality)). In these two cases, all other parameters are fixed but the amplitude ratio r is varied from 0 to 0.5. Increasing r complicates the swimmer geometry, and the hydrodynamic interactions are expected to be more significant for large r. For the case of *Culicoides melleus* (Fig. 3.9 a & b), we see good (even quantitative) agreement between the results form the slender body theory (solid lines) and the resistive force theory (dashed lines). However, for the case of *Tenebrio molitor* (Fig. 3.9 c & d), which has larger values of R and K, the deviation between the two models becomes significant for the same-chirality configuration (Fig. 3.9c) as r increases. There are even qualitative discrepancies: in the opposite-chirality configuration (Fig. 3.9c) for large values of r, the resistive force theory fails to capture the transition in the sign of $\langle U_z \rangle$ predicted by the slender body theory. Since no such transition is found when the hydrodynamic interactions are ignored, this transition may be attributed to nonlocal hydrodynamic interactions of the body with itself. In general, and perhaps unsurprisingly, we have shown that the local drag model breaks down when the geometry of the structure is sufficiently intricate.

3.3.5 Asymptotic analysis

In the locomotion of some species of spermatozoa, the minor wave amplitude is much smaller than the major wave amplitude (see Tables 3.1 & 3.2), which motivates us to perform an asymptotic analysis for $r \ll 1$. Such an asymptotic analysis linearizes the problem geometrically and allows the nonlinear effects to be taken into account order by order, making the problem more amenable to

mathematical analysis. However, even in the asymptotic consideration, three-dimensional force and torque balances do not yield tractable analytical results. Hence, in the spirit of Chwang and Wu [70], we perform the force and torque balances only in the longitudinal (z-) direction using the resistive force theory, which is expected to be at least qualitatively correct in the asymptotic limit $r \ll 1$. The local force f_z and torque m_z may be expressed as

$$f_z = c_{U_z F_z}(t,s)U_z + c_{\Omega_z F_z}(t,s)\Omega_z + c_{F_z}(t,s), \tag{3.16}$$

$$m_z = c_{U_z M_z}(t,s)U_z + c_{\Omega_z M_z}(t,s)\Omega_z + c_{M_z}(t,s), \tag{3.17}$$

where the coefficients are determined analytically from Eq. 3.6 (without the non-local operator) and the geometry of the swimmer (Eqs. 3.12 to 3.14). We consider regular perturbation expansions in r for every term in Eqs. 3.16 and 3.17, and enforce the force-free and torque-free conditions order by order. A non-zero time-averaged swimming velocity enters at $O(r^2)$. The leading order mean swimming velocities for the cases of same- and opposite-chirality configurations read

$$\begin{aligned}\tilde{U}_{\pm} \sim \frac{R^2 r^2}{2L^2\left(1+R^2K^2\right)^{3/2}} \times \Big\{ & \left(2-2L^2\right)(\xi-1) \\ & + R^2K^2\left[2(\xi-1\pm K) - L^2(2\xi-2\pm K)\right] \\ & - 2\left[\xi-1+R^2K^2(\xi-1\pm K)\right]\cos L \Big\},\end{aligned} \tag{3.18}$$

where $\xi = \xi_\perp/\xi_\parallel$ is the ratio of the drag coefficients in the normal direction to the longitudinal direction ($\xi_\parallel = 4\pi/c_0, \xi_\perp = 8\pi/(2+c_0)$). For very slender filaments, $\xi \approx 2$. We note that the substitution $K \to -K$ in Eq. 3.18 converts the same-chirality speed $\tilde{U}_+$ to the opposite-chirality speed $\tilde{U}_-$. The propulsion speed has a quadratic dependence on the minor wave amplitude for small r, which is also found in planar [34] and helical [75] geometries.

These asymptotic results (Eq. 3.18) are compared to the finite amplitude simulations (both the resistive force theory and the slender body theory predictions) in Fig. 3.10, for a very small amplitude ratio of $r = 0.01$ and a slenderness ratio of $\epsilon = 1/1000$. There is excellent agreement between the asymptotic results and the finite amplitude resistive force theory simulations. The discrepancy between the non-local slender body theory and the local drag model highlights the importance of non-local hydrodynamic interactions for such organisms.

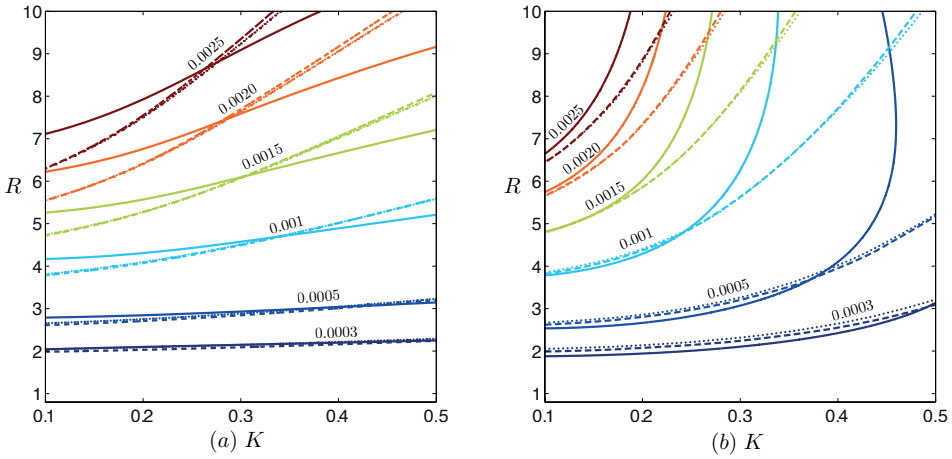

Figure 3.10: Comparison of the asymptotic results (dotted lines) with the results from finite-amplitude simulations using the resistive force theory (dashed lines) and the non-local slender body theory (solid lines). Shown are the contour lines of the average swimming velocity $\tilde{U}_{\pm}$ for the (a) same-chirality, and (b) opposite-chirality configuration for a small minor to major wave amplitudes ratio of $r = 0.01$.

We conclude by pointing out an intriguing theoretical curiosity, that drag anisotropy ($\xi \neq 1$) is not required for superhelical swimming: setting $\xi = 1$ in Eq. 3.18, non-zero mean propulsion velocities (of equal magnitude but opposite signs) are obtained for both chirality configurations,

$$\tilde{U}_{\pm}(\xi = 1) = \mp \frac{R^4 K^3 (L^2 - 2 + 2\cos L)}{2L(1 + R^2K^2)^{3/2}} r^2. \tag{3.19}$$

Note that Becker *et al.*'s [76] argument of the requirement of drag anisotropy for locomotion is only true for inextensible swimmers and does not apply here. The superhelical kinematics described (Eqs. 3.12 to 3.14) are only possible when extensibility is allowed; the minor helix is built upon another curved structure (the major helix) and local extension and contraction is implied in the wave kinematics. When extensibility is permitted, the relaxation of the drag anisotropy requirement has been recently shown [77]. That the swimming speed is non-zero is due to intrinsic variations in length (and hence drag) embedded in the curved geometry of the superhelices. A minor helix built upon a major helix has relatively shorter lengths in the regions closer to the longitudinal axis, creating an overall imbalance of hydrodynamic drag even in the isotropic drag case ($\xi = 1$). A similar example is a toroidal helix (a helix built upon a circle), which is an idealized model studied

recently for dinoflagellates [78]. We expect that the propagation of a wave along a toroidal helix should also require extensibility, and that propulsion is still possible even without drag anisotropy [77].

3.4 Discussion

In this chapter we have studied a morphologically interesting double-wave structure exhibited by various insect spermatozoa. The construction of such spermatozoa is considerably more complex than those for flagella which exhibit simpler planar or helical waves: the flagellum does not only have a more complicated 9+9+2 arrangement of microtubules but also mitochondrial derivatives and accessory bodies running along the axoneme [12]. We have mathematically idealized the double-wave structure as a superhelical structure and presented a hydrodynamic study on superhelical swimming. The available data is primitive and sparse; nevertheless, we consider the agreement between experimental measurements and the theory explored herein to be quite reasonable. Through numerical experiments, we have found that the major wave speed has little contribution to propulsion when the sperm head is small, as is the case for insect spermatozoa. When there is no sperm head, the propulsion speed is independent of the major wave speed and depends entirely upon the minor wave speed. We have also explored the dependence of the propulsion speed on the dimensionless major wave amplitude R and the ratio of the minor to major wave amplitudes r (Fig. 3.7), and counter-intuitive behaviors have been found for the opposite-chirality configuration. In particular, we have found that propulsion and wave propagation can occur in the same direction for superhelices in the opposite-chirality configuration.

The present study suggests that the major wave has negligible influence on the motility of a superhelical swimmer. This finding favors the recent hypothesis by Werner *et al.* [56] that the major helical wave is a static (non-propagating) structure; the minor wave structure is solely responsible for the motility, and the apparent major wave propagation is simply due to the passive rotation of the entire geometry (see Sec. 3.1). However, in the study by Baccetti *et al.* [13] on the motility of *Ceratitis capitata*, they have adopted the same experimental techniques as in Gibbons *et al.* [79], which distinguished the rolling frequency from the apparent

beat frequency. In their work, the rolling frequency was measured by stroboscopic observation of the eccentrically attached sperm head, and the flagellar beat frequency was measured by the same means with the sperm head adhered to the bottom of the observation dish. Using this method, the major wave speed measured should be taken as an active propagation speed. We are not in a position to provide a definite answer on whether or not the major wave propagates actively in actual insect spermatozoa. However, according to the present study, we suspect that there might be some biological reasons, other than motility, for the major wave to propagate actively. We also do not know if the propagation of the major wave is a biological prerequisite for the propagation of the minor wave. Further biological studies are required to answer these questions.

It is illuminating to compare the superhelical swimming studied here to regular helical swimming. The swimming trajectories are qualitatively different in the two cases: in regular helical swimming, the trajectory is a regular helix, whereas in superhelical swimming the trajectory is doubly-helicated. In addition, a regular helical flagellum cannot swim on its own; a sperm head is required to swim (since the absence of a sperm head renders the deformation of the regular helix a rigid body motion). In contrast, the propagation of superhelical waves along a flagellum is in general not equivalent to rigid body motion, and hence "head-less" swimming is possible. This might help explain the presence of only a small slender sperm head in insect spermatozoa. In other words, superhelical swimming can be viewed as an alternative mechanism to regular helical swimming when only a small sperm head is available.

Finally, a non-local slender body theory was used in this work and compared with a simpler and widely used local drag model. We showed that the resistive force theory failed to capture even the qualitative features of the swimmer when the geometry becomes complicated. The results suggest that further hydrodynamic studies on superhelical structures require more advanced models than the local resistive force theory, such as the slender body theory employed here. Optimization with respect to the efficiency of the swimmer taking into account of the viscous dissipation, and other energy costs due to bending and internal sliding of filaments [68], which have been neglected in this work, will be interesting for future work.

Chapter 3, in full, is a reprint of the material as it appears in Journal of The Royal Society Interface 2012. Pak, On Shun; Spagnolie, Saverio E.; Lauga, Eric, the Royal Society, 2012. The dissertation author was the primary investigator and author of this paper. Useful conversations with Dr. Michael Werner and Dr. Anne Swan are gratefully acknowledged.

Chapter 4

Propulsion of Flexible Nanowire Motors

Micro/nano-scale propulsion has attracted considerable recent attention due to its promise for biomedical applications such as targeted drug delivery. In this chapter, we report on a new experimental design and theoretical modelling of high-speed fuel-free magnetically-driven propellers which exploit the flexibility of nanowires for propulsion. These readily prepared nanomotors display both high dimensional propulsion velocities (up to $\approx 21\mu$m/s) and dimensionless speeds (in body lengths per revolution) when compared with natural microorganisms and other artificial propellers. Their propulsion characteristics are studied theoretically using an elastohydrodynamic model which takes into account the elasticity of the nanowire and its hydrodynamic interaction with the fluid medium. The critical role of flexibility in this mode of propulsion is illustrated by simple physical arguments, and is quantitatively investigated with the help of an asymptotic analysis for small-amplitude swimming. The theoretical predictions are then compared with experimental measurements and we obtain good agreement. Finally, we demonstrate the operation of these nanomotors in a real biological environment (human serum), emphasizing the robustness of their propulsion performance and their promise for biomedical applications.

4.1 Introduction

Micro/nano-scale propulsion in fluids is challenging due to the absence of the inertial forces exploited by biological organisms on macroscopic scales. The difficulties are summarized by Purcell's famous "scallop theorem" [18], which states that a reciprocal motion (a deformation with time-reversal symmetry) cannot lead to any net propulsion at low Reynolds numbers. Because of the potential of nano-sized machines in future biomedical applications [19], such as targeted drug delivery and microsurgery, interdisciplinary efforts by scientists and engineers have recently resulted in major advances in the design and fabrication of artificial micro/nano-scale locomotive systems [21–24].

Broadly speaking, these micro/nano-propellers can be classified into two categories, namely chemically-powered nanomotors [21–23] and externally-powered propellers [24]. Chemically-powered nanomotors generally deliver higher propulsion speeds, but due to the requirements for chemical fuels and reactions, their applications in real biological environments face a number of challenges. Externally-powered propellers are often actuated by external magnetic fields. Note that these externally-powered locomotive systems are often referred to micro- or nano-swimmers in the literatures, but strictly speaking, they do not represent true self-propulsion because of the presence of non-zero external torques. In this chapter, we reserve the terminology, "swimmers", to force-free and torque-free self-propelling bodies and refer to externally-powered locomotive systems as propellers, or motors.

According to their propulsion mechanisms, externally powered propellers can be further categorized into three groups. The first group includes helical propellers [80, 81], as inspired by helical bacterial flagella [2], which propel upon rotation imposed by external magnetic fields. The second group of propellers relies on a surface to break the spatial symmetry and provide one additional degree of freedom to escape the constraints from the scallop theorem, and hence are termed surface walkers [82–85]. Finally, the third type of propellers, referred to as flexible propellers, exploits the deformation of flexible filaments for propulsion. The new nanomotor presented in this chapter falls into this category. Dreyfus *et al.* [86] were the first to realize the idea experimentally by fabricating a 24μm long propeller based on a flexible filament, made of paramagnetic beads linked by DNA, and

attached to a red blood cell. Actuation was distributed along the filament by the paramagnetic beads; the presence of the red blood cell broke the front-back symmetry, and allowed the propagation of a traveling wave along the filament, leading to propulsion. Recently, Gao *et al.* [87] proposed a flexible nanowire motor made of only metallic nanowires (with three segments of Au, Ag and Ni) readily prepared using a template electrodeposition approach, and able to swim at speeds of up to $U \approx 6\mu$m/s for a size of $L \approx 6.5\mu$m. In contrast to the propeller proposed by Dreyfus *et al.* [86], the actuation in the device of Gao *et al.* [87] acted only on the magnetic Ni portion of the filament (the head), while the rest of nanomotor was passive.

In the current chapter, we present both a new design and a theoretical modelling approach for a flexible nanowire motor which offers an improved propulsion performance (up to $U \approx 21\mu$m/s at an actuation frequency (f) of 35Hz), approaching thus the speed of natural microscopic swimmers, such as *Escherichia coli* ($U \approx 30\mu$m/s at $f = 100$Hz) [2] while using a lower frequency. The effect of size and frequency can be scaled off by nondimensionalizing the propulsion speed by the intrinsic velocity scale (the product of body length and frequency, Lf) to obtain a dimensionless propulsion speed, U/Lf, which can be interpreted as the number of body lengths travelled per revolution of actuation (or also referred to as the stride length in terms of body length in the biomechanics literature). The nanomotor put forward in this chapter displays remarkable dimensionless propulsion speeds compared with natural microorganisms and other artificial locomotive systems.

After presenting the experimental method and its performance, we study the propulsion characteristics of this new high-speed flexible nanomotor theoretically via an analytical model. The critical role of flexibility in this mode of propulsion is established first using simple physical arguments, followed by an asymptotic analysis which predicts the filament shape and propulsion speed in different physical regimes. The theoretical predictions are compared with experimental measurements and we obtain good agreements. The improved propulsion performance of the new fuel-free nanowire motor makes it attractive for future biomedical applications, which we further illustrate by demonstrating the performance of the propulsion mechanism in an untreated human serum sample.

4.2 High-speed propulsion

4.2.1 Nanomotor design and fabrication

The nanowire motors described in this chapter were prepared using a common template-directed electrodeposition protocol. In contrast to the previous three-segment (Ni-Ag-Au) design by Gao *et al.* [87], the new design relies primarily on a 1.5μm-long Ni head and a 4μm-long flexible Ag tail (see a Scanning Electron Microscopy (SEM) image in Fig. 4.1b). A 0.3μm-long Au segment was also included (adjacent to the Ni segment) to protect the Ni segment from acid etching during the dissolution of the Cu sacrificial layer, and to allow functionalizing the motor with different types of biomolecules and cargos. Both the Ni and Au segments have a diameter of 200nm. While the Ni segment has a length of 1.5μm useful to generate sufficient magnetic torques, only a very short segment of Au (0.3μm) was used to minimize the overall fluid drag of the nanomotor. Flexibility of the silver segment (Fig. 4.1b) was achieved by its partial dissolution in hydrogen peroxide solution [87]. The dissolution step leads also to hydroxyl products that chemisorb on the Ag surface and result in AgOH and Ag_2O surface products. The dissolved Ag filament had a reduced diameter of approximately 100nm. For the hydrodynamic model considered in this chapter, the rigid short Au segment is hydrodynamically indistinguishable from the rigid Ni segment, and hence the Ni and Au segments are considered in the model as a single rigid 1.8μm-long segment (1.5μm Ni+ 0.3μm Au), i.e. the nanomotor has a total length of 5.8μm.

The speed of a nanomotor was measured using MetaMorph 7.6 software (Molecular Devices, Sunnyvale, CA), capturing movies at a frame rate of 30 frames per sec. The trajectory was tracked using a Metamorph tracking module and the results were statistically analyzed using Origin software. The speed measured in this manner is a time-averaged distance travelled per unit time. The measurements were performed when the nanomotors had reached an equilibrium position (in which case the image of the nanowire would stay focused under the microscope), which leads therefore to the time-averaged measurement of U in the laboratory frame. The equilibrium distance between the nanomotor and the bottom surface was estimated, by varying the focal plane of the microscope, to be at the scale of a few microns.

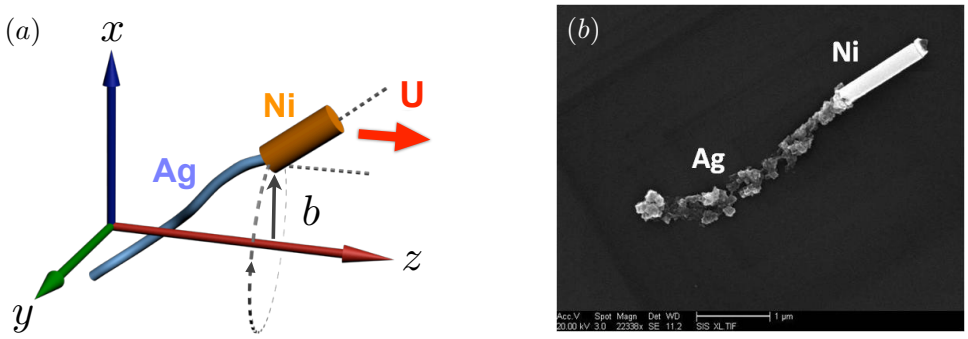

Figure 4.1: (a) Schematic representation of a Ni-Ag nanowire motor, and notation for the model. (b) Scanning Electron Microscopy (SEM) image showing the topography of Ni-Ag nanowire which was partially dissolved in 5% H_2O_2 for 1 minute.

4.2.2 Propulsion performance

The flexible nanomotors were driven by a magnetic field with an unsteady component of amplitude H_1, rotating sinusoidally in a plane perpendicular to a constant component, H_0. The magnetic field precessed about the direction of the constant magnetic field at an angular frequency $\Omega = 2\pi f$. The nanomotor was observed to propel unidirectionally (straight trajectories) in the direction of the constant magnetic field. In Fig. 4.2 we show two nearby identical nanomotors under the actuation of the external magnetic field at $f = 20$Hz. These two nanowires propel at essentially the same swimming speed along the same direction (the red lines are their trajectories in a period of 2 seconds), illustrating the stability of this mode of propulsion. For helical propellers [80,81], swimming is due to the rotation of rigid chiral objects and hence the swimming kinematics scales linearly with the applied field: a reversal of the direction of rotation of the magnetic field leads to propulsion in the opposite direction for these rigid chiral objects. In contrast, the flexible nanowire motors here exhibit uni-directional swimming, independent of the rotational direction of the external magnetic field. This is due to the nonlinear swimming kinematics arising from the flexibility of the nanowire. This simple test illustrates the fundamental difference between the propulsion of rigid chiral objects and flexible propellers. In our case, the direction of swimming can be controlled by altering the orientation of the axial constant component of the magnetic field, H_0.

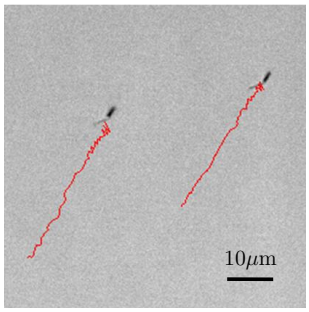

Figure 4.2: Two identical nanomotors swimming under the same magnetic field at a frequency $f = 20$Hz. The red lines display the superimposed location of the nanomotors over a 2-second interval.

We further show in Fig. 4.5(a) the trajectories of the same nanomotor at different frequencies (see captions for details) over a 3-second period. Upon the settings $H_1 = 10$G, $H_0 = 9.5$G, and $f = 15$Hz, we are able to achieve a propulsion speed of $U = 14.3 \pm 2.46\mu$m/s. The speed of 20 different nanomotors were measured, with all other experimental conditions kept fixed; the values of the swimming speeds, U, reported in this chapter are averaged quantities over these different nanomotors. One meaningful method of comparing the propulsion speed between various propeller designs consists in scaling the speed with the only intrinsic characteristic velocity scale of the propeller Lf, where L is a characteristic body length, and f is a characteristic frequency. This allows to quantify the distance travelled by the propeller in terms of body lengths per revolution of rotation. *Escherichia coli* bacteria [2] typically propel with $U/Lf \approx 0.03$ body lengths per revolution, while the flexible nanomotor reported here was able to travel 0.164 body lengths per revolution at $f = 15$Hz. The maximum dimensional speed achieved was $U = 20.8 \pm 3.07\mu$m/s with $f = 35$Hz, corresponding in that case to ≈ 0.1 body lengths per revolution. We then experimentally measured the speed-frequency characteristics of these flexible nanowire motors (results shown as symbols in Fig. 4.5b). In the next section we present a simple physical model for the locomotion of flexible nanomotors, and compare our theoretical predictions with these experimental measurements.

4.3 A minimal model for flexible nanomotors

4.3.1 Chiral propulsion

In this section, we illustrate the working principles of the flexible nanowire motors. First, we establish that it is essential for the nanowire to deform in a chiral fashion in order to achieve propulsion.

For low Reynolds number incompressible flows, the governing equations are the Stokes equation $\nabla p = \mu \nabla^2 \mathbf{u}$, and the continuity equation $\nabla \cdot \mathbf{u} = 0$, where μ is the shear viscosity, and p and $\mathbf{u}$ are the fluid pressure and the velocity field respectively. Two properties of the Stokes equation can be used to deduce the necessity of the nanowire being chiral in order to achieve net swimming, as shown by Childress [32]. First, it can be shown that the mirror image of a Stokes flow is also a Stokes flow. Therefore, suppose a nanowire swims with a velocity $\mathbf{U}$ along its rotation axis, then its mirror image will also swim at the same velocity $\mathbf{U}$ (see Fig. 4.3). Second, since time does not appear in Stokes equation, it only enters the problem as a parameter through the boundary conditions. This leads to the time reversibility of the Stokes equation, meaning that the velocity field $\mathbf{u}$ reverses its sign upon a $t \to -t$ time reversal. In the context of our nanowire motors, suppose the nanowire propels at a velocity $\mathbf{U}$, then when time is reversed, the nanowire will propel at a velocity $-\mathbf{U}$ (Fig. 4.3). If the deformation of the nanowire is not chiral, the mirror image of the nanowire can be superimposed with the original nanowire, and the only thing reversed in the mirror image is the rotational kinematics (*i.e.* if the original nanowire rotates clock-wisely, its mirror image will have exactly the same shape but rotates counter-wisely; note that the translational velocity is unchanged in the mirror image). In this case, one can also notice that the kinematics in the mirror image is the same as a time reversal of the original kinematics, except that the translational velocity is also reversed for the case of time-reversal ($-\mathbf{U}$, due to the time-reversibility of Stokes flows). In other words, we have now two nanowires (a mirror-imaged nanowire and a time-reversed nanowire) having exactly the same deformation kinematics but with opposite translational velocity ($-\mathbf{U} = \mathbf{U}$), and therefore we conclude that this can happen only if the translational velocity is identically zero ($\mathbf{U} = \mathbf{0}$). Therefore non-chiral deformation cannot lead to net propulsion. This simple physical argument shows that a com-

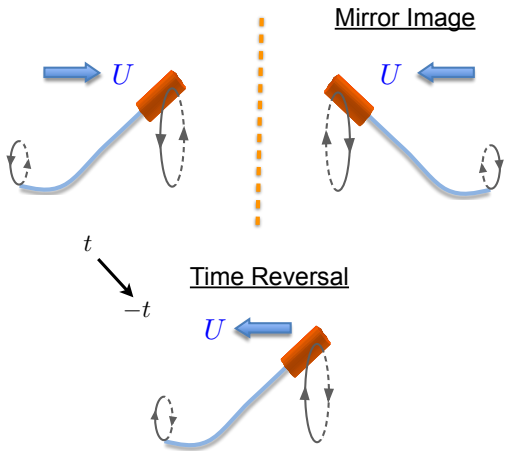

Figure 4.3: Physical explanation of the necessity of chiral deformation in achieving propulsion. If the deformation is not chiral, the kinematics of the mirror image of the nanowire is identical to the time-reversed kinematics, leading to $\mathbf{U} = \mathbf{0}$.

bination of rotational actuation and nanowire flexibility is critical for this mode of propulsion. Recently, the dynamics of tethered elastic filaments actuated by precessing magnetic fields has been studied [88–95] and chiral deformation along the filament has been found to produce propulsive force and fluid pumping. The swimming behaviours of an untethered flexible magnetic filament displaying chiral deformation was also addressed computationally [96].

4.3.2 Model setup

Next we show that a simple model taking into account the elasticity of the nanowire and its hydrodynamic interaction with the fluid medium captures the essential physics and provides quantitative agreements with experimental measurements. We first solve for the detailed shape of the silver filament, we then predict the propulsion speed, and finally we compare our results with the experimental measurements. Theoretical modelling of this type belongs to the general class of elastohydrodynamical problems, which has recently received a lot of attention in the literature [59, 60, 91, 97–101].

Under our theoretical framework, we model the magnetic Ni segment as a rigid slender rod (radius $a_m = 100$nm, length L_m=1.8μm) (the short Au segment is considered to be part of the rigid rod in this model, as discussed above, see

Fig. 4.1), and the flexible Ag nanowire (radius $a = 50$nm, length $L = 4\mu$m) as a classical Euler-Bernoulli beam [102]. We then employ a local fluid drag model, known as resistive force theory [16], to describe the fluid-body interaction. The use of a local and linear theory significantly simplifies the analysis and is expected to provide quantitative agreements because geometric nonlinearities and nonlocal hydrodynamic effects were proven to be subdominant for gentle distortions of a slender body in previous work [60, 98, 100].

Notation for the model is shown in Fig. 4.1(a). The external magnetic field precesses about the z-axis in the clock-wise direction, and can be described as $\mathbf{H} = [H_1 \cos\Omega t, -H_1 \sin\Omega t, H_0] = H_0[\mathrm{h}\cos\Omega t, -\mathrm{h}\sin\Omega t, 1]$, where $\mathrm{h} = H_1/H_0$ is the dimensionless relative strength of the rotating (H_1) and constant (H_0) components of the magnetic field. We study the regime where the nanowire follows synchronously the precessing magnetic field, rotating at the same angular frequency (Ω) as the magnetic field about the z-axis. In addition, we can move in a rotating frame in which the magnetic field is fixed and the shape of the flexible nanowire does not change with time. In this frame, the precessing magnetic field is given by $\mathbf{H} = H_0[\mathrm{h}, 0, 1]$, and the nanowire has a non-changing shape $\mathbf{r}(s) = [\mathbf{r}_\perp(s), z(s)] = [x(s), y(s), z(s)]$ in a background flow, $\mathbf{v}_b$, rotating counter-clockwise about the z-axis: $\mathbf{v}_b = \Omega\mathbf{e}_z \times \mathbf{r}_\perp = \Omega(-y, x, 0)$, where $\mathbf{e}_z$ is the unit vector in the z-direction and s is the arclength parameter along the filament.

4.3.3 Elastohydrodynamics at low Reynolds number

We describe the fluid-body interaction by resistive force theory, which states that the local fluid drag depends only on the local velocity of the filament relative to the background fluid (although in a non-isotropic fashion). This is thus a local drag model which ignores hydrodynamic interactions between distinct parts of the filament, but was shown to be quantitatively correct for gentle distortions of the filament shape [60, 98, 100]. The viscous force acting on the filament is thus expressed as

$$\mathbf{f}_{\mathrm{vis}} = -[\xi_\parallel \mathbf{tt} + \xi_\perp(1 - \mathbf{tt})] \cdot \mathbf{u}, \tag{4.1}$$

where $\mathbf{t}(s)$ is the local tangent vector, $\mathbf{u}(s) = \mathbf{U} - \mathbf{v}_b$ is the local velocity of the filament relative to the background flow $\mathbf{v}_b$, and $\mathbf{U}$ is the swimming velocity of the

nanomotor. Here, $\xi_\parallel$ and $\xi_\perp$ are the tangential and normal drag coefficients of a slender filament ($L \gg a$) and are given approximately by

$$\xi_\parallel = \frac{2\pi\mu}{\log(L/a) - 1/2},\ \xi_\perp = \frac{4\pi\mu}{\log(L/a) + 1/2}, \tag{4.2}$$

where μ is the viscosity of the fluid (water, $\mu = 10^{-3}\mathrm{Ns/m}^2$). Since the Ni and Ag segments have different aspect ratios (L_m/a_m for the Ni segment), a different set of drag coefficients ($\xi_{m\parallel},\ \xi_{m\perp}$) is used for the rigid segment.

When the flexible Ag filament of the nanomotor is deformed, elastic bending forces arise trying to minimize the bending energy. This elastic bending force can be obtained by taking a variational derivative of the energy functional $\mathcal{E} = \frac{1}{2}\int_0^L A\left(\partial^2\mathbf{r}/\partial s^2\right)^2 ds$, where A is the bending stiffness of the material. The elastic bending force is then given by

$$\mathbf{f}_{\text{elastic}} = -A\frac{\partial^4\mathbf{r}}{\partial s^4}. \tag{4.3}$$

Since we are in the low Reynolds number regime, inertial forces are negligible, and the local viscous fluid forces balance the elastic bending forces, $\mathbf{f}_{\text{vis}} + \mathbf{f}_{\text{elastic}} = 0$, which yields the equation governing the filament elastohydrodynamics

$$[\xi_\parallel \mathbf{tt} + \xi_\perp(1 - \mathbf{tt})] \cdot \mathbf{u} = -A\frac{\partial^4\mathbf{r}}{\partial s^4}. \tag{4.4}$$

The flexible Ag filament is clamped to the magnetic Ni segment, which is assumed to be rigid and straight. Hence, its position vector is given by $\mathbf{r}_m(s) = \mathbf{r}\mid_{s=L} + \mathbf{t}\mid_{s=L}(s - L)$, where $s \in [L, L + L_m]$.

4.3.4 Nondimensionalization

We now nondimensionalize the variables and equations and identify the relevant dimensionless parameters governing the physics of this problem. Specifically, we scale lengths by L, rotation rates by $\Omega = 2\pi f$, times by Ω^{-1}, velocities by $L\Omega$, fluid forces by $\xi_\perp L^2\Omega$, fluid torques by $\xi_\perp L^3\Omega$, elastic forces by A/L^2, and elastic torques by A/L. Using the same symbols for simplicity, the dimensionless elastohydrodynamic equation now reads

$$[\gamma^{-1}\mathbf{tt} + (1 - \mathbf{tt})] \cdot \mathbf{u} = -\mathrm{Sp}^{-4}\frac{\partial^4\mathbf{r}}{\partial s^4}, \tag{4.5}$$

where we have defined $\gamma = \xi_\perp/\xi_\parallel$, and $\mathrm{Sp} = L\left(\xi_\perp\Omega/A\right)^{1/4}$ is termed the sperm number, which characterizes the relative influence of the fluid and bending forces.

4.3.5 Asymptotic analysis

The geometrical nonlinearity of Eq. (4.5) renders the elastohydrodynamic equation only solvable via numerical simulation in most situations. Here we are able to illustrate the essential physics of flexible nanomotor propulsion analytically via an asymptotic analysis for the case where $\mathrm{h} = H_1/H_0$ is small. Such an approximation drops the geometrical nonlinearities and, as will be shown below, separates the task of determining the filament shape and swimming velocities of the nanomotor, as the axial velocities are one order of magnitude smaller than the transverse velocities, the axial swimming kinematics being thus slaved to the transverse kinematics [101]. Even with this simple model, we find that the theoretical predictions agree well with the experimental measurements. In the experiments, we do not observe very significant distortion of the flexible Ag filament, which might explain the success of this simple model.

As the nanomotor was observed to propel unidirectionally in the z-direction in the experiments (i.e. the direction about which the actuating magnetic field precesses), we write the swimming speed as $\mathbf{U} = (0, 0, U)$ and aim at predicting the leading order swimming speed in h. We do not expect any $O(\mathrm{h}^0)$ deformation nor swimming velocities, and hence the appropriate expansions for the deformation of the nanowire and the swimming speed are given by

$$\mathbf{r}_\perp(z) = \mathrm{h}\ \mathbf{r}_{\perp_1}(z) + \mathrm{h}^2\mathbf{r}_{\perp_2}(z) + O(\mathrm{h}^3), \tag{4.6}$$

$$U = \mathrm{h}\ U_1 + \mathrm{h}^2\ U_2 + O(\mathrm{h}^3), \tag{4.7}$$

where we have $s \approx z + O(\mathrm{h}^2)$.

The elastoydrodynamic equation is a fourth-order partial differential equation in space, and needs thus to be supplied with four boundary conditions. We prescribe dynamic boundary conditions at the free end $z = 0$, requiring it to be force-free and torque-free, which is $\partial^3\mathbf{r}/\partial z^3(z = 0) = 0$ and $\partial^2\mathbf{r}/\partial z^2(z = 0) = 0$ respectively. Since the deformed shape rotates about the z-direction, without loss of generality, we assume the Ni head lies on the $x - z$ plane. We then prescribe kinematic boundary conditions at the other end $z = 1$: $\mathbf{r}_\perp(z = 1) = (b, 0)$ and $\partial\mathbf{r}_\perp/\partial z(z = 1) = (\mathrm{h}, 0)$. From experimental observations, the value of b is seen to be negligibly small ($b \approx 0$) and is difficult to measure accurately. Here, for simplicity, we thus take $b = 0$ in our calculations below. In this geometric model,

we assume that the slope of the magnetic Ni head, $\partial x(z)/\partial z(z=1)$, follows the slope of the external field ($\mathrm{h} = H_1/H_0$), which is a good approximation when the magnetic field strength is strong or when the frequency of actuation is low, such that the Ni head can align closely with the external magnetic field. The magnitude of the magnetic torque can be compared with the viscous torque acting on the Ni head, and their ratio is given by the so-called Mason number, Ma. The ratio varies from 0.018 – 0.12, for frequency varying form 5Hz to 35Hz. One can also compare the magnetic torque to the characteristic viscous torque acting on the Ag filament, and it varies from 0.13 – 0.93, for the same range of frequency. In both cases, Ma is thus typically small and is at most $O(1)$ at high frequencies. Therefore, within the range of frequency explored in the experiment, our geometrical model is considered to be a valid approximation. At higher frequencies, we would get $\mathrm{Ma} \gg 1$, which would play a role in the boundary condition at $z = 1$. In that regime, the viscous torque would dominate the typical actuation torque by the magnetic field, and the Ni segment would therefore not be able to align with the magnetic field closely. We expect that the slope of the Ni rod might then be smaller than that of the magnetic field, and the phase lag between the motion of the Ni segment and the magnetic field could be substantial. As a result, a degradation in the propulsion performance would be expected to occur in this regime.

Determining the flexible filament shape: O(h) calculations

At order $O(\mathrm{h})$, the local viscous force is given by

$$\mathbf{f}_{\mathrm{vis}} = \mathrm{h}\ [-y_1(z), x_1(z), -\gamma^{-1}U_1] + O(\mathrm{h}^2). \tag{4.8}$$

From here, we can integrate the $O(\mathrm{h})$ local viscous force in the z-direction over the entire nanomotor and since this total force needs to vanish because of the absence of external forces, we find $U_1 = 0$: swimming occurs therefore at order $O(\mathrm{h}^2)$. The elastic force is given by $\mathbf{f}_{\mathrm{elastic}} = -\mathrm{h}\ \mathrm{Sp}^{-4}[\partial^4 x_1/\partial z^4, \partial^4 y_1/\partial z^4, 0] + O(\mathrm{h}^2)$. Balancing the local viscous and elastic forces in the transverse directions yield the hyper-diffusion equations [100]

$$-y_1 = \mathrm{Sp}^{-4}\frac{\partial^4 x_1}{\partial z^4}, \tag{4.9}$$

$$x_1 = \mathrm{Sp}^{-4}\frac{\partial^4 y_1}{\partial z^4}, \tag{4.10}$$

which govern the first order filament shape. The general solution to this system of partial differential equations is given by

$$x_1(z) = \sum_{n=1}^{8} A_n \exp\left(\mathrm{Sp}\ r_n z\right), \tag{4.11}$$

$$y_1(z) = \sum_{n=1}^{8} -A_n r_n^4 \exp\left(\mathrm{Sp}\ r_n z\right), \tag{4.12}$$

where r_n is the n-th eight roots of -1, and A_n are complex constants to be determined by the boundary conditions. The boundary conditions to this order at $z = 0$ are given by $\partial^3 x_1/\partial z^3(z = 0) = \partial^3 y_1/\partial z^3(z = 0) = \partial^2 x_1/\partial z^2(z = 0) = \partial^2 y_1/\partial z^2(z = 0) = 0$. The appropriate boundary conditions at $z = 1$ are given by $x_1(z = 1) = y_1(z = 1) = 0$, $\partial x_1/\partial z(z = 1) = 1$, and $\partial y_1/\partial z(z = 1) = 0$. The $O(\mathrm{h})$ filament shape is now completely determined.

Determining the swimming speed: O(h^2) calculations

At order $O(\mathrm{h}^2)$, the local viscous fluid force acting on the flexible filament in the z-direction is given by

$$\mathbf{e}_z \cdot \mathbf{f}_{\mathrm{vis}_2} = \begin{cases} -(\gamma^{-1} - 1)\Lambda(z) - \gamma^{-1} U_2 & , \ 0 \le z < 1, \\ \frac{\xi_{m\perp}}{\xi_\perp}\left[-(\gamma_m^{-1} - 1)\Lambda(z) - \gamma_m^{-1} U_2\right] & , \ 1 < z \le 1 + l_m, \end{cases}$$

where $l_m = L_m/L$, and we have introduced the function $\Lambda(z) = y_1(z)\partial x_1/\partial z(z) - x_1(z)\partial y_1/\partial z(z)$. Since the nanomotor is overall force-free, the second order swimming speed U_2 can be determined by integrating the local viscous fluid in the z-direction over the entire nanomotor and requiring this total force to vanish, i.e.

$$\int_0^{1+l_m} \mathbf{e}_z \cdot \mathbf{f}_{\mathrm{vis}_2} dz = 0, \tag{4.13}$$

and we see that the swimming speed is slaved to the first order filament shape $[x_1(z), y_1(z)]$ via the function $\Lambda(z)$. Upon simplification with Eqs. (4.9) and (4.10) and the boundary conditions at $z = 0$, we obtain

$$\begin{aligned} U_2 = & \frac{1-\gamma}{\mathrm{Sp}^4(1+\alpha l_m)} \times \\ & \left[\frac{\partial x_1}{\partial z}\frac{\partial^3 x_1}{\partial z^3} - \frac{1}{2}\left(\frac{\partial^2 x_1}{\partial z^2}\right)^2 + \frac{\partial y_1}{\partial z}\frac{\partial^3 y_1}{\partial z^3} - \frac{1}{2}\left(\frac{\partial^2 y_1}{\partial z^2}\right)^2\right]_{z=1}, \end{aligned} \tag{4.14}$$

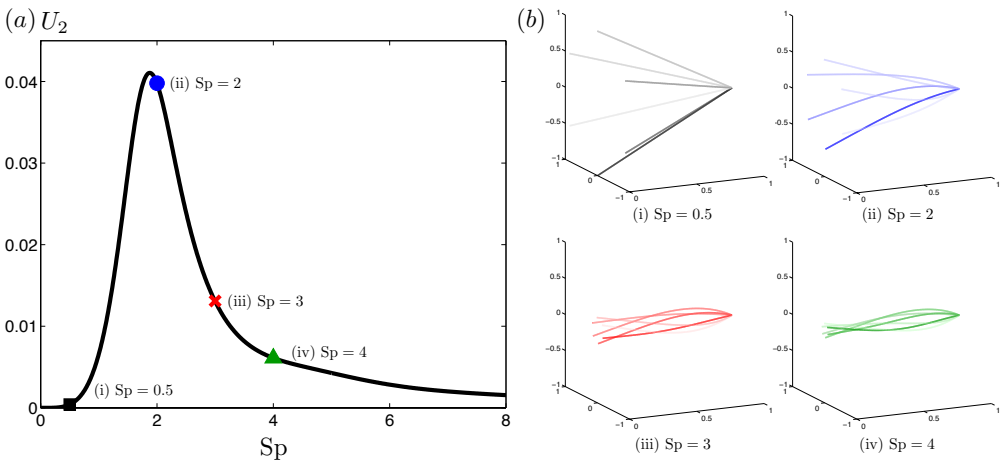

Figure 4.4: (a) Variation of the dimensionless propulsion speed at second order, U_2, with the sperm number, Sp. (b) Superimposed snapshots of predicted three-dimensional shape of the Ag nanowire at equal time intervals ($t = [T/6, 2T/6, ..., 5T/6, T]$ from dark to bright color, where T is the period of the rotating magnetic field), for four different sperm numbers. The Ni head is not shown here for simplicity.

where $\alpha = \xi_{m\parallel}/\xi_{\parallel}$. In dimensional form, the leading order swimming speed, is given by

$$U = \mathrm{h}^2 \frac{A(\xi_{\parallel} - \xi_{\perp})}{\xi_{\perp}(L\xi_{\parallel} + L_m\xi_{m\parallel})} \times \left[\frac{\partial x_1}{\partial z}\frac{\partial^3 x_1}{\partial z^3} - \frac{1}{2}\left(\frac{\partial^2 x_1}{\partial z^2}\right)^2 + \frac{\partial y_1}{\partial z}\frac{\partial^3 y_1}{\partial z^3} - \frac{1}{2}\left(\frac{\partial^2 y_1}{\partial z^2}\right)^2 \right]_{z=1} + O(\mathrm{h}^3). \tag{4.15}$$

As in previous work [60, 76, 91, 92, 101, 103], we observe that this mode of propulsion relies on the drag anisotropy of slender filaments, $\gamma = \xi_{\perp}/\xi_{\parallel} \neq 1$. Indeed, when $\gamma = 1$, the swimming speed vanishes. Note that for very slender filaments, we have $\gamma \approx 2$ (see Eq. 4.2).

We also see that the swimming speed scales quadratically with the relative strength of the rotating and constant components of the magnetic field, $U \sim \mathrm{h}^2$, for $\mathrm{h} \ll 1$. This scaling is confirmed by a complementary asymptotic calculation valid for low sperm numbers (see Sec. 4.5 for details).

Next, we plot our predicted dimensionless second order swimming speed as a function of the sperm number Sp (Fig. 4.4a) together with the predicted filament shapes (Fig. 4.4b), and observe three different characteristic regimes. The sperm number Sp is the most important dimensionless group governing the propulsion

performance. For Sp $\ll$ 1, bending forces dominate and the filament is effectively straight (Fig. 4.4b-i). Hence, the filament motion is almost kinematically reversible, and it produces small propulsion. Quantitatively, a small Sp asymptotic analysis presented in Sec. 4.5 reveals that the dimensionless swimming speed grows with the fourth power of the sperm number, $U_2 \sim \mathrm{Sp}^4$, for Sp $\ll$ 1. On the other hand, from Eqs. (4.11) and (4.12), we see that most deflection is concentrated around a small region $0 \leq z < 1/\mathrm{Sp}$, when Sp $\gg$ 1, due to the exponential decay of the solution amplitude. In this regime (Sp $\gg$ 1), the viscous forces dominate, and propulsion is inefficient because a large portion of the filament has small deflection and thus experiences drag but contributes to no thrust (Figs. 4.4b-iii & iv). As a result, we expect optimal swimming to occur when Sp is of order one, where the total drag of the nanomotor is kept low while the drag-induced bending is fully exploited to produce propulsion. This is confirmed in our calculation, and we observe the optimal sperm number to occur at Sp $\approx$ 2, which gives a maximum propulsion speed of $U_2 \approx 0.042$ (Fig. 4.4a). The filament shape close to optimal swimming (Sp = 2) is shown in Fig. 4.4b-ii.

4.4 Comparison with experiments

Under fixed magnitude of the rotating and constant components of the magnetic field, the swimming speed of a nanomotor was measured with the frequency of the magnetic field varying between 0 to 35Hz. The experiment was repeated on the same nanomotor for three different settings of magnetic field strengths (shown using three different symbols with error bars in Fig. 4.5b; a total of 20 different nanowires were sampled). The rotating magnetic field strength H_1 was kept constant at $H_1 = 10$G, and the constant magnetic field strength was set to be $H_0 = 14.3$G (blue squares), $H_0 = 11.8$G (red circles), and $H_0 = 9.5$G (green diamonds).

We then compare in Fig. 4.5b our theoretical predictions (solid lines) with experimental measurements, plotted as swimming velocity vs. frequency (main figure) or Sperm number (inset). In our theoretical model, the value of the bending stiffness A of the flexible filament is unknown. Standard bending stiffness of pure silver is inapplicable here since the dissolution of silver in hydrogen peroxide ren-

dered the filament a porous structure with significantly reduced strength and a different chemical composition (Ag_2O, AgOH). A value of $A = 3.6 \times 10^{-24}\text{Nm}^{-2}$ fits, with the least total squared errors, the experimental data with $H_1 = 10\text{G}$, $H_0 = 14.3\text{G}$ (blue squares), which is the case where our model is expected to work best as the ratio $h = H_1/H_0$ is the smallest. This bending stiffness is then used to predict the propulsion speed under different magnetic field settings (green and red solid lines in Fig. 4.5b, see captions for details).

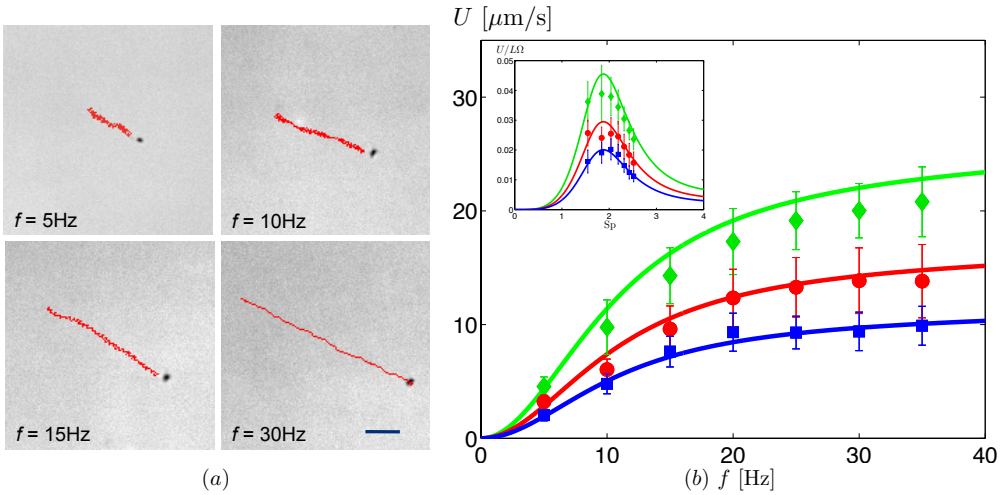

Figure 4.5: Dependence of the nanomotor swimming speed on the actuation frequency. (a) Superimposed trajectories of the same Ni-Ag nanomotor at different frequencies $f = 5$, 10, 15, 30Hz (as indicated) over a 3-second period (red lines), with $H_1 = 10\text{G}$ and $H_0 = 9.5\text{G}$. The scale bar is $10\mu\text{m}$. (b) Speed-frequency characteristics of flexible nanowire motors. Symbols represent experimental data for different setup of magnetic fields: blue squares ($H_1 = 10\text{G}$, $H_0 = 9.5\text{G}$); red circles ($H_1 = 10\text{G}$, $H_0 = 11.8\text{G}$); green diamonds ($H_1 = 10\text{G}$, $H_0 = 14.3\text{G}$). Error bars show standard deviations of the measured speeds (20 samples). The solids lines show the theoretical predictions (Eq. 4.15) with $A = 3.6 \times 10^{-24}\text{Nm}^2$. The inset in (b) displays the dependence of the swimming speed on the Sperm number, Sp.

The theoretical model is seen to capture both qualitatively and quantitatively the speed-frequency characteristics of these flexible nanomotors. Qualitatively, the rate of change of the swimming speed with respect to the frequency increases at low frequencies ($U \sim f^2$ for small f, as shown in the Sec. 4.5), but then gradually decreases as the frequency continues to increase, and eventually levels off at high frequencies. Physically, increasing the actuation frequency is equivalent

to increasing the sperm number. When the frequency is varied from 0 to 35Hz, it corresponds to a variation of the sperm number Sp from 0 to 2.6, experiencing a degradation in swimming performance beyond the optimal sperm number Sp ≈ 2, which corresponds to a frequency of around 15Hz in our experiment. This degradation manifests as a less-than linear speed-frequency variation (since the dimensional swimming speed scales as $L\Omega$, linearly in Ω) beyond the frequency 15Hz, resulting in the level-off at higher frequencies. As noted above, at very high frequencies, the magnetic Ni head will be unable to follow synchronously the rapid rotating magnetic field. The dynamics of propulsion will be more complicated in that regime, and the simple model presented here will likely be inapplicable.

The agreement between our theoretical model and our experimental results is very satisfactory. The discrepancies are larger for the setup $H_1 = 10\text{G}, H_0 = 9.5\text{G}$ (green lines and squares), which is expected because h ≈ 1.1 in this case and the asymptotic assumption of small h is less valid. Note that our measurements did not sample the low Sp regime as in our experiments, swimming at low frequencies appear to be significantly influenced by Brownian motion.

Our model has only one fitting parameter, the bending stiffness A, which – as explained above – we fit to the bottom data set in Fig. 4.5b, and use to predict the other two data sets. The estimated value we obtain from the fitting is equivalent to a pure silver nanowire of diameter $\approx$ 6nm (with elastic modulus, E = 80GPa), which is much smaller than the diameter of flexible segment observed. This is expected because the chemical composition of silver is altered after the dissolution, and a large portion of the flexible nanowire is indeed a thick layer of surface byproducts formed after the chemical reaction, which contributes little, if any, to the bending strength. The diameter of the actual structural filament that bears the bending loads is difficult to measure experimentally (see details of the structure in Fig. 4.1b). In addition, non-uniform chemical reactions lead to strong local defects or points of weakness along the nanowire, which might significantly reduce the bending strength. We can compare our estimated bending stiffness, $A = 3.6 \times 10^{-24}\text{Nm}^2$, with the bending stiffness of typical flagella of natural microscopic swimmers, such as eukaryotic spermatozoa, which also rely on the flexibility of flagella for propulsion. These biological filaments have their bending stiffnesses ranging from 10^{-24}Nm^2 [104] to 10^{-22}Nm^2 [105], which is the

range in which our estimated value lies.

4.5 Swimming at low sperm numbers

In this section, we consider another physically interesting asymptotic limit, the low sperm number limit, $\Gamma = \mathrm{Sp}^4 \ll 1$. The results in this asymptotic limit are not expected to provide quantitative agreements with the experimental measurements, since the value of Γ in the experiment is typically large. Nevertheless, this analysis still allows us to reveal different scaling behaviours of the propulsion speed at low sperm numbers. Keaveny and Maxey [96] investigated the propulsion of a flexible filament with distributed magnetic actuation. With a resistive force model, they considered the low sperm number limit and found that the propulsion speed scales with the fourth power of the sperm number, $U \sim \mathrm{Sp}^4$, at low sperm numbers. We will follow closely their method of solution and perform similar calculations here to show that the same scaling holds for our flexible nanowire motor subject to boundary actuation. An explicit formula for the leading order propulsion speed in Γ will be derived. Expanding this formula for small h will confirm our scaling of U with h from the small-h asymptotic analysis in the previous section (Sec. 4.3.5).

First, the problem is formulated below, taking into account the effects of twisting, self-spinning, and inextensibility of the nanowire. Denoting $\mathbf{N}(s,t)$ and $\mathbf{M}(s,t)$ as the resultant internal force and moment on a cross section, the local force and moment balances are

$$\frac{\partial \mathbf{N}}{\partial s} = (\xi_{\parallel} - \xi_{\perp})(\mathbf{t}\cdot\mathbf{u})\mathbf{t} + \xi_{\perp}\mathbf{u}, \tag{4.16}$$

$$\frac{\partial \mathbf{M}}{\partial s} + \mathbf{t}\times\mathbf{N} = \xi_r a^2(\omega\cdot\mathbf{t})\mathbf{t}, \tag{4.17}$$

where $\omega(s,t)$ is the angular velocity, and $\xi_r = 4\pi\mu$ is the resistive coefficient for the viscous torque produced by self-spinning (rotation about its own local axis, $\mathbf{t}$) of the filament. The internal moment $\mathbf{M}(s,t)$ has a constitutive relation

$$\mathbf{M} = A\mathbf{t}\times\frac{\partial \mathbf{t}}{\partial s} + K_t\frac{\partial \Psi}{\partial s}\mathbf{t}, \tag{4.18}$$

where K_t is the twist modulus of the filament and $\Psi(s,t)$ is the twist angle. In contrast to the propeller studied by Keaveny and Maxey [96], the magnetic torque

does not come into the local moment balance in our case, but only through the boundary condition. The boundary conditions are given by the balance of external forces and torques at the ends of the flexible filament. We have a free end at $s = 0$. The external forces and torques at $s = 1$ are given by the total viscous force and viscous torque together with the magnetic torque acting on the Ni segment, which is modelled as a slender rigid rod:

$$\mathbf{N}(s=0) = \mathbf{0}, \tag{4.19}$$

$$\mathbf{M}(s=0) = \mathbf{0}, \tag{4.20}$$

$$\mathbf{N}(s=1) = -L_m \left[(\xi_{m\parallel} - \xi_{m\perp})(\mathbf{t}\cdot\mathbf{u})\mathbf{t} + \xi_{m\perp}\mathbf{u})\right]_{s=1} + \xi_{m\perp}\frac{L_m^2}{2}\omega \times \mathbf{t} \mid_{s=1}, \tag{4.21}$$

$$\mathbf{M}(s=1) = M\mathbf{t} \mid_{s=1} \times \mathbf{H} - \xi_{m\perp}\left\{\frac{L_m^2}{2}\mathbf{t}\times\mathbf{u} + \frac{L_m^3}{3}[\omega - (\mathbf{t}\cdot\omega)\mathbf{t}]\right\}_{s=1}, \tag{4.22}$$

where $M = M_s a_m^2 \pi L_m$ is the strength of the magnetic moment of the Ni segment and $M_s = 485 \times 10^3 \mathrm{A/m}$ is the spontaneous magnetization of Ni.

To study the low sperm number limit, we adopt the following nondimensionalizations: we scale times with Ω^{-1}, lengths with L, $\mathbf{H}$ with H_0, elastic forces with A/L^2, and elastic torques with A/L. With these nondimensionalizations, the dimensionless equations (using the same variables for simplicity) now read

$$\frac{\partial \mathbf{N}}{\partial s} = \Gamma\left[(\gamma^{-1} - 1)(\mathbf{t}\cdot\mathbf{u})\mathbf{t} + \mathbf{u}\right], \tag{4.23}$$

$$R\Gamma(\omega\cdot\mathbf{t})\mathbf{t} = \mathbf{t}\times\frac{\partial^2\mathbf{t}}{\partial s^2} + \mathbf{t}\times\mathbf{N} + K\frac{\partial}{\partial s}\left(\frac{\partial\Psi}{\partial s}\mathbf{t}\right), \tag{4.24}$$

where $R = \xi_r a^2/\xi_\perp L^2$, $K = K_t/A$, and $\Gamma = \mathrm{Sp}^4$. The dimensionless boundary conditions are

$$\mathbf{N}(s=0) = \mathbf{0}, \tag{4.25}$$

$$\mathbf{M}(s=0) = \mathbf{0}, \tag{4.26}$$

$$\mathbf{N}(s=1) = -\Gamma\beta \times \left\{\left[(\gamma_m^{-1} - 1)(\mathbf{t}\cdot\mathbf{u})\mathbf{t} + \mathbf{u})\right] l_m + \frac{l_m^2}{2}\omega\times\mathbf{t}\right\}_{s=1}, \tag{4.27}$$

$$\mathbf{M}(s=1) = C_m\mathbf{t} \mid_{s=1} \times\mathbf{H} - \Gamma\beta\left\{\frac{l_m^2}{2}\mathbf{t}\times\mathbf{u} + \frac{l_m^3}{3}\left[\omega - (\mathbf{t}\cdot\omega)\mathbf{t}\right]\right\}_{s=1}, \tag{4.28}$$

where $l_m = L_m/L$, $\beta = \xi_{m\perp}/\xi_\perp$, $\gamma_m = \xi_{m\perp}/\xi_{m\parallel}$, and $C_m = M_s a_m^2 \pi L_m H_0 L/A$ is a dimensionless parameter characterizing the relative strength of the magnetic and

elastic torques. Finally, we have the inextensibility condition

$$\mathbf{t}(s,t)\cdot\mathbf{t}(s,t)=1. \tag{4.29}$$

Eqs. (4.23) through (4.29) completely describe the full swimming problem (within the realm of resistive force theory and classical elastic beam theory) without making any assumption. There is no restriction on the validity of the solution to this system, but the solution has to be obtained numerically, with special attention on the nonlinearities arising in the differential equation and the boundary conditions. To make analytical progresses, we consider the asymptotic limit $\Gamma \ll 1$, and calculate the leading order swimming speed in Γ. Following the method and notations by Keaveny and Maxey [96], we assume the filament attains a constant shape at steady-state and rotates about the z-axis synchronously with the external magnetic field, hence we write the dimensionless steady-state conformation of the filament as

$$x(s,t) = -b(s)\cos[t+\phi(s)], \tag{4.30}$$

$$y(s,t) = -b(s)\sin[t+\phi(s)], \tag{4.31}$$

$$z(s,t) = \alpha(s)+\tilde{U}t, \tag{4.32}$$

where $\tilde{U}=U/L\Omega$ is the dimensionless swimming speed in the z-direction, whereas $\alpha(s)$, $b(s)$, and $\phi(s)$ are geometrical unknowns to be determined. Like the small-h asymptotic analysis in Sec. 4.3.5 and in Ref. [96], here we have considered unidirectional swimming in the z-direction. In addition, since the functions $\alpha(s), b(s)$ and $\phi(s)$ are independent of time, we only find the solution at one specific time, $t=0$ [96]. The magnetic field at $t=0$ is given by $\mathbf{H}=[\mathrm{h},0,1]$. We seek expansions

in Γ in the form of

$$\mathbf{N} = \mathbf{N}_0 + \mathbf{N}_1\Gamma + O(\Gamma^2), \tag{4.33}$$

$$\mathbf{M} = \mathbf{M}_0 + \mathbf{M}_1\Gamma + O(\Gamma^2), \tag{4.34}$$

$$\frac{d\alpha}{ds} = \frac{d\alpha_0}{ds} + \frac{d\alpha_1}{ds}\Gamma + O(\Gamma^2), \tag{4.35}$$

$$\frac{db}{ds} = \frac{db_0}{ds} + \frac{db_1}{ds}\Gamma + O(\Gamma^2), \tag{4.36}$$

$$\frac{d\phi}{ds} = \frac{d\phi_1}{ds}\Gamma + O(\Gamma^2), \tag{4.37}$$

$$\frac{d\psi}{ds} = \frac{d\psi_1}{ds}\Gamma + O(\Gamma^2), \tag{4.38}$$

$$\tilde{U} = \tilde{U}_0 + \tilde{U}_1\Gamma + O(\Gamma^2), \tag{4.39}$$

and similar expansions hold for other variables. With these expansions, we can express the local tangent $\mathbf{t}(s)$ and velocity $\mathbf{u}(s,t)$ as

$$\mathbf{t}(s) = \mathbf{t}_0 + \mathbf{t}_1\Gamma + O(\Gamma^2), \tag{4.40}$$

$$= \left[-\frac{db_0}{ds}, 0, \frac{d\alpha_0}{ds}\right] + \left[-\frac{db_1}{ds}, -\frac{d\left(b_0\phi_1\right)}{ds}, \frac{d\alpha_1}{ds}\right]\Gamma + O(\Gamma^2), \tag{4.41}$$

$$\mathbf{u}(s) = \left[0, -b_0, \tilde{U}_0\right] + \left[b_0\phi_1, -b_1, \tilde{U}_1\right]\Gamma + O(\Gamma^2). \tag{4.42}$$

In the following section, we will perform the calculations order by order.

4.5.1 $O(\Gamma^0)$ calculations

The $O(\Gamma^0)$ local balance of forces and torques are given by

$$\frac{d\mathbf{N}_0}{ds} = \mathbf{0}, \tag{4.43}$$

$$\mathbf{0} = \mathbf{t}_0 \times \mathbf{N}_0 + \mathbf{t}_0 \times \frac{d^2\mathbf{t}_0}{ds^2} + K\frac{d}{ds}\left(\frac{d\Psi_0}{ds}\mathbf{t}_0\right), \tag{4.44}$$

with boundary conditions

$$\mathbf{N}_0(s=0) = \mathbf{0}, \tag{4.45}$$

$$\mathbf{M}_0(s=0) = \mathbf{0}, \tag{4.46}$$

$$\mathbf{N}_0(s=1) = \mathbf{0}, \tag{4.47}$$

$$\mathbf{M}_0(s=1) = C_m\mathbf{t}_0 \mid_{s=1} \times\mathbf{H}, \tag{4.48}$$

and inextensibility condition

$$\left(\frac{d\alpha_0}{ds}\right)^2 + \left(\frac{db_0}{ds}\right)^2 = 1. \tag{4.49}$$

The solution at this order is given by

$$\mathbf{N}_0(s) = \mathbf{0}, \tag{4.50}$$

$$\frac{d\alpha_0}{ds} = \frac{1}{\sqrt{1+\mathrm{h}^2}}, \tag{4.51}$$

$$\frac{db_0}{ds} = \frac{-\mathrm{h}}{\sqrt{1+\mathrm{h}^2}}, \tag{4.52}$$

$$\Psi_0(s) = \tilde{U}_0 = 0. \tag{4.53}$$

4.5.2 $O(\Gamma)$ calculations

The $O(\Gamma)$ local balance of forces and torques are given by

$$\frac{d\mathbf{N}_1}{ds} = (\gamma^{-1} - 1)(\mathbf{t}_0 \cdot \mathbf{u}_0)\mathbf{t}_0 + \mathbf{u}_0, \tag{4.54}$$

$$\mathbf{0} = \mathbf{t}_0 \times \mathbf{N}_1 + \mathbf{t}_0 \times \frac{d^2\mathbf{t}_1}{ds^2} + \mathbf{t}_1 \times \frac{d^2\mathbf{t}_0}{ds^2} + K\frac{d^2\Psi_1}{ds^2}\mathbf{t}_0, \tag{4.55}$$

with boundary conditions

$$\mathbf{N}_1(s=0) = \mathbf{0}, \tag{4.56}$$

$$\mathbf{M}_1(s=0) = \mathbf{0}, \tag{4.57}$$

$$\mathbf{N}_1(s=1) = -\beta l_m \left[(\gamma_m^{-1} - 1)(\mathbf{t}_0 \cdot \mathbf{u}_0)\mathbf{t}_0 + \mathbf{u}_0 + \frac{l_m}{2}\omega_0 \times \mathbf{t}_0\right]_{s=1}, \tag{4.58}$$

$$\mathbf{M}_1(s=1) = C_m\mathbf{t}_1 \mid_{s=1} \times\mathbf{H} - \beta l_m^2 \left\{\frac{\mathbf{t}_0 \times \mathbf{u}_0}{2} + \frac{l_m}{3}\left[\omega_0 - (\mathbf{t}_0 \cdot \omega_0)\mathbf{t}_0\right]\right\}_{s=1}, \tag{4.59}$$

and the inextensibility condition

$$\frac{d\alpha_1}{ds} = \mathrm{h}\frac{db_1}{ds}. \tag{4.60}$$

From the solution at $O(\Gamma^0)$, Eq. (4.52), we can integrate to get $b_0(s) = -\mathrm{h}s/\sqrt{1+\mathrm{h}^2} + C_1$, where C_1 is a constant to be determined. By satisfying the equations and boundary conditions at this order, we find that

$$C_1 = \frac{\mathrm{h}\left[1 + \beta l_m(2 + l_m)\right]}{2\sqrt{1+\mathrm{h}^2}(1 + \beta l_m)}. \tag{4.61}$$

The solution at this order is then given by

$$\frac{d(b_0\phi_1)}{ds} = \frac{\mathrm{h}s^4}{24\sqrt{1+\mathrm{h}^2}} - \frac{C_1 s^3}{6} + B_1, \tag{4.62}$$

$$\frac{db_1}{ds} = \frac{d\alpha_1}{ds} = \frac{d\Psi_1}{ds} = 0, \tag{4.63}$$

where

$$B_1 = \frac{\mathrm{h}}{24C_m\left(1+\mathrm{h}^2\right)(1+\beta l_m)}\Big\{2 + C_m\sqrt{1+\mathrm{h}^2}\left[1+\beta l_m(3+2l_m)\right] + 2\beta l_m\left[4 + l_m(6 + l_m(4+\beta l_m))\right]\Big\}. \tag{4.64}$$

4.5.3 $O(\Gamma^2)$ calculations

The $O(\Gamma^2)$ local balance of forces and torques are given by

$$\frac{d\mathbf{N}_2}{ds} = (\gamma^{-1}-1)(\mathbf{t}_1\cdot\mathbf{u}_0 + \mathbf{t}_0\cdot\mathbf{u}_1)\mathbf{t}_0 + \mathbf{u}_1, \tag{4.65}$$

$$R(\omega_1\cdot\mathbf{t}_0 + \omega_0\cdot\mathbf{t}_1)\mathbf{t}_0 = \mathbf{t}_0\times\mathbf{N}_2 + \mathbf{t}_1\times\mathbf{N}_1 + \mathbf{t}_0\times\frac{d^2\mathbf{t}_2}{ds^2} + \mathbf{t}_1\times\frac{d^2\mathbf{t}_1}{ds^2} + K\frac{d^2\Psi_2}{ds^2}\mathbf{t}_0, \tag{4.66}$$

with boundary conditions

$$\mathbf{N}_2(s=0) = \mathbf{0}, \tag{4.67}$$

$$\mathbf{M}_2(s=0) = \mathbf{0}, \tag{4.68}$$

$$\mathbf{N}_2(s=1) = -\beta l_m\Big[(\gamma_m^{-1}-1)(\mathbf{t}_0\cdot\mathbf{u}_1 + \mathbf{t}_1\cdot\mathbf{u}_0)\mathbf{t}_0 + \mathbf{u}_1 + \frac{l_m}{2}\left(\omega_0\times\mathbf{t}_1 + \omega_1\times\mathbf{t}_0\right)\Big]_{s=1}, \tag{4.69}$$

$$\mathbf{M}_2(s=1) = C_m\mathbf{t}_2\mid_{s=1}\times\mathbf{H} - \beta l_m^2\Big\{\frac{1}{2}\left(\mathbf{t}_0\cdot\mathbf{u}_1 + \mathbf{t}_1\cdot\mathbf{u}_0\right) + \frac{l_m}{3}\left[\omega_1 - (\mathbf{t}_1\cdot\omega_0 + \mathbf{t}_0\cdot\omega_1)\mathbf{t}_0 - (\mathbf{t}_0\cdot\omega_0)\mathbf{t}_1\right]\Big\}_{s=1}. \tag{4.70}$$

From the local balance of force (Eq. 4.65) with the boundary conditions at

$s = 0$ (Eq. 4.67), we find that $\mathbf{N}_2 = [N_{2x}, N_{2y}, N_{2z}]$ is given by

$$\begin{aligned} N_{2x}(s) = & \frac{\mathrm{h}}{\sqrt{1+\mathrm{h}^2}}\left(\gamma^{-1}-1\right)\times \\ & \left[J(s)+\frac{\tilde{U}_1 s}{\sqrt{1+\mathrm{h}^2}}+\frac{\mathrm{h}}{\sqrt{1+\mathrm{h}^2}}H(s)+\frac{\mathrm{h}}{\sqrt{1+\mathrm{h}^2}}C_3 s\right] \\ & + H(s) + C_3 s, \end{aligned} \tag{4.71}$$

$$N_{2y}(s) = -b_1 s, \tag{4.72}$$

$$\begin{aligned} N_{2z}(s) = & \frac{\gamma^{-1}-1}{\sqrt{1+\mathrm{h}^2}}\times \\ & \left[J(s)+\frac{\tilde{U}_1 s}{\sqrt{1+\mathrm{h}^2}}+\frac{\mathrm{h}}{\sqrt{1+\mathrm{h}^2}}H(s)+\frac{\mathrm{h}}{\sqrt{1+\mathrm{h}^2}}C_3 s\right] \\ & + U_1 s, \end{aligned} \tag{4.73}$$

where C_3 is an unknown integration constant and we define the functions

$$F(s) = \frac{d(b_0\phi_1)}{ds} = \frac{\mathrm{h}s^4}{24\sqrt{1+\mathrm{h}^2}} - \frac{C_1 s^3}{6} + B_1, \tag{4.74}$$

$$G(s) = \int_0^s F(s')ds' = \frac{\mathrm{h}s^5}{120\sqrt{1+\mathrm{h}^2}} - \frac{C_1 s^4}{24} + B_1 s, \tag{4.75}$$

$$H(s) = \int_0^s G(s')ds' = \frac{\mathrm{h}s^6}{720\sqrt{1+\mathrm{h}^2}} - \frac{C_1 s^5}{120} + B_1\frac{s^2}{2}, \tag{4.76}$$

$$J(s) = \int_0^s b_0(s')F(s')ds'. \tag{4.77}$$

Examining the force components N_{2x} and N_{2z}, we have two unknowns, namely U_1 and C_3. These two unknowns are determined by applying the boundary conditions at $s = 1$ (Eq. 4.69), yielding a 2×2 system of equations

$$\begin{pmatrix} A_{11} & A_{12} \\ A_{21} & A_{22} \end{pmatrix}\begin{pmatrix} \tilde{U}_1 \\ C_3 \end{pmatrix} = \begin{pmatrix} \mathrm{h}\Phi_1 + \beta l_m G(1) + \frac{\beta l_m^2}{2}F(1) + H(1) \\ \Phi_1 \end{pmatrix}, \tag{4.78}$$

where

$$A_{11} = A_{22} = -\left[\frac{h(\gamma^{-1}-1)}{1+\mathrm{h}^2} + \frac{\mathrm{h}\beta l_m(\gamma_m^{-1}-1)}{1+\mathrm{h}^2}\right], \tag{4.79}$$

$$A_{12} = -\left[\beta l_m + \frac{\mathrm{h}^2\beta l_m(\gamma_m^{-1}-1)}{1+\mathrm{h}^2} + 1 + \frac{\mathrm{h}^2(\gamma^{-1}-1)}{1+\mathrm{h}^2}\right], \tag{4.80}$$

$$A_{21} = -\left[\beta l_m + \frac{\beta l_m(\gamma_m^{-1}-1)}{1+\mathrm{h}^2} + 1 + \frac{\gamma^{-1}-1}{1+\mathrm{h}^2}\right], \tag{4.81}$$

$$\begin{aligned}\Phi_1 = {} & \frac{\gamma^{-1}-1}{\sqrt{1+\mathrm{h}^2}}\left[J(1) + \frac{\mathrm{h}}{\sqrt{1+\mathrm{h}^2}}H(1)\right] \\ & + \frac{\beta l_m(\gamma_m^{-1}-1)}{\sqrt{1+\mathrm{h}^2}}\left[\frac{\mathrm{h}}{\sqrt{1+\mathrm{h}^2}}G(1) + b_0(1)F(1)\right].\end{aligned} \tag{4.82}$$

Upon solving this system of linear equation, we arrive at an explicit formula for the leading order swimming speed

$$\tilde{U} = \tilde{U}_1\Gamma + O(\Gamma^2) \tag{4.83}$$

$$\begin{aligned}= {} & \frac{\mathrm{h}^2}{1440\left(1+\mathrm{h}^2\right)^{3/2}(1+\beta l_m)^2(\gamma\beta l_m + \gamma_m)}\times \\ & \Big\{5\gamma\gamma_m[1+\beta l_m(4+3l_m)]^2 - 4\gamma\beta l_m\left[4+\beta l_m(13+9l_m)\right] \\ & - 5\gamma_m - \gamma_m\beta l_m\left[24+30l_m+\beta l_m\left(28+84l_m+45l_m^2\right)\right]\Big\}\Gamma + O(\Gamma^2).\end{aligned} \tag{4.84}$$

Again, we can verify that when we have isotropic drag $\gamma = \gamma_m = 1$, then no swimming is possible, $\tilde{U}_1 = 0$.

4.5.4 Variation with the relative magnetic field strength, h

First, one can see that C_m, which is the ratio of the characteristic magnetic torque to the characteristic elastic torque, does not enter the formula for $\tilde{U}_1$ (Eq. 4.83), meaning that the absolute value of the magnetic field strength or the dipole moment strength has not yet played a role in the swimming speed at low sperm numbers. However, the relative strength of the rotating and constant magnetic field, $\mathrm{h} = H_1/H_0$, has an interesting effect here. From the small-h asymptotic analysis in Sec. 4.3.5, we knew swimming occurs at $O(\mathrm{h}^2)$ (Eq. 4.15), and hence

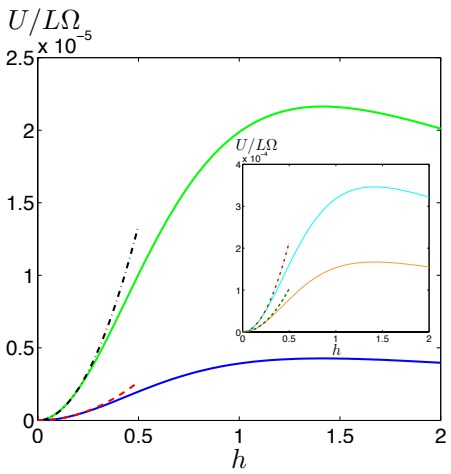

Figure 4.6: Variation of the dimensionless swimming speed, $U/L\Omega$, with the relative magnetic field strength, h, for different sperm numbers based on the low-Sp calculations: Sp = 0.2 (dark blue solid line), Sp = 0.3 (light green solid line). The red dotted (Sp = 0.2) and black dash-dotted (Sp = 0.3) lines are the corresponding results from the small-h calculations. Inset: Same plot for Sp = 0.5 (dark orange solid line) and Sp = 0.6 (light blue solid line). The green dotted (Sp = 0.5) and brown dash-dotted (Sp = 0.6) lines are the corresponding results from the small-h calculations.

the swimming speed (both dimensional or dimensionless) scales quadratically with h, $U \sim \mathrm{h}^2$, for $\mathrm{h} \ll 1$. This is confirmed by examining Eq. (4.83), where we have $\tilde{U} \sim \mathrm{h}^2/(1+\mathrm{h}^2)^{3/2} = \mathrm{h}^2 + O(\mathrm{h}^3)$ when expanded for small h. When the dimensionless swimming speeds from the two asymptotic analyses are plotted against h for small sperm numbers (Fig. 4.6, different lines represent results at various sperm numbers, see the caption for details), we see an excellent agreement when h is small, illustrating that the swimming speed does increase quadratically with h for small h (the dotted lines are the small-h asymptotic results). From the low sperm number results (solid lines), the swimming speed then experiences a maximum when h continues to increase (the small-h results are no longer valid in this regime), and eventually decreases with further increase in h. From the analytical expression (Eq. 4.83), we see that the maximum swimming speed occurs at $\mathrm{h} = \sqrt{2} \approx 1.41$.

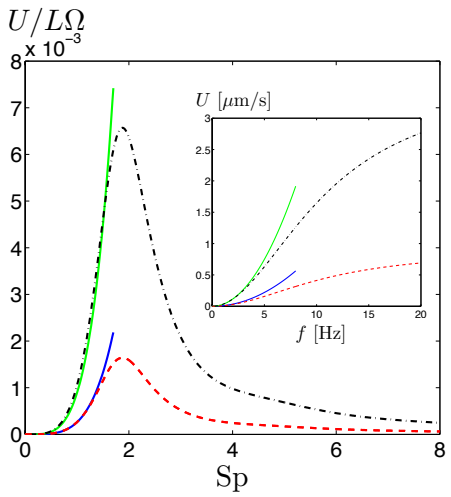

Figure 4.7: Variation of the dimensionless swimming speed, $U/L\Omega$, with the sperm number, Sp, based on the low-Sp calculations: h = 0.2 (dark blue solid line), h = 0.4 (light green solid line). The red dotted (h = 0.2) and black dash-dotted (h = 0.4) lines are the corresponding results from the small-h calculations. Inset: Variation of the dimensional swimming speed U with the frequency f based on the low-Sp calculations: h = 0.2 (dark blue solid line), h = 0.4 (light green solid line). The red dotted (h = 0.2) and black dash-dotted (h = 0.4) lines are the corresponding results from the small-h calculations. A bending stiffness of $A = 3.6 \times 10^{-24}$Nm^2 is used in the speed-frequency plot (inset).

4.5.5 Variation with the sperm number, Sp

From the small-h asymptotic analysis in the previous section(Sec. 4.3.5), we have illustrated the dependence of the dimensionless swimming speed on the sperm number, Sp (Fig. 4.4). Here, via the low sperm number asymptotic results (Eq. 4.83), we see quantitatively that the dimensionless swimming speed scales as the fourth power of the sperm number, $\tilde{U} = U/L\Omega \sim \Gamma \sim \mathrm{Sp}^4$, for low Sp. Since $\mathrm{Sp}^4 \propto f$, this also means that the dimensional swimming speed scales quadratically with the frequency $U \sim f^2$, for small f. We confirm this result by plotting the variation of the dimensionless swimming speed with the sperm number (Fig. 4.7), and the variation of the dimensional swimming speed with the frequency (Fig. 4.7 inset). We compare the low-Sp asymptotic results (h = 0.2, dark blue solid line; h = 0.4, light green solid line) with the corresponding small-h asymptotic results h = 0.2 (red dotted line) and h = 0.4 (black dash-dotted line), so that the small-h asymptotic assumption (h $\ll$ 1) is expected to be valid. We see the results from the

two asymptotic analyses agree with each other for sufficiently low sperm numbers (Fig. 4.7), or frequencies (Fig. 4.7 inset), confirming the scaling $U/L\Omega \sim \mathrm{Sp}^4$ ($U \sim f^2$), at low sperm numbers (low frequencies).

To summarize, in this section, with the help of a low-Sp asymptotic analysis, we have confirmed the scaling $U \sim \mathrm{h}^2$ for small h in Sec. 4.3.5, and established the complementary scalings $U/L\Omega \sim \mathrm{Sp}^4$ for small Sp, or equivalently $U \sim f^2$ for small f. Note that the results in this section are valid for very small Sp numbers, and hence are not expected to be useful for experimental comparison. In addition, C_m is assumed to be $O(1)$ throughout the calculations. Since $C_m \propto l_m$, the results here are invalid for $l_m \ll 1$ and $l_m \gg 1$.

4.6 Discussion

In this work, we designed and fabricated a high-speed fuel-free nanomotor utilizing the flexibility of nanowires for propulsion. These flexible nanomotors demonstrate a number of advantages: first, the fabrication process is relatively simple and involves a common template-directed electrodeposition protocol of nanowires; second, these nanowire motors are able to propel at high speeds, both dimensional (up to $\approx 21\mu$m/s) and dimensionless (up to 0.164 body lengths per revolution), and their performance compares very well with natural microorganisms and other synthetic locomotive systems; third, they are actuated by external magnetic field and do not require specific chemical environments (fuels) for propulsion, which is preferable for biomedical applications. Indeed, the performance of the nanomotors reported here is not affected by the presence of ions or other chemical species, and they are able to propel equally well in real biological settings. As an illustration, we have placed these flexible nanomotors in human serum, and observed similar propulsion behaviours (Fig. 4.8). This demonstrates an exciting potential of these flexible nanomotors for future biomedical applications such as targeted drug delivery systems, or cell manipulation.

The fundamental physics of the flexible nanomotors has been illustrated by a simple analytical elastohydrodynamic model. The propulsion characteristics were experimentally studied and compared with the theoretical model, with good agreement. Strictly speaking, the results of the asymptotic model presented in this

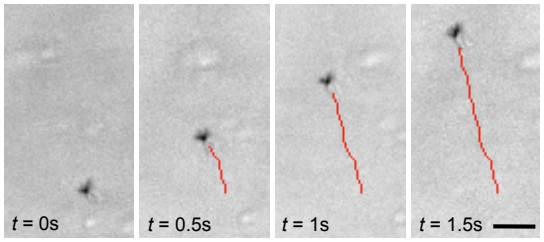

Figure 4.8: Time lapse images (time as indicated) of the motion of nanowire motor (velocity, $U = 15\mu$m/s) in human serum at $f = 15$Hz, with $H_1 = 10$G and $H_0 = 9.5$G. Scale bar is 5μm.

chapter are valid only for h $\ll 1$. However, as shown in other previous studies which compared asymptotic results with numerical and experimental studies [60,98,100], these asymptotic models often remain valid even up to h ~ 1, meaning that geometrical nonlinearities do not play very significant roles. Our results also ignore the hydrodynamic effect of the bottom surface close to which the nanomotors are propelling. As we estimated experimentally the distance of the filaments to the surface to be on the order of microns, and therefore on the order of the swimmer size, we do not expect strong hydrodynamic effects from the surface, which might explain the success of our simple modelling approach. Further progress in theoretical modelling most likely have to be obtained numerically. More accurate yet complicated descriptions of the hydrodynamic interactions can be achieved using methods such as slender body theory [65], or regularized Stokeslets [106]. Tension, self-spinning, and twist strains of the filament may also be considered for improvements.

Chapter 4, in full, is a reprint of the material as it appears in Soft Matter 2011. Pak, On Shun; Gao, Wei; Wang, Joseph; Lauga, Eric, the Royal Society of Chemistry, 2011. The dissertation author was the primary investigator and author of this paper. The dissertation author thanks Professor Eric Fullerton, Erik Shipton, and Daniel Kagan for their help on the magnetic setup, and Allen Pei, Adam Ponedal for assisting in the nanowire preparation. Useful discussions with Saverio Spagnolie are acknowledged.

Chapter 5

Extensibility enables locomotion under isotropic drag

Anisotropic viscous drag is usually believed to be a requirement for the low Reynolds number locomotion of slender bodies such as flagella and cilia. Here we show that locomotion under isotropic drag is possible for extensible slender bodies. After general considerations, a two-ring swimmer and a model dinoflagellate flagellum are studied analytically to illustrate how extensibility can be exploited for self-propulsion without drag anisotropy. This new degree of freedom could be useful for some complex swimmer geometries and locomotion in complex fluid environments where drag anisotropy is weak or even absent.

5.1 Introduction

Due to the absence of inertial forces, low-Reynolds number locomotion is subject to interesting mathematical and physical constraints [15–17]. In particular, locomotion by time-reversible strokes is ruled out by Purcell's scallop theorem [18,20]. To escape these constraints, microorganisms swim by either propagating deformation waves along slender appendages, termed flagella, or rotating them. Anisotropic viscous drag is believed to be the fundamental property enabling drag-based propulsion of slender filaments [16, 76, 107]. It is a classical result that for a slender filament moving in an unbounded Newtonian fluid, the Stokes drag is almost twice when moving perpendicular than parallel to its axis [16,108]. This drag

anisotropy allows propulsive forces to be created perpendicularly to the deformation of the filament. Under isotropic drag, it is generally accepted that locomotion of this kind would be impossible [60, 76, 103, 107, 109].

Unlike in Newtonian flows, drag laws in more complex media, and their consequences on locomotion, remain largely unexplored. Theoretical studies, via Brinkman models, suggest that porosity enhances drag anisotropy [110, 111], explaining, e.g., the increase in propulsion speed of *C. elegans* in a granular medium. Recent experiments also measured and characterized granular drag in beds of glass beads and granular media [112–115], which have been applied to study locomotion in sand [116]. Besides the fluid medium, the geometry of a swimming body also plays a role in the drag law. Some flagella, such as those of *Ochromonas*, possess rigid projections termed mastigonemes, protruding into the fluid [17]. In these geometries the viscous drag in the longitudinal direction of the flagellum is increased, possibly resulting in a more isotropic drag. In situations where drag anisotropy is weak or even absent, what are the alternative mechanisms, if any, offered by physics to achieve locomotion? In this chapter, we point out a new degree of freedom enabling inertialess swimming, namely extensibility. Using a general derivation and two simple geometrical models, we demonstrate that the periodic stretching and contraction of a filament allow self-propulsion even under isotropic drag.

5.2 General analysis

We start by considering the general calculation of Becker *et al.* [76] showing that drag anisotropy is required for the propulsion of inextensible swimmers. Here we revisit their derivation by relaxing the inextensibility condition. Consider a filamentous swimmer of total length $L(t)$, and denote by $\mathbf{r}(s,t)$ the instantaneous position of material points along the filament, where s is the arclength. The time rate of change of the average swimmer position, $\bar{\mathbf{r}}(t)$, is given by

$$\frac{d\bar{\mathbf{r}}}{dt} = \frac{d}{dt}\left[\frac{1}{L(t)}\int_0^{L(t)} \mathbf{r}(s,t)ds\right] \tag{5.1}$$

$$= \frac{\dot{L}}{L}\left[\mathbf{r}(L,t) - \frac{1}{L}\int_0^L \mathbf{r}ds\right] + \frac{1}{L}\int_0^L \frac{\partial \mathbf{r}}{\partial t}ds, \tag{5.2}$$

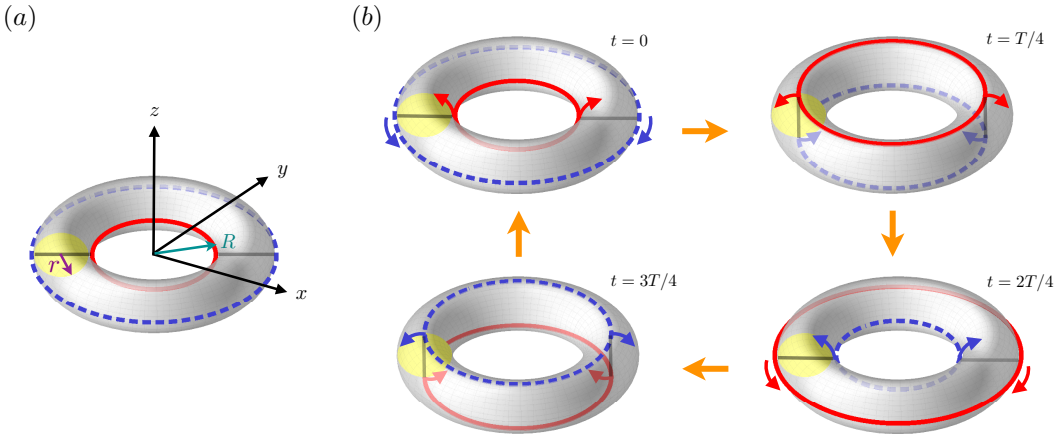

Figure 5.1: (a) Notation for the extensible two-ring swimmer. (b) Schematic illustration of its cyclic deformation over one period, T (see text for details).

where we have denoted $\dot{L} \equiv dL/dt$. Under isotropic drag, we have $\partial \mathbf{r}/\partial t = \mathbf{u} \propto \mathbf{f}$, where $\mathbf{f}$ is the local drag force per unit length, and thus $\int_0^L \partial \mathbf{r}/\partial t ds \propto \int_0^L \mathbf{f} ds = \mathbf{0}$ for force-free swimming. We therefore find that the second term in Eq. (5.2) disappears, and thus

$$\frac{d\bar{\mathbf{r}}}{dt} = \frac{\dot{L}}{L}\left[\mathbf{r}(L,t) - \bar{\mathbf{r}}\right]. \tag{5.3}$$

For an inextensible swimmer, $\dot{L}(t) = 0$, leading to $d\bar{\mathbf{r}}/dt = 0$: no net propulsion is possible under isotropic drag [76]. As a difference, for an extensible swimmer ($\dot{L} \neq 0$) no general conclusion can be drawn, suggesting the relaxation of the drag anisotropy requirement when extensibility is permitted. We demonstrate below how this additional degree of freedom can be exploited for self-propulsion by considering two simple examples.

5.3 Example 1: Motion of two extensible slender rings

As the first example, consider the motion of two extensible slender rings (red solid and blue dashed circles in Fig. 5.1) connected by two rotating rigid rods (each of length $2r$). As a result of the rod rotation, each ring expands and contracts periodically, tracing in time the surface of a torus of inner radius R and a circular

cross-section of radius r (see Fig. 5.1a). In Cartesian coordinates, the motion of each ring $\mathbf{r}(t) = [x(t), y(t), z(t)]$ can be described as

$$x(t) = \{R + r\,[1 - \cos(\omega t + \phi_0)]\}\cos\theta, \tag{5.4}$$

$$y(t) = \{R + r\,[1 - \cos(\omega t + \phi_0)]\}\sin\theta, \tag{5.5}$$

$$z(t) = r\sin(\omega t + \phi_0), \tag{5.6}$$

where, $\theta \in [0, 2\pi]$, $\omega = 2\pi/T$ is the angular frequency, T is the period of the motion, and ϕ_0 is the phase of the motion. We non-dimensionalize lengths by the inner radius of the torus R, time by $1/\omega$, and the dimensionless deformation kinematics of the two rings, $\tilde{\mathbf{r}}_{1,2}(\tilde{t}) = [\tilde{x}_{1,2}(\tilde{t}), \tilde{y}_{1,2}(\tilde{t}), \tilde{z}_{1,2}(\tilde{t})]$, are given by

$$\tilde{x}_{1,2}(\tilde{t}) = \left\{1 + \tilde{r}\left[1 - \cos(\tilde{t} + \phi_{1,2})\right]\right\}\cos\theta, \tag{5.7}$$

$$\tilde{y}_{1,2}(t) = \left\{1 + \tilde{r}\left[1 - \cos(\tilde{t} + \phi_{1,2})\right]\right\}\sin\theta, \tag{5.8}$$

$$\tilde{z}_{1,2}(\tilde{t}) = \tilde{r}\sin(\tilde{t} + \phi_{1,2}), \tag{5.9}$$

where we assign $\phi_1 = 0$ (red solid ring) and $\phi_2 = \pi$ (blue dashed ring). All tilde variables in this chapter are dimensionless.

We illustrate the cyclic deformation of this swimmer over one period in Fig. 5.1b. Hydrodynamically, material is being created/destroyed when a ring extends/contracts, introducing an additional mechanism for varying the hydrodynamic drag. The non-zero translational velocity expected to arise is a direct result of the imbalance of vertical viscous force due to the difference in the total arc-length of the two rings. Since the vertical motion and variation of the circumference of the two rings are out-of-phase, the vertical velocity of the ring with a larger circumference always points in the same direction (in the case considered here, in the $-z$ direction). Therefore, we expect a net unidirectional vertical force, and hence swimming, in this direction. Note that when the two rings have, instantaneously, exactly the same diameters (at $\tilde{t} = (2n+1)\pi/2$, where $n = 0, 1, 2, \ldots$; see the upper right and lower left panels in Fig. 5.1b), the viscous forces acting on the rings balance, and no swimming is produced. Note also that if there was only one ring, say $\tilde{\mathbf{r}}_1$, the vertical motion of the ring, would be exactly canceled by translational swimming velocity at the same speed, resulting in no apparent motion.

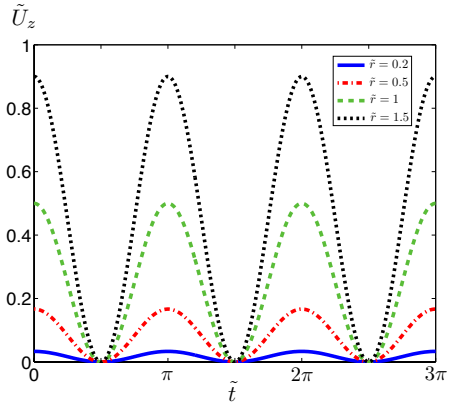

Figure 5.2: Time-variation of the dimensionless swimming velocity of the extensible two-ring swimmer, $\tilde{U}_z$, for different values of $\tilde{r}$.

Quantitatively, we apply a general local drag theory to this two-ring swimmer. We neglect the hydrodynamic impact of the rods connecting the rings. The local viscous force density acting on the filament is then given by $\mathbf{f} = -[\xi_{\parallel}\mathbf{tt} + \xi_{\perp}(1 - \mathbf{tt})] \cdot \mathbf{u}$, where $\mathbf{t}$ is the local tangent vector and $\mathbf{u}$ is the local velocity of the filament. The drag coefficients $\xi_{\parallel}$ and $\xi_{\perp}$ characterize the motion of a slender rod parallel and perpendicular to its axis respectively. Their specific values depend on the geometry of the rod and properties of the fluid medium. For a slightly distorted slender filament in an unbounded Newtonian fluid, Gray and Hancock [103, 107] derived explicit analytical expressions for the drag coefficients, which were later improved by Lighthill [117]. For more complex environments, these drag laws remain mostly unknown. Under isotropic drag, we have $\xi_{\perp} = \xi_{\parallel}$ [118–121]. Here, we keep their values general in the calculations, and show that the final swimming speed of the two-ring swimmer is independent of these coefficients. The swimmer hence works equally well under any local drag law, including isotropic drag.

The local velocity along a ring, $\mathbf{u} = \partial\mathbf{r}/\partial t + \mathbf{U} + \mathbf{\Omega} \times \mathbf{r}$, is composed of two parts: the prescribed deformation velocity, $\partial\mathbf{r}/\partial t$, and the unknown swimming velocities $\mathbf{U} + \mathbf{\Omega} \times \mathbf{r}$ to be determined. At low Reynolds numbers, the total force and total torque on a swimmer have to vanish. Hence, we have $\sum_{i=1}^{2} \int_0^{L_i(t)} \mathbf{f}_i ds_i = \sum_{i=1}^{2} \int_0^{L_i(t)} \boldsymbol{\tau}_i ds_i = \mathbf{0}$, where $\boldsymbol{\tau} = \mathbf{r} \times \mathbf{f}$ is the local viscous torque density, leading to six equations to determine the unknown swimming kinematics $(\mathbf{U}, \mathbf{\Omega})$. By symmetry, we have $\mathbf{\Omega} = \mathbf{0}$, and U_z is the only non-zero translational velocity

component. After some algebra we obtain the dimensionless swimming velocity

$$\tilde{U}_z = \left(\frac{\tilde{r}^2}{1+\tilde{r}}\right)\cos^2\tilde{t}. \tag{5.10}$$

We display the variation of the swimming velocity as a function of time for different values of $\tilde{r}$ in Fig. 5.2. We obtain unidirectional swimming ($\tilde{U}_z \geq 0$) at a time-averaged speed independent of the value of the drag coefficients, $\langle\tilde{U}_z\rangle = \tilde{r}^2/2(1+\tilde{r})$: this extensible two-ring swimmer can therefore self-propel under isotropic drag.

5.4 Example 2: A toroidal helix

This idea can be extended to more complicated geometries consisting of a curved structure built upon another curved structure, for instance, toroidal helices (a helix built upon a circle) and superhelices (a helix built upon another helix). A toroidal helix has been studied as an idealized geometrical model for dinoflagellates [78, 122]. A dinoflagellate can be propelled by propagating a toroidal helical wave, where the kinematics of such a wave implicitly assumes extensibility due to the intrinsic length differences in the geometry. Consider a toroidal helical wave with amplitude r, wave-number $k = 2\pi/\lambda$ and angular frequency ω, propagating along a circle of radius R (see Fig. 5.3 inset). When lengths are non-dimensionlized by $1/k$ and times by $1/\omega$, the dimensionless kinematics $\tilde{\mathbf{R}} = [\tilde{x}', \tilde{y}', \tilde{z}']$ can be expressed as

$$\tilde{x}'(\tilde{s}', \tilde{t}) = \tilde{R}\cos(\tilde{s}'/\tilde{R}) + \tilde{r}\cos(\tilde{s}' - \tilde{t})\cos(\tilde{s}'/\tilde{R}), \tag{5.11}$$

$$\tilde{y}'(\tilde{s}', \tilde{t}) = \tilde{R}\sin(\tilde{s}'/\tilde{R}) + \tilde{r}\cos(\tilde{s}' - \tilde{t})\sin(\tilde{s}'/\tilde{R}), \tag{5.12}$$

$$\tilde{z}'(\tilde{s}', \tilde{t}) = \pm\tilde{r}\sin(\tilde{s}' - \tilde{t}), \tag{5.13}$$

where $\tilde{s}' \in [0, 2\pi\tilde{R}]$ parametrizes the toroidal helix, and where all tilde parameters are dimensionless. Note that the dimensionless radius $\tilde{R}$ takes only integer values for a closed toroidal helix. The $\pm$ sign represents different chirality of the helix. We apply the same local drag model as above. In order to make analytical progress, we consider the small-amplitude limit $\tilde{r} \ll 1$ and perform asymptotic expansions in powers of $\tilde{r}$. Swimming occurs at $O(\tilde{r}^2)$ and takes the dimensionless form

$$\tilde{\mathbf{U}} = \left[0, 0, \pm\frac{\tilde{r}^2}{2\tilde{R}}\right], \quad \tilde{\mathbf{\Omega}} = \left[0, 0, \frac{1-\xi_\perp/\xi_\parallel}{\tilde{R}}\tilde{r}^2\right]. \tag{5.14}$$

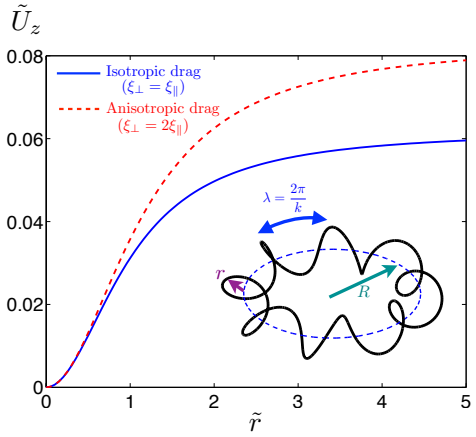

Figure 5.3: Dimensionless translational velocity $\tilde{U}_z$ as a function of the dimensionless toroidal wave amplitude, $\tilde{r} = rk$, under isotropic ($\xi_\perp = \xi_\parallel$, blue solid line) and anisotropic ($\xi_\perp = 2\xi_\parallel$, red dashed line) drag, for the case of $\tilde{R} = 8$. Inset: notation for a toroidal helix swimmer (see text for details).

While the rotational velocity $\tilde{\mathbf{\Omega}}$ vanishes under isotropic drag ($\xi_\perp/\xi_\parallel = 1$), the translational velocity $\tilde{\mathbf{U}}$ along the torus axis is independent of the drag coefficients. This is due to the intrinsic difference in length (and hence drag) embedded in the curved geometry of toroidal helices. The toroidal helix has shorter lengths on the sides closer to the center of the circle, creating an overall imbalance of hydrodynamic drag. It is interesting to compare two physical limits, namely when there is no drag anisotropy ($\xi_\perp = \xi_\parallel$) and when there is maximum drag anisotropy for an asymptotically slender filament in a Newtonian flow ($\xi_\perp = 2\xi_\parallel$). Using these values in the general local drag theory, we find that the axial propulsion velocity in these two limits are indistinguishable for small $\tilde{r}$ (Fig. 5.3), as predicted by the asymptotic analysis. As $\tilde{r}$ increases, the drag anisotropy increasingly enhances propulsion (up to $\sim 30\%$ when $\tilde{r} = 5$) but extensibility alone, under isotropic drag, still enables swimming with significant magnitudes. A similar example that could exploit extensibility to produce swimming under isotropic drag are superhelical waves, which serve as a geometrical model for insect spermatozoa [12].

5.5 Conclusions

In conclusion, in this chapter we have revisited the requirement of drag anisotropy to achieve self-propulsion at zero Reynolds number. We demonstrated explicitly, via two simple swimmers, that extensibility provides a mechanism for swimming under isotropic drag, which might be relevant for some complex swimmer geometries and motion in porous or other complex media where drag anisotropy is weak or absent. As a practical side-note, the two-ring swimmer described above could be actuated experimentally by external rotating magnetic fields if ferromagnetic materials, such as metal nanowires [123, 124], were used for the phantom rods.

Chapter 5, in full, is a reprint of the material as it appears in Physics of Fluids 2011. Pak, On Shun; Lauga, Eric, the American Institute of Physics, 2011. The dissertation author was the primary investigator and author of this paper. The dissertation author thanks Saverio Spagnolie and Gwynn Elfring for useful discussions.

Chapter 6

Pumping by flapping in a viscoelastic fluid

In a world without inertia, Purcell's scallop theorem states that in a Newtonian fluid a time-reversible motion cannot produce any net force or net flow. Here we consider the extent to which the nonlinear rheological behavior of viscoelastic fluids can be exploited to break the constraints of the scallop theorem in the context of fluid pumping. By building on previous work focusing on force generation, we consider a simple, biologically-inspired geometrical example of a flapper in a polymeric (Oldroyd-B) fluid, and calculate asymptotically the time-average net fluid flow produced by the reciprocal flapping motion. The net flow occurs at fourth order in the flapping amplitude, and suggests the possibility of transporting polymeric fluids using reciprocal motion in simple geometries even in the absence of inertia. The induced flow field and pumping performance are characterized and optimized analytically. Our results may be useful in the design of micro-pumps handling complex fluids.

6.1 Introduction

Imagining oneself attempting to swim in a pool of viscous honey, it is not hard to anticipate that, because of the high fluid viscosity, our usual swimming strategy consisting of imparting momentum to the surrounding fluid will not be effective. The world microorganisms inhabit is physically analogous to this situ-

ation [18]. As a result, microorganisms have evolved strategies which exploit the only physical force available to them – namely fluid drag – to propel themselves or generate net fluid transport. The success of these propulsion strategies is vital in many biological processes, including bacterial infection, spermatozoa locomotion and reproduction, and ciliary transport [33].

The fundamental physics of small-scale locomotion in simple (Newtonian) fluids is well understood [16, 17, 32]. In contrast, and although most biological fluids are non-Newtonian, many basic questions remain unanswered regarding the mechanics of motility in complex fluids. Since they usually include biopolymers, most biological fluids of interest display rheological properties common to both fluids (they flow and dissipate energy) and solids (they can store energy). Examples include the airway mucus, which acts as a renewable and transportable barrier along the airways of the lungs to guard against inhaled particulates and toxic substances [125], as well as cervical mucus, which is important for the survival and transport of sperm cells [126]. The influence of viscoelasticity of the fluid on cell locomotion has been experimentally quantified by a number of studies [25–31], including the change in the waveform, structure, and swimming path of spermatozoa in both synthetic polymer solutions and biological mucus [15]. Gastropod mucus is another common non-Newtonian biofluid, which is useful for adhesive locomotion, and its physical and rheological properties have been measured [127–129]. Modeling-wise, different constitutive models have been employed to study locomotion in complex fluids (see the short review in Ref. [51]). Among these models, the Oldroyd-B constitutive equation is the most popular, both because of its simplicity and the fact that it can be derived exactly from kinetic theory by modeling the fluid as a dilute solutions of elastic (polymeric) dumbbells [130–133]. Recent quantitative studies have suggested that microorganisms swimming by propagating waves along their flagella have a smaller propulsion speed in a polymeric fluid than in a Newtonian fluid [51, 134]. Likewise, a smaller net flow is generated by the ciliary transport of a polymeric fluid than a Newtonian fluid. Specifically, Lauga [51] considered the problem with a prescribed beating pattern along the flagellum, while Fu *et al.* [134] prescribed the internal force distribution instead; both studies suggest that viscoelasticity tends to decrease the propulsion speed.

In a Newtonian fluid, Purcell's scallop theorem states that swimming and

pumping in the absence of inertia can only be achieved by motions or body deformations which are not identical under a time-reversal symmetry (so-called "non-reciprocal" motion) [18]. This poses of course an interesting challenge in designing artificial swimmers and pumps in simple fluids, which has recently been addressed theoretically and experimentally (see the review in Ref. [16]). The question we are addressing in this chapter is the extent to which the scallop theorem holds in complex fluids. Because polymeric fluids display nonlinear rheological properties such as shear-dependance or normal-stress differences [131, 132], in general reciprocal motions are effective in polymeric fluids [135]. New propulsion and transport methods can therefore be designed on small scales to specifically take advantage of the intrinsic nonlinearities of the fluid. The goal of this chapter is to study such a system in the context of fluid pumping with a simplified geometrical setup where the pumping performance can be characterized analytically.

For simple flow geometries, it is not obvious a priori whether a simple oscillatory forcing of a nonlinear fluid leads to a net (rectified) flow. For example, for all Oldroyd-like fluids, a sinusoidally-forced Couette flow leads to zero time-averaged flow [131]. In previous work [136], we considered a biologically-inspired geometric example of a semi-infinite flapper performing reciprocal (sinusoidal) motion in a viscoelastic (Oldroyd-B) fluid in the absence of inertia. We showed explicitly that the reciprocal motion generates a net force on the flapper occurring at second order in the flapping amplitude, and disappearing in the Newtonian limit as dictated by the scallop theorem. However, there was no time-average flow accompanying the net force generation at second order [136]. Here, we report on the discovery of a net fluid flow produced by the reciprocal flapping motion in an Oldroyd-B fluid. The net flow transport is seen to occur at fourth order in the flapping amplitude, and is due to normal-stress differences. The dependence of the pumping performance on the actuation and material parameters is characterized analytically, and the optimal pumping rate is determined numerically. Through this example, we therefore demonstrate explicitly the breakdown of the scallop theorem in complex fluids in the context of fluid pumping, and suggest the possibility of exploiting intrinsic viscoelastic properties of the medium for fluid transport on small scales.

The geometric setup in this chapter is motivated by the motion of cilia-like biological appendages. Cilia are short flagella beating collaboratively to produce

locomotion or fluid transport [17, 137]. For example, cilia cover the outer surface of microorganisms such as *Paramecium* for self-propulsion. They are also present along our respiratory tracts to sweep up dirt and mucus and along the oviduct to transport the ova. Our setup is also relevant to the rigid projections attached to the flagellum of *Ochromonas*, known as mastigonemes, which protrude from the flagellum into the fluid [17]. As waves propagate along the flagellum, the mastigonemes are flapped back-and-forth passively through the fluid, a process which can lead to a change in the direction of propulsion of the organism [138–140].

Our study is related to the phenomenon known as steady (or "acoustic") streaming in the inertial realm [141–154], which has a history of almost two centuries after being first discovered by Faraday [141]. Under oscillatory boundary conditions, as in the presence of an acoustic wave or the periodic actuation of a solid body in a fluid, migration of fluid particles occur in an apparently purely oscillating flow, manifesting the presence of nonlinear inertial terms in the equation of motion. This phenomenon occurs in both Newtonian and non-Newtonian fluids [145–154]. In particular, it was found that the elasticity of a polymeric fluid can lead to a reversal of the net flow direction [145–148]. As expected from the scallop theorem, no steady streaming phenomenon can occur in a Newtonian fluid in the absence of inertia. However, as will be shown in this chapter, the nonlinear rheological properties of viscoelastic fluids alone can lead to steady streaming. In other words, we consider here a steady streaming motion arising purely from the viscoelastic effects of the fluid, ignoring any influence of inertia.

Recently, polymeric solutions have been shown to be useful in constructing microfluidic devices such as flux stabilizers, flip-flops and rectifiers [155, 156]. By exploiting the nonlinear rheological properties of the fluid and geometrical asymmetries in the micro-channel, microfluidic memory and control have been demonstrated without the use of external electronics and interfaces, opening the possibility of more complex integrated microfluidic circuit and other medical applications [155]. In the setup we study here, we do not introduce any geometrical asymmetries and exploit solely the non-Newtonian rheological properties of the polymeric fluid for microscopic fluid transport.

The structure of the chapter is the following. In Sec. 6.2, the flapping problem is formulated with the geometrical setup, governing equations, nondimen-

sionalization and the boundary conditions. In Sec. 6.3, we present the asymptotic calculations up to the fourth order (in flapping amplitude), where the time-average flow is obtained. We then characterize analytically the net flow in terms of the streamline pattern, directionality and vorticity distribution (Sec. 6.4). Next, we study the optimization of the flow with respect to the Deborah number (Sec. 6.5). Our results are finally discussed in Sec. 6.6.

6.2 Formulation

6.2.1 Geometrical setup

In this chapter, we consider a semi-infinite two-dimensional plane flapping sinusoidally with small amplitude in a viscoelastic fluid. The average position of the flapper is situated perpendicularly to a flat wall with its hinge point fixed in space (see Fig. 6.1). The flapper is therefore able to perform reciprocal motion with only one degree of freedom by flapping back-and-forth. Such a setup is directly relevant to the unsteady motion of cilia-like biological appendages (see Sec. 6.1).

It is convenient to adopt planar polar coordinates system for this geometrical setup. The instantaneous position of the flapper is described by the azimuthal angle $\theta(t) = \pi/2 + \epsilon\Theta(t)$, where $\Theta(t)$ is an order one oscillatory function of time and ϵ is a parameter characterizing the amplitude of the flapping motion. The polar vectors $\mathbf{e_r}(\theta)$ and $\mathbf{e}_\theta(\theta)$ are functions of the azimuthal angle, and the velocity field $\mathbf{u}$ is expressed as $\mathbf{u} = u_r\mathbf{e}_r + u_\theta\mathbf{e}_\theta$. In this work, we derive the velocity field in the the domain $(0 \leq \theta \leq \pi/2)$ in the asymptotic limit of small flapping amplitude, *i.e.* $\epsilon \ll 1$; the time-averaged flow in the domain $(\pi/2 \leq \theta \leq \pi)$ can then be deduced by symmetry.

6.2.2 Governing equations

We assume the flow to be incompressible and the Reynolds number of the fluid motion to be small, *i.e.* we neglect any inertial effects. Denoting the pressure field as p and the deviatoric stress tensor as $\boldsymbol{\tau}$, the continuity equation and Cauchy's

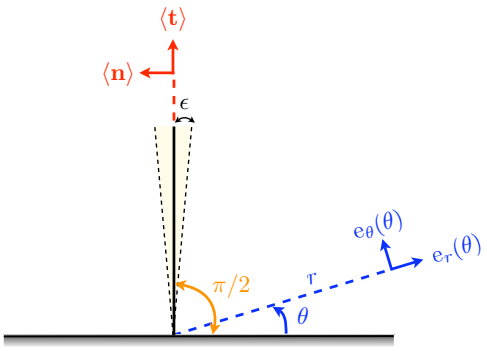

Figure 6.1: Geometrical setup and notations for the flapping calculation. A semi-infinite plane flaps sinusoidally with small amplitude ϵ around an average position at right angle with an infinite wall.

equation of motion are respectively

$$\boldsymbol{\nabla} \cdot \mathbf{u} = 0, \tag{6.1}$$

$$\boldsymbol{\nabla} p = \boldsymbol{\nabla} \cdot \boldsymbol{\tau}. \tag{6.2}$$

We also require constitutive equations, which relate stresses and kinematics of the flow, to close the system of equations. For polymeric fluids, the deviatoric stress may be decomposed into two components, $\boldsymbol{\tau} = \boldsymbol{\tau}^s + \boldsymbol{\tau}^p$, where $\boldsymbol{\tau}^s$ is the Newtonian contribution from the solvent and $\boldsymbol{\tau}^p$ is the polymeric stress contribution. For the Newtonian contribution, the constitutive equation is simply given by $\boldsymbol{\tau}^s = \eta_s \dot{\boldsymbol{\gamma}}$, where η_s is the solvent contribution to the viscosity and $\dot{\boldsymbol{\gamma}} = \boldsymbol{\nabla}\mathbf{u} + {}^t\boldsymbol{\nabla}\mathbf{u}$. For the polymeric contribution, many models have been proposed to relate the polymeric stress to kinematics of the flow [130–133]. We consider here the classical Oldroyd-B model, where the polymeric stress, $\boldsymbol{\tau}^p$, satisfies the upper-convected Maxwell equation

$$\boldsymbol{\tau}^p + \lambda \overset{\triangledown}{\boldsymbol{\tau}}^p = \eta_p \dot{\boldsymbol{\gamma}}, \tag{6.3}$$

where η_p is the polymer contribution to the viscosity and λ is the polymeric relaxation time. The upper-convected derivative for a tensor $\mathbf{A}$ is defined as

$$\overset{\triangledown}{\mathbf{A}} = \frac{\partial \mathbf{A}}{\partial t} + \mathbf{u} \cdot \boldsymbol{\nabla}\mathbf{A} - \left({}^t\boldsymbol{\nabla}\mathbf{u} \cdot \mathbf{A} + \mathbf{A} \cdot \boldsymbol{\nabla}\mathbf{u} \right), \tag{6.4}$$

and represents the rate of change of $\mathbf{A}$ in the frame of translating and deforming with the fluid. From Eq. (6.3), we can obtain the Oldroyd-B constitutive equation for the total stress, $\boldsymbol{\tau}$, as given by

$$\boldsymbol{\tau} + \lambda_1 \overset{\triangledown}{\boldsymbol{\tau}} = \eta \left(\dot{\boldsymbol{\gamma}} + \lambda_2 \overset{\triangledown}{\dot{\boldsymbol{\gamma}}} \right), \tag{6.5}$$

where $\eta = \eta_s + \eta_p$, $\lambda_1 = \lambda$, and $\lambda_2 = \eta_s \lambda / \eta$. Here, λ_1 and λ_2 are the relaxation and retardation times of the fluid respectively. The relaxation time is the typical decay rate of stress when the fluid is at rest, and the retardation time measures the decay rate of residual rate of strain when the fluid is stress-free [131, 132]. It can be noted that $\lambda_2 < \lambda_1$, and both are zero for a Newtonian fluid.

6.2.3 Nondimensionalization

Periodic flapping motion with angular frequency ω is considered in this chapter. Therefore, we nondimensionalize shear rates by ω and stresses by $\eta\omega$. Lengths are nondimensionalized by some arbitrary length scale along the flapper. Under these nondimensionalizations, the dimensionless equations are given by

$$\boldsymbol{\nabla} \cdot \mathbf{u} = 0, \tag{6.6a}$$

$$\boldsymbol{\nabla} p = \boldsymbol{\nabla} \cdot \boldsymbol{\tau}, \tag{6.6b}$$

$$\boldsymbol{\tau} + \mathrm{De}_1 \overset{\triangledown}{\boldsymbol{\tau}} = \dot{\boldsymbol{\gamma}} + \mathrm{De}_2 \overset{\triangledown}{\dot{\boldsymbol{\gamma}}}, \tag{6.6c}$$

where $\mathrm{De}_1 = \lambda_1 \omega$ and $\mathrm{De}_2 = \lambda_2 \omega$ are defined as the two Deborah numbers and we have adopted the same symbols for convenience.

6.2.4 Boundary conditions

The boundary condition in this problem can be simply stated; on the flat wall ($\theta = 0$), we have the no-slip and the no-penetration boundary conditions. In vector notation, we have therefore

$$\mathbf{u}(r, \theta = 0) = \mathbf{0} \tag{6.7}$$

along the flat wall.

Along the flapper, we also have the no-slip condition, $u_r(r, \theta = \pi/2 + \epsilon\Theta(t)) = 0$. The other boundary condition imposed on the fluid along the flapper is given by the rotation of the flapper, $u_\theta(r, \theta = \pi/2 + \epsilon\Theta(t)) = r\Omega(t)$, where $\Omega(t) = \epsilon\dot{\Theta}$. In vector notation, we have then

$$\mathbf{u}(r, \theta = \pi/2 + \epsilon\Theta(t)) = r\Omega(t)\mathbf{e}_\theta. \tag{6.8}$$

6.3 Analysis

Noting that a two-dimensional setup is considered, the continuity equation, $\boldsymbol{\nabla} \cdot \mathbf{u} = 0$, is satisfied by introducing the streamfunction $\Psi(r, \theta)$ such that $u_r = (\partial\Psi/\partial\theta)/r$ and $u_\theta = -\partial\Psi/\partial r$. The instantaneous position of the flapper is described by the function $\theta = \pi/2 + \epsilon\Theta(t)$, and we consider here a simple reciprocal flapping motion with $\Theta(t) = \cos t$. Since small amplitude flapping motion ($\epsilon \ll 1$) is considered, we will perform the calculations perturbatively in the flapping amplitude and seek perturbation expansions of the form

$$\{\mathbf{u}, \Psi, \boldsymbol{\tau}, p, \boldsymbol{\sigma}\} = \epsilon\{\mathbf{u}_1, \Psi_1, \boldsymbol{\tau}_1, p_1, \boldsymbol{\sigma}_1\} + \epsilon^2\{\mathbf{u}_2, \Psi_2, \boldsymbol{\tau}_2, p_2, \boldsymbol{\sigma}_2\} + \ldots, \tag{6.9}$$

where $\boldsymbol{\sigma} = -p\mathbf{1} + \boldsymbol{\tau}$ is the total stress tensor and all the variables in Eq. (6.9) are defined in the time-averaged domain $0 \leq \theta \leq \pi/2$. Since a domain-perturbation expansion is performed, careful attention has to be paid on the distinction between instantaneous and average geometry. Recall that the polar vectors $\mathbf{e}_r(\theta(t))$ and $\mathbf{e}_\theta(\theta(t))$ are functions of the azimuthal angle which oscillates in time. To distinguish the average geometry, we denote $\langle\mathbf{t}\rangle = \mathbf{e}_r(\pi/2)$ and $\langle\mathbf{n}\rangle = \mathbf{e}_\theta(\pi/2)$ as the average directions along and perpendicular to the flapper axis (See Fig. 6.1). In this chapter, $\langle \ldots \rangle$ denotes time-averaging.

In addition, we employ Fourier notation to facilitate the calculations. In Fourier notation, the actuation becomes $\Theta = \mathrm{Re}\{e^{it}\}$ and $\dot{\Theta} = \mathrm{Re}\{ie^{it}\}$. Because of the quadratic nonlinearities arising from boundary conditions and the constitutive

modeling, the velocity field can be Fourier decomposed into the anticipated form

$$\mathbf{u}_1 = \mathrm{Re}\{\tilde{\mathbf{u}}_1 e^{it}\}, \tag{6.10a}$$

$$\mathbf{u}_2 = \mathrm{Re}\{\tilde{\mathbf{u}}_2^{(0)} + \tilde{\mathbf{u}}_2^{(2)} e^{2it}\}, \tag{6.10b}$$

$$\mathbf{u}_3 = \mathrm{Re}\{\tilde{\mathbf{u}}_3^{(1)} e^{it} + \tilde{\mathbf{u}}_3^{(3)} e^{3it}\}, \tag{6.10c}$$

$$\mathbf{u}_4 = \mathrm{Re}\{\tilde{\mathbf{u}}_4^{(0)} + \tilde{\mathbf{u}}_4^{(2)} e^{2it} + \tilde{\mathbf{u}}_4^{(4)} e^{4it}\}, \tag{6.10d}$$

with similar decomposition and notation for all other vector and scalar fields.

We now proceed to analyze Eq. (6.6) order by order, up to the fourth order, where the time-average fluid flow occurs. The boundary conditions, Eqs. (6.7) and (6.8), are also expanded order by order about the average flapper position using Taylor expansions.

6.3.1 First-order solution

Governing equation

The first-order Oldroyd-B relation is given by

$$\boldsymbol{\tau}_1 + \mathrm{De}_1 \frac{\partial \boldsymbol{\tau}_1}{\partial t} = \dot{\boldsymbol{\gamma}}_1 + \mathrm{De}_2 \frac{\partial \dot{\boldsymbol{\gamma}}_1}{\partial t}, \tag{6.11}$$

which in Fourier space becomes

$$\tilde{\boldsymbol{\tau}}_1 = \frac{1 + i\mathrm{De}_2}{1 + i\mathrm{De}_1} \tilde{\dot{\boldsymbol{\gamma}}}_1. \tag{6.12}$$

We then note that we have $\boldsymbol{\nabla} \times \boldsymbol{\nabla} \cdot \boldsymbol{\tau} = 0$ by taking the curl of Eq. (6.6b). Therefore, we take the divergence and then curl of Eq. (6.12) to eliminate the stress and obtain the equation for the first-order streamfunction

$$\boldsymbol{\nabla}^4 \tilde{\Psi}_1 = 0. \tag{6.13}$$

Boundary conditions

At $\theta = \pi/2$, the boundary condition at this order is given by

$$\mathbf{u}_1 = r\dot{\Theta}\langle \mathbf{n} \rangle, \tag{6.14}$$

which becomes

$$\tilde{\mathbf{u}}_1 = ir\langle \mathbf{n} \rangle, \tag{6.15}$$

upon Fourier transformation. We also have the no-slip and no-penetration boundary condition at $\theta = 0$.

Solution

The solution satisfying the above equation and boundary conditions is given by

$$\tilde{\Psi}_1 = \frac{ir^2}{4}\left(\cos 2\theta - 1\right), \tag{6.16a}$$

$$\tilde{u}_{1r} = -\frac{ir}{2}\sin 2\theta, \tag{6.16b}$$

$$\tilde{u}_{1\theta} = \frac{ir}{2}\left(1 - \cos 2\theta\right). \tag{6.16c}$$

6.3.2 Second-order solution

Governing equation

The second-order Oldroyd-B relation is given by

$$\begin{aligned}
&\left(1 + \mathrm{De}_1\frac{\partial}{\partial t}\right)\boldsymbol{\tau}_2 - \left(1 + \mathrm{De}_2\frac{\partial}{\partial t}\right)\dot{\boldsymbol{\gamma}}_2 \\
&= \mathrm{De}_2\left[\mathbf{u}_1\cdot\boldsymbol{\nabla}\dot{\boldsymbol{\gamma}}_1 - \left({}^t\boldsymbol{\nabla}\mathbf{u}_1\cdot\dot{\boldsymbol{\gamma}}_1 + \dot{\boldsymbol{\gamma}}_1\cdot\boldsymbol{\nabla}\mathbf{u}_1\right)\right] \\
&- \mathrm{De}_1\left[\mathbf{u}_1\cdot\boldsymbol{\nabla}\boldsymbol{\tau}_1 - \left({}^t\boldsymbol{\nabla}\mathbf{u}_1\cdot\boldsymbol{\tau}_1 + \boldsymbol{\tau}_1\cdot\boldsymbol{\nabla}\mathbf{u}_1\right)\right].
\end{aligned} \tag{6.17}$$

Fourier transforming Eq. (6.17) and using Eq. (6.12), we obtain the two harmonics as

$$\begin{aligned}
&\left(1 + 2i\mathrm{De}_1\right)\tilde{\boldsymbol{\tau}}_2^{(2)} - \left(1 + 2i\mathrm{De}_2\right)\tilde{\dot{\boldsymbol{\gamma}}}_2^{(2)} \\
&= \frac{1}{2}\frac{\mathrm{De}_2 - \mathrm{De}_1}{1 + i\mathrm{De}_1}\left[\tilde{\mathbf{u}}_1\cdot\boldsymbol{\nabla}\tilde{\dot{\boldsymbol{\gamma}}}_1 - \left({}^t\boldsymbol{\nabla}\tilde{\mathbf{u}}_1\cdot\tilde{\dot{\boldsymbol{\gamma}}}_1 + \tilde{\dot{\boldsymbol{\gamma}}}_1\cdot\boldsymbol{\nabla}\tilde{\mathbf{u}}_1\right)\right],
\end{aligned} \tag{6.18}$$

and

$$\begin{aligned}
&\tilde{\boldsymbol{\tau}}_2^{(0)} - \tilde{\dot{\boldsymbol{\gamma}}}_2^{(0)} \\
&= \frac{1}{2}\frac{\mathrm{De}_2 - \mathrm{De}_1}{1 + i\mathrm{De}_1}\left[\tilde{\mathbf{u}}_1^*\cdot\boldsymbol{\nabla}\tilde{\dot{\boldsymbol{\gamma}}}_1 - \left({}^t\boldsymbol{\nabla}\tilde{\mathbf{u}}_1^*\cdot\tilde{\dot{\boldsymbol{\gamma}}}_1 + \tilde{\dot{\boldsymbol{\gamma}}}_1\cdot\boldsymbol{\nabla}\tilde{\mathbf{u}}_1^*\right)\right],
\end{aligned} \tag{6.19}$$

where the starred variables denote complex conjugates in this chapter. Finally, taking the divergence and then curl of both Eq. (6.18) and Eq. (6.19), and using

the knowledge of the first-order solution, we obtain the equation for the second-order streamfunctions as simply

$$\boldsymbol{\nabla}^4\tilde{\Psi}_2^{(2)} = 0, \tag{6.20a}$$

$$\boldsymbol{\nabla}^4\tilde{\Psi}_2^{(0)} = 0. \tag{6.20b}$$

Boundary conditions

The boundary condition at this order is given by

$$\mathbf{u}_2 = -\Theta\frac{\partial \mathbf{u}_1}{\partial\theta} - r\Theta\dot{\Theta}\langle\mathbf{t}\rangle, \tag{6.21}$$

when evaluated at $\theta = \pi/2$. In Fourier notation and with the first-order solution, the boundary conditions for the second-order average flow and the second harmonic read

$$\tilde{\mathbf{u}}_2^{(0)} = 0, \tag{6.22a}$$

$$\tilde{\mathbf{u}}_2^{(2)} = -\frac{ir}{2}\langle t\rangle. \tag{6.22b}$$

In addition, the no-slip and no-penetration boundary condition are imposed at $\theta = 0$.

Solution

The solution satisfying the second-order equation and the boundary conditions is given by

$$\tilde{\Psi}_2^{(0)} = 0, \tag{6.23a}$$

$$\tilde{\Psi}_2^{(2)} = \frac{ir}{4}\left(\frac{1}{2}\sin 2\theta - \frac{\pi}{4}\cos 2\theta - \theta + \frac{\pi}{4}\right), \tag{6.23b}$$

$$\tilde{u}_{2r}^{(2)} = \frac{ir}{4}\left(\cos 2\theta + \frac{\pi}{2}\sin 2\theta - 1\right), \tag{6.23c}$$

$$\tilde{u}_{2\theta}^{(2)} = -\frac{ir}{4}\left(\sin 2\theta - \frac{\pi}{2}\cos 2\theta - 2\theta + \frac{\pi}{2}\right). \tag{6.23d}$$

As anticipated, there is no time-averaged flow at second order, and we proceed with calculations at higher order.

6.3.3 Third-order solution

Governing equation

The third-order Oldroyd-B relation is given by

$$\begin{aligned}
&\left(1+\mathrm{De}_1\frac{\partial}{\partial t}\right)\boldsymbol{\tau}_3-\left(1+\mathrm{De}_2\frac{\partial}{\partial t}\right)\dot{\boldsymbol{\gamma}}_3\\
&=\mathrm{De}_2\left[\mathbf{u}_1\cdot\boldsymbol{\nabla}\dot{\boldsymbol{\gamma}}_2-\left({}^t\boldsymbol{\nabla}\mathbf{u}_1\cdot\dot{\boldsymbol{\gamma}}_2+\dot{\boldsymbol{\gamma}}_2\cdot\boldsymbol{\nabla}\mathbf{u}_1\right)\right]\\
&-\mathrm{De}_1\left[\mathbf{u}_2\cdot\boldsymbol{\nabla}\boldsymbol{\tau}_1-\left({}^t\boldsymbol{\nabla}\mathbf{u}_2\cdot\boldsymbol{\tau}_1+\boldsymbol{\tau}_1\cdot\boldsymbol{\nabla}\mathbf{u}_2\right)\right]\\
&+\mathrm{De}_2\left[\mathbf{u}_2\cdot\boldsymbol{\nabla}\dot{\boldsymbol{\gamma}}_1-\left({}^t\boldsymbol{\nabla}\mathbf{u}_2\cdot\dot{\boldsymbol{\gamma}}_1+\dot{\boldsymbol{\gamma}}_1\cdot\boldsymbol{\nabla}\mathbf{u}_2\right)\right]\\
&-\mathrm{De}_1\left[\mathbf{u}_1\cdot\boldsymbol{\nabla}\boldsymbol{\tau}_2-\left({}^t\boldsymbol{\nabla}\mathbf{u}_1\cdot\boldsymbol{\tau}_2+\boldsymbol{\tau}_2\cdot\boldsymbol{\nabla}\mathbf{u}_1\right)\right].
\end{aligned}\tag{6.24}$$

Aiming at obtaining the average flow at $O(\epsilon^4)$, we only need to calculate the first harmonic at $O(\epsilon^3)$ since the third harmonic will only enter the oscillatory part at $O(\epsilon^4)$ (see the fourth-order calculations for details). Therefore, upon Fourier transform, we obtain the first harmonic component of Eq. (6.24) as

$$\begin{aligned}
&(1+i\mathrm{De}_1)\,\tilde{\boldsymbol{\tau}}_3^{(1)}-(1+i\mathrm{De}_2)\,\tilde{\dot{\boldsymbol{\gamma}}}_3^{(1)}\\
&=\frac{1}{2}\frac{\mathrm{De}_2-\mathrm{De}_1}{1+2i\mathrm{De}_1}\left[\tilde{\mathbf{u}}_1^*\cdot\boldsymbol{\nabla}\tilde{\dot{\boldsymbol{\gamma}}}_2^{(2)}-\left({}^t\boldsymbol{\nabla}\tilde{\mathbf{u}}_1^*\cdot\tilde{\dot{\boldsymbol{\gamma}}}_2^{(2)}+\tilde{\dot{\boldsymbol{\gamma}}}_2^{(2)}\cdot\boldsymbol{\nabla}\tilde{\mathbf{u}}_1^*\right)\right]\\
&+\frac{1}{2}\frac{\mathrm{De}_2-\mathrm{De}_1}{1-i\mathrm{De}_1}\left[\tilde{\mathbf{u}}_2^{(2)}\cdot\boldsymbol{\nabla}\tilde{\dot{\boldsymbol{\gamma}}}_1^*-\left({}^t\boldsymbol{\nabla}\tilde{\mathbf{u}}_2^{(2)}\cdot\tilde{\dot{\boldsymbol{\gamma}}}_1^*+\tilde{\dot{\boldsymbol{\gamma}}}_1^*\cdot\boldsymbol{\nabla}\tilde{\mathbf{u}}_2^{(2)}\right)\right],
\end{aligned}\tag{6.25}$$

where we have used the constitutive relations given by Eqs. (6.12) and (6.18). Taking the divergence and then curl of Eq. (6.25), we obtain the equation for the first harmonic of the third-order streamfunction

$$\boldsymbol{\nabla}^4\tilde{\Psi}_3^{(1)}=\frac{3i\mathrm{De}_1(\mathrm{De}_1-\mathrm{De}_2)\,\cos 2\theta}{r^2(1-i\mathrm{De}_1)(1+2i\mathrm{De}_1)(1+i\mathrm{De}_2)}.\tag{6.26}$$

Boundary condition

At $\theta=\pi/2$, the boundary condition at this order is given by

$$\mathbf{u}_3=-\Theta\frac{\partial\mathbf{u}_2}{\partial\theta}-\frac{1}{2}\Theta^2\frac{\partial^2\mathbf{u}_1}{\partial\theta^2}-\frac{1}{2}r\dot{\Theta}\Theta^2\langle\mathbf{n}\rangle,\tag{6.27}$$

evaluating at $\theta=\pi/2$. The boundary condition for the first harmonic component, in Fourier space, is then given by

$$\tilde{\mathbf{u}}_3^{(1)}=\frac{ir\pi}{8}\langle\mathbf{t}\rangle-\frac{ir}{4}\langle\mathbf{n}\rangle.\tag{6.28}$$

At $\theta=0$, we also have the no-slip and no-penetration boundary condition.

Solution

The solution at this order has the form

$$\tilde{\Psi}_3^{(1)} = \frac{r^2}{2}\Bigg[\left(\frac{\pi^2}{8}\alpha + \frac{\pi^2-4}{32}i\right)\cos 2\theta - \frac{\pi}{4}\left(\alpha+\frac{i}{4}\right)\sin 2\theta + \frac{\pi}{2}\left(\alpha+\frac{i}{4}\right)\theta + \left(\frac{4-\pi^2}{32}i - \frac{\pi^2}{8}\alpha\right) + \alpha\theta\sin 2\theta\Bigg], \tag{6.29a}$$

$$\tilde{u}_{3,r}^{(1)} = \frac{r}{2}\Bigg[\left(\frac{4-\pi^2}{16}i - \frac{\pi^2}{4}\alpha\right)\sin 2\theta - \frac{\pi}{2}\left(\alpha+\frac{i}{4}\right)\cos 2\theta + \frac{\pi}{2}\left(\alpha+\frac{i}{4}\right) + \alpha(2\theta\cos 2\theta + \sin 2\theta)\Bigg], \tag{6.29b}$$

$$\tilde{u}_{3,\theta}^{(1)} = -r\Bigg[\left(\frac{\pi^2}{8}\alpha + \frac{\pi^2-4}{32}i\right)\cos 2\theta - \frac{\pi}{4}\left(\alpha+\frac{i}{4}\right)\sin 2\theta + \frac{\pi}{2}\left(\alpha+\frac{i}{4}\right)\theta + \left(\frac{4-\pi^2}{32}i - \frac{\pi^2}{8}\alpha\right) + \alpha\theta\sin 2\theta\Bigg], \tag{6.29c}$$

where we have defined the constant

$$\alpha = \frac{3i\mathrm{De}_1(\mathrm{De}_2 - \mathrm{De}_1)}{8(1-i\mathrm{De}_1)(1+2i\mathrm{De}_1)(1+i\mathrm{De}_2)}. \tag{6.30}$$

6.3.4 Fourth-order solution

Governing equation

Finally, the fourth-order Oldroyd-B relation is given by

$$\begin{aligned}
&\left(1+\mathrm{De}_1\frac{\partial}{\partial t}\right)\boldsymbol{\tau}_4 - \left(1+\mathrm{De}_2\frac{\partial}{\partial t}\right)\dot{\boldsymbol{\gamma}}_4 \\
&= \mathrm{De}_2\left[\mathbf{u}_1\cdot\boldsymbol{\nabla}\dot{\boldsymbol{\gamma}}_3 - \left({}^t\boldsymbol{\nabla}\mathbf{u}_1\cdot\dot{\boldsymbol{\gamma}}_3 + \dot{\boldsymbol{\gamma}}_3\cdot\boldsymbol{\nabla}\mathbf{u}_1\right)\right] \\
&- \mathrm{De}_1\left[\mathbf{u}_1\cdot\boldsymbol{\nabla}\boldsymbol{\tau}_3 - \left({}^t\boldsymbol{\nabla}\mathbf{u}_1\cdot\boldsymbol{\tau}_3 + \boldsymbol{\tau}_3\cdot\boldsymbol{\nabla}\mathbf{u}_1\right)\right] \\
&+ \mathrm{De}_2\left[\mathbf{u}_2\cdot\boldsymbol{\nabla}\dot{\boldsymbol{\gamma}}_2 - \left({}^t\boldsymbol{\nabla}\mathbf{u}_2\cdot\dot{\boldsymbol{\gamma}}_2 + \dot{\boldsymbol{\gamma}}_2\cdot\boldsymbol{\nabla}\mathbf{u}_2\right)\right] \\
&- \mathrm{De}_1\left[\mathbf{u}_2\cdot\boldsymbol{\nabla}\boldsymbol{\tau}_2 - \left({}^t\boldsymbol{\nabla}\mathbf{u}_2\cdot\boldsymbol{\tau}_2 + \boldsymbol{\tau}_2\cdot\boldsymbol{\nabla}\mathbf{u}_2\right)\right] \\
&+ \mathrm{De}_2\left[\mathbf{u}_3\cdot\boldsymbol{\nabla}\dot{\boldsymbol{\gamma}}_1 - \left({}^t\boldsymbol{\nabla}\mathbf{u}_3\cdot\dot{\boldsymbol{\gamma}}_1 + \dot{\boldsymbol{\gamma}}_1\cdot\boldsymbol{\nabla}\mathbf{u}_3\right)\right] \\
&- \mathrm{De}_1\left[\mathbf{u}_3\cdot\boldsymbol{\nabla}\boldsymbol{\tau}_1 - \left({}^t\boldsymbol{\nabla}\mathbf{u}_3\cdot\boldsymbol{\tau}_1 + \boldsymbol{\tau}_1\cdot\boldsymbol{\nabla}\mathbf{u}_3\right)\right].
\end{aligned} \tag{6.31}$$

Since we wish to characterize the time-average flow, $\tilde{\mathbf{u}}_4^{(0)}$, we calculate the time-average of Eq. (6.31) and obtain

$$\begin{aligned}
&\tilde{\boldsymbol{\tau}}_4^{(0)} - \tilde{\dot{\boldsymbol{\gamma}}}_4^{(0)} \\
&= \frac{1}{2}\mathrm{De}_2\left[\tilde{\mathbf{u}}_1^* \cdot \boldsymbol{\nabla}\tilde{\dot{\boldsymbol{\gamma}}}_3^{(1)} - \left({}^t\boldsymbol{\nabla}\tilde{\mathbf{u}}_1^* \cdot \tilde{\dot{\boldsymbol{\gamma}}}_3^{(1)} + \tilde{\dot{\boldsymbol{\gamma}}}_3^{(1)} \cdot \boldsymbol{\nabla}\tilde{\mathbf{u}}_1^*\right)\right] \\
&- \frac{1}{2}\mathrm{De}_1\left[\tilde{\mathbf{u}}_1^* \cdot \boldsymbol{\nabla}\tilde{\boldsymbol{\tau}}_3^{(1)} - \left({}^t\boldsymbol{\nabla}\tilde{\mathbf{u}}_1^* \cdot \tilde{\boldsymbol{\tau}}_3^{(1)} + \tilde{\boldsymbol{\tau}}_3^{(1)} \cdot \boldsymbol{\nabla}\tilde{\mathbf{u}}_1^*\right)\right] \\
&+ \frac{1}{2}\mathrm{De}_2\left[\tilde{\mathbf{u}}_2^{(2)*} \cdot \boldsymbol{\nabla}\tilde{\dot{\boldsymbol{\gamma}}}_2^{(2)} - \left({}^t\boldsymbol{\nabla}\tilde{\mathbf{u}}_2^{(2)*} \cdot \tilde{\dot{\boldsymbol{\gamma}}}_2^{(2)} + \tilde{\dot{\boldsymbol{\gamma}}}_2^{(2)} \cdot \boldsymbol{\nabla}\tilde{\mathbf{u}}_2^{(2)*}\right)\right] \\
&- \frac{1}{2}\mathrm{De}_1\left[\tilde{\mathbf{u}}_2^{(2)*} \cdot \boldsymbol{\nabla}\tilde{\boldsymbol{\tau}}_2^{(2)} - \left({}^t\boldsymbol{\nabla}\tilde{\mathbf{u}}_2^{(2)*} \cdot \tilde{\boldsymbol{\tau}}_2^{(2)} + \tilde{\boldsymbol{\tau}}_2^{(2)} \cdot \boldsymbol{\nabla}\tilde{\mathbf{u}}_2^{(2)*}\right)\right] \\
&+ \frac{1}{2}\mathrm{De}_2\left[\tilde{\mathbf{u}}_3^{(1)*} \cdot \boldsymbol{\nabla}\tilde{\dot{\boldsymbol{\gamma}}}_1 - \left({}^t\boldsymbol{\nabla}\tilde{\mathbf{u}}_3^{(1)*} \cdot \tilde{\dot{\boldsymbol{\gamma}}}_1 + \tilde{\dot{\boldsymbol{\gamma}}}_1 \cdot \boldsymbol{\nabla}\tilde{\mathbf{u}}_3^{(1)*}\right)\right] \\
&- \frac{1}{2}\mathrm{De}_1\left[\tilde{\mathbf{u}}_3^{(1)*} \cdot \boldsymbol{\nabla}\tilde{\boldsymbol{\tau}}_1 - \left({}^t\boldsymbol{\nabla}\tilde{\mathbf{u}}_3^{(1)*} \cdot \tilde{\boldsymbol{\tau}}_1 + \tilde{\boldsymbol{\tau}}_1 \cdot \boldsymbol{\nabla}\tilde{\mathbf{u}}_3^{(1)*}\right)\right]. \qquad (6.32)
\end{aligned}$$

As done previously, we take the divergence and then curl of Eq. (6.32), and invoke the lower-order constitutive relations Eqs. (6.12), (6.18) and (6.25), to obtain the equation for streamfunction of the average flow

$$\boldsymbol{\nabla}^4\tilde{\Psi}_4^{(0)} = \beta\frac{A_4\sin 2\theta + B_4\cos 2\theta + C_4\sin 4\theta}{r^2}, \qquad (6.33)$$

where

$$\beta = \frac{\mathrm{De}_2 - \mathrm{De}_1}{2(1+De_1^2)(2\mathrm{De}_1 - i)}, \qquad (6.34)$$

$$A_4 = 8\alpha - \mathrm{De}_1 + 8i\alpha\mathrm{De}_1 + 4i\mathrm{De}_1^2 + 16\alpha\mathrm{De}_1^2, \qquad (6.35)$$

$$B_4 = 2\pi\left(1 + i\mathrm{De}_1 + 2\mathrm{De}_1^2)(\alpha + \alpha^*\right), \qquad (6.36)$$

$$\begin{aligned}
C_4 = -2\big(&8\alpha + 8i\alpha\mathrm{De}_1 + 3i\mathrm{De}_1^2 + 16\alpha\mathrm{De}_1^2 \\
&+ 4\alpha^* + 4i\mathrm{De}_1\alpha^* + 8\mathrm{De}_1^2\alpha^*\big). \qquad (6.37)
\end{aligned}$$

Boundary conditions

At $\theta = \pi/2$, the boundary condition at this order is written as

$$\mathbf{u}_4 = -\Theta\frac{\partial\mathbf{u}_3}{\partial\theta} - \frac{1}{2}\Theta^2\frac{\partial^2\mathbf{u}_2}{\partial\theta^2} - \frac{1}{6}\Theta^3\frac{\partial^3\mathbf{u}_1}{\partial\theta^3} + \frac{1}{6}r\dot{\Theta}\Theta^3\langle\mathbf{t}\rangle, \qquad (6.38)$$

which we then Fourier-transform to obtain the boundary condition for $\tilde{\mathbf{u}}_4^{(0)}$. In addition, since we are only interested in the time-averaged flow, *i.e.*, real part of

the solution $\mathrm{Re}\{\tilde{\mathbf{u}}_4^{(0)}\}$, the boundary condition at $\theta = \pi/2$ can be simplified as

$$\mathrm{Re}\{\tilde{\mathbf{u}}_4^{(0)}\} = \frac{r\,(8-\pi^2)}{8}\mathrm{Re}\{\alpha\}\langle \mathbf{t}\rangle, \tag{6.39}$$

where

$$\mathrm{Re}\{\alpha\} = \frac{-3\mathrm{De}_1(\mathrm{De}_1-\mathrm{De}_2)(\mathrm{De}_1+\mathrm{De}_2+2\mathrm{De}_1^2\mathrm{De}_2)}{8(1+\mathrm{De}_1^2)(1+4\mathrm{De}_1^2)(1+\mathrm{De}_2^2)}. \tag{6.40}$$

Finally, as usual, we have the no-slip and no-penetration boundary conditions at $\theta = 0$.

Solution

Solving the inhomogeneous biharmonic equation with the boundary conditions above, we obtain our main result, namely the analytical formula for the time-averaged flow as

$$\begin{aligned}\mathrm{Re}\left\{\tilde{\Psi}_4^{(0)}\right\} =& \frac{r^2\mathrm{De}_1\left(\mathrm{De}_1-\mathrm{De}_2\right)\left(2\mathrm{De}_2\mathrm{De}_1^2+\mathrm{De}_1+\mathrm{De}_2\right)}{512\left(\mathrm{De}_1^2+1\right)^2\left(4\mathrm{De}_1^2+1\right)\left(\mathrm{De}_2^2+1\right)} \\ &\Big[32\pi-3\pi^3+8\pi\mathrm{De}_1\mathrm{De}_2-3\pi^3\mathrm{De}_1\mathrm{De}_2+24\pi\mathrm{De}_1^2+4\theta\big(-20+3\pi^2 \\ &-12\mathrm{De}_1^2-8\mathrm{De}_1\mathrm{De}_2+3\pi^2\mathrm{De}_1\mathrm{De}_2\big)+\sin 4\theta\left(-4-12\mathrm{De}_1^2+8\mathrm{De}_1\mathrm{De}_2\right) \\ &+\cos 2\theta(-32\pi+3\pi^3+48\theta-24\pi\mathrm{De}_1^2+48\theta\mathrm{De}_1^2-8\pi\mathrm{De}_1\mathrm{De}_2 \\ &+3\pi^3\mathrm{De}_1\mathrm{De}_2)+\sin 2\theta(24-6\pi^2+24\mathrm{De}_1^2-24\pi\theta\mathrm{De}_1^2-6\pi^2\mathrm{De}_1\mathrm{De}_2 \\ &+24\pi\theta\mathrm{De}_1\mathrm{De}_2)\Big]\cdot\end{aligned} \tag{6.41a}$$

$$\begin{aligned}\mathrm{Re}\left\{\tilde{u}_{4r}^{(0)}\right\} =& \frac{r\mathrm{De}_1\left(\mathrm{De}_2-\mathrm{De}_1\right)\left(2\mathrm{De}_2\mathrm{De}_1^2+\mathrm{De}_1+\mathrm{De}_2\right)}{256\left(\mathrm{De}_1^2+1\right)^2\left(4\mathrm{De}_1^2+1\right)\left(\mathrm{De}_2^2+1\right)} \\ &\Big[40-6\pi^2+24\mathrm{De}_1^2+16\mathrm{De}_1\mathrm{De}_2-6\pi^2\mathrm{De}_1\mathrm{De}_2+\cos 4\theta(8+24\mathrm{De}_1^2 \\ &-16\mathrm{De}_1\mathrm{De}_2)+\sin 2\theta(-32\pi+3\pi^3+48\theta-12\pi\mathrm{De}_1^2+48\theta\mathrm{De}_1^2 \\ &-20\pi\mathrm{De}_1\mathrm{De}_2+3\pi^3\mathrm{De}_1\mathrm{De}_2)+\cos 2\theta(-48+6\pi^2-48\mathrm{De}_1^2+24\pi\theta\mathrm{De}_1^2 \\ &+6\pi^2\mathrm{De}_1\mathrm{De}_2-24\pi\theta\mathrm{De}_1\mathrm{De}_2)\Big]\cdot\end{aligned} \tag{6.41b}$$

$$\mathrm{Re}\left\{\tilde{u}_{4\theta}^{(0)}\right\} = \frac{r\mathrm{De}_1\left(\mathrm{De}_2-\mathrm{De}_1\right)\left(2\mathrm{De}_2\mathrm{De}_1^2+\mathrm{De}_1+\mathrm{De}_2\right)}{256\left(\mathrm{De}_1^2+1\right)^2\left(4\mathrm{De}_1^2+1\right)\left(\mathrm{De}_2^2+1\right)}$$
$$\Big[32\pi-3\pi^3+8\pi\mathrm{De}_1\mathrm{De}_2-3\pi^3\mathrm{De}_1\mathrm{De}_2+24\pi\mathrm{De}_1^2+4\theta\big(-20+3\pi^2$$
$$-12\mathrm{De}_1^2-8\mathrm{De}_1\mathrm{De}_2+3\pi^2\mathrm{De}_1\mathrm{De}_2\big)+\sin 4\theta\left(-4-12\mathrm{De}_1^2+8\mathrm{De}_1\mathrm{De}_2\right)$$
$$+\cos 2\theta(-32\pi+3\pi^3+48\theta-24\pi\mathrm{De}_1^2+48\theta\mathrm{De}_1^2-8\pi\mathrm{De}_1\mathrm{De}_2$$
$$+3\pi^3\mathrm{De}_1\mathrm{De}_2)+\sin 2\theta(24-6\pi^2+24\mathrm{De}_1^2-24\pi\theta\mathrm{De}_1^2-6\pi^2\mathrm{De}_1\mathrm{De}_2$$
$$+24\pi\theta\mathrm{De}_1\mathrm{De}_2)\Big]. \qquad (6.41c)$$

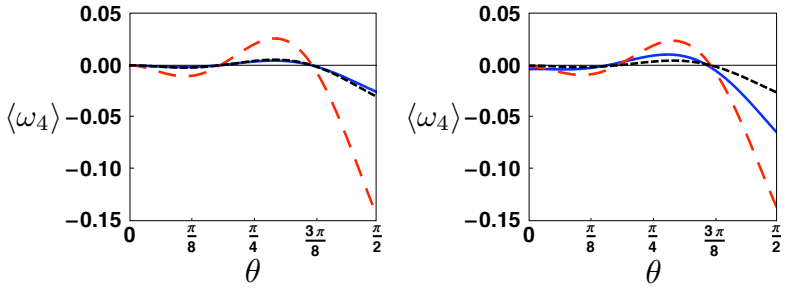

Figure 6.2: Time-averaged vorticity, $\langle\omega_4\rangle$, as a function of polar angle θ. (a): Fixed Deborah number (De = 100) and $\eta_s/\eta = 0.1$ (blue solid line), 0.01 (red dashed lines) and 0.001 (black dotted line); (b): Fixed relative viscosity ($\eta_s/\eta = 0.1$) and De = 1 (blue solid line), 10 (red dashed line), and 100 (black dotted line).

6.4 Characterization of the time-averaged flow

In the analysis above, we have computed the flow field perturbatively up to order $O(\epsilon^4)$ and found that a nonzero time-averaged flow occurs at that order, as described by Eq. (6.41). Hereafter, for convenience, we rewrite the two Deborah numbers as $\mathrm{De}_1 = \mathrm{De}$ and $\mathrm{De}_2 = \mathrm{De}\zeta$, where $\zeta = \eta_s/\eta$ is the relative viscosity of the solvent vs. total fluid. The creation of a net flow by the tethered flapping motion demonstrates explicitly that Purcell's scallop theorem breaks down in a viscoelastic fluid. This suggests that reciprocal flapping-like motion can be exploited for pumping polymeric fluids in simple geometries even in the absence of inertia – a situation which is impossible in Newtonian fluids. In the following sections, we explore the properties of this time-average flow and its dependance on both the

actuation frequency and material properties of the fluid.

6.4.1 Streamline and vorticity pattern

With the streamfunction explicitly calculated, we can easily compute the flow streamlines, as well as the flow vorticity, given by $\langle\omega_4\rangle = -\boldsymbol{\nabla}^2\langle\Psi_4\rangle$, or

$$\begin{aligned}\langle\omega_4\rangle =& \frac{\mathrm{De}^3(1-\zeta)\left(1+\zeta+2\mathrm{De}^2\zeta\right)}{128\left(1+\mathrm{De}^2\right)^2\left(1+4\mathrm{De}^2\right)\left(1+\mathrm{De}^2\zeta^2\right)} \\ & \Big[-32\pi-24\mathrm{De}^2\pi+3\pi^3-8\mathrm{De}^2\pi\zeta+3\mathrm{De}^2\pi^3\zeta \\ & -4\left(-20-12\mathrm{De}^2+3\pi^2-8\mathrm{De}^2\zeta+3\mathrm{De}^2\pi^2\zeta\right)\theta \\ & +\left(24\mathrm{De}^2\pi-24\mathrm{De}^2\pi\zeta\right)\cos 2\theta+\left(48+48\mathrm{De}^2\right)\sin 2\theta \\ & +\left(-12-36\mathrm{De}^2+24\mathrm{De}^2\zeta\right)\sin 4\theta\Big]. \end{aligned} \tag{6.42}$$

We see that the vorticity is only a function of the polar angle θ between the wall and the flapper. The vorticity is plotted as a function of the angle θ in Fig. 6.2 for different relative viscosities (Fig. 6.2a) and different Deborah numbers (Fig. 6.2b). The locations where the vorticity changes its sign are apparently invariant and occur around $\theta \approx 3\pi/16$ (from negative to positive) and $\theta \approx 3\pi/8$ (from positive to negative). The streamline pattern and vorticity distribution are also qualitatively similar for different Deborah numbers and relative viscosities, as illustrated in Fig. 6.3 for different Deborah numbers ($\mathrm{De} = 1$ and $\mathrm{De} = 100$) at a fixed relative viscosity of 0.1. It can be noted that, keeping the relative viscosity fixed, increasing the Deborah number leads to more inclined streamlines (greater vertical velocity components) near the flat wall ($\theta = 0$).

6.4.2 Directionality of the flow

As shown from the arrows in the streamline pattern in Fig. 6.3, the flapping motion draws the polymeric fluid towards the hinge point at an acute angle, and pumps the fluid away from the hinge point along both the flat wall and the average flapper position. To illustrate this directionality further, we plot in Fig. 6.4 the radial velocity per unit radius against the polar angle for different relative viscosities (Fig. 6.4a) and Deborah numbers (Fig. 6.4b). Again, the locations where the

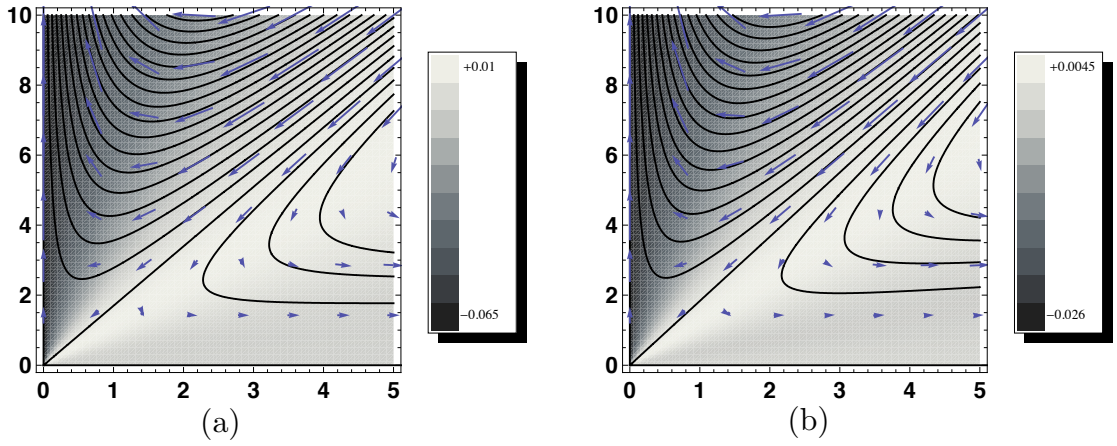

Figure 6.3: Streamline and vorticity pattern for $\eta_s/\eta = 0.1$; (a): De $= 1$; (b): De $= 100$. The grayscale map displays the value of the vorticity, with legend shown on the right of each plot.

radial velocity changes its sign are apparently invariant under the change of relative viscosity or Deborah number, and occur around $\theta \approx \pi/4$ (positive to negative) and $\theta \approx 7\pi/16$ (negative to positive).

6.5 Optimization

Having identified the basic flow patterns generated by the flapping motion, we now turn to a possible optimization of the pumping performance. Specifically, we address the question: what is the optimal Deborah number at which the largest flow can be generated? Since different optimality criteria can be defined, we consider here three different "optimality measures" for the net flow, and show they all generate essentially the same conclusion.

Flow along the boundary

Since the flapping motion pumps the fluid away from the hinge point along the average flapper position, one natural measure of the pumping performance is the magnitude of flow along the average flapper position ($\theta = \pi/2$). Note that the velocity field is directly proportional to the radius, and recall that the velocity is only radial along the average flapper position as required by symmetry. Consequently, the dependence of the intrinsic flow strength upon the Deborah

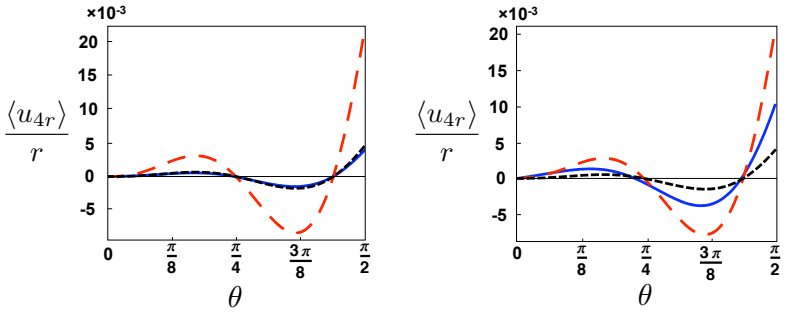

Figure 6.4: Net flow velocity along the average flapper position, $\langle u_{4r}\rangle/r$, as a function of the polar angle θ. (a): fixed Deborah number (De = 100) and $\eta_s/\eta =$ 0.1 (blue solid line), 0.01 (red dashed line) and 0.001 (black dotted line); (b) fixed relative viscosity ($\eta_s/\eta = 0.1$) and De = 1 (blue solid line), 10 (red dashed line), and 100 (black dotted line).

number can be characterized by the ratio between the radial velocity along the average flapper position and the radial distance,

$$\begin{aligned} U_b\left(\mathrm{De},\zeta\right) &= \frac{\langle u_{4r}\rangle(r,\theta=\pi/2)}{r} \\ &= \frac{3\mathrm{De}^3\left(\pi^2-8\right)\left(1-\zeta\right)\left(1+\zeta+2\mathrm{De}^2\zeta\right)}{64\left(1+5\mathrm{De}^2+4\mathrm{De}^4\right)\left(1+\mathrm{De}^2\zeta^2\right)}, \end{aligned} \tag{6.43}$$

which is plotted for different relative viscosities in Fig. 6.5a. From Eq. (6.43), we see that for small values of De, $U_b \sim \mathrm{De}^3$, whereas for large values of De, $U_b \sim 1/\mathrm{De}$, and therefore an optimal Deborah number is expected to exist. This is confirmed in Fig. 6.5a, where we see that for each value of the relative viscosity, there is an optimal value of the Deborah number where the flow along the boundary is maximal. For small relative viscosities, we note the presence of two local peaks (in contrast, only one exists for $\eta_s/\eta = 10^{-1}$). Physically, by decreasing the relative viscosity, we are varying the retardation time of the fluid, while keeping the relaxation time fixed. The position of the second peak changes correspondingly and commensurately when the relative viscosity is varied by orders of magnitude, while the position the first peak is unchanged. When the relative viscosity is set to zero (zero retardation time, which is a singular limit), we see in Fig. 6.5a a single peak at essentially the same Deborah number as before. From these observations, we deduce that the two local optimal Deborah numbers arise from two different properties of the fluid, respectively relaxation and retardation. For small relative

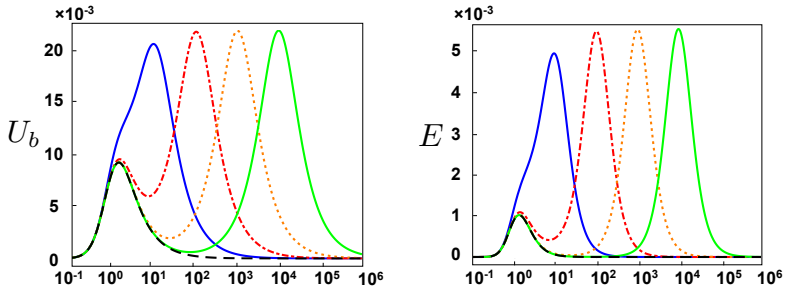

Figure 6.5: Dependence of pumping performance with the Deborah number, for two different pumping measures. (a): Reduced flow velocity along the average flapper position, U_b; (b): Reduced kinetic energy, E. For both cases: $\eta_s/\eta = 0.1$ (left solid line, blue); $\eta_s/\eta = 0.01$ (red dot-dashed line); $\eta_s/\eta = 0.001$ (orange dotted line); $\eta_s/\eta = 0.0001$ (right solid line, green); $\eta_s/\eta = 0$ (black dashed line).

viscosities, the small local optimal Deborah number can be attributed to relaxation while the larger local optimal Deborah number can be attributed to retardation, and it disappears in the singular (and unphysical) limit of zero retardation.

Kinetic energy

Another possible optimization measure is related to the total kinetic energy of the average flow. Since the velocity field is directly proportional to the radius, it takes the general form $\langle u_{4r} \rangle = r f(\theta)$ and $\langle u_{4\theta} \rangle = r g(\theta)$, where the functions $f(\theta)$ and $g(\theta)$ can be found from Eq. (6.41). Therefore, the dependence of the total kinetic energy of the average flow upon the Deborah number can be characterized by a reduced energy given by the integral over the polar angle

$$E(\mathrm{De}, \zeta) = \int_0^{\pi/2} [f(\theta)]^2 + [g(\theta)]^2 \, d\theta, \tag{6.44}$$

and is given analytically by

$$\begin{aligned}E(\mathrm{De},\zeta) =& \frac{\mathrm{De}^6\pi(-1+\zeta)^2\left(1+\zeta+2\mathrm{De}^2\zeta\right)^2}{98304\left(1+\mathrm{De}^2\right)^4\left(1+4\mathrm{De}^2\right)^2\left(1+\mathrm{De}^2\zeta^2\right)^2} \\ & \Big[-2074-4028\mathrm{De}^2-2058\mathrm{De}^4+1054\pi^2+858\mathrm{De}^2\pi^2-144\mathrm{De}^4\pi^2 \\ & -174\pi^4-45\mathrm{De}^2\pi^4+36\mathrm{De}^4\pi^4+9\pi^6-120\mathrm{De}^2\zeta+88\mathrm{De}^4\zeta \\ & +1250\mathrm{De}^2\pi^2\zeta+1146\mathrm{De}^4\pi^2\zeta-303\mathrm{De}^2\pi^4\zeta-117\mathrm{De}^4\pi^4\zeta \\ & +18\mathrm{De}^2\pi^6\zeta-104\mathrm{De}^4\zeta^2+52\mathrm{De}^4\pi^2\zeta^2-93\mathrm{De}^4\pi^4\zeta^2+9\mathrm{De}^4\pi^6\zeta^2\Big].\end{aligned} \tag{6.45}$$

With a fixed relative viscosity, for small values of De, we have $E \sim \mathrm{De}^6$, whereas $E \sim 1/\mathrm{De}^2$ for large values of De, so an optimal De should exist. The function $E(\mathrm{De},\zeta)$ is plotted for different values of the relative viscosity in Fig. 6.5b, and similarly to the previous section we see indeed the existence of an optimal value of De for each ζ.

Enstrophy

Finally, we also consider the dependence of the enstrophy of the flow upon the Deborah number. The total enstrophy of the flow is proportional to the integral

$$\mathcal{E}(\mathrm{De},\zeta) = \int_0^{\pi/2} \omega_4^2 d\theta, \tag{6.46}$$

which can be analytically calculated to be

$$\begin{aligned}\mathcal{E} =& \frac{\mathrm{De}^6\pi(-1+\zeta)^2\left(1+\zeta+2\mathrm{De}^2\zeta\right)^2}{98304\left(1+\mathrm{De}^2\right)^4\left(1+4\mathrm{De}^2\right)^2\left(1+\mathrm{De}^2\zeta^2\right)^2} \\ & \Big[-1800-14256\mathrm{De}^2-12744\mathrm{De}^4+616\pi^2+2424\mathrm{De}^2\pi^2+1440\mathrm{De}^4\pi^2 \\ & -120\pi^4-72\mathrm{De}^2\pi^4+9\pi^6+10656\mathrm{De}^2\zeta+11232\mathrm{De}^4\zeta-1192\mathrm{De}^2\pi^2\zeta \\ & -456\mathrm{De}^4\pi^2\zeta-168\mathrm{De}^2\pi^4\zeta-72\mathrm{De}^4\pi^4\zeta+18\mathrm{De}^2\pi^6\zeta-288\mathrm{De}^4\zeta^2 \\ & -368\mathrm{De}^4\pi^2\zeta^2-48\mathrm{De}^4\pi^4\zeta^2+9\mathrm{De}^4\pi^6\zeta^2\Big].\end{aligned} \tag{6.47}$$

The variation of $\mathcal{E}$ with De turns out to be very similar to the one for E (Eq. 6.45, shown in Fig. 6.5b), and is not reproduced here.

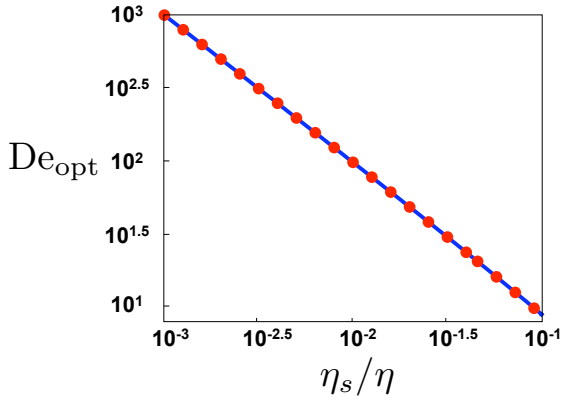

Figure 6.6: Optimal Deborah number, $\mathrm{De}_{\mathrm{opt}}$, as a function of relative viscosity, η_s/η, by optimizing (a) the flow along the average position of the flapper $\theta = \pi/2$ (blue solid line) and (b) the flow kinetic energy (red dots).

Optimal Deborah number

We next compute numerically the optimal Deborah number, maximizing the pumping measures in both Eqs. (6.43) and (6.45), as a function of the relative viscosity. The results are displayed in Fig. 6.6. The optimality conditions turn out to quantitatively agree for both pumping measures, and correspond to an inverse linear relationship between $\mathrm{De}_{\mathrm{opt}}$ and ζ. This scaling is confirmed by an asymptotic analysis of the exact analytical formula for $\mathrm{De}_{\mathrm{opt}}$ found by setting the partial derivative of Eq. (6.43) to zero, and showing that indeed $\mathrm{De}_{\mathrm{opt}} \sim 1/\zeta$ for small values of ζ.

6.6 Discussion

In this chapter, we have considered what is arguably the simplest geometrical setup to demonstrate that net fluid pumping can be obtained from the purely sinusoidal forcing of a viscoelastic fluid. The fluid was modeled as an Oldroyd-B fluid both for simplicity and because of the physical relevance of the model. The main result we obtained is the time-averaged flow, described by Eq. (6.41), generated by the reciprocally flapping motion. In accordance with the scallop theorem, setting the Deborah number to zero in Eq. (6.41) leads to no flow, but a net flow occurs for all nonzero values of De. Our calculations allow us to demonstrate

explicitly the breaking of the scallop theorem in the context of fluid pumping, and suggest the possibility of taking advantage of the intrinsic nonlinearities of complex fluids for their transport. Physically, such flow is being driven by normal-stress differences arising in the fluid and due to the stretching of the polymeric microstructures by the background flow. The calculation was done asymptotically for small-amplitude flapping, and the net flow occurs at fourth order. As in the classic work by Moffatt [157], our results should be understood as similarity solutions which are valid close enough to the fixed hinge point such that the inertial effects are negligible. The advantage of such theoretical treatment is that it allows us to obtain the entire flow field analytically, in particular the spatial structure of the flow, and the dependance of the net pumping on the actuation parameters (the flapping frequency) and the material properties of the fluid (relaxation time and viscosities). Taking advantage of these analytical results, we have been able to analytically optimize the pumping performance, and derive the optimal Deborah number as a function of the fluid ratio of solvent to total viscosity. Although we have considered here the simplest geometrical and dynamical setup possible, the results motivate future work which will focus on the flapping of three-dimensional finite-size appendages in polymeric fluids.

We now turn to the relevance of our results to biological transport. In Newtonian fluids, only the non-reciprocal component of the motion of cilia – *i.e.* the difference between their effective and recovery strokes – affects fluid transport [17, 158]. In contrast, we show in this chapter that the back-and-forth components of cilia motion, which is reciprocal, does influence transport in the case of viscoelastic biological fluids. The effect is expected to be crucial since the typical Deborah number in ciliary transport is large, and elastic effects of the fluid are therefore likely to be significant. For example, from rheological measurements [159–161], we know the relaxation time of respiratory mucus ranges between $\lambda \approx 30 - 100$ s, and that of the cervical mucus present in female reproductive tract ranges from $\lambda \approx 1 - 100$ s [159, 162]. In addition, cilia typically oscillate at frequencies of $f = \omega/2\pi \approx 5 - 50$ Hz [17], and therefore, ciliary transport of mucus occurs at large (or very large) Deborah numbers, $\mathrm{De} = \lambda\omega \sim 10$ to 10^4.

In addition, the results of our chapter should be contrasted with previous work. It was shown in Ref. [51] that the presence of polymeric stresses leads to a

decrease of the speed at which a fluid is pumped by a waving sheet – in that case a complex fluid led therefore to a degradation of the transport performance. In contrast, we demonstrate in the current chapter a mode of actuation which is rendered effective by the presence of polymeric stresses – the complex fluid leads therefore in this case to an improvement of the transport performance. For a general actuation gait, it is therefore not known a priori whether the presence of a complex fluid will lead to a degradation or an improvement of the pumping performance, and whether or not a general classification depending on the type of actuation gait can be derived remains a question to be addressed in the future.

Chapter 6, in full, is a reprint of the material as it appears in Physical Review E 2010. Pak, On Shun; Normand, Thibaud; Lauga, Eric, the American Physical Society, 2010. The dissertation author was the primary investigator and author of this paper.

Chapter 7

Micropropulsion and microrheology in complex fluids via symmetry breaking

Many biological fluids have polymeric microstructures and display non-Newtonian rheology. We take advantage of such nonlinear fluid behavior and combine it with geometrical symmetry-breaking to design a novel small-scale propeller able to move only in complex fluids. Its propulsion characteristics are explored numerically in an Oldroyd-B fluid for finite Deborah numbers while the small Deborah number limit is investigated analytically using a second-order fluid model. We then derive expressions relating the propulsion speed to the rheological properties of the complex fluid, allowing thus to infer the normal stress coefficients in the fluid from the locomotion of the propeller. Our simple mechanism can therefore be used either as a non-Newtonian micro-propeller or as a micro-rheometer.

7.1 Introduction

The physics of low Reynolds number locomotion is relatively well explored in the Newtonian limit (see reviews in Refs. [15–18] and references therein). Beyond improving our understanding of biological processes, applications of these physical principles led to progress in the design of synthetic micro-swimmers for potential future biomedical applications [16, 20, 21, 24, 86]. In contrast, fundamental prop-

erties of life in complex, non-Newtonian, flows remain surprisingly unaddressed. Non-Newtonian flow behaviors can be appreciated through well-known manifestations from daily life, for example the climbing of dough up kitchen mixing blades (termed rod-climbing, or Weissenberg, effect) or the remarkable behavior of Silly Putty, a popular toy which bounces like a solid rubber ball when thrown to the floor but melts like a fluid when left on a surface for some time [131, 163, 164].

Many situations exist wherein microorganisms encounter biological fluids which have polymeric microstructures and non-Newtonian rheological properties. For example, spermatozoa swim through the viscoelastic cervical mucus and along the mucus-covered fallopian tubes [15, 26–28, 31, 43]; cilia lie in a layer of mucus along the human respiratory tract [165]; *Helicobacter pylori*, a bacterium causing ulcer, locomotes through mucus lining of the stomach [166]; spirochetes moves through host tissue during infection [167]; in biofilms, bacteria are embedded in cross-linked polymer gels [168–172].

Physically and mathematically, the presence of polymeric stresses in a complex fluid means that the usual properties associated with the absence of inertia in the Newtonian limit cease to be valid, in particular kinematic reversibility and the linearity of the flow equations. In return, non-Newtonian effects such as stress relaxation, normal stress differences, and shear-rate dependent viscosity manifest themselves [131, 132, 163, 164] .

Past theoretical and experimental studies have investigated the waveforms and swimming paths of microorganisms in complex fluids [15, 16, 26–28, 30, 31, 173, 174]. An active discussion in the biomechanics community has recently focused on the simple question: does fluid elasticity enhance or deteriorate propulsion at the microscopic scale? Theoretical studies on infinite models [51, 134, 175] showed that, for fixed body-frame kinematics, the propulsion speed decreases in a viscoelastic fluid. Numerical studies on a finite swimmer [176] demonstrated that the propulsion speed could be enhanced by the presence of polymeric stress for some prescribed kinematics. Experimental investigations suggested evidences for both [177, 178]. It was also shown that reciprocal actuation on a fluid, unable to provide net locomotion or flow transport in the Newtonian case, can be rendered effective by viscoelasticity [135, 136, 179]. The presence of polymeric stress has also interesting consequences on the rate of flagellar synchronization [180].

Normal stress differences in a complex fluid are responsible for a number of important non-Newtonian effects [131, 163, 164] including the rob-climbing effect mentioned above impacting many applications such as mixing, and the swelling of polymer melts when extruded from dies in manufacturing processes posing constraints on the rate of extrusion. In a pure shear flow with an arbitrary Reynolds number and a shear rate $\dot{\gamma}$, assuming that the flow is in the $x-$direction and the velocity varies in the $y-$direction, the $z-$direction being called the neutral direction [131], the first and second normal stress coefficients are defined as $\Psi_1 = (\tau_{xx} - \tau_{yy})/\dot{\gamma}^2$ and $\Psi_2 = (\tau_{yy} - \tau_{zz})/\dot{\gamma}^2$ respectively, where τ_{ij} are the components of the deviatoric stress tensor. In a Newtonian flow, there are no normal stress differences ($\Psi_1 = \Psi_2 = 0$), whereas for polymeric fluids typically $\Psi_1 > 0$ and $\Psi_2 < 0$. The magnitude of the second normal stress coefficient is usually much smaller than that of the first normal stress coefficient ($|\Psi_2| \ll \Psi_1$). In the rob-climbing phenomenon, both first and second normal stress coefficients contribute to the effect [131]. However, due to its small magnitude, the effect of the second normal stress coefficient is shadowed by that of the first normal stress difference [131]. The existence of the second normal stress difference can be demonstrated in a free-surface flow driven by gravity through a tilted trough: a Newtonian fluid has a flat free surface (with negligible meniscus effect), while the free surface of a non-Newtonian fluid becomes convex due to second normal stresses [181–183].

In this work, we propose a simple mechanism able to take advantage of the presence of normal stress differences to propel in a complex fluid. Our geometry, shown in Fig. 7.1, consists of two linked small spheres propelling under the action of an external torque, a setup we will refer to as a "snowman". Locomotion is enabled solely by the presence of normal stress differences, and no motion exists in a Newtonian environment, a fact that can in turn be used to infer the normal stress coefficients of a complex fluid. In essence, as complex fluids lead to new modes of small-scale propulsion, symmetrically the presence of propulsion in an environment can be used to locally probe the rheological properties of the fluid.

The first normal stress coefficient of a fluid can be measured directly from a conventional cone-and-plate rheometer [131, 163, 164]; the measurement of the second normal stress coefficient however has been a longstanding challenge [184–187]. A number of methods were proposed (see a review in Ref. [187]), including

a modified cone-and-plate rheometry with pressure transducers [131, 185], a subtle evaluation of a combination of cone-and-plate and parallel-plate experiments [184], rheo-optical measurements [184, 186], and the use of a cone-and-partitioned plate tool [187]. Recently, a microrheological technique was proposed to measure the first and second normal stress coefficients [188]. In microrheology, colloidal probes are either actively driven, or passively diffusing, and their dynamics allows to infer local rheological information. Microrheology enjoys many advantages over conventional macroscopic rheological measurements [189,190], including the reduction in sample size, the ability to probe spatially-inhomogeneous environments, and the possibility of performing measurements in living cells [189–192]. The mechanism we propose in this chapter would be classified as "active" microrheology, a situation where colloidal probes are actively manipulated to drive the material out of equilibrium and probe its nonlinear mechanical properties [189, 193]. We offer in this chapter an alternative microrheological technique capable of probing both first and second stress coefficients by using only kinematic measurements.

This chapter is organized as follows. In Sec. 7.2, we introduce the geometric and kinematic setup of our proposed mechanism and the polymeric fluid models adopted in our study. We first investigate in Sec. 7.3 the propulsion characteristics of the snowman in a complex fluid, followed in Sec. 7.4 by the method of inferring the normal stress coefficients from its locomotion. We then provide a qualitative, and intuitive, explanation of the locomotion enabled by normal stresses in Sec. 7.5 before concluding the chapter in Sec. 7.6.

7.2 Setup

7.2.1 Kinematics

By symmetry, the rotation of a single sphere in any homogeneous fluid produces no net locomotion. Inserting a second sphere, of different size, breaks the geometrical symmetry and can potentially allow locomotion. We first consider the rotation of two unequal spheres touching each other as a single rigid body (see the geometry and notations in Fig. 7.1), the "snowman" geometry. We label the line of centers of the spheres as the z-axis. Without loss of generality, we assume the

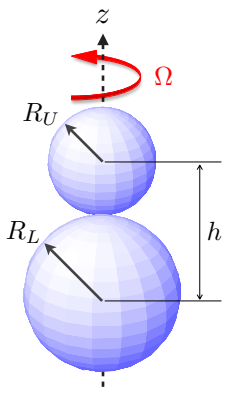

Figure 7.1: Geometrical setup of two spheres ("snowman") rotating with angular velocity Ω along their separation axis. The radii of the upper and lower spheres are denoted by R_U and R_L respectively. The centers of the spheres are separated by a distance, h (for touching spheres, $h = R_U + R_L$).

radius of the upper sphere (R_U) is smaller than that of the lower sphere ($R_L \geq R_U$). The distance between the centers of the spheres is denoted by h. For the case of touching spheres, we thus have $h = R_U + R_L$.

From a kinematic standpoint we assume that the rigid body rotates with a steady angular velocity about the z-axis, $\mathbf{\Omega} = (0, 0, \Omega > 0)$, but is otherwise free to move. Given that the snowman is axisymmetric, the only direction it could potentially move is the z-direction. We assume the net hydrodynamic force acting on the snowman is zero for all times (free-swimming condition), and aim at computing the rigid body (swimming) velocity necessary to maintain force-free motion.

In a Newtonian fluid without inertia, it is straightforward to show using kinematic reversibility and reflection symmetry that a rotating snowman cannot swim – a result true for any degree of geometrical asymmetry. The central question at the heart of this chapter is: Can elasticity of the fluid enable propulsion of the snowman? We answer this question in the following sections by studying the locomotion of a rotating snowman in polymeric fluids described by the two constitutive relations.

7.2.2 Polymeric fluid dynamics

We consider an incompressible low-Reynolds-number flow in a complex fluid. Denoting the velocity field as $\mathbf{u}$ and the fluid stress as $\boldsymbol{\sigma} = -p\mathbf{I} + \boldsymbol{\tau}$, where p is the pressure, and $\boldsymbol{\tau}$ is the deviatoric stress tensor, the conservation of mass and momentum are given by the continuity equation and Cauchy's equation of motion respectively

$$\boldsymbol{\nabla} \cdot \mathbf{u} = 0, \tag{7.1}$$

$$\boldsymbol{\nabla} \cdot \boldsymbol{\sigma} = 0. \tag{7.2}$$

For closure, we require a constitutive equation relating the deviatoric stresses $\boldsymbol{\tau}$ to the kinematics of the flow. Obviously a large number of models have been proposed in the past to describe polymeric fluids. In this work two constitutive equations are used to study the viscoelastic locomotion of a snowman.

Oldroyd-B fluid

The classical Oldroyd-B constitutive equation is arguably the most famous constitutive model for polymeric fluids [131, 132, 163, 164]. It has a sound physical origin and can be derived from a kinetic theory of polymers in the dilute limit by modeling polymeric molecules as linearly elastic dumbbells. The predictions also agree well with experimental measurements up to order one Weissenberg numbers, although it is known to suffer deficiencies for larger values [131, 132, 163, 164]. In an Oldroyd-B fluid, the deviatoric stress is the sum of two components, $\boldsymbol{\tau} = \boldsymbol{\tau}^s + \boldsymbol{\tau}^p$, where $\boldsymbol{\tau}^s$ and $\boldsymbol{\tau}^p$ denote, respectively, the Newtonian solvent contribution and polymeric contribution to the stress. The constitutive relation for the Newtonian contribution is given by $\boldsymbol{\tau}^s = \eta_s \dot{\boldsymbol{\gamma}}$, where $\dot{\boldsymbol{\gamma}} = \boldsymbol{\nabla}\mathbf{u} + \boldsymbol{\nabla}\mathbf{u}^T$ is the rate of strain tensor and η_s is the solvent contribution to the viscosity. The momentum equation can thus be written as

$$-\boldsymbol{\nabla} p + \eta_s \boldsymbol{\nabla} \cdot \dot{\boldsymbol{\gamma}} + \boldsymbol{\nabla} \cdot \boldsymbol{\tau}^p = 0, \tag{7.3}$$

The polymeric stress $\boldsymbol{\tau}^p$ is then assumed to be governed by the upper-convected Maxwell equation

$$\boldsymbol{\tau}^p + \lambda \overset{\triangledown}{\boldsymbol{\tau}^p} = \eta_p \dot{\boldsymbol{\gamma}}, \tag{7.4}$$

where λ is the polymeric relaxation time and η_p is the polymer contribution to the viscosity [131, 163, 164]. The upper-convected derivative for a tensor $\mathbf{A}$ is defined as

$$\overset{\triangledown}{\mathbf{A}} = \frac{\partial \mathbf{A}}{\partial t} + \mathbf{u} \cdot \boldsymbol{\nabla} \mathbf{A} - (\boldsymbol{\nabla} \mathbf{u}^T \cdot \mathbf{A} + \mathbf{A} \cdot \boldsymbol{\nabla} \mathbf{u}), \tag{7.5}$$

which calculates the rate of change of $\mathbf{A}$ while translating and deforming with the fluid.

Combining the Newtonian and polymeric constitutive relations, we obtain the Oldroyd-B constitutive equation for the total stress, $\boldsymbol{\tau}$, as

$$\boldsymbol{\tau} + \lambda \overset{\triangledown}{\boldsymbol{\tau}} = \eta(\dot{\boldsymbol{\gamma}} + \lambda_2 \overset{\triangledown}{\dot{\boldsymbol{\gamma}}}), \tag{7.6}$$

where the total viscosity is given by $\eta = \eta_s + \eta_p$, and $\lambda_2 = \lambda\zeta$ denote the retardation times (we define the relative viscosity $\zeta = \eta_s/\eta < 1$). For steady shear of an Oldroyd-B fluid, both the viscosity and the first normal stress coefficient are constant, and the second normal stress coefficient is zero [131]. The Oldroyd-B fluid is the model we will use for our numerical approach.

Second-order fluid

For slow and slowly varying flows, the second-order fluid model applies. It is the first non-Newtonian term in a systematic asymptotic expansion of the relationship between the stress and the rate of strain tensors called the retarded-motion expansion. It describes small departures from Newtonian fluid behavior, and the instantaneous constitutive equation is given in this model by

$$\boldsymbol{\tau} = \eta\dot{\boldsymbol{\gamma}} - \frac{1}{2}\Psi_1 \overset{\triangledown}{\dot{\boldsymbol{\gamma}}} + \Psi_2(\dot{\boldsymbol{\gamma}} \cdot \dot{\boldsymbol{\gamma}}), \tag{7.7}$$

where Ψ_1 and Ψ_2 are the first and second normal stress coefficients respectively. Note that if $\lambda = 0$ while $\lambda_2 \neq 0$ in the Oldroyd-B model, Eq. (7.6), it reduces to a second-order fluid with a vanishing second normal stress coefficient ($\Psi_2 = 0$) [131]. The second-order fluid model will enable us to derive theoretically the behavior of the snowman for small deformations.

7.2.3 Non-dimensionalization

We non-dimensionalize lengths by the radius of the lower sphere R_L, times by $1/\Omega$, and use the total fluid viscosity, η, to provide the third fundamental

unit. Hence, velocities, shear rates, and stresses are scaled by $R_L\Omega$, Ω, and $\eta\Omega$ respectively. The dimensionless radius of the upper sphere becomes then $r^* = R_U/R_L$ while the lower sphere has now radius 1. We have $h^* = h/R_L$ denoting the dimensionless distance between the centers of the sphere ($h^* = 1 + r^*$ for two touching spheres). Both spheres rotate at the same dimensionless unit speed, $\Omega^* = 1$. The starred variables represent dimensionless variables in this chapter. The Deborah number [131, 163, 164], $\mathrm{De} = \lambda\Omega$, is a dimensionless number defined as the ratio of a characteristic time scale of the fluid (the polymeric relaxation time, λ) to a characteristic time scale of the flow system ($1/\Omega$), and appears in the dimensionless momentum equation and upper-convected Maxwell equation

$$-\boldsymbol{\nabla} p^* + \zeta \boldsymbol{\nabla} \cdot \dot{\boldsymbol{\gamma}}^* + \boldsymbol{\nabla} \cdot \boldsymbol{\tau}^{p*} = 0, \tag{7.8}$$

$$\boldsymbol{\tau}^{p*} + \mathrm{De}\, \overset{\triangledown}{\boldsymbol{\tau}}^{p*} = (1-\zeta)\, \dot{\boldsymbol{\gamma}}^*. \tag{7.9}$$

The limit $\mathrm{De} = 0$ corresponds to a Newtonian fluid.

The upper-convected Maxwell equation of the polymeric stress, Eq. (7.9), can be combined with the constitutive relation of the Newtonian contribution to obtain the dimensionless Oldroyd-B constitutive equation for the total stress $\boldsymbol{\tau}^*$ as

$$\boldsymbol{\tau}^* + \mathrm{De}\, \overset{\triangledown}{\boldsymbol{\tau}}^* = \dot{\boldsymbol{\gamma}}^* + \mathrm{De}_2\, \overset{\triangledown}{\dot{\boldsymbol{\gamma}}}^*, \tag{7.10}$$

where we have defined another Deborah number, De_2, in terms of the retardation time, $\mathrm{De}_2 = \lambda_2\Omega = \mathrm{De}\zeta$.

The dimensionless constitutive relation for a second-order fluid is now given by

$$\boldsymbol{\tau}^* = \dot{\boldsymbol{\gamma}}^* - \mathrm{De}_{\mathrm{so}} \left(\overset{\triangledown}{\dot{\boldsymbol{\gamma}}}^* + B \dot{\boldsymbol{\gamma}}^* \cdot \dot{\boldsymbol{\gamma}}^* \right), \tag{7.11}$$

where we have defined another Deborah number for the second-order fluid, namely $\mathrm{De}_{\mathrm{so}} = \Psi_1\Omega/2\eta$, and $B = -2\Psi_2/\Psi_1 \geq 0$.

Importantly, we note that the definition of the Deborah number of an Oldroyd-B fluid is different from that of a second-order fluid, because the relaxation time of an Oldroyd-B fluid is defined only by the polymer, whereas the relaxation time of a second-order is defined by both the polymer and the solvent [194]. The two Deborah numbers are related by the relation $\mathrm{De}_{\mathrm{so}} = \mathrm{De}(1-\zeta)$. We shall mostly

use the Deborah number defined for an Oldroyd-B fluid (De) for the presentation of our final results, since we feel it is the one with the most intuitive definition. The Oldroyd-B equation is valid up to moderate De, and the second order fluid is valid for small De (or $\mathrm{De_{so}}$), and we thus expect the results from both models to match when De (or $\mathrm{De_{so}}$) is sufficiently small.

7.3 Propulsion of snowman in a complex fluid

As argued in Sec. 7.2.1, asymmetry alone does not lead to net locomotion upon rotating a snowman in a Newtonian fluid. We now explore the effects of fluid elasticity on the propulsion of a snowman: Does it even move? Which direction does it go? And how fast? Using the Oldroyd-B fluid model, we first explore numerically the propulsion characteristics of the snowman from small to moderate Deborah numbers. Next, the small De limit is studied analytically via the second-order fluid model.

7.3.1 Moderate Deborah number

We employed a finite element model to compute the polymeric flow as described by Eqs. (7.8) and (7.9). A formulation called the Discrete Elastic-Viscous Split Stress (DEVSS-G) [195, 196] is implemented here to improve numerical stability. The momentum equation, Eq. (7.8), is rewritten as

$$\boldsymbol{\nabla}\cdot\mu_a(\boldsymbol{\nabla}\mathbf{u}^*+\boldsymbol{\nabla}\mathbf{u}^{*T})-\boldsymbol{\nabla}p^*+\boldsymbol{\nabla}\cdot\boldsymbol{\tau}^{p*}-\boldsymbol{\nabla}\cdot(\mu_a-\zeta)(\mathbf{G}+\mathbf{G}^T)=0, \qquad (7.12)$$

where the tensor $\mathbf{G}\equiv\boldsymbol{\nabla}\mathbf{u}^*$ is introduced as a finite element approximation of the velocity gradient tensor $\boldsymbol{\nabla}\mathbf{u}^*$. An additional elliptic term, $\boldsymbol{\nabla}\cdot\mu_a(\boldsymbol{\nabla}\mathbf{u}^*+\boldsymbol{\nabla}\mathbf{u}^{*T})-\boldsymbol{\nabla}\cdot\mu_a(\mathbf{G}+\mathbf{G}^T)$, is added into the momentum equation for stabilization [197]. In the limit that the mesh size in the finite element approximation tends to zero, $\mathbf{G}$ approaches $\boldsymbol{\nabla}\mathbf{u}^*$ and the elliptic term vanishes, reducing Eq. (7.12) to Eq. (7.8). $\mathbf{G}$ is also used to approximate the velocity gradient term $\boldsymbol{\nabla}\mathbf{u}^*$ in the constitutive equation, Eq. (7.9). For simulations in this work, we choose $\mu_a = 1$ as in Liu *et al.* [196].

A Galerkin method is used to discretize the momentum equations, continuity equation, and the equation for the additional unknown $\mathbf{G}$. Quadratic ele-

ments are used for $\mathbf{u}^*$ and linear elements for both p^* and $\mathbf{G}$. The streamline-upwind/Petrov-Galerkin(SUPG) [198] method is adopted to discretize the constitutive equation, Eq. (7.9), to improve numerical stability. The resulting weak form of the model is formulated as

$$\{\mathbf{S} + \frac{h_c}{U_c}\mathbf{u}^* \cdot \nabla \mathbf{S},$$
$$\boldsymbol{\tau}^{p*} + \mathrm{De}(\mathbf{u}^* \cdot \nabla \boldsymbol{\tau}^{p*} - \mathbf{G}^T \cdot \boldsymbol{\tau}^{p*} - \boldsymbol{\tau}^{p*} \cdot \mathbf{G}) - \ (1 - \zeta\ )(\mathbf{G} + \mathbf{G}^T)\} = 0, \qquad (7.13)$$

where $\mathbf{S}$ denotes the test function for $\boldsymbol{\tau}^{p*}$, h_c is a characteristic mesh size, and U_c is the magnitude of a local characteristic velocity (we choose the norm of $\mathbf{u}^*$ as U_c). The framework for the implementation is provided by the commercial software COMSOL, which was successfully used for simulating the locomotion of squirmers in a viscoelastic fluid at low Reynolds numbers [199].

We perform three-dimensional axisymmetric simulations on a two-dimensional mesh constructed with triangle elements. Sufficiently refined mesh is generated near rotating objects to resolve the thin stress boundary layers, necessary to overcome numerical instabilities [200, 201] and improve accuracy. We validate our implementation by comparing numerical and analytical values of the hydrodynamic torque on a rotating sphere in the Newtonian fluid. For the viscoelastic model, we validate our approach against the simulations in Lunsmann *et al.* [202] of a sedimenting sphere in a tube filled with Oldroyd-B fluid and the analytical results in Bird *et al.* [131] of a rotating sphere in a second-order fluid.

Equipped with our computational model, we are able to show that fluid elasticity does indeed enable the propulsion of the snowman provided the two spheres have unequal sizes ($r^* < 1$). The snowman always swim in the positive z-direction (see Fig. 7.1), *i.e.* from the larger to the smaller sphere. For illustration, we compute the dimensionless propulsion speed, $U^* = U/R_L\Omega$, of a typical snowman ($r^* = R_U/R_L = 0.5$) as a function of the Deborah number, De (red dot-dashed line, Fig. 7.2), for a fixed relative viscosity $\zeta = 0.5$. When $\mathrm{De} = 0$, the fluid reduces to the Newtonian limit and we recover that no propulsion is possible in this case. For small values of De, the propulsion speed appears to grow linearly with De, a result confirmed analytically in the next section. A maximum swimming speed is reached at $\mathrm{De} \approx 1.75$, before decaying as De continues to increase.

In addition to the primary flow (the Newtonian component, $\mathrm{De} = 0$), elastic

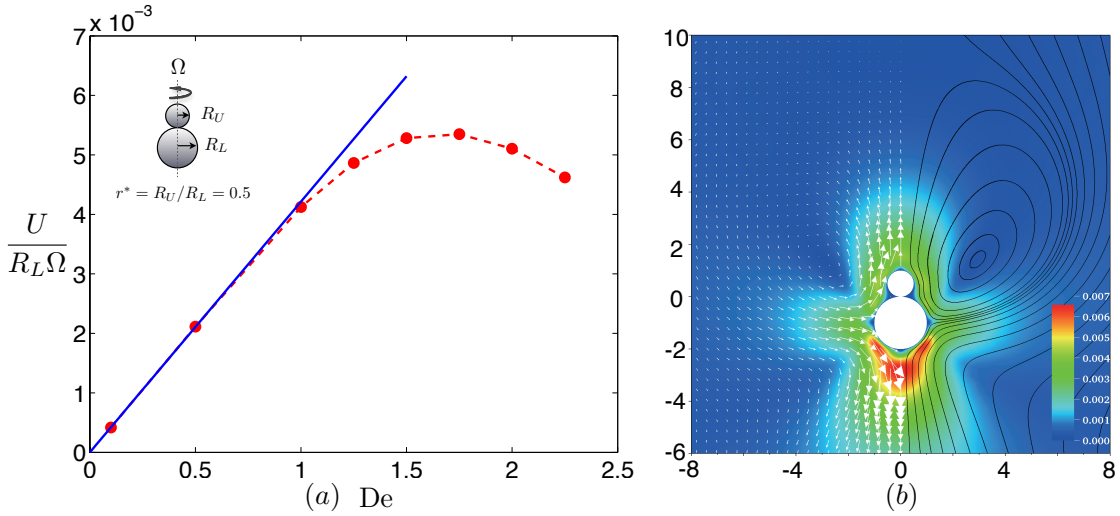

Figure 7.2: Demonstration of snowman locomotion. For a radii ratio ($r^* = R_U/R_L$) of 0.5 and $\zeta = 0.5$, we plot: (a) Dimensionless propulsion speed, $U/R_L\Omega$, as a function of the Deborah number, De. Red dot-dashed line: numerical results in an Oldroyd-B fluid; blue solid line: theoretical calculation using the reciprocal theorem in a second-order fluid, Eq. 7.36; (b) The streamline pattern and speed (shaded/color map) of the secondary flow for De = 0.1 (streamline patterns at higher De are qualitatively similar).

stresses around the snowman generate a secondary flow, understood simply as the difference between the total flow and the Newtonian component. A typical secondary flow pattern is shown in the frame of the snowman in Fig. 7.2b (De = 0.1 and $\zeta = 0.5$). We depict the velocity vectors and streamlines with the shaded/color map representing the flow speed. Fluid is drawn towards the snowman parallel to the equatorial plane and then expelled along the axis, while a ring vortex is detected in the front. The maximum speed of the secondary flow is observed at the rear of the snowman, only about 0.7% of the characteristic speed of the primary flow $R_L\Omega$.

7.3.2 Small Deborah number

To provide a theoretical approach to the snowman locomotion and to quantify the connection between locomotion and rheology in the following sections we now consider the second-order fluid, which we remind is valid in the small-De limit

only (Eq. 7.11). All variables are expanded in powers of the Deborah number, $\mathrm{De_{so}}$, as

$$\boldsymbol{\sigma} = \boldsymbol{\sigma}_0 + \mathrm{De_{so}}\boldsymbol{\sigma}_1 + O(\mathrm{De_{so}}^2), \tag{7.14}$$

$$\mathbf{u} = \mathbf{u}_0 + \mathrm{De_{so}}\mathbf{u}_1 + O(\mathrm{De_{so}}^2), \tag{7.15}$$

$$\dot{\boldsymbol{\gamma}} = \dot{\boldsymbol{\gamma}}_0 + \mathrm{De_{so}}\dot{\boldsymbol{\gamma}}_1 + O(\mathrm{De_{so}}^2), \tag{7.16}$$

$$\mathbf{U} = \mathbf{U}_0 + \mathrm{De_{so}}\mathbf{U}_1 + O(\mathrm{De_{so}}^2), \tag{7.17}$$

where $\mathbf{U}$ denotes the propulsion velocity, $\mathbf{U} = (0, 0, U)$. Other variables are expanded similarly. We drop the stars hereafter for simplicity, and all variables in this section are dimensionless unless otherwise stated. The locomotion problem is then solved order by order.

Zeroth-order solution

The zeroth order solution, $\{\boldsymbol{\sigma}_0 = -p_0\mathbf{I} + \dot{\boldsymbol{\gamma}}_0, \mathbf{u}_0\}$, satisfies the Stokes equations,

$$\boldsymbol{\nabla} \cdot \boldsymbol{\sigma}_0 = \mathbf{0}, \tag{7.18}$$

$$\boldsymbol{\nabla} \cdot \mathbf{u}_0 = 0, \tag{7.19}$$

where $\boldsymbol{\sigma}_0 = -p_0\mathbf{I}+\dot{\boldsymbol{\gamma}}_0$. This is the Newtonian flow for two touching spheres rotating (at a rate of $\boldsymbol{\Omega}$) about the line of their centers (z-axis). The exact solution in terms of analytical functions was given by Takagi [203] in tangent-sphere coordinates. No propulsion occurs in the Newtonian limit, $\mathbf{U}_0 = \mathbf{0}$, as expected.

First-order solution

The first order solution $(\boldsymbol{\sigma}_1, \mathbf{u}_1)$ of the main problem satisfies

$$\boldsymbol{\nabla} \cdot \boldsymbol{\sigma}_1 = \mathbf{0}, \tag{7.20}$$

$$\boldsymbol{\nabla} \cdot \mathbf{u}_1 = 0, \tag{7.21}$$

where

$$\boldsymbol{\sigma}_1 = -p_1\mathbf{I} + \dot{\boldsymbol{\gamma}}_1 - \overset{\triangledown}{\dot{\boldsymbol{\gamma}}}_0 - B\dot{\boldsymbol{\gamma}}_0 \cdot \dot{\boldsymbol{\gamma}}_0. \tag{7.22}$$

To compute the value of the first order propulsion velocity, $\mathbf{U}_1$, we will use a version of the reciprocal theorem for Stokes flows adapted to self-propulsion in viscoelastic fluids [135, 188, 204–210].

Consider an auxiliary problem with identical geometry, $\{\boldsymbol{\sigma}_{\text{aux}}, \mathbf{u}_{\text{aux}}\}$, satisfying

$$\boldsymbol{\nabla} \cdot \boldsymbol{\sigma}_{\text{aux}} = \mathbf{0}, \tag{7.23}$$

$$\boldsymbol{\nabla} \cdot \mathbf{u}_{\text{aux}} = 0. \tag{7.24}$$

Taking the inner product of Eq. (7.20) with $\mathbf{u}_{\text{aux}}$, minus the inner product of Eq. (7.23) with $\mathbf{u}_1$, and integrating over the entire fluid volume, we have trivially

$$\int_{V_f} \mathbf{u}_{\text{aux}} \cdot (\boldsymbol{\nabla} \cdot \boldsymbol{\sigma}_1) - \mathbf{u}_1 \cdot (\boldsymbol{\nabla} \cdot \boldsymbol{\sigma}_{\text{aux}}) dV = 0. \tag{7.25}$$

Using vector calculus we can rewrite the integral in the following form [211]

$$\int_{V_f} \boldsymbol{\nabla} \cdot (\mathbf{u}_{\text{aux}} \cdot \boldsymbol{\sigma}_1 - \mathbf{u}_1 \cdot \boldsymbol{\sigma}_{\text{aux}}) dV = \int_{V_f} (\boldsymbol{\nabla} \mathbf{u}_{\text{aux}} : \boldsymbol{\sigma}_1 - \boldsymbol{\nabla} \mathbf{u}_1 : \boldsymbol{\sigma}_{\text{aux}}) dV. \tag{7.26}$$

The left-hand side of Eq. (7.26) can be converted to a sum of surface integrals by the divergence theorem while the right-hand side can be simplified using the first-order constitutive equation, Eq. (7.22), leading to

$$\sum_{\alpha} \int_{S_\alpha} \mathbf{n} \cdot (\mathbf{u}_{\text{aux}} \cdot \boldsymbol{\sigma}_1 - \mathbf{u}_1 \cdot \boldsymbol{\sigma}_{\text{aux}}) dS = \int_{V_f} \left[\left(\overset{\triangledown}{\dot{\boldsymbol{\gamma}}}_0 + B \dot{\boldsymbol{\gamma}}_0 \cdot \dot{\boldsymbol{\gamma}}_0 \right) : \boldsymbol{\nabla} \mathbf{u}_{\text{aux}} \right] dV, \tag{7.27}$$

where S_α denotes the surface of different spheres ($\alpha = 1, 2$) and $\mathbf{n}$ represents the outward normal vector on the surface. The important simplification which took place in the right hand-side of Eq. (7.26) is that all Newtonian terms included in $\boldsymbol{\sigma}_{\text{aux}}$ and $\boldsymbol{\sigma}_1$ have canceled each other out by symmetry, and thus the only piece remaining in the right-hand side of Eq. (7.27) is the non-Newtonian contribution [205, 210].

Now, let $\mathbf{U}_1$ and $\boldsymbol{\Omega}_1$ be the (unknown) first order translational and rotational velocities of the spheres in our main problem, while the translational and rotational velocities of the spheres in the auxiliary problem (known) are given by

$\mathbf{U}_{\text{aux}}$ and $\boldsymbol{\Omega}_{\text{aux}}$. On the surface S_α of one sphere, the no-slip and no-penetration boundary conditions lead to

$$\mathbf{u}_{\text{aux}} = \mathbf{U}_{\text{aux}} + \boldsymbol{\Omega}_{\text{aux}} \times \mathbf{r}, \tag{7.28}$$

$$\mathbf{u}_1 = \mathbf{U}_1 + \boldsymbol{\Omega}_1 \times \mathbf{r}, \tag{7.29}$$

where $\mathbf{r}$ is the position vector describing the surface. With these boundary conditions, the integral relation, Eq. (7.27), becomes

$$\begin{aligned} \sum_\alpha \mathbf{U}^\alpha_{\text{aux}} \cdot \int_{S_\alpha} \mathbf{n} \cdot \boldsymbol{\sigma}_1 dS + \boldsymbol{\Omega}^\alpha_{\text{aux}} \cdot \int_{S_\alpha} \mathbf{r} \times (\mathbf{n} \cdot \boldsymbol{\sigma}_1) dS \\ -\mathbf{U}^\alpha_1 \cdot \int_{S_\alpha} \mathbf{n} \cdot \boldsymbol{\sigma}_{\text{aux}} dS - \boldsymbol{\Omega}^\alpha_1 \cdot \int_{S_\alpha} \mathbf{r} \times (\mathbf{n} \cdot \boldsymbol{\sigma}_{\text{aux}}) dS \\ = \int_{V_f} \left[\left(\overset{\triangledown}{\dot{\boldsymbol{\gamma}}}_0 + B \dot{\boldsymbol{\gamma}}_0 \cdot \dot{\boldsymbol{\gamma}}_0 \right) : \boldsymbol{\nabla} \mathbf{u}_{\text{aux}} \right] dV. \end{aligned} \tag{7.30}$$

In Eq. (7.30), the integrals $\int_{S_\alpha} \mathbf{n} \cdot \boldsymbol{\sigma}_1 dS$ and $\int_{S_\alpha} \mathbf{r} \times (\mathbf{n} \cdot \boldsymbol{\sigma}_1) dS$ represent the net hydrodynamic force and torque acting on the sphere α by the first order flow field. Let us denote $\mathbf{F}^\alpha_1 = -\int_{S_\alpha} \mathbf{n} \cdot \boldsymbol{\sigma}_1 dS$ and $\mathbf{T}^\alpha_1 = -\int_{S_\alpha} \mathbf{r} \times (\mathbf{n} \cdot \boldsymbol{\sigma}_1) dS$ the net external force ($\mathbf{F}^\alpha_1$) and external torque ($\mathbf{T}^\alpha_1$) acting on each sphere; the appearance of a minus sign comes from the fact that the total force and torque (external + fluid) acting on a body have to sum to zero in the absence of inertia. In the free-swimming case there is an additional stronger constraint, namely the total external force (or equivalently, the total fluid force) has to remain zero at all instant (we will enforce this constraint shortly). Defining also $\mathbf{F}^\alpha_{\text{aux}}$ and $\mathbf{T}^\alpha_{\text{aux}}$ as the external force and torque required to balance the fluid drag and torque on each sphere in the auxiliary problem we see that Eq. (7.30) is transformed into

$$\begin{aligned} \sum_\alpha -\mathbf{U}^\alpha_{\text{aux}} \cdot \mathbf{F}^\alpha_1 - \boldsymbol{\Omega}^\alpha_{\text{aux}} \cdot \mathbf{T}^\alpha_1 + \mathbf{U}^\alpha_1 \cdot \mathbf{F}^\alpha_{\text{aux}} + \boldsymbol{\Omega}^\alpha_1 \cdot \mathbf{T}^\alpha_{\text{aux}} \\ = \int_{V_f} \left[\left(\overset{\triangledown}{\dot{\boldsymbol{\gamma}}}_0 + B \dot{\boldsymbol{\gamma}}_0 \cdot \dot{\boldsymbol{\gamma}}_0 \right) : \boldsymbol{\nabla} \mathbf{u}_{\text{aux}} \right] dV. \end{aligned} \tag{7.31}$$

The above relation remains actually true for any number of spheres and kinematics. In the case of a snowman, we have two spheres connected as a rigid body in both the main and auxiliary problems, hence $\mathbf{U}^1_1 = \mathbf{U}^2_1 = \mathbf{U}_1$, $\boldsymbol{\Omega}^1 = \boldsymbol{\Omega}^2 = \boldsymbol{\Omega}_1$, $\mathbf{U}^1_{\text{aux}} = \mathbf{U}^2_{\text{aux}} = \mathbf{U}_{\text{aux}}$, and $\boldsymbol{\Omega}^1_{\text{aux}} = \boldsymbol{\Omega}^2_{\text{aux}} = \boldsymbol{\Omega}_{\text{aux}}$. In the main problem we impose a rotational rate $\boldsymbol{\Omega}$ on the snowman, which has been accounted for in

the zeroth order (Newtonian) solution, hence $\mathbf{\Omega}_n^\alpha = 0$ for all $n \geq 1$. In addition, we define in the main problem the total external force and torque acting on the rigid body as $\mathbf{F}_1 = \mathbf{F}^1 + \mathbf{F}^2$, $\mathbf{T}_1 = \mathbf{T}^1 + \mathbf{T}^2$, and in the auxiliary problem $\mathbf{F}_{\text{aux}} = \mathbf{F}^1_{\text{aux}} + \mathbf{F}^2_{\text{aux}}$, and $\mathbf{T}_{\text{aux}} = \mathbf{T}^1_{\text{aux}} + \mathbf{T}^2_{\text{aux}}$. Using these simplifications the general relation, Eq. (7.31), simplifies to

$$-\left(\mathbf{U}_{\text{aux}} \cdot \mathbf{F}_1 + \mathbf{\Omega}_{\text{aux}} \cdot \mathbf{T}_1\right) + \mathbf{U}_1 \cdot \mathbf{F}_{\text{aux}} = \int_{V_f} \left[\left(\overset{\triangledown}{\dot{\boldsymbol{\gamma}}}_0 + B\dot{\boldsymbol{\gamma}}_0 \cdot \dot{\boldsymbol{\gamma}}_0 \right) : \boldsymbol{\nabla} \mathbf{u}_{\text{aux}} \right] dV \cdot \tag{7.32}$$

We now need to find an auxiliary problem that facilitates the determination of the first order propulsion velocity, $\mathbf{U}_1$, in the main problem. An appropriate candidate is the translation of two touching spheres along the line of their centers without rotation, $\mathbf{\Omega}_{\text{aux}} = 0$. The exact analytical solution was given by Cooley and O'Neill [212]. By choosing this auxiliary problem, the relation further simplifies to

$$-\mathbf{U}_{\text{aux}} \cdot \mathbf{F}_1 + \mathbf{U}_1 \cdot \mathbf{F}_{\text{aux}} = \int_{V_f} \left[\left(\overset{\triangledown}{\dot{\boldsymbol{\gamma}}}_0 + B\dot{\boldsymbol{\gamma}}_0 \cdot \dot{\boldsymbol{\gamma}}_0 \right) : \boldsymbol{\nabla} \mathbf{u}_{\text{aux}} \right] dV \cdot \tag{7.33}$$

If we do not allow the spheres to translate along the z-axis, $\mathbf{U}_1 = 0$, an external force, $\mathbf{F}_1$, is required to hold the snowman in place given by

$$-\mathbf{U}_{\text{aux}} \cdot \mathbf{F}_1 = \int_{V_f} \left[\left(\overset{\triangledown}{\dot{\boldsymbol{\gamma}}}_0 + B\dot{\boldsymbol{\gamma}}_0 \cdot \dot{\boldsymbol{\gamma}}_0 \right) : \boldsymbol{\nabla} \mathbf{u}_{\text{aux}} \right] dV \cdot \tag{7.34}$$

On the other hand, if we allow the snowman to translate freely without imposing any external forces, $\mathbf{F}_1 = 0$, then the first order propulsion velocity, $\mathbf{U}_1$, can be determined from

$$\mathbf{U}_1 \cdot \mathbf{F}_{\text{aux}} = \int_{V_f} \left[\left(\overset{\triangledown}{\dot{\boldsymbol{\gamma}}}_0 + B\dot{\boldsymbol{\gamma}}_0 \cdot \dot{\boldsymbol{\gamma}}_0 \right) : \boldsymbol{\nabla} \mathbf{u}_{\text{aux}} \right] dV, \tag{7.35}$$

where both $\mathbf{F}_{\text{aux}}$ and the integral are expressed in terms of known Newtonian solutions of the main and auxiliary problems. Since the propulsion velocity $\mathbf{U}_1$ (with magnitude U_1) and the force in the auxiliary problem $\mathbf{F}_{\text{aux}}$ (with magnitude F_{aux}) act both vertically, the first order propulsion speed is finally given by

$$U_1 = \frac{1}{F_{\text{aux}}} \int_{V_f} \left[\left(\overset{\triangledown}{\dot{\boldsymbol{\gamma}}}_0 + B\dot{\boldsymbol{\gamma}}_0 \cdot \dot{\boldsymbol{\gamma}}_0 \right) : \boldsymbol{\nabla} \mathbf{u}_{\text{aux}} \right] dV, \tag{7.36}$$

where a positive value represents upward propulsion.

Using Eq. (7.36) with the zeroth-order solution [203] and the auxiliary Newtonain solution [212] we are able to determine theoretically the leading order propulsion speed of the snowman, $U = \mathrm{De_{so}} U_1 + O(\mathrm{De_{so}}^2) = \mathrm{De}(1-\zeta)U_1 + O(\mathrm{De}^2)$. The quadrature is performed in the tangent-sphere coordinates, with somewhat lengthy differential operations in evaluating the integrand. Our asymptotic results are shown in Fig. 7.2 as a blue solid line. We see that our results predict very well the propulsion speed of the snowman for small De when compared with numerical computations of the Oldroyd-B fluid (red dot-dashed line, in Fig. 7.2), and the agreement is excellent up to $\mathrm{De} \sim 1$.

Note that in order to compare the results between the second-order fluid calculation and the Oldroyd-B numerics, the dimensionless parameter $B = -2\Psi_2/\Psi_1$ in the second-order fluid has to be taken to be zero because the second normals stress coefficient is zero in the Oldroyd-B model. Experimentally, indeed we have $B \ll 1$. Mathematically, the propulsion velocity varies linearly with B, and a transition of propulsion direction occurs at $B = 1$. Such a transition also occurs in the direction of radial flow for a single rotating sphere in a second-order fluid (see Sec. 7.5 for a related discussion).

7.3.3 Propulsion characteristics

Anticipating the section where we make the link between rheology and locomotion, we now investigate the impact of the snowman geometry on its propulsion performance in the low-De regime where our asymptotic results via reciprocal theorem are quantitatively accurate.

Touching spheres

In the case of two touching sphere ($h^* = 1 + r^*$), the only free dimensionless geometric parameter is the ratio of the radius of the upper to that of the lower spheres $r^* = R_U/R_L \in [0, 1]$. In the limit $r^* = 0$, the snowman reduces to a single sphere, while the limit $r^* = 1$ corresponds to two equal touching spheres; in both cases, there is no propulsion by symmetry. We therefore expect an optimal ratio r^* for a maximum propulsion speed. Using the reciprocal theorem, Eq. (7.36), we calculate the propulsion speed as a function of r^* (Fig 7.3, blue solid line) and

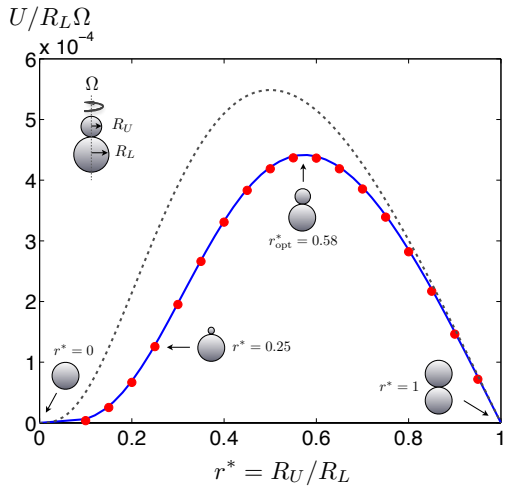

Figure 7.3: Propulsion speed of snowman with two touching spheres as a function of the ratio of radii at De = 0.1 and $\zeta = 0.5$. Red dots: numerical results in an Odroyd-B fluid. Blue solid line: theoretical calculation for second-order fluid. Black dotted line: simplified analytical model (Eq. 7.51).

compare with the numerical results in an Oldroyd-B fluid (Fig. 7.3, red dots) at De = 0.1 and a typical relative viscosity $\zeta = 0.5$. The asymptotic results agree very well with the Oldroyd-B computations. The optimal sphere size ratio occurs at $r^*_{\rm opt} \approx 0.58$. In addition to our computations and theoretical calculations, and based on physical understanding of the behavior of a single rotating sphere in a second-order fluid, a simplified analytical model can be constructed to predict the snowman dynamics with results shown as a black dotted line in Fig. 7.3; the details of this simple model are given in Sec. 7.5.

Separated spheres

Next, we let the two spheres be separated at a distance $h^* > 1+r^*$ (no longer touching). The two spheres still rotate at the same speed as a rigid body and the separation distance is kept fixed by connecting the spheres with a drag-less slender rigid rod (a mathematically phantom rod) with negligible hydrodynamic contribution. Experimentally, this may be realized using, for example, using nanowires [1]. To compute the propulsion speed by the method described in Sec. 7.3.2 and

[1]If the drag on the slender rod is taken into account in modeling, the overall force balance should include the small contribution from the drag on the rod, which will slightly decrease the

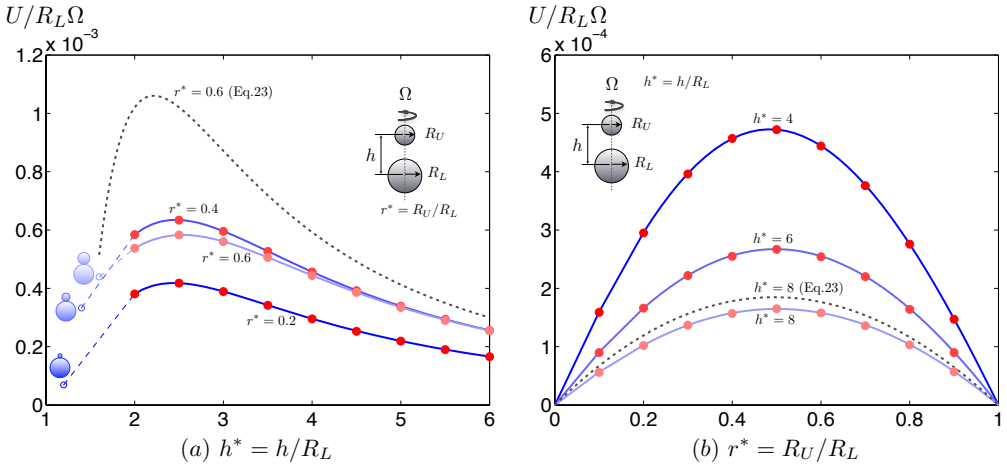

Figure 7.4: Propulsion speed of a separated snowman as a function of (a) the separation distance, and (b) ratio of the radii, at De = 0.1 and $\zeta = 0.5$. Red dots: numerical results in an Odroyd-B fluid. Blue solid line: second-order fluid analytical calculation. Black dotted line: simplified model (Eq. 7.50).

therefore Eq. (7.36), we need two new Newtonian solutions, namely the zeroth-order solution and the auxiliary problem. The zeroth order solution considers two separated unequal spheres rotating at the same rate in a Newtonian fluid, the exact solution of which was given by Jeffery [213] in bi-spherical coordinates. The appropriate auxiliary problem is the translation in a Newtonian fluid of the same two-sphere geometry along their axis of symmetry. Stimson and Jeffery [214] calculated that exact solution also in bi-spherical coordinates.

For very separated spheres $h^* \gg 1$, the propulsion is expected to decay with the separation distance. Hydrodynamic interactions between the two spheres is weak in this limit and each sphere behaves approximately as a single rotating sphere which does not propel. In Fig. 7.4a, the variation of the propulsion speed as a function of the separated distance is calculated for different fixed values of r^*. The propulsion speed decays as expected for large h^*. Interestingly, a non-monotonic variation occurs when the spheres are close to each other (small h^*). The swimming speed first increases with h^*, reaching a maximum around $h^* \approx 2.5$, before decaying to zero with further increase in h^*. In Sec. 7.5, a simple physical explanation to this non-monotonicity is discussed; the black dotted line in Fig. 7.4a corresponds

propulsion speed of the snowman.

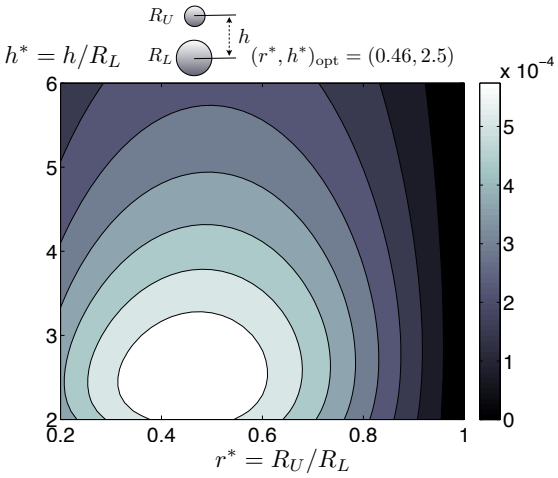

Figure 7.5: Optimization snowman propulsion. Iso-values of the dimensionless propulsion speed with dimensionless separation distance, h^*, and ratio of sphere radii, r^*. The optimal geometry for maximum propulsion speed is given by $(r^*, h^*)_{\text{opt}} = (0.46, 2.5)$. A schematic diagram showing the optimal geometry is drawn to scale above.

to the predictions by a simplified analytical model based on this explanation.

For separated spheres, we can again vary the radii ratio, r^*, at different fixed separated distance h^* (Fig. 7.4b) and results similar to the case of touching spheres is observed: for any value of h^* there exists an optimal value of r^* at which the dimensionless propulsion speed reaches a maximum. The simplified model (Sec. 7.5) again captures this trend qualitatively (black dotted line, Fig. 7.4b).

Finally, by plotting the isovalues of the propulsion speed as a function of both r^* and h^* (Fig. 7.5), we are able to optimize the snowman geometry for the overall maximum propulsion speed. The optimal geometry occurs at $(r^*, h^*) = (0.46, 2.5)$, and a schematic diagram of the optimal snowman is drawn to-scale in Fig. 7.5.

7.4 Microrheology via snowman

7.4.1 Scaling

In the sections above we have derived an analytical expression, valid in the small De regime, relating the propulsion speed to the intrinsic properties of the complex fluid, namely the normal stress coefficients (Eq. 7.36). Turning all dimensionless variables back in dimensional form, this relationship reads formally

$$U = \left(C_1^{\mathrm{S}}\Psi_1 + C_2^{\mathrm{S}}\Psi_2\right)\frac{R_L\Omega^2}{\eta}, \tag{7.37}$$

where C_1^{S} and C_2^{S} are dimensionless coefficients depending solely on the snowman geometry (h^* and r^*) and defined as

$$C_1^{\mathrm{S}} = \frac{\int_{V_f^*} \overset{\triangledown}{\dot{\boldsymbol{\gamma}}}_0^* : \boldsymbol{\nabla}^* \mathbf{u}_{\mathrm{aux}}^* dV^*}{2F_{\mathrm{aux}}^*}, \tag{7.38}$$

$$C_2^{\mathrm{S}} = -\frac{\int_{V_f^*} (\dot{\boldsymbol{\gamma}}_0^* \cdot \dot{\boldsymbol{\gamma}}_0^*) : \boldsymbol{\nabla}^* \mathbf{u}_{\mathrm{aux}}^* dV^*}{F_{\mathrm{aux}}^*}. \tag{7.39}$$

Since the second normal stress coefficient Ψ_2 is usually much smaller than the first normal stress coefficients Ψ_1, we might ignore Ψ_2 and obtain an estimation of Ψ_1 by measuring the propulsion speed of a snowman U, *i.e.*

$$\Psi_1 \approx \frac{U}{C_1^{\mathrm{S}}}\frac{\eta}{R_L\Omega^2}, \tag{7.40}$$

where C_1^{S} depends only on geometry and can be computed using Eq. (7.38). This expression demonstrates the use of locomotion (U) to probe the local non-Newtonian properties of the fluid (Ψ_1).

7.4.2 Second Experiment: Repulsion of two equal spheres

In scenarios where both values of Ψ_1 and Ψ_2 are desired, a second experiment is necessary to obtain a second, independent, measurement of a combination of the normal stress coefficients. We propose to measure in the second experiment the relative speed (repulsion) of two rotating equal spheres of radius R_E, with their centers separated by a distance h (see Fig. 7.6 inset for notations and geometry). Should the two equal spheres be connected as a rigid body, no propulsion would

occur by symmetry. However, if the equal spheres are not connected but allowed to freely translate along their separation axis, upon imposing rotation they will translate with velocities of equal magnitude but opposite directions provided the fluid is non-Newtonian.

We adopt the same non-dimensionalizations as previous sections (all lengths are now scaled by R_E) and drop the stars for simplicity; all variables in this section are dimensionless unless otherwise stated. Denoting the dimensionless velocity of the lower sphere as $\mathbf{V}$, we again expand the repulsion velocity in powers of $\mathrm{De_{so}}$, $\mathbf{V} = \mathrm{De_{so}}\mathbf{V}_1 + O(\mathrm{De_{so}}^2)$, and determine the first order velocity $\mathbf{V}_1$ using our use of the reciprocal theorem as described in Sec. 7.3.2. By symmetry, the upper sphere translates with velocity $-\mathbf{V}$ (equal speed but opposite direction as the lower sphere).

In this scenario we have to again define two setups, one for the main problem and one for the auxiliary problem. For the main problem, we consider the rotational motion of two free equal spheres about their line of centers [213]. Since the motion is force-free ($\mathbf{F}_1^\alpha = 0$ at each instant), Eq. (7.36) simplifies to

$$-\mathbf{\Omega}^1_{\mathrm{aux}} \cdot \mathbf{T}^1 - \mathbf{\Omega}^2_{\mathrm{aux}} \cdot \mathbf{T}^2 + \mathbf{U}^1_1 \cdot \mathbf{F}^1_{\mathrm{aux}} + \mathbf{U}^1_2 \cdot \mathbf{F}^2_{\mathrm{aux}} = \int_{V_f} \left[\left(\overset{\triangledown}{\dot{\boldsymbol{\gamma}}}_0 + B\dot{\boldsymbol{\gamma}}_0 \cdot \dot{\boldsymbol{\gamma}}_0 \right) : \boldsymbol{\nabla} \mathbf{u}_{\mathrm{aux}} \right] dV, \tag{7.41}$$

where $\mathbf{\Omega}_1^\alpha = 0$ for the same reason as explained in Sec. 7.3.2.

For the auxiliary problem, we consider the Newtonian translational motion ($\mathbf{\Omega}^\alpha_{\mathrm{aux}} = 0$) of two equal spheres moving towards each other at the same speed and hence force, $\mathbf{F}^1_{\mathrm{aux}} = -\mathbf{F}^2_{\mathrm{aux}} = \mathbf{F}^E_{\mathrm{aux}}$. The exact solution to this problem was found by Brenner [215] in bi-spherical coordinates. We therefore have

$$\left(\mathbf{U}^1_1 - \mathbf{U}^2_1\right) \cdot \mathbf{F}^E_{\mathrm{aux}} = \int_{V_f} \left[\left(\overset{\triangledown}{\dot{\boldsymbol{\gamma}}}_0 + B\dot{\boldsymbol{\gamma}}_0 \cdot \dot{\boldsymbol{\gamma}}_0 \right) : \boldsymbol{\nabla} \mathbf{u}_{\mathrm{aux}} \right] dV. \tag{7.42}$$

Note that the main problem here is a special case of that considered in Sec. 7.3.2, but the auxiliary problem is completely different. We however still use the same symbols as in Sec. 7.3.2 for simplicity.

By symmetry, the two equal spheres propel with equal speed in opposite directions $\mathbf{U}^2_1 = -\mathbf{U}^1_1 = \mathbf{V}_1$, hence

$$-2\mathbf{V}_1 \cdot \mathbf{F}^E_{\mathrm{aux}} = \int_{V_f} \left[\left(\overset{\triangledown}{\dot{\boldsymbol{\gamma}}}_0 + B\dot{\boldsymbol{\gamma}}_0 \cdot \dot{\boldsymbol{\gamma}}_0 \right) : \boldsymbol{\nabla} \mathbf{u}_{\mathrm{aux}} \right] dV. \tag{7.43}$$

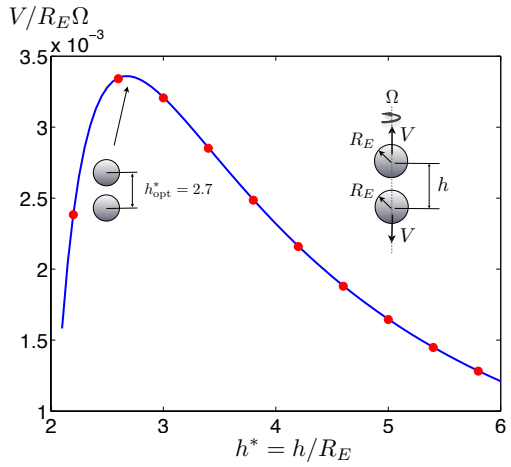

Figure 7.6: Dimensionless repulsion speed, $V/R_E\Omega$, of two equal co-rotating spheres as a function of their dimensionless separation distance, h^*, at De $= 0.1$ and $\zeta = 0.5$. Red dots: numerical results in an Odroyd-B fluid. Blue solid line: theoretical calculation for a second-order fluid.

Since the repulsion velocity $\mathbf{V}_1$ (with magnitude V_1) and the force in the auxiliary problem $\mathbf{F}^E_{\rm aux}$ (with magnitude $F^E_{\rm aux}$) both act vertically, the equation above can be rewritten as

$$V_1 = -\frac{1}{2F^E_{\rm aux}} \int_{V_f} \left[\left(\overset{\triangledown}{\dot{\boldsymbol{\gamma}}}_0 + B\dot{\boldsymbol{\gamma}}_0 \cdot \dot{\boldsymbol{\gamma}}_0 \right) : \boldsymbol{\nabla} \mathbf{u}_{\rm aux} \right] dV, \tag{7.44}$$

where a positive value of V_1 represents repulsion.

The only dimensionless parameter in this second experiment is the ratio of the separation distance to the radius of the spheres, which we write as $h^* = h/R_L$. Using Eq. (7.44) we calculate the repulsion speed ($V_1 > 0$) as a function of the dimensionless separation h^* (blue solid line, Fig. 7.6, for De $= 0.1$ and $\zeta = 0.5$), and the results are found to be in excellent agreement with the Oldroyd-B calculations (red dots, Fig. 7.6).

Back to dimensional variables, the leading order repulsion speed is formally given by

$$V = \left(C_1^{\rm E} \Psi_1 + C_2^{\rm E} \Psi_2 \right) \frac{R_E \Omega^2}{\eta}, \tag{7.45}$$

where $C_1^{\rm E}$ and $C_2^{\rm E}$ are dimensionless coefficients evaluated with the solution to the

main and auxiliary problems described above

$$C_1^{\mathrm{E}} = -\frac{\int_{V_f^*} \overset{\triangledown}{\dot{\boldsymbol{\gamma}}}_0^* : \boldsymbol{\nabla}^* \mathbf{u}_{\mathrm{aux}}^* dV^*}{4F_{\mathrm{aux}}^*}, \tag{7.46}$$

$$C_2^{\mathrm{E}} = \frac{\int_{V_f^*} (\dot{\boldsymbol{\gamma}}_0^* \cdot \dot{\boldsymbol{\gamma}}_0^*) : \boldsymbol{\nabla}^* \mathbf{u}_{\mathrm{aux}}^* dV^*}{2F_{\mathrm{aux}}^*}. \tag{7.47}$$

7.4.3 Determination of normal stress coefficients

From measuring both the propulsion speed U of a snowman (given by Eq. 7.37) and repulsion speed V of the equal spheres (given by Eq. 7.45), we now have enough information to deduce both the first and second normal stress coefficeints (Ψ_1, Ψ_2). If we choose the same radius for the lower sphere in both experiments $R_E = R_L$ (we use R_L hereafter), we can write Eqs. (7.37) and (7.45) in a matrix form as

$$\begin{pmatrix} U \\ V \end{pmatrix} = \begin{pmatrix} C_1^{\mathrm{S}} & C_2^{\mathrm{S}} \\ C_1^{\mathrm{E}} & C_2^{\mathrm{E}} \end{pmatrix} \begin{pmatrix} \Psi_1 \\ \Psi_2 \end{pmatrix} \frac{R_L \Omega^2}{\eta}, \tag{7.48}$$

where we denote by $\mathbf{C}$ the matrix containing the dimensionless coefficients (C_1^{S},C_2^{S}, C_1^{E},C_2^{E}) in Eq. (7.48). The matrix $\mathbf{C}$ depends only on three geometric parameters, namely the ratio of the radii of the spheres in the snowman ($r^* = R_U/R_L$), the dimensionless separation distance in the snowman ($h_{\mathrm{S}}^* = h/R_L$) and that for the equal spheres in the second experiment ($h_{\mathrm{E}}^* = h/R_E$). The coefficients of the matrix can be readily computed via Eqs. (7.38)–(7.39) and Eqs. (7.46)–(7.47), and thus the matrix in Eq. (7.48) can be inverted to obtain the values of Ψ_1 and Ψ_2.

For practical implementation of this microrheological technique, measurement errors in the velocity of the snowman are inevitable and depend on the specific equipment employed for tracking the motion of the probe. However, the geometry of the snowman can be designed so that Ψ_1 and Ψ_2 are insensitive to measurement errors in the velocities U and V. The condition number (CN) of the matrix $\mathbf{C}$ to be inverted represents the maximum amplification factor of the relative measurement errors. The maximum relative errors in the normal stress coefficients would be equal to the condition number multiplied by the maximum relative measurement error. A small condition number is therefore desired. Similarly to the study by Khair and Squires [188], we now investigate the value of

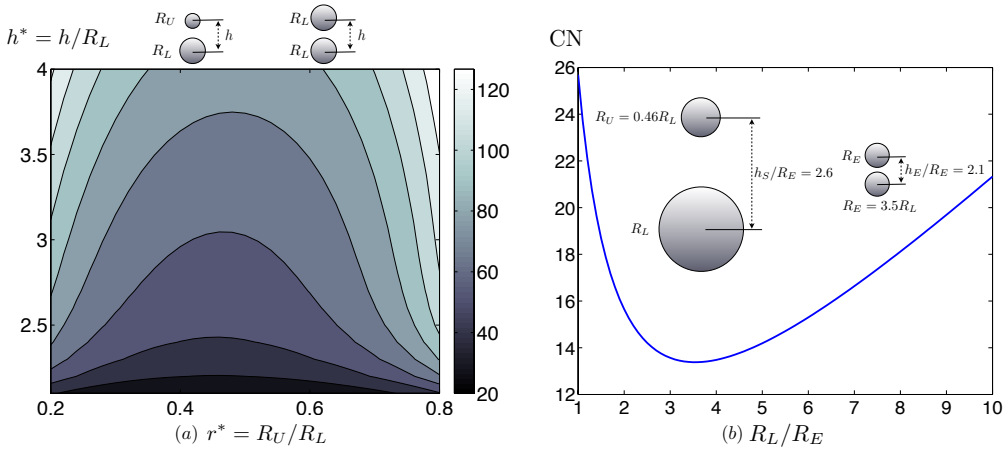

Figure 7.7: (a) Condition number (CN) for the matrix $\mathbf{C}$ as a function of sphere size ratio (r^*) and dimensionless separation distance ($h^* = h^*_{\mathrm{S}} = h^*_{\mathrm{E}}$). (b) CN as a function of R_L/R_E, for $r^* = 0.46$, $h^*_{\mathrm{S}} = 2.6$, and $h^*_{\mathrm{E}} = 2.1$.

condition number as a function of the geometry. To simplify the parametric studies, we first adopt the same separation distance in the first and second experiments ($h^*_{\mathrm{S}} = h^*_{\mathrm{E}} = h^* = h/R_L$), and explore the dependence of the condition number on r^* and h^*, with results shown in Fig. 7.7a. The condition number does not vary monotonically with the parameters, which implies that optimization is possible. Under this requirement and within the ranges of values considered ($r^* \in [0.2, 0.98]$ and $h^* \in [2.1, 4]$), the geometry yielding the lowest condition number is $r^* = 0.46$ and $h^* = 2.1$ (the corresponding condition number for $\mathbf{C}$ is ≈ 27.6). When the requirement of $h^*_{\mathrm{S}} = h^*_{\mathrm{E}}$ is removed, by examining all combinations of the parametric values within the ranges ($r^* \in [0.2, 0.98]$, $h^*_{\mathrm{S}} \in [2.1, 4]$, and $h^*_{\mathrm{E}} \in [2.1, 4]$), the minimum CN obtainable appears to be ≈ 25.7 with $r^* = 0.46$, $h^*_{\mathrm{S}} = 2.6$, and $h^*_{\mathrm{E}} = 2.1$.

The condition number can be further fine-tuned if we allow $R_L \neq R_E$, in which case we have the new matrix relation

$$\begin{pmatrix} U \\ V \end{pmatrix} = \begin{pmatrix} C_1^{\mathrm{S}} & C_2^{\mathrm{S}} \\ C_1^{\mathrm{E}} R_E/R_L & C_2^{\mathrm{E}} R_E/R_L \end{pmatrix} \begin{pmatrix} \Psi_1 \\ \Psi_2 \end{pmatrix} \frac{R_L \Omega^2}{\eta}. \tag{7.49}$$

The modified dimensionless matrix $\tilde{\mathbf{C}}$ in Eq. (7.49) now depends on one more parameter R_L/R_E, which is the ratio of the lower sphere radius in the snowman, R_L, to that of the equal sphere, R_E. In Fig. 7.7b, we investigate the dependence

of the condition number of $\tilde{\mathbf{C}}$ with this new parameter, and adopt for all other parameters the optimal geometric parameters we determined before ($r^* = 0.46$, $h_{\mathrm{S}}^* = 2.6$, and $h_{\mathrm{E}}^* = 2.1$). The variation turns out to be also non-monotonic, and a minimum is achieved when $R_L/R_E = 3.5$ with CN ≈ 13.4. A schematic diagram showing the corresponding geometrical setup of the two sets of experiment is given to scale in the inset of Fig. 7.7. The condition number could be brought further down with a full four-dimensional parametric study and expanding the domains of the parametric studies. However, geometries yielding a lower CN may correspond to a negligible speeds undesirable for measurement. The current geometry ($r^* = 0.46$, $h_{\mathrm{S}}^* = 2.6$, $h_{\mathrm{E}}^* = 2.1$, and $R_L/R_E = 3.5$) has both a relatively low CN and a high propulsion speed, making it ideal for experimental implementation. It is interesting to note that the optimal geometry for a small condition number we find here is close to the optimal geometry producing the maximum propulsion speed for the snowman ($r^* = 0.46$, $h_{\mathrm{S}}^* = 2.5$) determined in Sec. 7.3.3.

7.5 Qualitative physical explanation

In this section, we turn to an explanation of the physical origin of the non-Newtonian propulsion of a snowman. Based on physical intuition we present a simple model which successfully captures all the qualitative features of this mode of propulsion.

We first look into the simplest related problem, that of a single sphere rotating in a complex fluid (a textbook problem discussed, for example in Ref. [131]). Non-Newtonian stresses lead to the creation of a secondary flow in which the fluid moves towards the sphere in the equatorial plane and away from the sphere near the axis of rotation (see the inset of Fig. 7.8 for an illustration of the secondary flow field) [131].

This secondary flow can be understood physically as a consequence of the hoop stresses along the curved streamlines. Polymer molecules in the fluid get stretched by the flow, leading to an extra tension along streamlines. The presence of that extra tension along the closed circular streamlines leads to an inward radial contraction (like a stretched rubber band) pushing the fluid to thus go up vertically in both directions (by continuity) to produce the secondary flow. Notably, this

secondary flow is independent of the direction of rotation of the sphere.

The argument for locomotion of the snowman is then the following. Based on the one-sphere result, we see that when the two spheres in a snowman are aligned vertically and subject to a rotation they generate secondary flows and push against each other. For a single sphere, the strength of the secondary flow increases with the size of the sphere [131]. Consequently the smaller sphere is being pushed harder by the larger sphere than it is able to push against, and hence the two-sphere system is subject to a force imbalance, leading to propulsion. This physical understanding agrees with our results: propulsion always occurs in the direction of the smaller sphere, independently of the direction of rotation. Should the two spheres not be connected as a rigid body but free to translate vertically, they would repel each other, explaining physically our results in Sec. 7.4.2.

Based on this intuitive argument, we can now construct a simple mathematical model. Using the same notations as above, for a sphere of radius R rotating with an angular velocity Ω in a second-order fluid, the leading order solution $\mathbf{v}(\phi, r, \theta)$ in spherical coordinates [131] is $\mathbf{v}^* \equiv \mathbf{v}/R\Omega = (1/r^*)^2 \sin\theta\ \mathbf{e}_\phi + \mathrm{De_{so}}(1-B)[(1/2r^{*2} - 3/2r^{*4} + 1/r^{*5})(3\cos^2\theta - 1)\ \mathbf{e}_r - 3(1/r^{*4} - 1/r^{*5})\sin\theta\cos\theta\ \mathbf{e}_\theta] + O\left(\mathrm{De_{so}}^2\right)$. The Newtonian component of the flow field ($\mathrm{De_{so}} = 0$) is the primary flow field, and it has only a azimuthal (ϕ) component. The secondary flow field, proportional to $\mathrm{De_{so}}$, is due to fluid elasticity and has only radial (r) and polar (θ) components. As expected, the dimensional secondary flow $\mathbf{v}$ is quadratic in Ω, confirming our physical intuition that it should be independent of the direction of rotation of the sphere. In the case where $B < 1$ (recall that $B = -2\Psi_2/\Psi_1$), the relevant limit for polymeric fluids, the secondary flow occurs in the direction intuited above and shown in the inset of Fig. 7.8. Note that the secondary flow field of a rotating single sphere would switch its direction when B went above one, explaining the switch in the propulsion direction of a snowman reported in Sec. 7.3.2 in that limit.

The dimensionless fluid velocity along the vertical axis ($\theta = 0$) is given by $\mathbf{v}^*(r, \theta = 0) = \mathrm{De_{so}}\,(1/r^{*2} - 3/r^{*4} + 2/r^{*5})\ \mathbf{e}_r(\theta = 0)$, where we have set $B = 0$ to allow comparison with the numerical results. The velocity along the vertical axis, shown in Fig. 7.8, is expected to display non-monotonic variation with the distance from the sphere since the velocity decreases to zero both in the far field and on the solid surface. This is at the origin of the non-monotonic dependence of

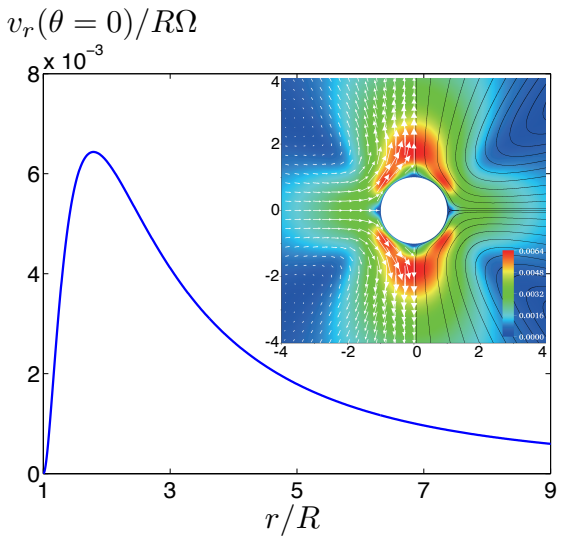

Figure 7.8: Rotation of a single sphere in a second order fluid. Radial velocity along the rotation axis ($\theta = 0$) as a function of r/R at De $= 0.1$ and $\zeta = 0.5$. Inset: streamline pattern and velocity (shaded/color map) of the corresponding secondary flow.

the snowman propulsion speed with the separation distance between the spheres shown in Fig. 7.4a.

The forces experienced by the upper and lower spheres can be approximately estimated by considering the individual flow fields generated by their own rotation without the presence of the other sphere. We place an upper sphere at a distance $h^* = h/R_L$ from the center of the lower sphere. Using the same notations as in the previous sections, the dimensionless velocity generated by the lower sphere, and evaluated at the location of the upper sphere, is given by $\mathbf{v}_L^*(h^*) = \mathrm{De}_{\mathrm{so}}\left(1/h^{*2} - 3/h^{*4} + 2h^{*5}\right)\ \mathbf{e}_r^L(\theta^L = 0)$, where $\mathbf{e}_r^L(\theta^L = 0)$ is the unit radial vector in the polar direction $\theta^L = 0$, with respect to the coordinates system at the center of the lower sphere. Similarly, the dimensionless velocity generated by the upper sphere at the same distance, h^*, but measured from the center of the upper sphere is given by $\mathbf{v}_U^*(h^*) = r^*\mathrm{De}_{\mathrm{so}}\left[(r^*/h^*)^2 - 3\,(r^*/h^*)^4 + 2\,(r^*/h^*)^5\right]\ \mathbf{e}_r^U(\theta^U = \pi)$, where $\mathbf{e}_r^U(\theta^U = \pi)$ is the unit radial vector in the polar direction $\theta^U = \pi$, with respect to the coordinates system at the center of the upper sphere. Note that $\mathbf{e}_r^U(\theta^U = \pi) = -\mathbf{e}_r^L(\theta^L = 0)$. As a simple approximation, we estimate the viscous drag force experienced by the upper and lower spheres to be $\mathbf{F}_U^* \sim 6\pi r^* \mathbf{v}_L^*(h^*)$ and

$\mathbf{F}_L^* \sim 6\pi \mathbf{v}_U^*(h^*)$ respectively. The difference between these two forces results in a net propulsive thrust. When dividing by an approximation of the translational resistance of the snowman at zero Deborah number with no hydrodynamic interactions, $6\pi(1+r^*)$, we obtain a simple estimate of the dimensionless propulsion speed as $U^* \approx |\mathbf{F}_U^* + \mathbf{F}_L^*|/6\pi(1+r^*)$. This leads to

$$U^* \approx \frac{|r^*\mathbf{v}_L^*(h^*) + \mathbf{v}_U^*(h^*)|}{(1+r^*)} = \mathrm{De_{so}} \frac{r^*\left[3h^*(r^{*4}-1) - h^{*3}(r^{*2}-1) - 2r^{*5}+2\right]}{h^{*5}(1+r^*)}. \tag{7.50}$$

In Eq. (7.50), we verify that U^* vanishes when $r^* = 0$ (single sphere) and $r^* = 1$ (equal spheres). For the case of touching spheres ($h^* = 1+r^*$), Eq. (7.50) simplifies to

$$U^*_{\mathrm{touch}} \approx \mathrm{De_{so}} \frac{2r^{*3}(1-r^*)}{(1+r^*)^6}. \tag{7.51}$$

Does this simple model capture the essential propulsion characteristics? In Fig. 7.3, we plot the dimensionless propulsion speed of a touching snowman estimated by this simple model (Eq. 7.51) as a function of r^* (black dotted line) and compare with the theoretical results from the reciprocal theorem approach (blue solid line) and the numerical computations (red symbols). The simple model correctly predicts the order of magnitude and captures qualitatively the variation with r^*. For non-touching snowman, the qualitative model (Eq. 7.50) also captures qualitatively the variation of the dimensionless propulsion speed with h^* (black dotted line for $r^* = 0.6$, Fig. 7.4a), also predicting an optimal separation distance and therefore supporting our understanding of a non-monotonic dependence with h^* as arising from the non-monotonicity of the single-sphere velocity (Fig. 7.8). As expected, Eq. (7.50) also captures the non-monotonic variation with respect to r^* for separated snowman (black dotted line for $h^* = 8$, Fig. 7.4b).

7.6 Discussion and Conclusions

In this work, we present the design and mathematical modeling for a new non-Newtonian swimmer – the snowman – which propels only in complex fluids by exploiting asymmetry and the presence of normal stress differences under rotational actuation. The simple shape of our swimmer makes it ideally suited for

experimental measurements. Note that if kept in place, the snowman would then act as a micro-pump for complex fluids.

The propulsion characteristics of the snowman are investigated by a combination of numerical computations (moderate values of De in an Odroyd-B fluid) and analytical treatment (small De in a second-order fluid). The underlying physics of propulsion, relying on elastic hoop stresses and geometrical asymmetry, is explained and based on this physical understanding a simple analytical model capturing all qualitative features is successfully constructed. Note that since, as a rule of thumb, inertial and elastic effects tend to produce secondary flows in opposite directions [131], we expect that an inertial (instead of viscoelastic) snowman should swim in the opposite direction (from small to large sphere).

The two-sphere setup proposed in this work is arguably the simplest geometry able to swim in a complex fluid under uniform rotation. It of course simplifies the analysis since the required Newtonian solutions to be used in our integral approach are all available. Any axisymmetric but top-down asymmetric geometry should also work, for example a cone, and clearly there remains room for shape optimization in that regard. Additionally, studying the snowman dynamics under a time-varying rotation could lead to a rich dynamics with potentially non-trivial stress relaxation effects.

One of the main ideas put forward in this work is the use of locomotion as a proxy to probe the local non-Newtonian properties of the fluid. The snowman can be used as a micro-rheometer to estimate the first normal stress coefficient on its own, or to measure both the first and second normal stress coefficients with the help of another complementary experiment. Khair and Squires [188] recently proposed to measure normal stress coefficients by pulling microrheological probes and measuring the relative forces on the probes. In our work, we propose alternatively to perform only kinematic measurements of the sphere speeds instead of forces, which could present an interesting alternative from an experimental standpoint.

We finally comment on a potential experimental implementation of the snowman technique. We are aware of a number of rotational micro-manipulation techniques (see a short review in Ref. [216]). For example, spinning micro-particles may be achieved by the use of optical tweezers and birefringent objects [217]. Birefringence allows the transfer of angular momentum from the circularly po-

larized laser to the particle, producing controlled rotation. By rotating spherical birefringent crystals (vaterite), this technology has been implemented as a micro-viscometer to probe fluid viscosity [216, 218, 219]. A similar mechanism may be useful for the two-sphere setup in this work although simultaneous rotation of two spheres may introduce experimental challenges. Our dual-purpose snowman, both a micro-propeller and a micro-rheometer, invites experimental implementation and verification.

Chapter 7, in full, is a reprint of the material as it appears in Physics of Fluids 2012. Pak, On Shun; Zhu, Lailai; Brandt, Luca; Lauga, Eric, the American Institute of Physics, 2012. The dissertation author was the primary investigator and author of this paper.

Bibliography

[1] R. Rikmenspoel and C. A. Isles. Digitized precision measurements of the movements of sea urchin sperm flagella. *Biophys. J.*, 47:395–410, 1985.

[2] L. Turner, W. S. Ryu, and H. C. Berg. Real-time imaging of fluorescent flagellar filaments. *J. Bacteriol.*, 182:2793–2801, 2000.

[3] S. L. Tamm. Ciliary motion in Paramecium: A scanning electron microscope study. *J. Cell Biol.*, 55:250–255, 1972.

[4] B. Baccetti. Insect sperm cells. *Adv. Insect Physiol.*, 9:315–397, 1972.

[5] S. K. Curtis and D. B. Benner. Movement of spermatozoa of Megaselia scalaris (Diptera: Brachycera: Cyclorrhapha: Phoridae) in artificial and natural fluids. *J. Morphol.*, 210:85–99, 1991.

[6] J. R. Linley. Activity and motility of spermatozoa of Culicoides melleus (Diptera: Ceratopogonidae). *Entomol. Exp. Appl.*, 26:85–96, 1979.

[7] B. Baccetti, A. G. Burrini, R. Dallai, F. Giusti, M. Mazzini, T. Renieri, F. Rosati, and G. Selmi. Structure and function in the spermatozoon of Tenebrio molitor (the spermatozoon of Arthropoda. XX). *J. Mechanochem. Cell Motil.*, 2:149–161, 1973.

[8] C. Bressac, D. Joly, J. Devaux, C. Serres, D. Feneus, and D. Lachaise. Comparative kinetics of short and long sperm in sperm dimorphic Drosophila species. *Cell Motil. Cytoskel.*, 19:269–274, 1991.

[9] D. M. Phillips. Structural variants in invertebrate sperm flagella and their relationship to motility. In M. A. Sleigh, editor, *Cilia and Flagella*, pages 379–402. Academic Press, London, New York, 1974.

[10] M. A. Swan. The generation and propagation of double waves in mosquito (Aedes notoscriptus) sperm-tails. *Gamete Res.*, 4:241–250, 1981.

[11] B. Baccetti, A. G. Burrini, R. Dallai, V. Pallini, P. Periti, F. Piantelli, F. Rosati, and G. Selmi. Structure and function in the spermatozoon of

Bacilus rossius: The spermatozoon of Arthropoda. XIX. *J. Ultrastruct. Res.*, 44:1–73, 1973.

[12] M. Werner and L. W. Simmons. Insect sperm motility. *Biol. Rev.*, 83:191–208, 2008.

[13] B. Baccetti, B. H. Gibbons, and I. R. Gibbons. Bidirectional swimming in spermatozoa of Tephritid flies. *J Submicrosc. Cytol. Pathol.*, 21:619–625, 1989.

[14] A. A. Biewener. *Animal Locomotion*. Oxford University Press, Oxford, New York, 2003.

[15] L. J. Fauci and R. Dillon. Biofluidmechanics of reproduction. *Annu. Rev. Fluid Mech.*, 38:371–394, 2006.

[16] E. Lauga and T. Powers. The hydrodynamics of swimming microorganisms. *Rep. Prog. Phys.*, 72:096601, 2009.

[17] C. Brennen and H. Winet. Fluid mechanics of propulsion by cilia and flagella. *Annu. Rev. Fluid Mech.*, 9:339–398, 1977.

[18] E. M. Purcell. Life at low Reynolds number. *Am. J. Phys.*, 45:3–11, 1977.

[19] B. J. Nelson, I. K. Kaliakatsos, and J. J. Abbott. Microrobots for minimally invasive medicine. *Annu. Rev. Biomed. Eng.*, 12:55–85, 2010.

[20] E. Lauga. Life around the scallop theorem. *Soft Matt.*, 7:3060–3065, 2011.

[21] Joseph Wang. Can man-made nanomachines compete with nature biomotors? *ACS Nano*, 3:4–9, 2009.

[22] T. Mirkovic, N.S. Zacharia, G. D. Scholes, and G. A. Ozin. Fuel for thought: chemically powered nanomotors out-swim nature's flagellated bacteria. *ACS Nano*, 4:1782–1789, 2010.

[23] T. E. Mallouk and A. Sen. Powering nanorobots. *Sci. Am.*, 300:72–77, 2009.

[24] S. J. Ebbens and J. R. Howse. In pursuit of propulsion at the nanoscale. *Soft Matt.*, 6:726–738, 2010.

[25] J. B. Shukla, B. R. P. Rao, and R. S. Parihar. Swimming of spermatozoa in cervix: Effects of dynamical interaction and peripheral layer viscosity. *J. Biomech.*, 11:15–19, 1978.

[26] D. F. Katz, R. N. Mills, and T. R. Pritchett. The movement of human spermatozoa in cervical mucus. *J. Reprod. Fertil.*, 53:259–265, 1978.

[27] D. F. Katz and A. A. Berger. Flagellar propulsion of human-sperm in cervical-mucus. *Biorheology*, 17:169–175, 1980.

[28] D. F. Katz, T. D. Bloom, and R. H. Bondurant. Movement of bull spermatozoa in cervical mucus. *Biol. Reprod.*, 25:931–937, 1981.

[29] R. Rikmenspoel. Movement and active moments of bull sperm flagella as a function of temperature and viscosity. *J. Exp. Biol.*, 108:205, 1984.

[30] S. Ishijima, S. Oshio, and H. Mohri. Flagellar movement of human spermatozoa. *Gamete Res.*, 13:185–197, 1986.

[31] S. S. Suarez and X Dai. Hyperactivation enhances mouse sperm capacity for penetrating viscoelastic media. *Biol. Reprod.*, 46:686–691, 1992.

[32] S. Childress. *Mechanics of Swimming and Flying*. Cambridge University Press, Cambridge, UK, 1981.

[33] D. Bray. *Cell Movements*. Garland Publishing, New York, NY, 2000.

[34] G. I. Taylor. Analysis of the swimming of microscopic organisms. *Proc. R. Soc. Lond. A*, 209:447–461, 1951.

[35] J. E. Drummond. Propulsion by oscillating sheets and tubes in a viscous fluid. *J. Fluid Mech.*, 25:787–793, 1966.

[36] A. J. Reynolds. The swimming of minute organisms. *J. Fluid Mech.*, 23:241–260, 1965.

[37] E. O. Tuck. A note on a swimming problem. *J. Fluid Mech.*, 31:305–308, 1968.

[38] T. Y. T. Wu. Swimming of a waving plate. *J. Fluid Mech.*, 10:321–344, 1961.

[39] T. Y. T. Wu. Hydrodynamics of swimming propulsion. Part 1. Swimming of a two-dimensional flexible plate at variable speeds in an inviscid fluid. *J. Fluid Mech.*, 46:337–355, 1961.

[40] S. Childress. Inertial swimming as a singular perturbation. In *Proc. ASME 2008 Dynamic Systems and Control Conference*, Ann Arbor, Michigan, USA, 20-22 October 2008. DSCC2008210.

[41] J. R. Blake. Infinite models for ciliary propulsion. *J. Fluid Mech.*, 49:209–222, 1971.

[42] M. Jaffrin and A. Shapiro. Peristaltic pumping. *Annu. Rev. Fluid Mech.*, 3:13–36, 1971.

[43] S. S. Suarez and A. A. Pacey. Sperm transport in the female reproductive tract. *Hum. Reprod. Update*, 12:23–37, 2006.

[44] W. J. Shack and T. J. Lardner. A long wavelength solution for a microorganism swimming in a channel. *Bull. Math. Biol.*, 36:435–444, 1974.

[45] D. F. Katz. On the propulsion of microorganisms near solid boundaries. *J. Fluid Mech.*, 64:33–49, 1974.

[46] R. E. Smelser, W.J. Shack, and T.J. Lardner. The swimming of spermatozoa in an active channel. *J. Biomech.*, 7:349–355, 1974.

[47] J. B. Shukla, P. Chandra, and R. Sharma. Effects of peristaltic and longitudinal wave motion of the channel wall of movement of micro-organisms: application to spermatozoa transport. *J. Biomech.*, 21:947–954, 1988.

[48] T. K. Chaudhury. On swimming in a visco-elastic liquid. *J. Fluid Mech.*, 95:189–197, 1979.

[49] L. D. Sturges. Motion induced by a waving plate. *J. Non-Newt. Fluid Mech.*, 8:357–364, 1981.

[50] G. R. Fulford, D. F. Katz, and R. L. Powell. Swimming of spermatozoa in a linear viscoelastic fluid. *Biorheology*, 35:295–309, 1998.

[51] E. Lauga. Propulsion in a viscoelastic fluid. *Phys. Fluids*, 19:083104, 2007.

[52] M. E. Erdogan. A note on an unsteady flow of a viscous fluid due to an oscillating plane wall. *Int. J. Nonlinear Mech.*, 35:1–6, 2000.

[53] P. P. Valkó and J. Abate. Comparison of sequence accelerators for the gave method of numerical laplace transform inversion. *Comput. Math. Appl.*, 48:629–636, 2004.

[54] B. G. M. Jamieson, R. Dallai, and B. A. Afzelius. *Insects: Their Spermatozoa and Phylogeny*. Science Publishers Inc., Enfield, New Hampshire, USA, 1999.

[55] E. H. Morrow. How the sperm lost its tail: the evolution of aflagellate sperm. *Biol. Rev.*, 79:795–814, 2004.

[56] M. Werner, T. Tscheulin, T. Speck, D. Zissler, and K. Peschke. Ultrastructure and motility pattern of the spermatozoa of Aleochara curtula (Coleoptera, Staphylinidae). *Arth. Struct. & Dev.*, 31:243–254, 2002.

[57] M. Werner, C. Gack, T. Speck, and K. Peschke. Queue up, please! Spermathecal filling in the rove beetle Drusilla canaliculata (Coleoptera, Staphylinidae). *Naturwissenschaften*, 94:837–841, 2007.

[58] S. Jung, K. Mareck, L. Fauci, and M. Shelley. Rotational dynamics of a superhelix towed in a Stokes fluid. *Phys. Fluids*, 19:103105, 2007.

[59] C. H. Wiggins, D. Riveline, A. Ott, and R. E. Goldstein. Trapping and wiggling: elastohydrodynamics of driven microfilaments. *Biophys. J.*, 74:1043–1060, 1998.

[60] T. S. Yu, E. Lauga, and A. E. Hosoi. Experimental investigations of elastic tail propulsion at low reynolds number. *Phys. Fluids*, 18:091701, 2006.

[61] I. H. Riedel-Kruse, A. Hilfinger, J. Howard, and F. Julicher. How molecular motors shape the flagellar beat. *HFSP J.*, 1:192–208, 2007.

[62] R. E. Johnson. An improved slender-body theory for stokes flow. *J. Fluid Mech.*, 99:411–431, 1980.

[63] K. E. Atkinson. *The Numerical Solution of Integral Equations of the Second Kind*. Cambridge University Press, Cambridge, U. K., 1997.

[64] T. Götz. *Interactions of fibers and flow: asymptotics, theory and numerics*. PhD thesis, University of Kaiserslautern, Germany, 2000.

[65] A. K. Tornberg and M. J. Shelley. Simulating the dynamics and interactions of flexible fibers in stokes flows. *J. Comput. Phys.*, 196:8–40, 2004.

[66] J. Lighthill. *Mathematical Biofluiddynamics*. SIAM, Philadelphia, PA, 1975.

[67] S. Chattopadhyay, R. Moldovan, C. Yeung, and X. L. Wu. Swimming efficiency of bacterium Escherichia coli. *Proc. Natl. Acad. Sci. U.S.A.*, 103:13712–13717, 2006.

[68] S. E. Spagnolie and E. Lauga. The optimal elastic flagellum. *Phys. Fluids*, 22:031901, 2010.

[69] S. E. Spagnolie and E. Lauga. Comparative hydrodynamics of bacterial polymorphism. *Phys. Rev. Lett.*, 106:058103, 2011.

[70] A. T. Chwang and T. Y. Wu. A note on the helical movement of microorganisms. *Proc. R. Soc. Lond. B*, 178:327–346, 1971.

[71] J. B. Keller and S. I. Rubinow. Swimming of flagellated microorganisms. *Biophys. J.*, 16:151–170, 1976.

[72] L. Margulis, M. Chapman, R. Guerrero, and J. Hall. The last eukaryotic common ancestor (leca): Acquisition of cytoskeletal motility from aerotolerant spirochetes in the proterozoic eon. *Proc. Natl. Acad. Sci. U.S.A.*, 103:13080–13085, 2006.

[73] D. Nicastro, J. R. McIntosh, and W. Baumeister. 3d structure of eukaryotic flagella in a quiescent state revealed by cryo-electron tomography. *Proc. Natl. Acad. Sci. U.S.A.*, 102:15889–15894, 2005.

[74] S. Chattopadhyay and X. L. Wu. The effect of long-range hydrodynamic interaction on the swimming of a single bacterium. *Biophys. J.*, 96:2023–2028, 2009.

[75] G. I. Taylor. The action of waving cylindrical tails in propelling microscopic organisms. *Proc. R. Soc. Lond. A*, 211:225–239, 1952.

[76] L. E. Becker, S. A. Koehler, and H. A. Stone. On self-propulsion of micromachines at low reynolds number: Purcell's three-link swimmer. *J. Fluid Mech.*, 490:15–35, 2003.

[77] O. S. Pak and E. Lauga. Extensibility enables locomotion under isotropic drag. *Phys. Fluids*, 23:081702, 2011.

[78] H. Nguyen, R. Ortiz, R. Cortez, and L. Fauci. The action of waving cylindrical rings in a viscous fluid. *J. Fluid Mech.*, 671:574–586, 2011.

[79] B. H. Gibbons, B. Baccetti, and I. R. Gibbons. Live and reactivated motility in the 9+0 flagellum of Anguilla sperm. *Cell Motil.*, 5:333–350, 1985.

[80] L. Zhang, J. J. Abbott, L. Dong, K. E. Peyer, B. E. Kratochvil, H. Zhang, C. Bergeles, and B. J. Nelson. Characterizing the swimming properties of artificial bacterial flagella. *Nano Lett.*, 9:3663–3667, 2009.

[81] A. Ghosh and P. Fischer. Controlled propulsion of artificial magnetic nanostructured propellers. *Nano Lett.*, 9:2243–2245, 2009.

[82] P. Tierno, R. Golestanian, I. Pagonabarraga, and F. Sagués. Controlled swimming in confined fluids of magnetically actuated colloidal rotors. *Phys. Rev. Lett.*, 101:218304, 2008.

[83] P. Tierno, O. Güell, F. Sagués, R. Golestanian, and I. Pagonabarraga. Controlled propulsion in viscous fluids of magnetically actuated colloidal doublets. *Phys. Rev. E*, 81:011402, 2010.

[84] C. E. Sing, L. Schmid, M. F. Schneider, T. Franke, and A. Alexander-Katz. Controlled surface-induced flows from the motion of self-assembled colloidal walkers. *Proc. Natl. Acad. Sci. U.S.A.*, 107:535–540, 2010.

[85] L. Zhang, T. Petit, Y. Lu, B. E. Kratochvil, K. E. Peyer, R. Pei, J. Lou, and B. J. Nelson. Controlled propulsion and cargo transport of rotating nickel nanowires near a patterned solid surface. *ACS Nano*, 4:6228–6234, 2010.

[86] R. Dreyfus, J. Baudry, M. L. Roper, M. Fermigier, H. A. Stone, and J. Bibette. Microscopic artificial swimmsers. *Nature*, 437:862–865, 2005.

[87] W. Gao, S. Sattayasamitsathit, K. M. Manesh, D. Weihs, and J. Wang. Magnetically powered flexible metal nanowire motors. *J. Am. Chem. Soc.*, 132:14403–14405, 2010.

[88] Y. W. Kim and R. R. Netz. Pumping fluids with periodically beating grafted elastic filaments. *Phys. Rev. Lett.*, 96:158101, 2006.

[89] M. Manghi, X. Schlagberger, and R. R. Netz. Propulsion with a rotating elastic nanorod. *Phys. Rev. Lett.*, 96:068101, 2006.

[90] H. Wada and R. R. Netz. Non-equilibrium hydrodynamics of a rotating filament. *Europhys. Lett.*, 75:645–651, 2006.

[91] N. Coq, O. du Roure, J. Marthelot, D. Bartolo, and M. Fermigier. Rotational dynamics of a soft filament: Wrapping transition and propulsive forces. *Phys. Fluids*, 20:051703, 2008.

[92] N. Coq, O. du Roure, M. Fermigier, and D. Bartolo. Helical beating of an actuated elastic filament. *J. Phys.: Condens. Matter*, 21:204109, 2009.

[93] B. Qian, T. R. Powers, and K. S. Breuer. Shape transition and propulsive force of an elastic rod rotating in a viscous fluid. *Phys. Rev. Lett.*, 100:078101, 2008.

[94] N. Coq, S. Ngo, O. du Roure, M. Fermigier, and D. Bartolo. Three-dimensional beating of magnetic microrods. *Phys. Rev. E*, 82:041503, 2010.

[95] M. T. Downton and H. Stark. Beating kinematics of magnetically actuated cilia. *Europhys. Lett.*, 85:44002, 2009.

[96] E. E. Keaveny and M. R. Maxey. Spiral swimming of an artificial micro-swimmer. *J. Fluid Mech.*, 598:293–319, 2008.

[97] K. E. Machin. Wave propagation along flagella. *J. Exp. Biol.*, 35:796–806, 1958.

[98] C. H. Wiggins and R. E. Goldstein. Flexive and propulsive dynamics of elastica at low reynolds number. *Phys. Rev. Lett.*, 80:3879–3882, 1998.

[99] C. P Lowe. Dynamics of filaments: modelling the dynamics of driven microfilaments. *Philos. T. R. Soc. B*, 358:1543–1550, 2003.

[100] T. R. Powers. Role of body rotation in bacterial flagellar bundling. *Phys. Rev. E*, 65:040903, 2002.

[101] E. Lauga. Floppy swimming: Viscous locomotion of actuated elastica. *Phys. Rev. E*, 75:041916, 2007.

[102] L. D. Landau and E. M. Lifshitz. *Theory of Elasticity*. Pergamon Press, Oxford, 1986.

[103] J. Gray and G. J. Hancock. The propulsion of sea-urchin spermatozoa. *J. Exp. Biol.*, 32:802–814, 1955.

[104] S. Fujime, M. Maruyama, and S. Asakura. Flexural rigidity of bacterial flagella studied by quasielastic scattering of laser light. *J. Mol. Biol.*, 68:347–354, 1972.

[105] H. Hoshikawa and R Kamiya. Elastic properties of bacterial flagellar filaments: Ii. determination of the modulus of rigidity. *Biophys. Chem.*, 22:159–166, 1985.

[106] R. Cortez, L. Fauci, N. Cowen, and R. Dillon. Simulation of swimming organisms: coupling internal mechanics with external fluid dynamics. *Comput. Sci. Eng.*, 6:38–45, 2004.

[107] G.J. Hancock. The self-propulsion of microscopic organisms through liquids. *Proc. R. Soc. Lond. A*, 217:96–121, 1953.

[108] J. Happel and H. Brenner. *Low Reynolds number hydrodynamics: with special applications to particulate media*. Noordhoff International Publishing, Netherlands, 1973.

[109] S. Camalet and F. Julicher. Generic aspects of axonemal beating. *New J. Phys.*, 2:24, 2000.

[110] A. M. Leshansky. Enhanced low-Reynolds-number propulsion in heterogeneous viscous environments. *Phys. Rev. E*, 80:051911, 2009.

[111] S. Jung. Caenorhabditis elegans swimming in a saturated particulate system. *Phys. Fluids*, 22:031903, 2010.

[112] R. Soller and S. A. Koehler. Drag and lift on rotating vanes in granular beds. *Phys. Rev. E*, 74:021305, 2006.

[113] G. Hill, S. Yeung, and S. A. Koehler. Scaling vertical drag forces in granular media. *Europhys. Lett.*, 72:137–143, 2005.

[114] Y. Ding, N. Gravish, and D. I. Goldman. Drag induced lift in granular media. *Phys. Rev. Lett.*, 106:028001, 2011.

[115] N. Gravish, P. B. Umbanhowar, and D. I. Goldman. Force and flow transition in plowed granular media. *Phys. Rev. Lett.*, 105:128301, 2010.

[116] R. D. Maladen, Y. Ding, C. Li, and D. I. Goldman. Undulatory swimming in sand: Subsurface locomotion of the sandfish lizard. *Science*, 325:314–318, 2009.

[117] J. Lighthill. Flagellar hydrodynamics: The john von neumann lecture, 1975. *SIAM Rev.*, 18:161–230, 1976.

[118] L. Bourdieu, T. Duke, M. B. Elowitz, D. A. Winkelmann, S. Leibler, and A. Libchaber. Spiral defects in motility assays: A measure of motor protein force. *Phys. Rev. Lett.*, 75:176–179, 1995.

[119] R. E. Goldstein and S. A. Langer. Nonlinear dynamics of stiff polymers. *Phys. Rev. Lett.*, 75:1094–1097, 1995.

[120] R. E. Goldstein, T. R. Powers, and C. H. Wiggins. Viscous nonlinear dynamics of twist and writhe. *Phys. Rev. Lett.*, 80:5232–5235, 1998.

[121] M. J. Shelley and T. Ueda. The stokesian hydrodynamics of flexing, stretching filaments. *Physica D*, 146:221–245, 2000.

[122] I. Miyasaka, K. Nanba, K. Furuya, Y. Nimura, and A. Azuma. Functional roles of the transverse and longitudinal flagella in the swimming motility of prorocentrum minimum (dinophyceae). *J. Exp. Biol.*, 207:3055–3066, 2004.

[123] A. K. Bentley, J. S. Trethewey, A. B. Ellis, and W. C. Crone. Magnetic manipulation of copper-tin nanowires capped with nickel ends. *Nano Lett.*, 4:487–490, 2004.

[124] K. Keshoju, H. Xing, and L. Sun. Magnetic field driven nanowire rotation in suspension. *Appl. Phys. Lett.*, 91:123114, 2007.

[125] J. M. Samet and P. W. Cheng. The role of airway mucus in pulmonary toxicology. *Environ. Health Persp.*, 102:89–103, 1994.

[126] A. I. Yudin, F. W. Hanson, and D. F. Katz. Human cervical mucus and its interaction with sperm: a fine-structural view. *Biol. Reprod.*, 40:661–671, 1989.

[127] M. W. Denny and J. M. Gosline. The physical-properties of the pedal mucus of the terrestrial slug, ariolimax-columbianus. *J. Exp. Biol.*, 88:375–393, 1980.

[128] R. H. Ewoldt, C. Clasen, A. E. Hosoi, and G. H. McKinley. Rheological fingerprinting of gastropod pedal mucus and synthetic complex fluids for biomimicking adhesive locomotion. *Soft Matter*, 3:634–643, 2007.

[129] R. H. Ewoldt, A. E. Hosoi, and G. H. McKinley. New measures for characterizing nonlinear viscoelasticity in large amplitude oscillatory shear. *J. Rheol.*, 52:1427–1458, 2008.

[130] J. G. Oldroyd. On the formulation of rheological equations of state. *Proc. R. Soc. Lond. A*, 200:523–541, 1950.

[131] R. B. Bird, R. C. Armstrong, and O. Hassager. *Dynamics of Polymeric Liquids*, volume 1. Wiley-Interscience, New York, 2 edition, 1987.

[132] R. B. Bird, C. F. Curtiss, R. C. Armstrong, and O. Hassager. *Dynamics of Polymeric Liquids*, volume 2. Wiley-Interscience, New York, 2 edition, 1987.

[133] M. W. Johnson and D. Segalman. Model for viscoelastic fluid behaviour which allows non-affine deformation. *J. Non-Newt. Fluid Mech.*, 24:255–270, 1977.

[134] H. C. Fu, T. R. Powers, and C. W. Wolgemuth. Theory of swimming filaments in viscoelastic media. *Phys. Rev. Lett.*, 99:258101, 2007.

[135] E. Lauga. Life at high Deborah number. *Europhys. Lett.*, 86:64001, 2009.

[136] Thibaud Normand and Eric Lauga. Flapping motion and force generation in a viscoelastic fluid. *Phys. Rev. E*, 78:061907, 2008.

[137] I. R. Gibbons. Cilia and flagella of eukaryotes. *J. Cell Biol.*, 91:107s–124s, 1981.

[138] T. L. Jahn, M. D. Landman, and J. R. Fonseca. The mechanism of locmotion in flagellates. ii. function of the mastigonemes of ochromonas. *J. Protozool*, 11:291–296, 1964.

[139] M. E. J. Holwill and M. A. Sleigh. Propulsion by hispid flagella. *J. Exp. Biol.*, 47:267–276, 1967.

[140] C. Brennen. Locomotion of flagellates with mastigonemes. *J. Mechanochem. Cell Motil.*, 3:207–217, 1976.

[141] M. Faraday. On a peculiar class of accoustical figures; and on certain forms assumed by groups of particles upon vibrating elastic surfaces. *Trans. Roy. Soc. London*, 121:229–340, 1831.

[142] J. W. S. Rayleigh. *The Theory of Sound.* Dover Publications, New York, 1945.

[143] H. Schlichting. *Boundary-Layer Theory.* McGraw-Hill, New York, 1968.

[144] N. Riley. Oscillatory viscous flows. review and extension. *J. Inst. Maths. Applics.*, 3:419–434, 1967.

[145] C. Chang and W. Schowalter. Flow near an oscillating cylinder in dilute viscoelastic fluid. *Nature*, 252:686–688, 1974.

[146] P. W. James. Elastico-viscous flow around a circular cylinder executing small amplitude, high frequency oscillations. *J. Non-Newt. Fluid Mech.*, 2:99–107, 1977.

[147] S. Rosenblat. Reversal of secondary flow in non-newtonian fluids. *J. Fluid Mech.*, 85:387–400, 1978.

[148] G. Bohme. On steady streaming in viscoelastic liquids. *J. Non-Newt. Fluid Mech.*, 44:149–170, 1992.

[149] K. C. Bagchi. Flow of non-newtonian fluid contained in a fixed circular cylinder due to the longitudinal oscillation of a concentric circular cylinder. *Appl. Sci. Res.*, 16:131–140, 1966.

[150] K. R. Frater. Acoustic streaming in an elastico-viscous fluid. *J. Fluid Mech.*, 30:689–697, 1967.

[151] K. R. Frater. Drag on a circular cylinder oscillating in an elastico-viscous fluid. *Z. Angew. Math. Phys.*, 19:510–512, 1968.

[152] C. Goldstein and W. R. Schowalter. Further studies of fluid nonlinearity: The orthogonal rheometer and the oscillating sphere. *Trans. Soc. Rheol.*, 19:1–19, 1975.

[153] C. F. Chang. Boundary layer analysis of oscillating cylinder flows in a viscoelastic liquid. *Z. Angew. Math. Phys.*, 28:283–288, 1977.

[154] C. F. Chang and W. R. Schowalter. Secondary flow in the neighborhood of a cylinder oscillating in a viscoelastic fluid. *J. Non-Newt. Fluid Mech..*, 6:47–67, 1979.

[155] A. Groisman, M. Enzelberger, and S. R. Quake. Microfluidic memory and control devices. *Science*, 300:955–958, 2003.

[156] A. Groisman and S. R. Quake. A microfluidic rectifier: Anisotropic flow resistance at low reynolds numbers. *Phys. Rev. Lett.*, 92:094501, 2004.

[157] H. K. Moffatt. Viscous and resistive eddies near a sharp corner. *J. Fluid Mech.*, 18:1–18, 1964.

[158] J. R. Blake and M. A. Sleigh. Mechanics of ciliary locomotion. *Biol. Rev.*, 49:85–125, 1974.

[159] S. H. Hwang, M. Litt, and W. C. Forsman. Rheological properties of mucus. *Rheol. Acta*, 8:438–448, 1969.

[160] A. Gilboa and A. Silberberg. In-situ rheological characterization of epithelial mucus. *Biorheology*, 13:59–65, 1976.

[161] S. K. Lai, Y. Y. Wang, D. Wirtz, and J. Hanes. Micro- and macrorheology of mucus. *Adv. Drug Deliver. Rev.*, 61:86–100, 2009.

[162] P. Y. Tam, D. F. Katz, and S. A. Berger. Non-linear viscoelastic properties of cervical-mucus. *Biorheology*, 17:465–478, 1980.

[163] Ronald G. Larson. *The Structure and Rheology of Complex Fluids*. Oxford University Press, New York, NY, 1999.

[164] F. A. Morrison. *Understanding Rheology*. Oxford University Press, New York, NY, 2001.

[165] M. A. Sleigh, J. R. Blake, and N. Liron. The propulsion of mucus by cilia. *Am. Rev. Respir. Dis.*, 137:726–741, 1988.

[166] C. Montecucco and R. Rappuoli. Living dangerously: how helicobacter pylori survives in the human stomach. *Nat. Rev. Mol. Cell Biol.*, 2:457–466, 2001.

[167] C. W. Wolgemuth, N. W. Charon, S. F. Goldstein, and R. E. Goldstein. The flagellar cytoskeleton of the spirochetes. *J. Mol. Microbiol. Biotechnol.*, 11:221–227, 2006.

[168] George O'Toole, Heidi B. Kaplan, and Roberto Kolter. Biofilm formation as microbial development. *Annu. Rev. Microbiol.*, 54:49–79, 2000.

[169] R. M. Donlan and J. W. Costerton. Biofilms: Survival mechanisms of clinically relevant microorganisms. *Clinic. Microbiol. Rev.*, 15:167–193, 2002.

[170] J W Costerton, K J Cheng, G G Geesey, T I Ladd, J C Nickel, M Dasgupta, and T J Marrie. Bacterial biofilms in nature and disease. *Annu. Rev. Microbiol.*, 41:435–464, 1987.

[171] J W Costerton, Z Lewandowski, D E Caldwell, D R Korber, and H M Lappin-Scott. Microbial biofilms. *Annu. Rev. Microbiol.*, 49:711–745, 1995.

[172] J. N. Wilking, T. E. Angelini, A. Seminara, M. P. Brenner, and D. A. Weitz. Biofilms as complex fluids. *MRS Bull.*, 36:385–391, 2011.

[173] H. C. Fu, C. W. Wolgemuth, and T. R. Powers. Beating patterns of filaments in viscoelastic fluids. *Phys. Rev. E*, 78:041913, 2008.

[174] M. W. Harman, S. M. Dunham-Ems, M. J. Caimano, A. A. Belperron, L. K. Bockenstedt, H. C. Fu, J. D. Radolf, and C. W. Wolgemuth. The heterogeneous motility of the lyme disease spirochete in gelatin mimics dissemination through tissue. *Proc. Natl. Acad. Sci. U.S.A.*, 109:3059–3064, 2012.

[175] H. C. Fu, C. W. Wolgemuth, and T. R. Powers. Swimming speeds of filaments in nonlinearly viscoelastic fluids. *Phys. Fluids*, 21:033102, 2009.

[176] J. Teran, L. J. Fauci, and M. Shelley. Viscoelastic fluid response can increase the speed and efficiency of a free swimmer. *Phys. Rev. Lett.*, 104:038101, 2010.

[177] X. N. Shen and P. E. Arratia. Undulatory swimming in viscoelastic fluids. *Phys. Rev. Lett.*, 106:208101, 2011.

[178] B. Liu, T. R. Powers, and K. S. Breuer. Force-free swimming of a model helical flagellum in viscoelastic fluids. *Proc. Natl. Acad. Sci. U.S.A.*, 108:19516–19520, 2011.

[179] O. S. Pak, T. Normand, and E. Lauga. Pumping by flapping in a viscoelastic fluid. *Phys. Rev. E*, 81:036312, 2010.

[180] G. J. Elfring, O. S. Pak, and E. Lauga. Two-dimensional flagellar synchronization in viscoelastic fluids. *J. Fluid Mech.*, 646:505–515, 2010.

[181] A. S. Wineman and A.C. Pipkin. Slow viscoelastic flow in tilted troughs. *Acta Mech.*, 2:104–115, 1966.

[182] R. I. Tanner. Some methods for estimating the normal stress functions in viscometric flows. *Trans. Roc. Rheol.*, 14:483–507, 1970.

[183] E. Couturier, F. Boyer, O. Pouliquen, and E. Guazzelli. Suspensions in a tilted trough: second normal stress difference. *J. Fluid Mech.*, 686:26–39, 2011.

[184] E. E. Brown, W. R. Burghardt, H. Kahvand, and D. C. Venerus. Comparison of optical and mechanical measurements of second normal stress difference relaxation following step strain. *Rheol. Acta*, 34:221–234, 1995.

[185] S. G. Baek and J. J. Magda. Monolithic rheometer plate fabricated using silicon micromachining technology and containing miniature pressure sensors for N_1 and N_2 measurements. *J. Rheol.*, 47:1249–1260, 2003.

[186] A. Kulkarni, S. Kharchenko, and R. Kannan. Rheo-optical measurements of the first and third normal stresses of homopolymer poly(vinyl methyl ether) melt. *Rheol. Acta*, 45:951–958, 2006.

[187] T. Schweizer. Measurement of the first and second normal stress differences in a polystyrene melt with a cone and partitioned plate tool. *Rheol. Acta*, 41:337–344, 2002.

[188] A. S. Khair and T. M. Squires. Active microrheology: A proposed technique to measure normal stress coefficients of complex fluids. *Phys. Rev. Lett.*, 105:156001, 2010.

[189] T. M. Squires and T. G. Mason. Fluid mechanics of microrheology. *Annu. Rev. Fluid Mech.*, 42:413–438, 2010.

[190] T. A. Waigh. Microrheology of complex fluids. *Rep. Prog. Phys.*, 68:685–742, 2005.

[191] D Weihs, T G Mason, and M A Teitell. Bio-microrheology: A frontier in microrheology. *Biophys. J.*, 91:4296–4305, 2006.

[192] D. Wirtz. Particle-tracking microrheology of living cells: Principles and applications. *Annu. Rev. Biophys.*, 38:301–326, 2009.

[193] T. M. Squires. Nonlinear microrheology: Bulk stresses versus direct interactions. *Langmuir*, 24:1147–1159, 2008.

[194] E. F. Lee, D. L. Koch, and Y. L. Joo. Cross-stream forces and velocities of fixed and freely suspended particles in viscoelastic poiseuille flow: Perturbation and numerical analyses. *J. Non-Newt. Fluid*, 165:1309–1327, 2010.

[195] R. Guénette and M. Fortin. A new mixed finite element method for computing viscoelastic flows. *J. Non-Newt. Fluid Mech.*, 60:27 – 52, 1995.

[196] A. W. Liu, D. E. Bornside, R. C. Armstrong, and R. A. Brown. Viscoelastic flow of polymer solutions around a periodic, linear array of cylinders: comparisons of predictions for microstructure and flow fields. *J. Non-Newt. Fluid Mech.*, 77:153 – 190, 1998.

[197] J. Sun, M. D. Smith, R. C. Armstrong, and R. A. Brown. Finite element method for viscoelastic flows based on the discrete adaptive viscoelastic stress splitting and the discontinuous galerkin method: DAVSS-G/DG. *J. Non-Newt. Fluid Mech.*, 86:281–307, 1999.

[198] J. M. Marchal and M. J. Crochet. A new mixed finite element for calculating viscoelastic flow. *J. Non-Newt. Fluid Mech.*, 26:77–114, 1987.

[199] L. Zhu, E. Lauga, and L. Brandt. Self-propulsion in viscoelastic fluids: pushers vs. pullers. *Phys. Fluids*, 24:051902, 2012.

[200] F. P. T. Baaijens. Mixed finite element methods for viscoelastic flow analysis: a review. *J. Non-Newt. Fluid Mech.*, 79:361–385, 1998.

[201] K. Walters and M. F. Webster. The distinctive CFD challenges of computational rheology. *Int. J. Numer. Meth. Fluids*, 43:577–596, 2003.

[202] W. J. Lunsmann, L. Genieser, R.C. Armstrong, and R.A. Brown. Finite element analysis of steady viscoelastic flow around a sphere in a tube: calculations with constant viscosity models. *J. Non-Newt. Fluid Mech.*, 48:63–99, 1993.

[203] H. Takagi. Slow rotation of two touching spheres in viscous fluid. *J. Phys. Soc. Jpn.*, 36:875–877, 1974.

[204] B. P. Ho and L. G. Leal. Migration of rigid spheres in a two-dimensional unidirectional shear flow of a second-order fluid. *J. Fluid Mech.*, 76:783–799, 2010.

[205] B. Chan, N. J. Balmforth, and A. E. Hosoi. Building a better snail: Lubrication and adhesive locomotion. *Phys. Fluids*, 17:113101, 2005.

[206] P. Brunn. The slow motion of a sphere in a second-order fluid. *Rheol. Acta*, 15:163–171, 1976.

[207] P. Brunn. The behavior of a sphere in non-homogeneous flows of a viscoelastic fluid. *Rheol. Acta*, 15:589–611, 1976.

[208] L. G. Leal. The slow motion of slender rod-like particles in a second-order fluid. *J. Fluid Mech.*, 69:305–337, 1975.

[209] L. G. Leal. Particle motinos in a viscous fluid. *Annu. Rev. Fluid Mech.*, 12:435–476, 1980.

[210] R. J. Phillips. Dynamic simulation of hydrodynamically interacting spheres in a quiescent second-order fluid. *J. Fluid Mech.*, 315:345–365, 1996.

[211] L. G. Leal. *Advanced Transport Phenomena: Fluid Mechanics and Convective Transport Processes*. Cambridge University Press, New York, 2007.

[212] M. B. A. Cooley and M. E. O'Neill. On the slow motion of two spheres in contact along their line of centres through a viscous fluid. *Math. Proc. Cambridge*, 66:407–415, 1969.

[213] G. B. Jeffery. On the steady rotation of a solid of revolution in a viscous fluid. *P. Lond. Math. Soc.*, (Series 2) 14:327–338, 1915.

[214] M. Stimson and G. B. Jeffery. The motion of two spheres in a viscous fluid. *Proc. R. Soc. Lond. A*, 111:110–116, 1926.

[215] H. Brenner. The slow motion of a sphere through a viscous fluid towards a plane surface. *Chem. Eng. Sci.*, 16:242–251, 1961.

[216] A. I. Bishop, T. A. Nieminen, N. R. Heckenberg, and H. Rubinsztein-Dunlop. Optical microrheology using rotating laser-trapped particles. *Phys. Rev. Lett.*, 92:198104, 2004.

[217] M. E. J. Friese, T. A. Nieminen, N. R. Heckenberg, and H. Rubinsztein-Dunlop. Optical alignment and spinning of laser-trapped microscopic particles. *Nature*, 394:348–350, 1998.

[218] G. Knöner, S. Parkin, N. R. Heckenberg, and H. Rubinsztein-Dunlop. Characterization of optically driven fluid stress fields with optical tweezers. *Phys. Rev. E*, 72:031507, 2005.

[219] S. J. Parkin, G. Knöner, T. A. Nieminen, R. Heckenberg, N, and H. Rubinsztein-Dunlop. Picoliter viscometry using optically rotated particles. *Phys. Rev. E*, 76:041507, 2007.